Author:
Faruque, Imad

Title:
Developing indistinguishable heralded single-photon sources in silicon photonics

Developing indistinguishable heralded single-photon sources in silicon photonics

Imad I. Faruque

Primary Supervisor: Prof. Mark G. Thompson
Secondary Supervisor: Prof. John G. Rarity

A dissertation submitted to the University of Bristol in accordance with the requirements for award of the degree of Doctor of Philosophy in the Faculty of Science, School of Physics, May 2018

58599 words

Path entanglement of a pure single-photon propagating in a photonic circuit. This image is drawn by artist Milica Prokic for the *European Researcher's Night 2015* based on the heralded single-photon sources presented in this thesis.

Abstract

Quantum photonics is one of the newest strands of research that shares the border between fundamental science and state of the art technology. Many of the visions of quantum photonics, for example, linear optical quantum computing, require ideal single-photon sources (SPSs). A key pre-requisite of an ideal SPS is the near unity ($> 99\%$) indistinguishability among single-photons from multiple SPSs. This is a true measure of scalability, as multiple indistinguishable SPSs can be integrated on a single chip for performing complex quantum information algorithms. To date, higher than 95% indistinguishability has not been shown in any photonic platform. Silicon on insulator (SOI) photonics is one of the platforms that promises a near ideal heralded SPS. It also offers mature fabrication technology, truly scalable architecture and a roadmap to electronic integration. If higher than 99% indistinguishable SPSs are achieved, it will pave the way to implement adequately complex algorithms that cannot be reproduced using classical computers. The primary focus of this thesis is to investigate ways to achieve and compare indistinguishable heralded SPSs in the SOI photonic platform. Specifically, we have chosen two well-known structures as heralded SPSs: nanowire waveguides and micro-ring resonators. Although the brightness and purity of the single-photons generated in those two structures are investigated both theoretically and experimentally, the indistinguishability data is scarce in the literature. In fact, the indistinguishability of the micro-ring resonator heralded SPSs has not been experimentally demonstrated in SOI or any other photonic platform. The intrinsic resonance enhancement in the resonator predicts high brightness and purity simultaneously with high indistinguishability. Thus, designing and implementing on-chip photon indistinguishability measurement (PIM) circuits for micro-ring resonator SPSs cover a significant portion of this thesis. Also, the purity of the designed heralded SPSs has been simulated, and the effects of the possible imperfections of the PIM circuits along with practical SPSs have been investigated with numerical models. As such, the study presented here provides insights into the indistinguishability of the heralded SPSs to build scalable quantum technologies in SOI photonic platform.

সংক্ষিপ্তসার

কোয়ান্টাম ফোটনিকস মৌলিক বিজ্ঞান এবং সর্বাধুনিক প্রযুক্তির সীমানায় অবস্থানকারী একটি নতুনতম গবেষণার ধারা। কোয়ান্টাম ফোটনিকস এর প্রয়োগগুলোর মধ্যে অন্যতম রৈখিক-আলোক কোয়ান্টাম কম্পিউটিং এর জন্য আদর্শ একক-ফোটন উৎস (SPS) প্রয়োজন। আদর্শ SPS এর একটি প্রধান যোগ্যতা হচ্ছে একাধিক SPS হতে নির্গত একক-ফোটনগুলো প্রায় সম্পূর্ণ (৯৯%) অভিন্ন (indistinguishable) হতে হবে। এই যোগ্যতা আনুপাতিক হারে সার্কিট বড় করার (scalable) একটি সঠিক পরিমাপ, যাতে একটি জটিল কোয়ান্টাম অ্যালগরিদম সম্পাদনের জন্য অনেক অভিন্ন SPS একটি চিপে একত্রিত করা যায়। এখন পর্যন্ত ৯৫% চেয়ে বেশি SPS এর অভিন্নতা কোনও ফোটনিক মাধ্যমেই অর্জিত হয়নি। ফোটনিকস এর মাধ্যমগুলোর মধ্যে একটি বিশেষ মাধ্যম হল সিলিকন অন ইনসুলেটর (SOI) ফোটনিকস যা একটি আদর্শ SPS এর প্রতিশ্রুতি দেয়। এছাড়াও SOI ফোটনিকস এর পরিপক্ক ফ্যাব্রিকেশন প্রযুক্তি, সত্যিকারের স্কেলেবল নির্মাণকৌশল এবং ইলেকট্রনিক ইন্টিগ্রেশন এর একটি রোডম্যাপ আছে। যদি এই মাধ্যমে ৯৯% এর চেয়ে বেশি অভিন্ন SPS অর্জন করা যায়, তাহলে এটি দিয়ে পর্যাপ্ত পরিমানে জটিল অ্যালগরিদম সম্পাদন করা যাবে যা ক্লাসিক্যাল কম্পিউটার দিয়ে করা সম্ভব নয়। অতএব, এই গবেষণার মূল উদ্দেশ্য হল SOI ফোটনিকস ব্যবহার করে অভিন্ন SPS অর্জনের উপায়গুলি খুঁজে বের করা এবং তুলনা করা। এই লক্ষ্যে আমরা দুটি সুপরিচিত কাঠামো বেছে নিয়েছি: ন্যানোওয়ার ওয়েভগাইড এবং মাইক্রো-রিং রেজনেটর। যদিও ঐ দুটি কাঠামো হতে উৎপন্ন একক ফোটন এর উজ্জ্বলতা এবং বিশুদ্ধতা ব্যাপকভাবে তাত্ত্বিক ও পরীক্ষামূলকভাবে গবেষণা করা হয়েছে, কিন্তু অভিন্নতা সক্রান্ত তথ্য অপ্রতুল। শুধুমাত্র তিনটি পরীক্ষা এখন পর্যন্ত ওয়েভগাইড এর অভিন্নতা গবেষণা করেছে। আর মাইক্রো-রিং রেজনেটর এর অভিন্নতা SOI অথবা অন্য কোনও মাধ্যমেই পরীক্ষা করা হয়নি। যেহেতু রেজনেটর এর অনুনাদকতা একক ফোটন এর উচ্চ উজ্জ্বলতার এবং বিশুদ্ধতার প্রতিশ্রুতি দেয়, সুতরাং মাইক্রো-রিং রেজনেটর SPS এর জন্য একই-চিপে ফোটন অভিন্নতার পরিমাপ (PIM) সার্কিট ডিজাইন এবং বাস্তবায়ন এই প্রবেন্ধর একটি গুরুত্বপূর্ণ অংশ। এছাড়াও, এখানে ব্যবহৃত একক-ফোটন উৎসের বিশুদ্ধতা সিমুলেশন করা হয়েছে এবং PIM সার্কিটের সম্ভাব্য ত্রুটির প্রভাব সাংখ্যিক মডেল দিয়ে পরীক্ষা করা হয়েছে। সার্বিকভাবে, এই প্রবন্ধে উপস্থাপিত একক-ফোটন উৎসের গবেষণা SOI ফোটনিকস দিয়ে স্কেলেবল কোয়ান্টাম প্রযুক্তি নির্মাণের জন্য অন্তর্দৃষ্টি প্রদান করে।

Dedication and Acknowledgements

First of all, I would like to thank my primary supervisor Mark for offering me a PhD project in silicon quantum photonics on an exciting topic. I have loved the project and came to enjoy all the little quarks the experiments offered. I also want to thank my secondary supervisor John for his valuable scientific insights. My heartfelt thanks to EU for providing the PhD fellowship through Marie Curie ITN, PICQUE.

Before I joined CQP (which later became QET Labs), the last experiment with micro-ring resonator sources was done by Damien, Erman and Josh on achieving higher brightness. I started my PhD where others left off (graduated!), that is investigating purity and indistinguishability of heralded single-photon sources (especially resonant structures) for quantum technologies. Therefore, a special thank goes to Damien for instigating the on-chip PIM circuits at the very beginning of my PhD. The collective knowledge contributed by all the members (past & present) of the QET Labs and the common drive and aspirations for building large, complex and scalable quantum photonic circuits have certainly influenced me, for which, I want to thank all the members of the QET Labs including the ones I never met.

I sincerely appreciate the constructive criticisms provided by Dr Graham Marshall and Dr Gary Sinclair on my scientific discourse and thesis writing style, without which many finer arguments in this thesis would have been obscured.

I am also thankful to Dr Andrew Murray for wire-bonding the chip; Adrian Crimp, Josh Hugo, Patrick Alexander, Bart Dworzanski for making various mechanical parts for the experiments and Magnus Loutit for helping with various electronics.

A special thank also goes to Gary for providing pastoral care from time to time. I also want to thank my friends and colleagues (in no particular order) Jorge, Jorge, Andy, Javier, Döndu, Laurent, Jianwei, Phil, Josh, Dan, Jeremy, Will, Euan, Gerardo, Milica, Alex, Caroline, Kim, Briony and many others for making my PhD more interesting.

I am grateful to my parents, brother, sister-in-law and my nephew for supports throughout my PhD. Knowing our place in the midst of society is essential to carry out sound research. Therefore, I dedicate this work to humanity.

Contributions

Our *heralded single-photon sources in silicon photonics* group has three members, Dr Damien Bonneau, Dr Gary F. Sinclair and I. We often had meetings discussing simulation & experimental results. Therefore, claiming individual ownership for a concerted effort belittles everyone's contribution. Nevertheless, following the PhD thesis guideline, my contribution in relation to other members of the QET Labs are mentioned below to the best of our knowledge.

The circuit designs, optical setups, instrumentations and experiments, specifically, the primary work in my thesis—the on-chip PIM with micro-ring resonator sources—are done by me.

On the performed simulations, I would like to thank Dr Gary F. Sinclair and Dr Damien Bonneau for providing support and guidance, in particular, for SFWM with NLSE and for purity/device imperfections simulations respectively.

Reconfiguring the DTU-tele chip for performing PIM was done together with Dan Llewellyn and Dr Jianwei Wang. This chip was manufactured by Dr Yunhong Ding (DTU) and designed by Dr Jianwei Wang. The first free-space optical setup for off-chip HOM dip measurements with waveguide sources was built together with Dr Takafumi Ono.

Unless specified explicitly, all other experiments and simulations mentioned in this thesis have been performed by me.

Author’s Declaration

I declare that the work in this dissertation was carried out in accordance with the requirements of the University’s Regulations and Code of Practice for Research Degree Programmes and that it has not been submitted for any other academic award. Except where indicated by specific reference in the text, the work is the candidate’s own work. Work done in collaboration with, or with the assistance of, others, is indicated as such. Any views expressed in the dissertation are those of the author.

SIGNED: ..... DATE:.....

Contents

List of Figures

List of Tables

List of Abbreviations

CAR Coincidence to Accidental Ratio

DSPS Deterministic Single-Photon Source

DWDM Dense Wavelength Division Multiplexer

EDFA Erbium Doped Fibre Amplifier

FBG Fibre Bragg Gratings

FWHM Full Width Half Maximum

HBT Hanbury-Brown-Twiss interferometer

HOM Hong-Ou-Mandel

HSPS Heralded Single-Photon Source

ITU International Telegraphic Unit

JSA Joint Spectral Amplitude

MZI Mach-Zehnder Interferometer

OSA Optical Spectrum Analyser

PIM Photon Indistinguishability Measurement

QI Quantum Interference

SFWM Spontaneous Four Wave Mixing

SNSPD Superconducting Nanowire Single Photon Detector

SOI Silicon on Insulator

SPDC Spontaneous Parametric Down Conversion

SPS Single-Photon Source

StFWM Stimulated Four Wave Mixing

VGC Vertical Grating Couplers

Chapter 1

Introduction

Light and the particle of light have invoked curiosity since the early days of humanity. Ancient Greece considered fire (≡ light) as one of the four fundamental elements of the world. The early Indian subcontinent considered light as one of the five fundamental elements of the universe, from which other elements emerge. The idea of light, its fundamental constituents and properties, such as colour, was a subject of scholarly debate throughout history. Although most of those ideas appear crude in the 21^{st} century, our modern physics reveals that the photon, the fundamental particle of light, is versatile and can be considered as a fundamental particle of the universe from which other elements emerge.

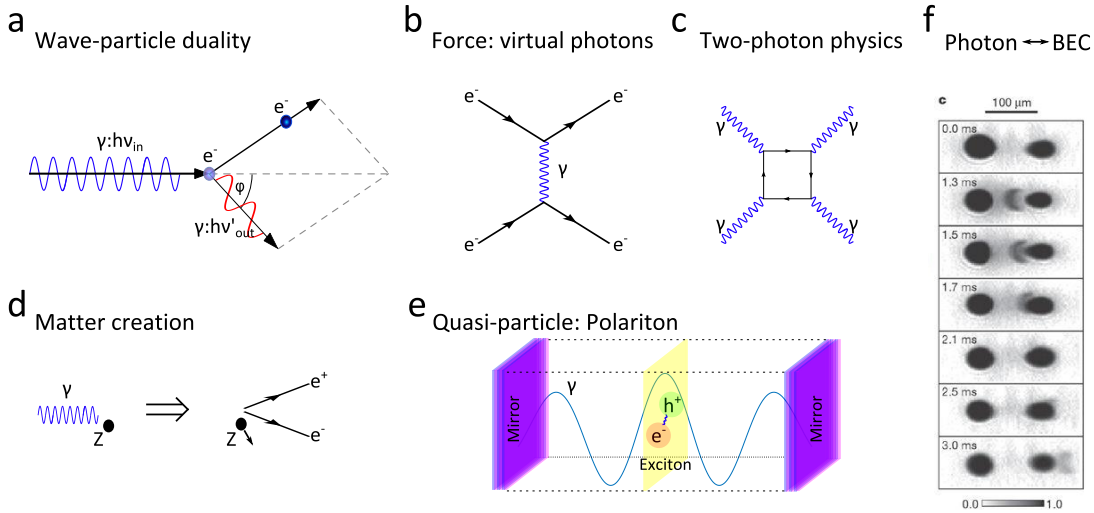

Figure 1.1: Photon: a key quantum particle of the universe. (a) Compton scattering. Elastic scattering of a photon with an electron changes the wavelength of the photon showing wave and particle behaviour simultaneously. (b) Virtual photon, the carrier of the electromagnetic force, causes the electron-electron repulsion in this Feynman diagram. (c) Two-photon physics, showing photon-photon scattering in the vacuum. (d) Electron-positron pair production from gamma rays. (e) Photons combined with excitons (electron-hole pairs) can form polaritons. (f) Light can be stopped entirely and transformed into a matter wave in Bose-Einstein condensate (BEC) and revived. All the images in this figure have been adapted from Wikipedia except (f) which has been adapted from *Ginsberg et al., Nature 445, 623—626 (2007)* [1].

The photon is one of the elementary quantum particles and the particle of light. It demonstrates the wave-particle duality in Compton scattering (Fig. 1.1 (a)). Photons are the quanta of the electromagnetic field which is one of the four fundamental forces in the universe. In fact, photons or more accurately virtual photons are also the force particles of the electromagnetic field. Figure 1.1 (b) shows Feynman diagram of the electron-electron (e^-—e^-) repulsion mediated by a virtual photon γ. Photons are bosons and can form superfluids [2, 3]. Photons are also their own anti-particles. When an electron-positron pair annihilates each other, they release the energy as gamma rays (photons). The reverse process, matter creation, is mediated by the presence of a nucleus, and electron-positron pairs are produced from very high energy gamma rays (photons) (Fig. 1.1 (d)). A photon can be combined with other quasiparticles such as an exciton (electron-hole pair in a semiconductor) and form another quasi-particle called polariton (Fig. 1.1 (e)).

In the above examples, photons appear to be fundamental particles in many different types of physics, but a question remains whether the photon is indivisible such as an electron or it constitutes more versatile fundamental elements. In two-photon physics, high energy photons (gamma rays) have been collided with each other to investigate the constituents of the photons and to observe photon-photon scattering (Fig. 1.1 (c)). This is quite in contrast with our usual experience of stargazing, as photons travelling through vacuums for billions of years unperturbed, reach our eyes. Also, contrary to the popular belief that photons always travel at the speed of light, this has been dramatically violated using slow light medium. As shown in Fig. 1.1 (f), a light pulse is slowed down and completely stopped when it encountered first of the two Bose-Einstein condensates (BECs). It transferred all the information to the matter wave which then propagated to the second BEC. At the end of that BEC, the light pulse is revived again retaining all the information [1]. Actually, photons produced in the core of the sun may take millions of years to reach the surface due to a slow down, but then only 8.3 minutes to reach the earth.

In general, photonics, the scientific and technological pursuit of photons is invigorating. It not only evokes one's curiosity but also relates the scientific truth to the big philosophical questions, such as *what is the universe made of* and *where is our place in it*.

1.1 Motivation

Photonics stands at the border of science and cutting-edge technology. The present scientific knowledge of the photon not only satiates our curiosity but it also holds immense possibilities in the form of futuristic technologies. For instance, attosecond pulses have enabled space-time measurements with sub-atomic scale precision. This has been used to measure real time-resolved propagation of electromagnetic field oscillations (not just the envelope) [4] and chemical reactions with sub-femtosecond resolutions [5] (Fig. 1.2 (a)) to name a few applications. High precision and table-top optical clocks are being developed using optical frequency combs which are generated with standard integrated-photonic components (Fig. 1.2 (b)). Another high precision application of photonic technology is the use of Michelson interferometer to detect graviton (the particle of the gravitational field) propagation in LIGO (Fig. 1.2 (c)). A state of the art photonic spectroscopy method [6] revealed the quantum walk performed by the excitons generated during photosynthesis process and its efficient (near unity) transfer of excitons to the reaction centre [7], which is one of the topics that started the revolutionary field of quantum biology [8]. Last but not least is the photonic quantum computing. Photonic quantum computing can revolutionise our current understanding of the physical world. This promise is due to the

fact that nature is governed by quantum mechanics and quantum computers operate on the very same principle, unlike classical computers. Therefore, the quantumness of nature can only be understood using a quantum computer free of the classical limitations. Also, quantum computation has shown advantages over classical computation, for example, Shor's algorithm can factorise prime numbers more efficiently [11]. Thus, it can break the RSA public key encryption [12], which is the underlying principle of online banking. Figure 1.2 (d) shows one possible implementation of quantum computing using measurement-based cluster states of photonic qubits entangled in a large matrix along with feedforward networks (e.g. electronic integration) [10]. Most of the measurement based quantum computing schemes—generalised teleportation model [13] and one-way quantum computing [14]—require a large number of identical physical qubits such as $> 10^6$ [15, 16] as also envisioned by Google's quantum computing in Fig. 1.3. Identical photonic qubits also require identical single-photon sources.

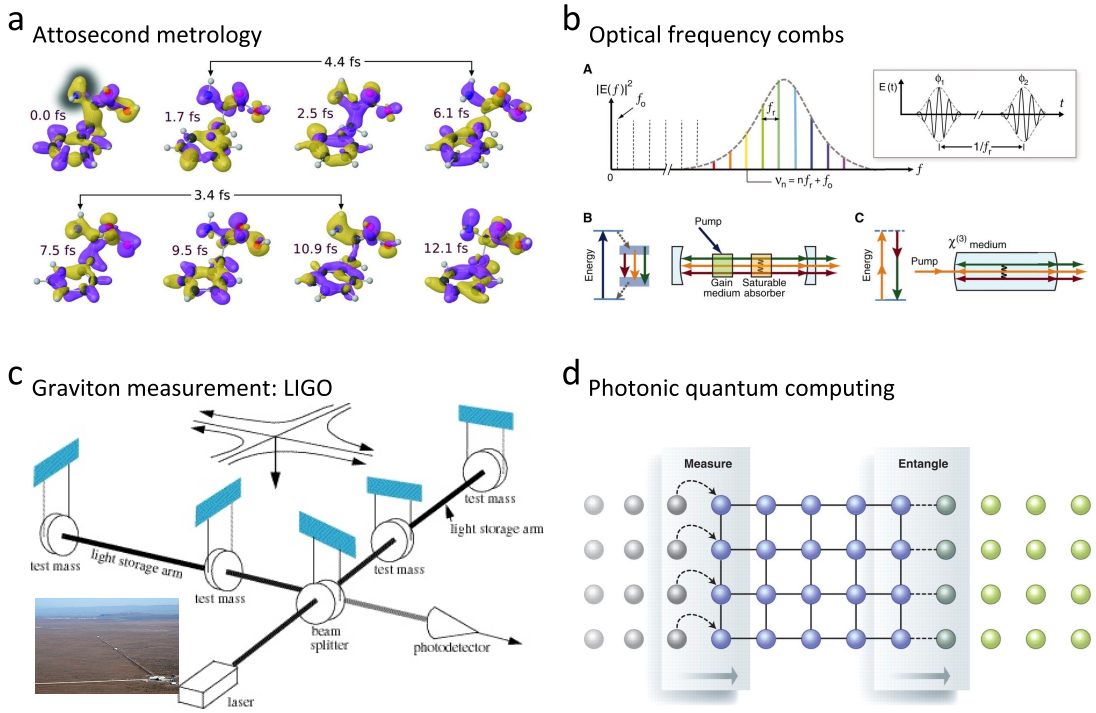

Figure 1.2: Photonic technologies. (a) Attosecond pulses can dynamically capture the chemical reactions with attosecond precision. This image is adapted from *Calegari et al, Science 346, 336-339 (2014)* [5]. (b) Table-top generation scheme of optical frequency comb adapted from *Kippenberg et al, Science 332, 555-559 (2011)* [9]. (c) Gravitational wave measurement in LIGO using Michelson interferometer—another photonic technology. This image and the aerial view in the inset are adapted from Wikipedia. (d) Cluster state generation and preparation using the entangled matrix of pure and indistinguishable single-photons for photonic quantum computing. This figure is adapted from *O'Brien, Science 318, 1567-1570 (2007)* [10].

There are many photonic platforms which have the capability to integrate electronics and photonics on a single chip. Silicon photonics is one such platform. In fact, silicon photonics is one of the most promising platforms for near-term implementation of quantum technologies. Silicon photonics is a mature platform with existing roadmap to electronic integration, such as a proof of principle demonstration of electronics + photonics integration [17], even though silicon is not the best material from the perspective of a photonic or even electronic components. For example, compound (III-V or II-VI) or hetero-

junction semiconductors show high electronic speeds and better optical non-linearities. However, silicon has established large scale integration and standardised photonic fabrication. Silicon foundries offer low-cost multi-project wafers with relatively low loss waveguides. The key advantage of silicon is the combination of its moderate nonlinearity, ability to increase complexity and existing roadmap of electronic integration. In fact, today's silicon electronic industry produces microprocessor chips containing high component density, an excess of 20 billion ($\gg 10^6$) transistors. Therefore, Silicon on Insulator (SOI) photonic platform represents a good choice to implement quantum computing schemes.

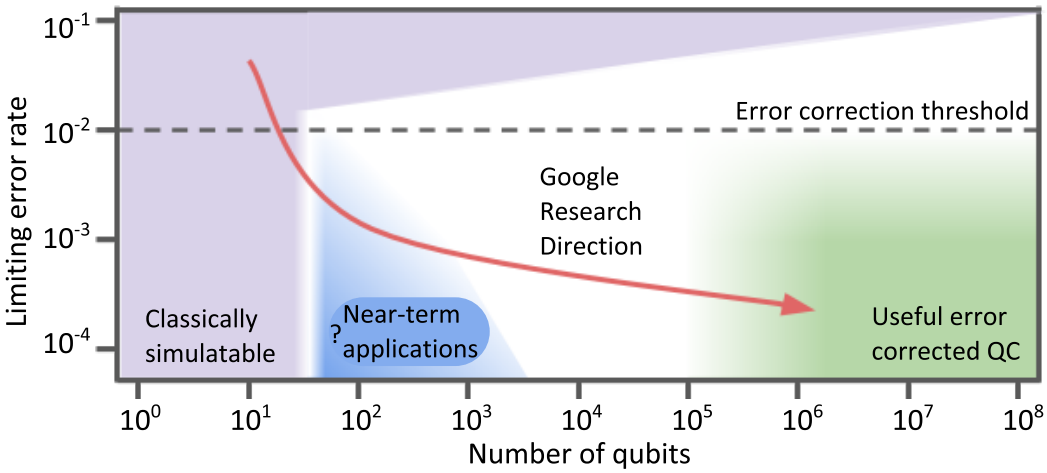

Figure 1.3: The vision of quantum computing research direction published by Google showing that for an error corrected computing an excess of 10^6 physical qubits are required. That corresponds to a large array of indistinguishable sources for photonic qubits. Such a high density of components has only been demonstrated in fabricating the processor chips containing more than 20 billion (20×10^9) transistors. This image is adapted from `https://research.googleblog.com/2018/03/a-preview-of-bristlecone-googles-new.html`.

A modular implementation of cluster state quantum computing scheme requires near unity indistinguishable single-photons, as every photon interferes with at most 3 nearest neighbour photons [18]. From photonic qubit's perspective, this requires an array of near ideal single-photon sources. Near unity indistinguishability among single-photon sources is one of the figures of merit of an ideal Single-Photon Source (SPS). Highly indistinguishable single-photon sources are also desirable for other quantum technologies such as quantum metrology and quantum communications. This is the primary reason for choosing silicon photonics to develop near ideal single-photon sources in this thesis. If SPSs in silicon can be shown with 99% indistinguishability with high brightness, considering silicon's scalability, it will have the advantage over other platforms leading to the earliest demonstration of quantum supremacy.

1.2 Structure of the thesis

The goal of this thesis is to design and characterise bright, pure and indistinguishable heralded single-photon sources in silicon photonics. We have chosen popular structures such as nano-wire waveguides and micro-ring resonators. Also, we want to relate the design parameters of such structures with the figures of merit of an ideal SPS. We aim to construct a model that gives a perspective on the limitations of such a characterisation

method and the SPSs.

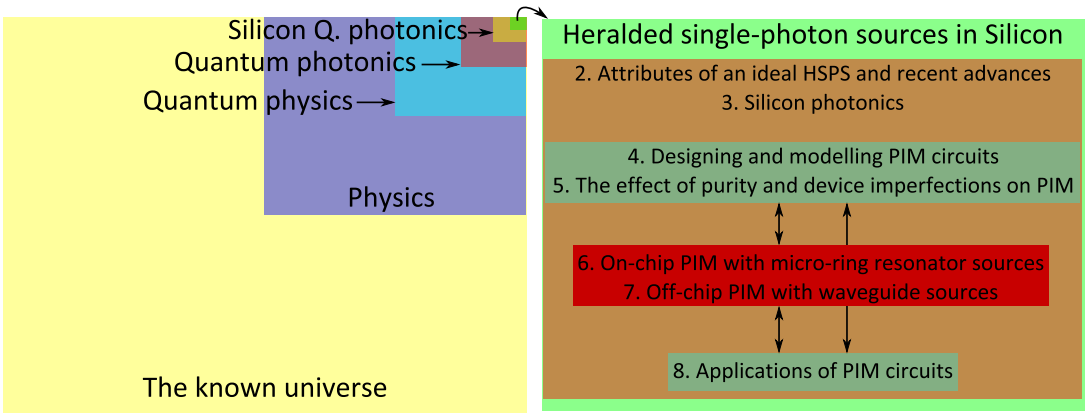

Figure 1.4: Structure of the thesis. The area of the research in this thesis is equivalent to a drop in the ocean. Yet, in this thesis, by developing indistinguishable single-photon sources in silicon photonics, we hope to glimpse the universe.

The next two chapters of this thesis contain literature reviews, figures of merit used for SPSs characterisations and a brief review of the silicon photonic components used in this thesis. The methods and definitions mentioned in these chapters will be used in the rest of the thesis. Afterwards, the designs and models of the silicon photonic circuit for Photon Indistinguishability Measurement (PIM) has been explained. Next, we simulated the effect of imperfect SPS and imperfect photonic circuit on PIMs. Finally, we have presented the experiments: on-chip PIM with micro-ring resonator SPSs, off-chip PIM with waveguide SPSs and an application of the PIM for a teleportation experiment.

PART I

Silicon photonics and recent advances in heralded single-photon sources

This part contains two chapters on background theories and literature reviews. Chap. 2 begins with the figures of merit of a Heralded Single-Photon Source (HSPS), and concludes with recent advances of HSPS in silicon photonics compared to other platforms. Chap. 3 introduces general silicon photonics and its usability for quantum photonic technologies such as to design the PIM circuits.

Chapter 2

Attributes of an ideal HSPS and recent advances

Contents

Spontaneous emission of photons is a natural phenomenon frequently observed in the biological world. Planktons fluoresce while fireflies convert chemical energy to light. In non-organic materials, spontaneous emission of gamma rays (photons) from radioactive materials had been made well known by Henri Becquerel and Marie Skłodowska-Curie. Nevertheless, the origin of the word *photon* and its first scientific usage is debatable.

[1] *Quantum & Lichtquanta*

Photon has been first defined[1] in the context of fundamental energy unit (quantum) of light in explaining photo-electric effect by Max Planck and Albert Einstein. This quantisation is referred to as first quantisation. However, a photon as a quantum of electromagnetic radiation had not been defined until after the electromagnetic field was quantised. This is usually referred to as second quantisation. In the view of the quantisations, a single-photon is broadly defined as the single indivisible quantum of the electromagnetic radiation that contains all the properties of that radiation. In this definition, the dependence of the electromagnetic field of the photon on spectral, spatial or any other attributes is not constrained. The only condition is that a single-photon quantum state has to contain only one quantum of the electromagnetic field of the quantum system in discussion.

Historically, the spontaneous emission from the atomic cascades was the first experimental source of single-photons [19]. Subsequently, nonlinear optical processes and artificial molecules (quantum dots) have gained popularity to generate single-photons. An ideal single-photon source: emits single-photons on demand (deterministic / unity heralding efficiency); provides a sufficient rate of single-photons (high brightness); emits each photon in a single optical mode (high purity) and has photons from multiple sources indistinguishable from one another (high indistinguishability). The quality of a practical single-photon source is based on these figures of merits, as depicted in Fig. 2.1. Indistinguishability of a practical single-photon source is essential for scalable photonic quantum technologies (e.g. quantum computing).

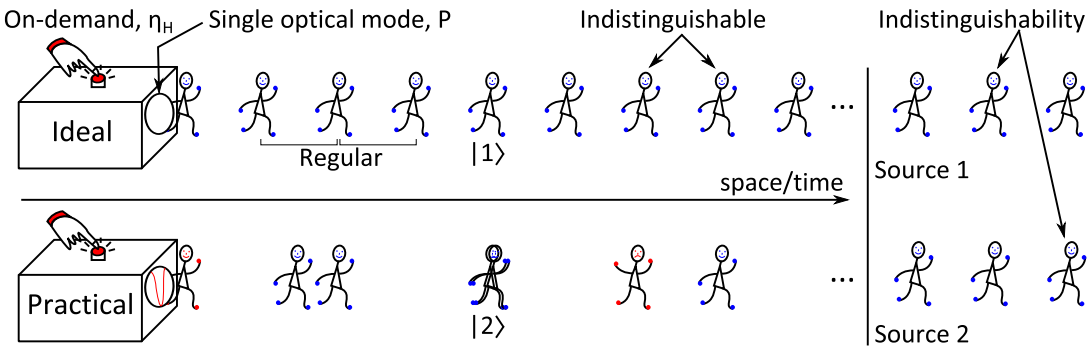

Figure 2.1: A comparison between ideal and practical single-photon sources. η_H: heralding efficiency; P: purity; $|1\rangle$: single-photon state and $|2\rangle$: two-photon state. The diagram on the right shows the indistinguishability between two ideal single-photon sources.

In the past few years, quantum photonic technology emerged as the next leading technology of the world. Single-photon sources are one of the key pre-requisites of quantum photonic technology. Significant works have been carried out in producing near ideal single-photon sources in solid state platforms (e.g. quantum dots) and nonlinear optical platforms (e.g. parametric down conversion, four wave mixing). In this chapter, first, the various types of platforms of the single-photon sources will be mentioned. Then, we will focus on the spontaneous four wave mixing sources. Afterwards, the figures of merit of an ideal source will be discussed. Lastly, recent progress on the single-photon sources achieved in different platforms will be briefly compared.

2.1 Types of single photon source

Single-photon sources have been implemented in a variety of photonic platforms. Mostly, they fall into two broad categories: Deterministic Single-Photon Source (DSPS) and Heralded Single-Photon Source (HSPS). Both of these categories can be viewed as effective

two level systems as discussed in the next section.

2.1.1 An effective 2-level system

Photons are energy quanta. According to one of the fundamental rules of physics, the energy conservation:

> Energy cannot be created or destroyed, it can only be transformed from one form to another.

Therefore, we cannot create single-photons but can only transform other forms of energy to become single-photons. The above principle actually stems from the symmetry in time as explained by Noether's theorem which relates symmetries with conservation principles. Therefore, during the photon emission process other symmetries such as space and angles give rise to linear and angular momentum conservation rules. A single photon emission process has to follow all of the conservation principles. The single-photons generated by the non-linear optical process, used in this thesis, have the same polarisation as the pump. Thus, in all our calculations, only energy and linear momentum conservation will be considered.

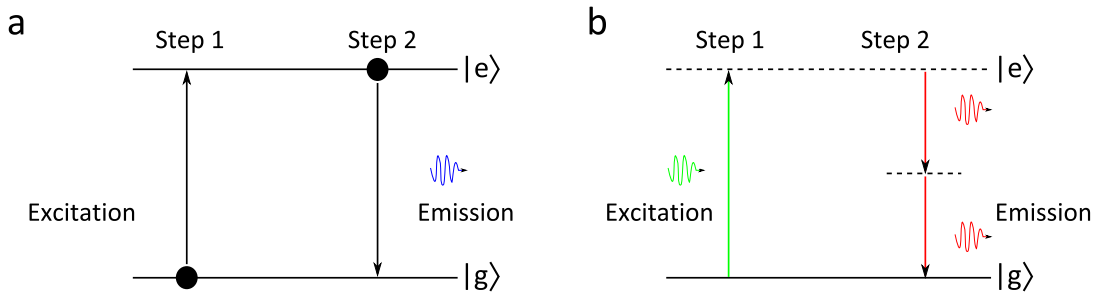

Figure 2.2: Effective two level systems. (a) A two-level system showing the bottom and top levels as atomic ground energy state $|g\rangle$ and excited energy state $|e\rangle$ respectively. Step 1: the atom is excited to the higher energy level $|e\rangle$. Step 2: the atom returns to its lowest energy level $|g\rangle$ naturally, and emits a single-photon to conserve the energy. It is assumed that it is a direct bandgap material to facilitate photon emission. Also, in practice, as two-level system cannot reach steady state with 100% throughput of single-photons, three- or four-level systems are used. (b) A nonlinear optical process, spontaneous parametric down conversion (SPDC), can also be viewed as an effective two level system [20]. In SPDC, a photon from the pump laser is absorbed and then two new photons with half of the energy of the pump photon are emitted.

An ideal way to generate single-photons is to excite an atomic system (DSPSs) to a higher energy level by means of electrical, optical or other forms of energy. For example, Fig. 2.2 (a) describes the excitation of a system from the ground energy state $|g\rangle$ to the excited energy state $|e\rangle$. We know that any system naturally tends to return or stay to its lowest energy state $|g\rangle$. According to the Jaynes-Cummings model [21], when the system returns to the $|g\rangle$ state, it dissipates this energy into the vacuum electromagnetic bath and brings a virtual photon into existence. Considering the system under discussion permits such radiative transitions, a single photon will manifest as spontaneous emission. The frequency (ω) or colour of the single-photon is related to the energy difference between the two levels:

$$E_{|e\rangle} - E_{|g\rangle} = \hbar\omega \tag{2.1}$$

where, $\hbar$ is related to the Planck constant, $h = 2\pi\hbar$.

The quantum-mechanical description of the nonlinear optical processes such as SPDC (Fig. 2.2 (b)) or SFWM describe similar underlying physics. The primary difference with nonlinear optical processes is that the energy levels are represented as virtual energy levels (specified by dotted lines) [20]. Virtual energy levels are not eigenstates of an atom but the combined energy of the atomic energy state and the radiation field. Nonlinear optical phenomena are matter mediated and strongly depend on the material properties. The aforementioned energy and momentum of a single-photon are interdependent through the dispersion relation of the material. This relation is particularly important for nonlinear optical processes to determine the phase-matching (momentum conservation) conditions.

The Jaynes-Cummings model can explain single-photon emission from both atomic transitions and nonlinear optical phenomena using the effective two level system. In the next section, the physical process of practical DSPSs and HSPSs will be briefly discussed.

2.1.2 Deterministic single-photon source (DSPS)

Deterministic single photon sources are either atomic or molecular systems, or systems that modify material structures to mimic atomic systems. These are called deterministic, because as soon as the system is excited, a single photon emission is guaranteed through the relaxation process. However, the collection efficiencies of the single-photons are not unity in practical systems, which counteracts the concept of guaranteed photons. Popular deterministic sources include atomic vapours, cold atoms, quantum dots, colour/defect centres, large organic molecules etc.

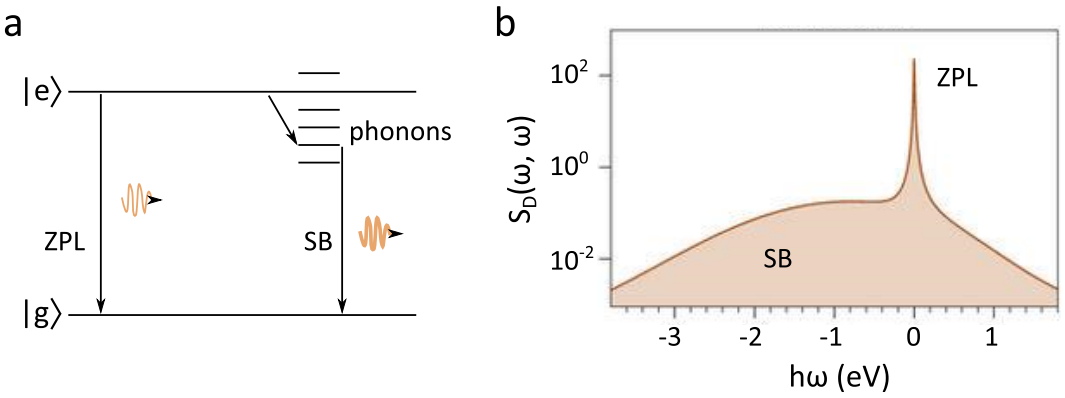

Figure 2.3: Phonon assisted emission from quantum dots. (a) Shows spontaneous emission of photons from excited state $|e\rangle$ to the ground state $|g\rangle$ or the zero phonon line (ZPL). When the lattice vibrational modes or phonons also participate, the emitted photons constitute the sidebands (SB). (b) Shows the photon emission spectrum: photon emission probability as a function of frequency or energy ($\hbar\omega$). Due to the phonon assisted emission, the photons have sidebands unique to that specific quantum dot. These figures are adapted from *Iles-Smith et al, Nat. Phot. 11(8), 521-526 (2017)* [22].

Quantum Dots and quantum LEDs

Quantum dots are a promising candidate for deterministic single-photon sources. A quantum dot structure is made in solid-state direct band-gap material system to enable radiative transitions. III-V semiconductor system (such as InAs or GaAs) or compound semiconductor materials such as InGaAs are some popular choices. In these semiconductor materials, the energy bands can be engineered to give rise to quantum well or quantum dot structures resembling well defined atomic energy levels. The quantum particle that gets trapped in such a structure is called an exciton (bounded electron-hole pair). An exciton

can be excited in two major ways which subsequently emits photons during relaxation: photoluminescence and electroluminescence. In photoluminescence, a laser light is used with a wavelength matching the transition energy (resonant excitation) or slightly detuned from it (non-resonant excitation). Electroluminescence uses electrical current as an excitation. Quantum dots that use electroluminescence, are called quantum LEDs. Quantum LEDs are more scalable as they do not need any external sources (lasers) for excitation. To date, the indistinguishability and consistency of single-photons from electroluminescence are much lower than photoluminescence systems.

Solid state lattices contain vibrational modes of energy that contribute during the photon emission process. The quantum particle of lattice vibration is called phonon. Transition to a phonon energy level is non-radiative. The ground state ($|g\rangle$) does not have any phonon levels, and therefore, the emission to $|g\rangle$ is called the zero phonon line (ZPL). ZPL transition from $|e\rangle$ to $|g\rangle$ radiates the desired photons, as shown in Fig. 2.3. The figure also shows that the phonon assisted transition results in a broad sideband (SB). This SB strongly affects the quality of the single-photon such as spectral indistinguishability and brightness reduction. A cavity built around a quantum dot can suppress the SB and enhance the ZPL emission. The physics of the photon-emission process in quantum dots under various circumstances is captured by non-Markovian processes [23]. Such analysis in conjunction with the presence of a cavity can be found in [22].

Atomic, molecular & colour centre systems

The principle of single-photon emission from atomic, molecular or colour centres is same as for the quantum dots. The first experimental single-photon source of light was atomic cascades [19]. In that experiment, mercury atoms ^{202}Hg were excited by electron bombardment (cathode-ray-tube electron gun) and subsequent cascaded atomic transitions were used. It showed that second quantisation is necessary to account such photo-emission process. Due to the subsequent photon emission in subsequent transitions, an atomic cascade resembles a photon-pair source. In recent years, rubidium isotope ^{87}Rb in vapour cell has been used for single-photon generation and single-photon non-linear optics [24]. Large organic molecules have become popular as single-photon sources [25] as they fall under two-level systems while at the same time the chemical formulae can be engineered to give certain spectral response. In addition, the organic molecules are large enough to pick up using optical tweezers and place them on a waveguide or a cavity. That facilitates guided emission and spectral engineering through photonic circuits with high collection efficiencies.

Colour centres in diamonds or defects centres in silicon have also been used as single-photon emitters. They are particularly popular as they operate in room temperature [26] and the spin property of the atomic transition can also be used for quantum-bit (qubit) processing.

2.1.3 Heralded single-photon source (HSPS)

A heralded single photon source (HSPS) generates pairs of single-photons, in contrast to DSPSs. Detecting one of the single-photons of a pair heralds the presence of the other single-photon, hence the name HSPS.

Two most common nonlinear optical processes of generating photon pairs are: second order and third order non-linear processes corresponding to $\chi^{(2)}$ and $\chi^{(3)}$ susceptibility respectively. These are essentially the dominant susceptibility tensors after the linear one $\chi^{(1)}$. The susceptibility tensors are material properties and their values depend on the sym-

metry of the atomic arrangements and other atomic properties. During the propagation of light they contribute to the polarisation response of the material. Usually, the magnitudes of $\chi^{(2)}$ and $\chi^{(3)}$ are significantly smaller than the linear susceptibility. In a low intensity light propagation, the light beams do not interact with each other due to the linearity property of the linear susceptibility. Any nonlinear process requires light-beams, known as pumps, with high enough intensities to mediate interactions with the matter. These interactions drive the material's response such that the higher order susceptibilities start to play roles in the polarisation response of the material. These susceptibilities couple the propagation equations of the light beams, and generate photons with new frequencies. Historically, these photon-pairs are called signal-idlers. One major difference between DSPSs and HSPSs is that generation of signal-idler photon pairs in HSPSs is probabilistic. In contrast, detecting the idler single-photon guarantees the presence (heralding) of the signal single-photon, which can then be multiplexed to make a near-deterministic single-photon source.

Spontaneous parametric down conversion (SPDC) and spontaneous four wave mixing (SFWM) processes are the two most popular processes of photon-pair generation. Usually, the value of $\chi^{(3)}$ is weaker than $\chi^{(2)}$. In centro-symmetric materials, such as silicon, $\chi^{(2)}$ vanishes, making $\chi^{(3)}$ dominant. The HSPSs discussed in this thesis are based on $\chi^{(3)}$ (SFWM).

Spontaneous parametric down conversion based HSPSs

The $\chi^{(2)}$ susceptibility facilitates the spontaneous parametric down conversion process. Figure 2.2 (b) describes the process, where a photon from a strong pump beam (ω_p) disappears into the vacuum, and two new photons (ω_s, ω_i) come into existence. The energy and momentum of the whole process involving all three photons are conserved:

$$Energy\ conservation: \quad \hbar\omega_p = \hbar\omega_s + \hbar\omega_i \tag{2.2}$$

$$Momentum\ conservation: \quad \vec{k}_p = \vec{k}_s + \vec{k}_i \tag{2.3}$$

In degenerate SPDC, the central frequencies of the new photons have half the frequency of the original pump photon, $\omega_{s0} = \omega_{i0} = \omega_p/2$. The figures of merit of the SPDC photon-pairs are intricately related to the $\chi^{(2)}$ tensor and other properties such as the geometrical dimensions of the HSPS. SPDC sources have been extensively researched in the past decades and until now they are the best single-photon sources available in terms of brightness, purity and indistinguishability.

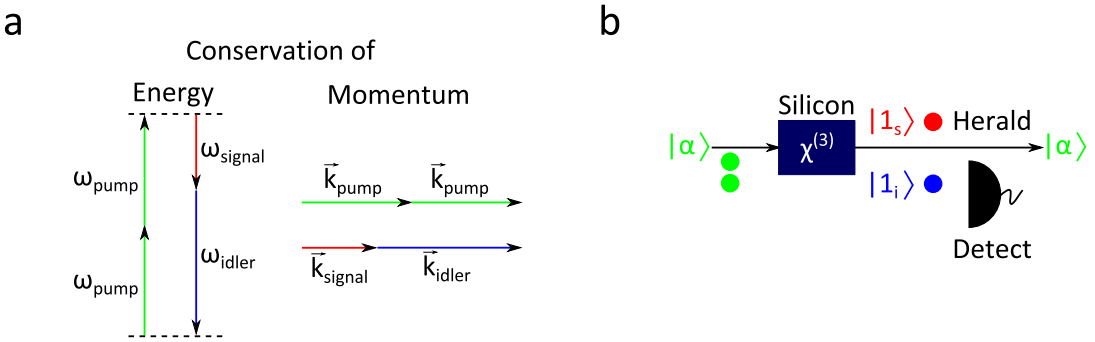

Figure 2.4: Spontaneous four wave mixing (SFWM): (a) Energy and momentum conservation of the absorbed and generated photon-pairs. (b) Detecting one photon of the photon-pair, we can herald the presence of the other photon. Thus, it acts as a heralded single-photon source.

Spontaneous four wave mixing based HSPSs

The $\chi^{(3)}$ susceptibility facilitates the spontaneous four wave mixing process. Figure 2.4 describes the process where two photons from the strong pump beam (ω_p) disappear into the vacuum and two new photons (ω_s, ω_i) come into existence. The energy and momentum of the whole process involving all four photons are conserved:

$$Energy\ conservation: \quad 2\hbar\omega_p = \hbar\omega_s + \hbar\omega_i \tag{2.4}$$

$$Momentum\ conservation: \quad 2\vec{k}_p = \vec{k}_s + \vec{k}_i \tag{2.5}$$

Here, the nonlinear phase shift contribution during momentum conservation is not included.

The conservation principles and the properties of the single-photons depend strongly on the $\chi^{(3)}$ tensor and the properties of the pump beam. The value of the nonlinear susceptibility ($\chi^{(3)}$) coefficient depends on the material properties such as the symmetry of the atomic arrangements and atomic properties. The strength of the nonlinear process such as SFWM depends on the strength of the non-linearity of the material and the intensity of the pump light. In fact, when a strong laser with intensity I propagates through a $\chi^{(3)}$ material, the refractive index can be expressed as [20],

$$n = n_0 + n_2 I \tag{2.6}$$

where, n_0 is the refractive index of the material and n_2 is the intensity dependent refractive index. Our primary material of choice for the photonic circuits, silicon, has an inversion symmetry resulting in a strong $\chi^{(3)}$ and a vanishing $\chi^{(2)}$. Silicon has a value of $\chi^{(3)}$ =2.8×10^{-18} m^2/V^2 and $n_2 = 2.7 \times 10^{-14}$ cm^2/W [20]. These values are considerably higher than other materials with inversion symmetry. For example, it is 100 times higher than the glass which is used to make optical fibre. Moreover, the high refractive index value of silicon ($n = 3.41$) can guide the light in a tightly confined waveguide structure with effective cross sectional area of $500\ nm \times 220\ nm$ or even smaller. That, in turn, increases the intensity of the light beam inside the waveguides compared to an optical fibre. The effective nonlinearity of a waveguide is expressed in relation to the effective area A_{eff} occupied by the guided mode for a particular wavelength λ_0,

$$\gamma = \frac{2\pi c\ n_2}{\lambda_0 A_{eff}} \tag{2.7}$$

Due to A_{eff}, the actual value of γ depends on the waveguide geometry and the surrounding media of the waveguide. For a strip waveguide of $500\ nm \times 220\ nm$, typical values of $\gamma = 400/(m.W)$. To put this into perspective, it is remarkable to consider that the intensity of a $1\ mW$ power of light ($1550\ nm$ wavelength) inside such a waveguide exceeds the intensity of the light at the surface of the sun's corona.

Quantitative analysis of the SFWM pair-generation is essential to the design of a photon-pair HSPS. Maxwell's electromagnetic wave equations describe both classical pump and single-photon light propagation through any material structure. Non-linear Schrödinger equation arising from Maxwell's equations is useful in understanding the parasitic effects of nonlinearity on pair generation. Such analysis is an essential first step in describing the environment in which the photon-pair generation takes place [27]. Instead, in this section, we will qualitatively discuss the final outcome of the quantum mechanical description of the SFWM process to define the attributes of an ideal heralded single photon source. Afterwards, the quantitative discussion of these attributes will follow.

Quantum mechanically, the interactions among the pump beam and the signal-idler photon-pairs can be described by an effective Hamiltonian $\hat{H}_{int}$ [28–30],

$$\hat{H}_{int} = N \int\int d\omega_s d\omega_i f(\omega_s, \omega_i)\ \hat{a}^\dagger(\omega_s)\ \hat{a}^\dagger(\omega_i) + H.c. \tag{2.8}$$

where the normalisation constant N is related to the strength of the interaction, the bi-photon function $f(\omega_s, \omega_i)$ contains energy and momentum conservation of the interaction, $H.c.$ represents Hermitian conjugate, and $\hat{a}^\dagger(\omega_s)$, $\hat{a}^\dagger(\omega_i)$ represent creation operators of signal and idler photons which act on the vacuum and generate signal and idler photons. The above expression of $\hat{H}_{int}$ can relate and define the figures of merit of the heralded single-photon sources discussed in the following section.

2.2 Figures of merit of heralded single-photon sources

The figures of merits commonly used for a heralded single-photon sources are brightness, purity, heralding efficiency and indistinguishability as described in Fig. 2.1. The characterisation schemes to quantify the figures of merit of a HSPS are elaborated in the following sub-sections.

2.2.1 Brightness

The brightness refers to the coincidence count rate (expressed as CC) of the photon-pairs generation from a HSPS. It is related to the normalisation constant N in Eq. 2.8. N is proportional to the intensity of the pump beam and the strength of the $\chi^{(3)}$ non-linear interaction, and depends on the conservation principles. The exact analytical relation between N and the rate CC depends on many factors, such as the strength of the non-linearity, energy and momentum conservation, application of filters, actual geometry of the HSPS etc. Also, we know from the preceding section that the SFWM process depends on the powers of the two pump fields. Hence the quadratic dependence of SFWM on the power (P) of a single pump field. For a CW pump with frequency ω_p, waveguide HSPS of length L_{Wg} and photon collection bandwidth $\Delta\Omega$, the effective brightness of the HSPS γ_{eff} and the rate CC can be expressed as [31–33][2],

[2] Eq. (38) in [33]

$$\gamma_{eff} = \frac{L_{Wg}^2 \gamma^2 \Delta\Omega}{4\pi} \hbar\omega_p \tag{2.9}$$

$$CC = \gamma_{eff} P^2 \tag{2.10}$$

where, γ is the effective non-linearity containing $\chi^{(3)}$ which is mentioned in the last section. A similar expression can be obtained for the pulsed pump [27]. In an experiment, $\Delta\Omega$ is fixed by the collection bandwidth of the filter. Thus, γ_{eff} can be viewed as the intrinsic photon-pair generation efficiency of a HSPS, per unit squared power of the pump laser in per unit of time. In terms of waveguide's geometry, γ_{eff} is proportional to the length squared L_{Wg}^2 and inversely proportional to the effective cross-sectional area squared A_{eff}^2 (hidden in γ).

A micro-ring resonator resonantly enhances optical fields through the cavity structure, and the brightness is expected to be higher. If the field enhancement on resonance (ω_p) is expressed as $f_E(\omega_p)$, then the intrinsic efficeincy γ_{eff} and rate CC of photon-pair generation can be expressed as [33, 34][3]:

[3] Eq. (62) in [33]

$$\gamma_{eff} = \frac{1}{2} L_{Rg} \gamma^2 |f_E(\omega_p)|^6 \hbar\omega_p v_g \tag{2.11}$$

$$CC = \gamma_{eff} P^2 \tag{2.12}$$

where, L_{Rg} is the length of the cavity and v_g is the group velocity of the photon's wavepacket. A similar expression can be obtained for pulsed pump [32]. The dependence of γ_{eff} on the geometry of the resonator is related by the field enhancement $f_E(\omega_p)$ (Sec. 4.2.4). It strongly depends on the round-trip loss of the cavity which depends on the specific geometrical structure of the cavity.

According to the above Eqs. 2.10 and 2.12, once all the design and material parameters (e.g. L, $\chi^{(3)}$, v_g) of HSPSs are fixed, the rate CC depends quadratically on the pump power P. Therefore, γ_{eff} can be used as a metric of brightness of HSPSs under the same experimental conditions. For a pulsed laser experiment, if the average pump power is P_{avg}, and the repetition rate of the laser is R, then the brightness is also defined by the average photon-pairs generated per pulse,

$$\bar{n} = \frac{\gamma_{eff} P_{avg}^2}{R} \tag{2.13}$$

In the following, common measurement techniques to extract γ_{eff} are discussed.

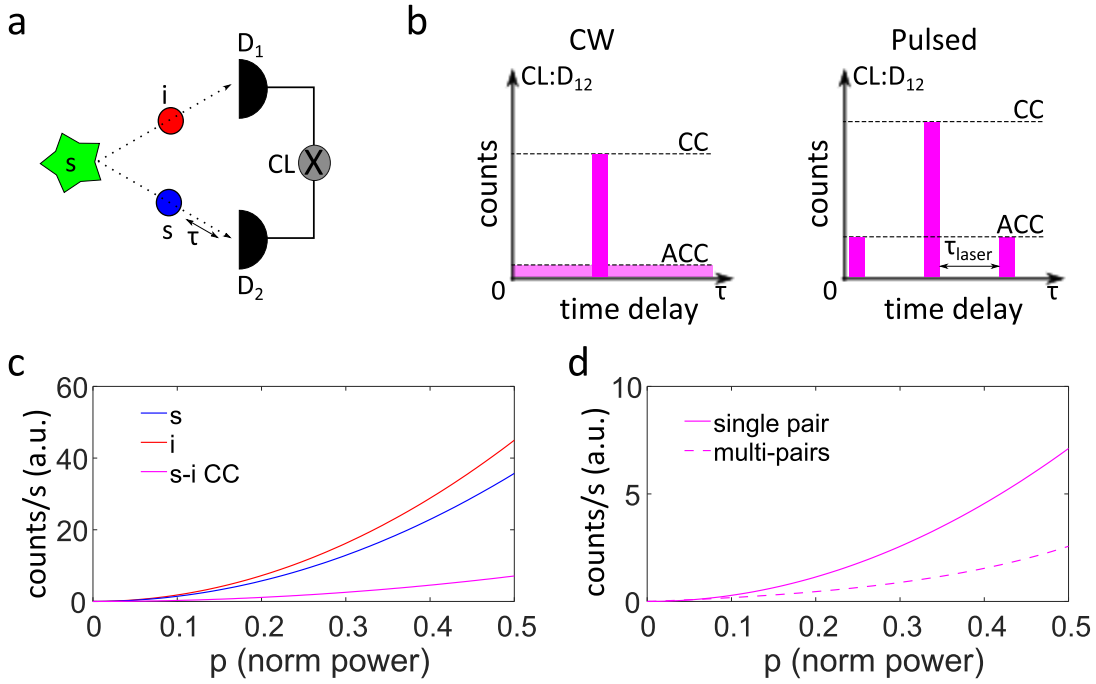

Figure 2.5: Estimating HSPS's brightness. (a) Brightness of the generated photon pairs is measured by detecting signal photons (s), idler photons (i) and both of them together (s-i) as coincidence events by a coincidence logic (CL) unit. (b) Coincidence counts measurements under continuous wave (CW) and pulsed configurations using time-interval analysis. The signal and idler photons may experience different amounts of delays before being detected by D_1 and D_2. For a specific delay corresponding to the simultaneous generation of signal-idler photons, the coincidence is the highest. That is the measure of brightness (CC). In all other delays the coincidence is counted as accidentals (ACC). (c) A plot of signal, idler and coincidence as a function of normalised power following Eqs. 2.14, 2.15, 2.16. (d) A relative comparison of the coincidence rate without (Eq. 2.16) and with (Eq. 2.32) non-linear losses and multi-pair emission.

Two-fold measurements

Considering that the above expressions (Eq. 2.10, 2.12) of brightness are proportional to the square of the pump power, the detection rate of signal ($C(s)$), idler ($C(s)$) and the signal-idler coincidence ($C(s,i)$) can be expressed by the following set of equations commonly used in the literature [32, 35]:

$$C(s) = (\eta_s \gamma_{eff}) P^2 + \beta_s P + DC_s \tag{2.14}$$

$$C(i) = (\eta_i \gamma_{eff}) P^2 + \beta_i P + DC_i \tag{2.15}$$

$$CC(s,i) = (\eta_i \eta_s \gamma_{eff}) P^2 + ACC \tag{2.16}$$

Here, DC represents dark counts and ACC represents accidentals. η_s and η_i represent the detection efficiencies for the signal and idler channels respectively. Figure 2.5 (a,b) depict the experimental configuration and Fig. 2.5 (c) plots the above equations as a function of the pump power (P). The experimental data is first fitted with quadratic equations:

$$C_k = a_k P^2 + b_k P + c_k \tag{2.17}$$

$$CC = a_{si} P^2 + ACC(P) \tag{2.18}$$

where, $k = \{s, i\}$ represents signal or idler. The coefficients a_k of the quadratic term is related to the detection efficiencies (η) and generation efficiency γ_{eff} and can be extracted by using:

$$\gamma_{eff} = \frac{a_s a_i}{a_{si}} \tag{2.19}$$

$$\eta_s = \frac{a_{si}}{a_i} \tag{2.20}$$

$$\eta_i = \frac{a_{si}}{a_s} \tag{2.21}$$

If the width of the coincidence window is τ_w, then the Coincidence to Accidental Ratio (CAR) is defined as,

$$CAR = \frac{CC(s,i)}{C(s)C(i)\tau_w} \tag{2.22}$$

In practice, the above model is sufficient provided that we have photon number resolving (PNR) detectors and can always herald only single-photon states, or if the power is low enough that the multi-pair emission is negligible and the non-linear losses in the system are negligible. This model of brightness estimation needs modification, particularly, accounting for multi-pair emissions for measurements usually done with non-PNR detectors. In the following, the origin of the multi-pair emission and the three-fold measurement technique as an estimation method are discussed.

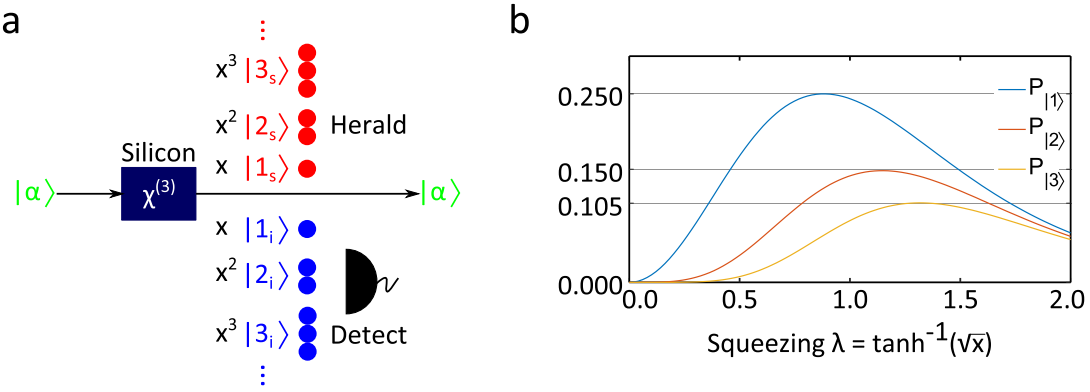

Figure 2.6: Multi-pair emission. (a) Multi-pair emission from a photon-pair source with squeezing strength $x = |tanh(\lambda)|^2$. (b) Detection probability of the multi-photon states with respect to squeezing λ: single-photon state $P_{|1\rangle}$, two-photon state $P_{|2\rangle}$ and three-photon state $P_{|3\rangle}$.

Multi-pair emission effect

The origin of multi-pair emission can be understood from the expression of wavefunction of the photon pairs derived using Eq. 2.8. For pure signal-idler photon-pairs (explained in more detail in section 2.2.4), the interaction Hamiltonian can be simplified as,

$$\hat{H}_{int} = \lambda\, \hat{C}_s^\dagger \hat{C}_i^\dagger + H.c. \tag{2.23}$$

This is a Hamiltonian for single mode twin-beam squeezer [28][4] with squeezing λ, and creation operator for signal and idler photons $\hat{C}_s^\dagger$ and $\hat{C}_i^\dagger$ respectively. The wavefunction is expressed in terms of the number state bases using Baker-Hausdorf lemma[5] [28] as,

[4] in section 7.7

[5] used in the third following line

$$|\Psi\rangle = exp\left(\frac{-i}{\hbar}\hat{H}_{int}\right)\ |0,0\rangle \tag{2.24}$$

$$= exp\left(\frac{-i}{\hbar}(\lambda\ \hat{C}_s^\dagger\hat{C}_i^\dagger + H.c.)\right)\ |0,0\rangle \tag{2.25}$$

$$= \frac{1}{cosh(|\lambda|)}\ \sum_{n=0}^{\infty}(-e^{i\theta_\lambda})^n\ tanh^n(|\lambda|)\ |n,n\rangle \tag{2.26}$$

$$= \sqrt{1-x}\ \sum_{n=0}^{\infty}(-e^{i\theta_\lambda})^n\ \sqrt{x^n}\ |n,n\rangle \tag{2.27}$$

$$= \sqrt{1-x}\left(|0,0\rangle - e^{i\theta_\lambda}\sqrt{x}|1,1\rangle + e^{i2\theta_\lambda}\sqrt{x^2}|2,2\rangle + ...\right) \tag{2.28}$$

where, λ is the squeezing parameter and also the eigenvalues of the Schmidt decomposition for a multi-mode twin-beam squeezers as explained in Sec. 2.2.4. The squeezing strength x is directly related to the generation probability of each photon-number term as explained below. The strength x and the argument θ_λ are expressed as,

$$x = tanh^2(|\lambda|) \leq 1 \tag{2.29}$$

$$\theta_\lambda = \angle\lambda \tag{2.30}$$

The squeezing strength x is related to the average photon-number per pulse through,

$$\bar{n} = \langle n\rangle = sinh^2(|\lambda|) = \frac{x}{1-x} \tag{2.31}$$

Considering x is always less than unity, the most dominant term in the above expression (Eq. 2.28) of $|\Psi\rangle$ is the vacuum term $|0,0\rangle$, confirming that most of the time in the SFWM process, nothing happens and the strong pump beam propagates through the structure without any change or non-linear interaction. The next dominant term is the single photon term $|1,1\rangle$ with coefficient $\sqrt{x}$. The detection of this term is proportional to $P_{|1\rangle} = (1-x)\ x$. At low values of x, it reduces to, $x \propto |\lambda|^2 \propto \gamma_{eff}^2$, which is consistent with the system of Eq. 2.16. Although small, at high enough input power (high x) the higher order terms, such as $|2,2\rangle$, start to contribute to the photon counts. A relative comparison of the strength of the different terms in the above equation is plotted in Fig. 2.6 (b).

This wave-function $|\Psi\rangle$ of the photon pairs generation and the detection is depicted by the cartoon in Fig. 2.6 (a). As we use non-photon number resolving detectors, detecting idler photons in $|1\rangle$ or $|2\rangle$ (or higher order) states cannot be differentiated and the heralding will always assume $|1\rangle$ state for signal photons even when it is $|2\rangle$ state. This will erroneously add single-photon counts from all the higher order photon number states, while the above count rate equations are only valid for single-photon number state $|1\rangle$. A more accurate rate equation can be found in [36],

$$CC = \frac{x\eta_i\eta_s(x^2(1-\eta_i)(1-\eta_s)-1)}{(1-x(1-\eta_i))(1-x(1-\eta_s))(x(1-\eta_i)(1-\eta_s)-1)} \tag{2.32}$$

Here, the η_i and η_s has been modified to include the non-linear losses (Two-photon absorption and free carrier absorption). Figure 2.5 (c) compares this equation with Eq. 2.16, showing that the estimation of the brightness is lower in this method.

Three-fold measurements ($g_H^{(2)}$)

The measurement based way to correct for multi-pair emission effect in estimating brightness is to perform a three-fold coincidence count measurement, commonly known as conditional (heralded) second order correlation $g_H^{(2)}$. The main idea in this scheme is that placing an even-split beam-splitter in the path of heralded photons acts as a pseudo PNR detector.

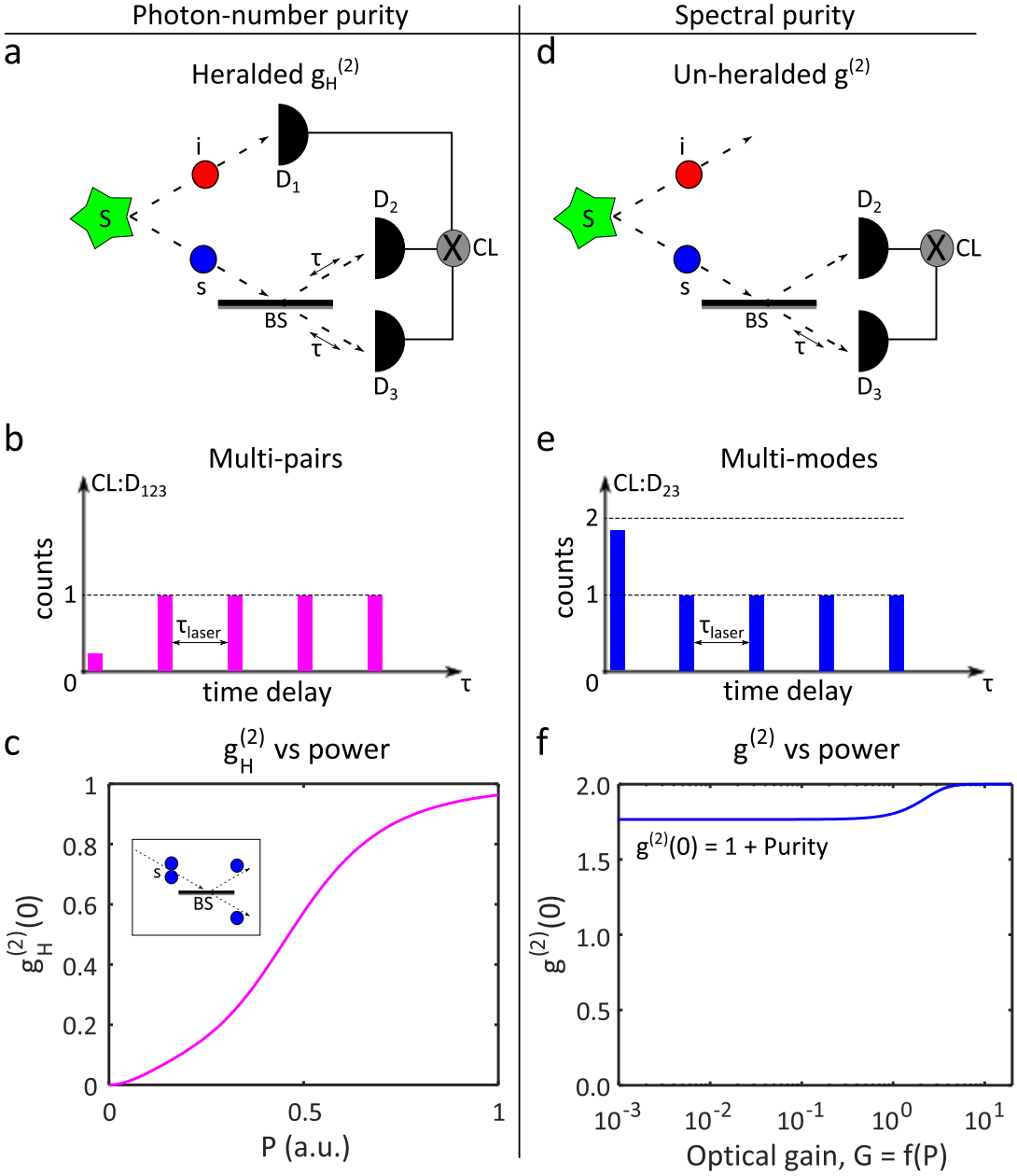

Figure 2.7: A cartoon of heralded $g_H^{(2)}$ and un-heralded $g^{(2)}$ measurements. $g_H^{(2)}$ quantifies the multi-pair contamination and photon-number purity. $g^{(2)}$ quantifies the multi-mode contribution and spectral purity. The relation between $g^{(2)}$ and spectral purity is non-intuitive [30, 37]. (a) The idler photons are detected (D_1) and herald the presence of the signal photons, which pass through an even beam-splitter (BS). The photons from both of the output ports of the beam-splitter are detected (D_2, D_3), and the whole event is counted as a 3-fold coincidence. (d) $g^{(2)}$ measurement (Sec. 6) is an un-heralded 2-fold measurement and does not include idler detector (D_1). Raw data collected using the coincidence logic unit (CL) as a function of time delay (τ) for (b) $g_H^{(2)}$ and (e) $g^{(2)}$. (c) The form of $g_H^{(2)}$ as a function of power P, shows the strong presence of multi-photon states at high pump power. (f) Usually, $g^{(2)}$ is not affected by optical gain G (function of power) unless the gain is very high.

As shown in Fig. 2.7 (a), the detection of the idler photons heralds the presence of signal photons which are then passed through an even beam-splitter. If the incoming signal photons are in the single photon state ($|1\rangle$), then they will go through only one of the output ports of the beam-splitter. Therefore, only one of the detectors will detect the photon and there will be no three-fold coincidences (Fig. 2.7 (b)). If the incoming signal photon is in a two-photon state ($|2\rangle$) or higher order, then it will go through both of the output ports of the beam-splitter and there will be three-fold coincidence events. Thus, the absence of the three-fold events can effectively separate the single-photon states. The sum of the strictly two-fold coincidences ($D_{12\bar{3}} + D_{1\bar{2}3}$) in this scheme is used to estimate the brightness using Eq. 2.16.

It is important to note that a two-photon (and higher order events) also has a finite probability of exiting through only one of the output ports of the beam-splitter. That will result in false counts in the single-photon state photon pairs counts. Nevertheless, the combined probability of all the higher order terms ($|2\rangle$, $|3\rangle$ etc) leaving through only one of the output ports is relatively small compared to leaving through both ports. Thus, the scheme sufficiently mitigates the effect of multi-pair emissions.

The outcome of this scheme is usually presented by a ratio of single-pair emission and multi-pair emission. Effectively, the ratio of two-fold events and three-fold events is plotted as a function of the input pump power (squeezing strength x):

$$g_H^{(2)}(0) = \frac{D_{123} D_1}{D_{12} D_{13}} \tag{2.33}$$

where, D_{123} is the three-fold coincidence event on detectors 1, 2 and 3, D_{ij} is the two-fold events on detectors i and j, and D_1 is the rate of the heralding idler photons. The experimental data can be fitted with the following equation which expresses that the multi-pair emission rate is a function of higher order terms of input pump power:

$$g_H^{(2)}(0) = \frac{\Sigma_{k\geq 2}\ a_k P^k}{1 + \Sigma_{k\geq 2}\ a_k P^k} \tag{2.34}$$

where a_k are fitting parameters and P is the optical power. This expression is similar to the expression used in [38].

All of the above analysis are valid for both nanowire waveguide and micro-ring resonator heralded single-photon sources and will hence be used in Chap. 6 and 7 to evaluate the experimental data.

2.2.2 Heralding efficiency and photon number purity

Heralding efficiency refers to the efficiency with which one can herald the presence of a single-photon. A heralding efficiency of 50% means if we herald the presence of single-photons 100 times, in reality, only about 50 of them will actually have a single-photon. If the two-fold signal-idler coincidence event is denoted by D_{s-i} and the heralding idler singles events as D_i, then the heralding efficiency is defined as:

$$\eta_H = \frac{D_{s-i}}{D_i} \tag{2.35}$$

Photon number purity has a definition similar to the above. If the heralding photon has $|1\rangle$ state and we detect the heralded photon in the state $|1\rangle$ with absolute certainty, then the photon number purity is unity. It means, detecting the heralding photon (idler) should project the heralded photon (signal) in a single-photon state only and not in a mixed state with vacuum (representing loss) state or with multi-photon state ($|2\rangle$, $|3\rangle$ etc). Therefore, detection loss and the multi-pair emission effect ($g_H^{(2)}(0)$) plays a role in determining photon-number purity. Even if the heralding efficiency (η_H) is high, for a high value

of $g_H^{(2)}(0)$, the photon-number purity will be low due to multi-pairs. If photon-number resolving detectors (PNRD) are used, the multi-pair emission can be discarded and the η_H will also represent photon-number purity.

In state of the art experiments, the heralding efficiency of the HSPSs in silicon are relatively low (about a percent). This is due to a few factors. The most common and important factor is the collection efficiency of the photons and the loss in the detection channels. For example, if we herald the presence of a single-photon then due to loss sometimes the photon will be lost even though we predict the presence of that photon. In silicon photonics that can be associated with lossy output couplers and the non-unity efficiency of the single-photon detectors in telecom wavelengths. The state of the art output couplers (vertical grating couplers) in silicon at telecom wavelength has 81% efficiency ($-0.9\ dB$ loss) [39] and certain design proposals promise 89% efficiency ($-0.5\ dB$ loss) [40]. The commercially available single photon detectors at telecom wavelengths offer about 80% (*Photon Spot*) efficiency at the moment. Therefore, even using the state of the art technology, the combination of these two factors can bring down the heralding efficiency of an ideal photon-pair sources to a maximum of 71% at telecom wavelength.

The other reasons of low heralding efficiency are dependent on particular structures of the HSPSs. For a waveguide HSPS, the heralding efficiency has a trade-off with the spectral purity of the sources (elaborated in Sec. 5.1.2). For the micro-ring resonator HSPSs, the non-unity out-coupling coefficient κ of signal and idler photons leads to a reduction in the heralding efficiency. The small κ contributes to the field enhancement to the cavity, but at the same time only a small fraction of the generated signal-idler photons inside the cavity can escape to the outside world. Sometimes, only one of the signal and idler photons of a photon-pair leave the cavity at the same time, resulting in broken pairs [32]. In the literature, the best heralding efficiency is calculated as 68% for slightly over-coupled micro-ring resonator HSPSs [41].

2.2.3 Spatial mode and polarisation mode purity

The purity of the spatial mode (or polarisation mode) refers to the generation of signal and idler in spatial modes such that detecting the heralding idler photon will project the heralded signal photon into a well defined single (non-mixed) spatial mode. In silicon photonic circuits the spatial modes are defined by the eigenmodes of propagation of the waveguide structure. As the waveguide can be designed to support only a fundamental spatial mode for a particular polarisation, it is assumed that the spatial mode purity is unity.

Our choice of waveguide—nanowire or strip waveguide—supports fundamental TE and TM propagating mode for $500\ nm \times 220\ nm$ dimensions (Sec. 3.1.1). As our choice of grating coupler only supports TE mode of coupling, it can be assumed that the SFWM process only involves the fundamental TE modes and the corresponding purity is unity.

2.2.4 Spectral purity

The purity in the spectral domain refers to the generation of signal and idler photons without any spectral correlation such that when a heralding idler photon is detected, the heralded signal photon is projected into a single spectral mode. Spectral purity is relatively hard to achieve for parametric heralded sources due to the interplay among strong pump beam (energy conservation and non-linear phase contribution), phase matching function and material and waveguide dispersion relations. All of these interactions are captured by the bi-photon wavefunction $f(\omega_s, \omega_i)$ in the interaction Hamiltonian H_{int} in

Eq. 2.8. The spectral purity is achieved when the signal and idler photons are spectrally uncorrelated, that is $f(\omega_s, \omega_i)$ is a separable function in signal and idler frequencies:

$$f(\omega_s, \omega_i) = h(\omega_s) \times g(\omega_i) \tag{2.36}$$

where, $h(\omega_s)$ and $g(\omega_i)$ contain the spectral shape of the signal and idler photons respectively.

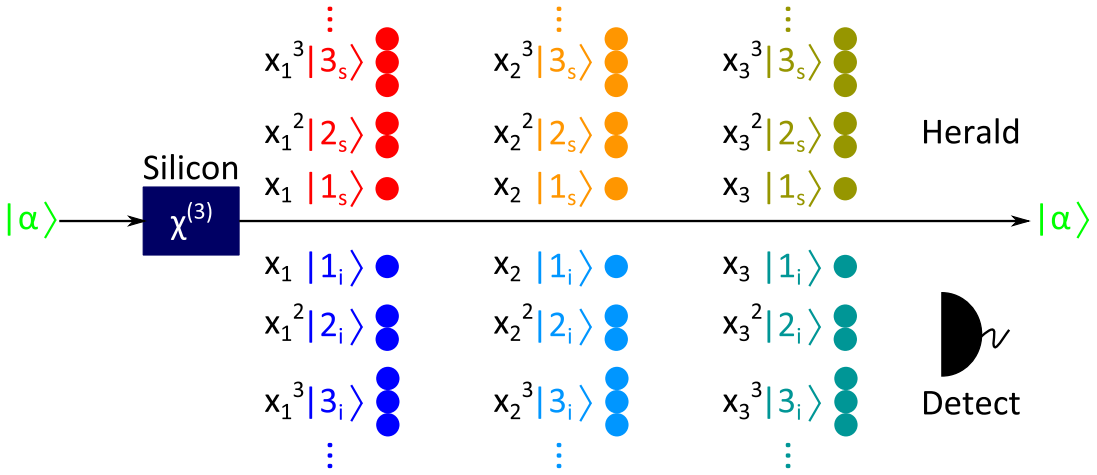

Figure 2.8: Multi-mode single-photon spectra with multi-pair emission in each mode from spectrally impure photon-pair sources. The squeezing strengths x_1, x_2 and x_3 values of the three orthogonal optical modes 1, 2 and 3 respectively depend on the shape of the JSA.

Quantification of the spectral purity (P)

The calculation of the spectral purity and the origin of the separability of $f(\omega_s, \omega_i)$ is related to its proximity to the pure product state (Eq. 2.36) and subsequent calculation of the heralded signal density matrix ρ_s. In order to quantify spectral purity, the separability of bi-photon function ($f(\omega_s, \omega_i)$) needs to be expressed in a quantifiable manner. For a non-separable $f(\omega_s, \omega_i)$, it can be expressed as a sum of orthogonal separable signal and idler functions h_k and g_k using the Schmidt decomposition:

$$f(\omega_s, \omega_i) = \sum_{k=1}^{\infty} \lambda'_k h_k(\omega_s) \times g_k(\omega_i) \tag{2.37}$$

where λ'_k are Schmidt coefficients. If the net optical gain is G, then these coefficients are normalised according to the normalisation of the wavefunction,

$$G^2 = \sum \lambda'^2_k \tag{2.38}$$

$$\lambda_k = \frac{\lambda'_k}{G} \tag{2.39}$$

If only λ_1 exists (i.e. $\lambda_k = 0$ for $k > 1$), then the above reduces to Eq. 2.36 and become spectrally pure. Therefore, the relative strengths of the Schmidt coefficients λ_k essentially quantify the spectral purity. In general, the purity is quantified by how close the Schmidt decomposition results into only one major/dominant term in the series expression. Each term ($\lambda_k h_k(\omega_s) \times g_k(\omega_i)$) in the above equation can be viewed as a single mode squeezer with squeezing λ_k [28]. While writing the general wavevector as a multi-mode squeezer, the sum ($\sum$) in Eq. 2.37 will become a tensor product ($\otimes$) of the k single mode twin-beam

squeezer with strength λ_k [30, 37] through the H_{int}[6],

[6] $\hat{H}_{\lambda_k} = \lambda_k \hat{h}_k(\omega_s)\hat{g}_k(\omega_i) + H.c.$.

$$
\begin{aligned}
|\Psi\rangle &= exp\left(\frac{-i}{\hbar}\hat{H}_{int}\right)\ |0,0\rangle \\
&= exp\left(\frac{-i}{\hbar}\sum \hat{H}_{\lambda_k}\right)\ |0,0\rangle && (2.40)\\
&= \underset{k}{\otimes}\ exp\left(\frac{-i}{\hbar}\hat{H}_{\lambda_k}\right)\ |0,0\rangle && (2.41)\\
&= \underset{k}{\otimes}\ \sqrt{1-x_k}\ \sum_{n_k=0}^{\infty}(-e^{i\theta_{\lambda_k}})^{n_k}\ \sqrt{x^{n_k}}\ |n_k,n_k\rangle && (2.42)
\end{aligned}
$$

where k is the number of optical modes, x_k is the squeezing strength of k_{th} mode (Eq. 2.29) and $|n_k, n_k\rangle$ represents n number of signal and idler photons in k_{th} mode. The above expression is depicted in Fig. 2.8 showing that each HSPS acts as a conglomeration of k HSPSs where k is the number of non-zero optical modes. If the density matrix of the whole system is $\hat{\rho} = |\Psi\rangle\langle\Psi|$, then the density matrix of the heralded signal photons can be expressed by tracing out the idler photon state $|k_i\rangle$,

$$\hat{\rho}_s = tr_i(\hat{\rho}) = \sum_{k_i=1}^{\infty}\langle k_i||\Psi\rangle\langle\Psi||k_i\rangle \tag{2.43}$$

Hence, the purity (P) is quantified by the following two equations,

$$P = tr(\hat{\rho}_s^2) = \sum \lambda_k^4 \tag{2.44}$$

$$K_{Schmidt} = \frac{1}{P} = \frac{1}{\sum \lambda_k^4} \tag{2.45}$$

where, $K_{Schmidt}$ is called the Schmidt number. If there is only one element in the above expression ($k_i = 1$ only), then it corresponds to a separable signal-idler spectra in the bi-photon function and $tr(\hat{\rho}_s^2) = tr(\hat{\rho}_s)$ will be true. In general, this statement is also used to specify that a state is pure.

Expressing $f(\omega_s, \omega_i)$: joint spectral amplitude (JSA)

The separability of the bi-photon function is linked to the spectral construction of signal-idler correlation stemming from the SFWM process. The expression of SFWM bi-photon function helps to gain insight into the process [31]:

$$f(\omega_s, \omega_i) = \int d\omega_p \alpha(\omega_p)\alpha(\omega_s + \omega_i - \omega_p)\phi_{match} \tag{2.46}$$

The first part of the equation $\alpha(\omega_p)\alpha(\omega_s + \omega_i - \omega_p)$ is related to the energy conservation as it picks up two photons from the pump envelope with frequency ω_p and $(\omega_s + \omega_i - \omega_p)$. This part mimics autocorrelation function of the pump envelope constrained by the energy conservation (Eq. 2.4) and sets the effective energy bandwidth for the signal and idler as shown in Fig. 2.9 (a). The second part of the expression is related to momentum conservation or phase matching function and can be expressed as

$$\phi_{match} = sinc^2\left(\frac{\Delta k\ L}{2}\right) \tag{2.47}$$

where, Δk is the phase or momentum mismatch, and L is the SFWM interaction length. Thus, the bi-photon function can be loosely written as,

$$f(\omega_s, \omega_i) = (Energy\ Conservation) \times (Momentum\ Conservation)$$

Fig. 2.9 (a) describes the above equation. The quantitative expression of the bi-photon function (Eq. 2.46) is required to calculate the spectral purity of our photon-pair sources

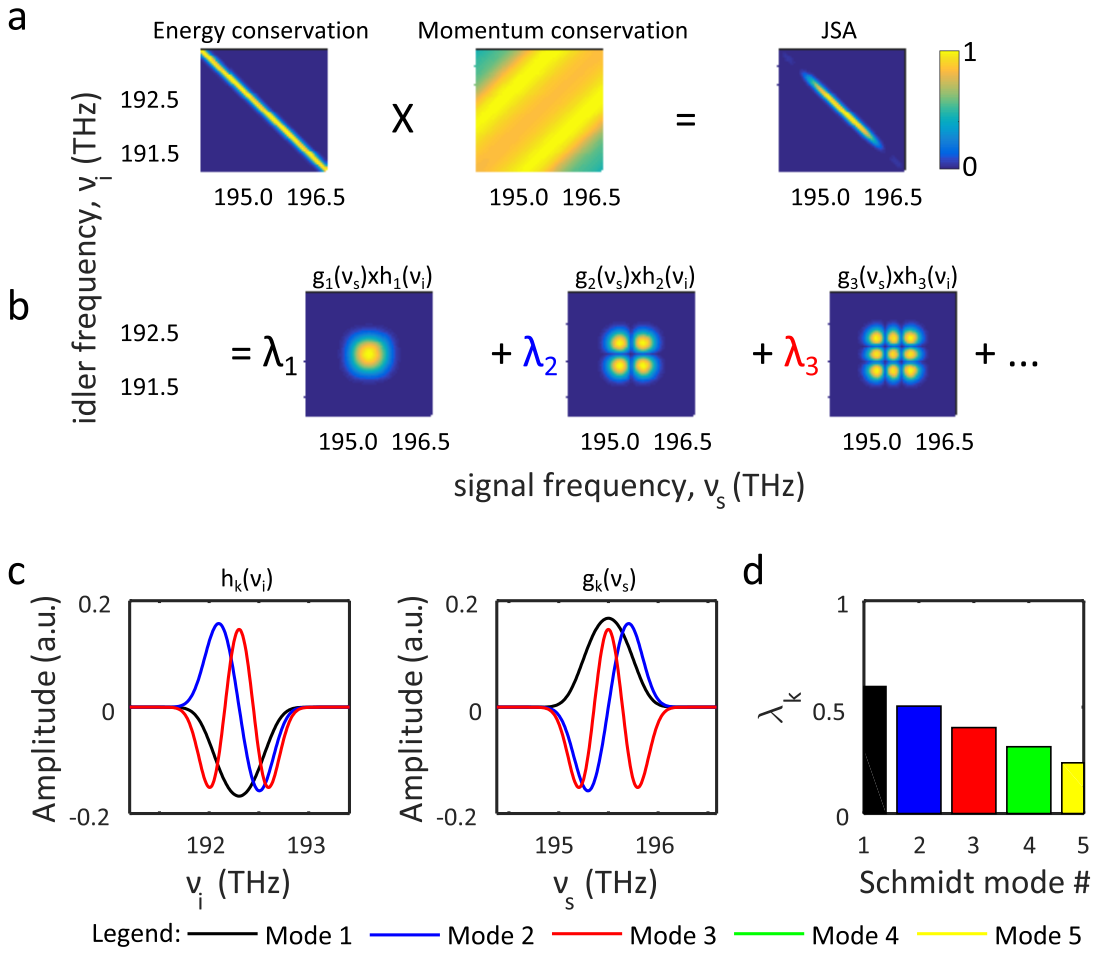

Figure 2.9: JSA and Schmidt decomposition. (a) Pump envelope of a $sech$ pulse of $500\ pm$ FWHM, showing energy conservation bandwidth; phase matching or momentum conservation of a silicon-nanowire waveguide of $14.5\ mm$ length; JSA as the outcome of energy and momentum conservations. (b) Schmidt decomposition of this JSA showing the first three terms. (c) The signal ($g(\nu_s)$) and idler ($h(\nu_i)$) photons' spectra of the first three Schmidt modes. (d) The relative amplitude λ_k of the normalised squeezing for the first five modes.

which strongly depends on the choice of the structure, waveguides or micro-ring resonators. The plot of the amplitude of the bi-photon function in terms of signal and idler frequency is called the joint spectral amplitude (JSA). JSA is the graphical and quantitative representation of the signal-idler spectral correlation. It is sufficient to quantify purity of a heralded single-photon source. As mentioned in the last section and shown in Fig. 2.9 (b), the JSA can be decomposed into orthogonal signal-idler spectral modes using Schmidt decompositions. The Schmidt coefficients (λ_k) are then used to estimate purity P (Eq. 2.44).

Estimation of purity using joint spectral intensity (JSI) measurements

Conceptually, the most straight-forward measurement of JSA is to put a single-photon spectrometer in each of the signal and idler photons' output arms. This joint measurement of signal-idler photons' frequency is used to reconstruct joint spectral intensity (JSI) [42]. JSI does not include the phase information and therefore only serves as an upper-bound of the purity calculated from it. Due to the flux rate (∼brightness) of the single-photons, this aforementioned measurement requires a long integration time of the detectors. Also, most single-photon spectrometers have poor wavelength resolution, thus they are not

able to resolve finer features. In recent years, stimulated non-linear optical processes

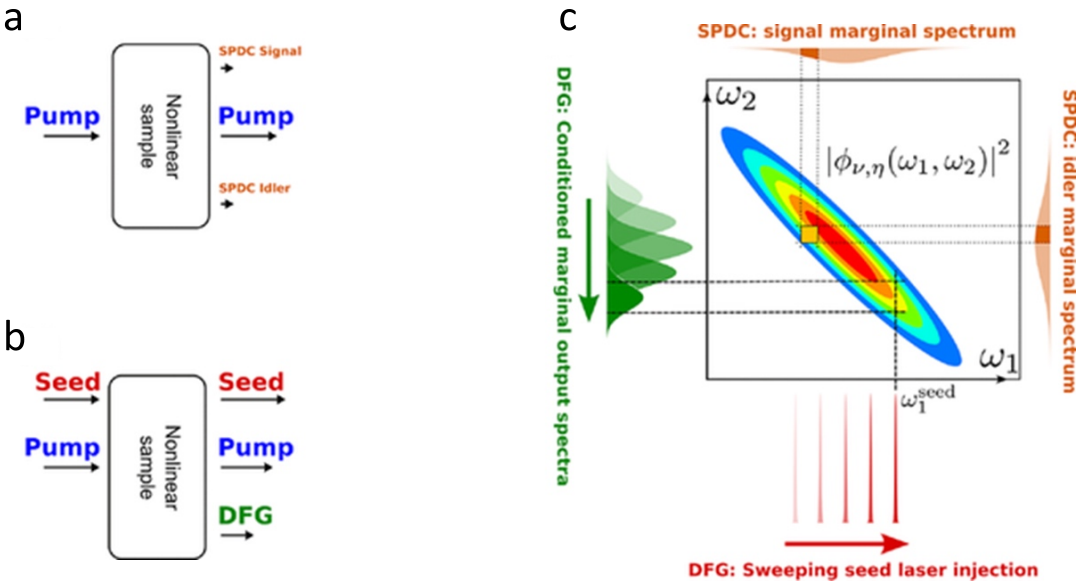

Figure 2.10: Reconstructing JSI using stimulated nonlinear process. This figure is adapted from *Eckstein et al. Laser & Photonics Reviews, 80 (5), 2014* [43]. Using a monochromatic seed continuous wave (CW) laser in the place of the SPDC signal photons, a stimulated idler photon has been generated as the difference frequency generation (DFG). By sweeping the seed laser in frequency and recording generated idler photons' spectra, the JSI can be reconstructed.

have been used to reconstruct the JSI [43]. Figure 2.10 shows the stimulated process: difference frequency generation (DFG) to estimate the JSI of a SPDC HSPS. Here the signal photons are mimicked by a monochromatic CW laser called seed laser, and the generated idler is detected by a classical optical spectrum analyser (OSA). Also, different techniques to measure joint spectral phase (JSP) has been invented [44,45] in recent years to re-construct the full JSA.

Estimation of purity using un-heralded $g^{(2)}$ measurements

[7] Sec. 7.7: Eq. 7.183

It has been known that for a pure single mode twin beam squeezer, the un-heralded (i.e. not detected) photons of the photon-pairs behave as a thermal state [28][7]. Such a state also resembles a mixed state when measured in a Hanbury-Brown-Twiss (HBT) experiment (Fig. 2.7 (d,e)) with the corresponding $g^{(2)}(0)$ approaching 2. If the single-photon state is spectrally pure (only one temporal/Schmidt mode), then $g^{(2)} = 2$ (maximally mixed). It has been shown recently that for low values of squeezing (optical gain $G << 1$) for low pump power, the $g^{(2)}$ and the spectral purity (P) is related by [30, 37],

$$g^{(2)}(0) = 1 + \frac{\sum_k sinh^4(\lambda'_k)}{\left[\sum_k sinh^2(\lambda'_k)\right]^2} \tag{2.48}$$

$$\approx 1 + \frac{\sum_k G^4\lambda_k^4}{\left[\sum_k G^2\lambda_k^2)\right]^2}$$

$$= 1 + P \tag{2.49}$$

[8] $\sum \lambda_k^2 = 1$

where, λ'_k are the non-normalised eigenvalues of the Schmidt decomposition (Eq. 2.39)[8]. The above equation is valid when G is small enough ($G << 1$) such that $sinh(\lambda'_k) \approx \lambda'_k$. As shown in Fig. 2.7 (d), in this HBT configuration, idler photons are not detected, hence the name *un-heralded*. The signal photons are passed through an even beam-splitter (BS) and

the outcomes are detected by two detectors (D_2, D_3) as a function of time delay (τ). This experiment essentially resembles a auto-correlation of the signal photons' wave-packets. At delay $\tau = 0$, the photon wave-packets overlap maximally on the BS and results in the highest peak in the 2-fold counts as shown in Fig. 2.7 (e). The other peaks in this histogram corresponds to the time delay of non-overlapping photons' wave-packets, and thus used to normalise the counts. If no other nonlinear process is considered during the photon-pair generation, then $g^{(2)}(0)$ will not depend on the input power[9].

[9] if $G >> 1$, $g^{(2)} \approx 2$ will overestimate P

$g^{(2)}$ measurement is simpler compared to the JSA measurement while estimating the same purity value. Also, $g^{(2)}$ measurement includes the effect of both amplitude and phase of the photons compared to the JSI that only considers amplitudes. In contrast, As $g^{(2)}$ is a HBT experiment of only the signal channel, the presence of background noise affects the measurement results drastically. Usually, background noises are uncorrelated in time. Thus, measurements including both signal and idler photons, which are highly correlated in time, naturally discard such noise.

2.2.5 Indistinguishability

Indistinguishability is the true measure of a scalable heralded single photon source. Indistinguishability refers to the degree of identicalness among the heralded single-photons emitted from multiple sources. A complex quantum algorithm implemented through a quantum photonic circuit often requires multiple identical single-photon sources. Thus, indistinguishability is one of the most important metrics of a HSPS.

Indistinguishability is measured using a phenomenon called quantum interference first experimentally demonstrated by Hong, Ou and Mandel [46]. Figure 2.11 (a) shows a cartoon of quantum interference between two heralded single-photon sources (S1 and S2): the heralded single-photons (s_1, s_2) from both sources are incident on an evenly split beam-splitter (BS) and have four possible outcomes of leaving the beam-splitter. As shown in Fig. 2.11 (b), both photons can reflect or transmit (anti-bunching), and one of them can transmit while the other reflects (bunching). If both of the photons are identical in all degrees of freedom such as spatial mode, polarisation, spectrum and arrival time on the beam-splitter then the wavefunctions of those two single-photons overlap completely on the beam-splitter. That results in the two photons bunching and leaving the beam-splitter together through either of the two output ports. Therefore, to measure the indistinguishability we vary, for example, the relative time delay between the two incoming photons and keep recording the 4-fold coincidence values as shown in Fig. 2.11 (c). When the photons' wavepackets completely overlap in time ($\tau = 0$) and they are indistinguishable, they will bunch together at the output and there will be a drop in the 4-fold counts. The degree of indistinguishability is quantified by measuring this coincidence rate drop, such as for complete indistinguishability the rate drops to zero. For BS with reflectivity R and transmissivity T, P_{4F} can be expressed as [46],

$$P_{4F} = N\ (R^2 + T^2 - 2RTV_{HOM}\ e^{-(\delta\tau/\sigma_\tau)^2}) \tag{2.50}$$

where N is a normalisation constant, V_{HOM} represents the visibility of the interference, and the Gaussian part of the expression corresponds to the filter and pump spectra and the spectra of the photons. From experimental point of view, the visibility can also be expressed as,

$$V_{HOM} = \frac{P_{4F}(\tau \to \infty) - P_{4F}(\tau = 0)}{P_{4F}(\tau \to \infty)} \tag{2.51}$$

The above interference can also be performed in a Mach-Zehnder interferometer (MZI) as shown in Fig. 2.11 (d) and (e). Here, complete indistinguishability corresponds to the

100% visibility (V_{MZI}) of interference fringes [47, 48], while complete distinguishability refers to the fringe visibility of 33%. The rate of 4-fold coincident events (P_{4F}) and visibility for both cases for a perfect MZI can be expressed in terms of the MZI phase (Φ_{MZI}):

$$P_{4F.I} = |cos(\Phi_{MZI})|^2 \tag{2.52}$$

$$P_{4F.D} = |cos^2(\Phi_{MZI}/2)|^2 + |sin^2(\Phi_{MZI}/2)|^2 \tag{2.53}$$

$$V_{MZI} = \frac{(P_{4F})_{max} - (P_{4F})_{min}}{(P_{4F})_{max} + (P_{4F})_{min}} \tag{2.54}$$

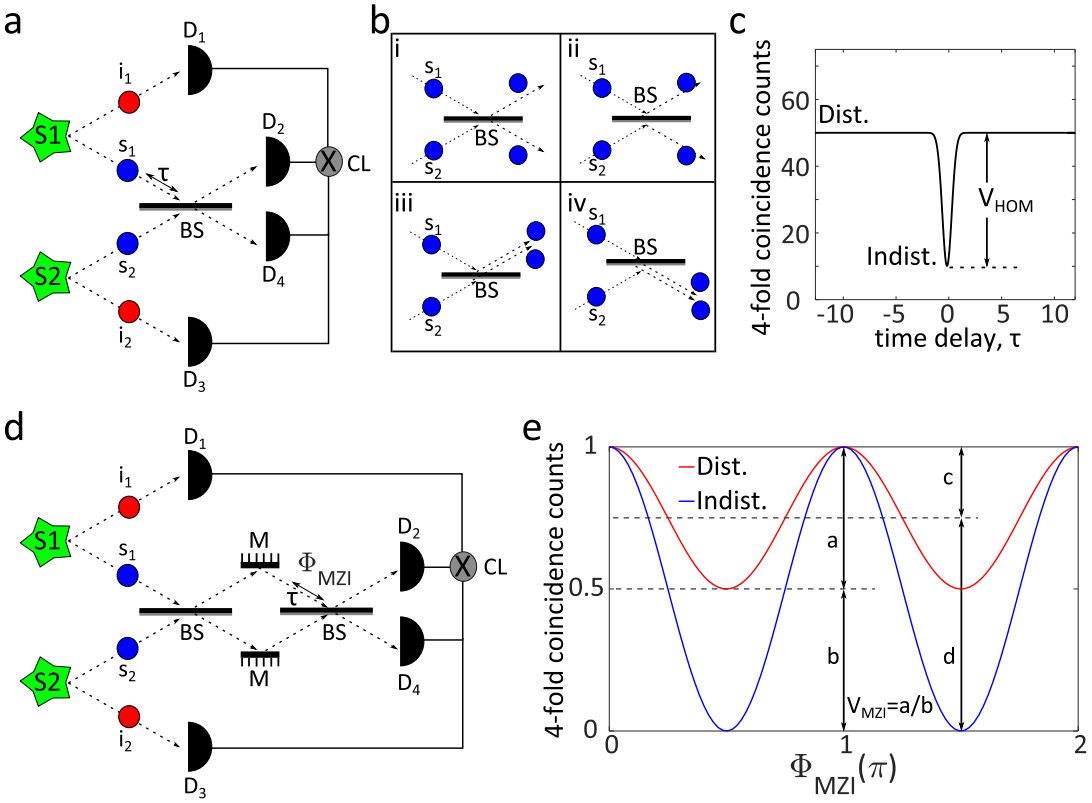

Figure 2.11: Measuring indistinguishability. BS: even beam-splitter, M: mirror, D: detectors, CL: coincidence logic unit. (a) HOM interference experiment with heralded single-photon sources. Signal photons s_1 and s_2 from source S1 and source S2 are interfered on a BS. A delay line is used to vary the arrival time (τ) of the signal photons from source S2. (b) This interference has four possible outcomes: i) and ii) both s_1 and s_2 come out of different ports, iii) and iv) both s_1 and s_2 come out of the same port which is called bunching. (c) Four-fold coincidence is plotted against τ and a drop in the count rate is observed due to the bunching of the indistinguishable photons [46]. The count rate will drop to zero for completely indistinguishable sources. (d) The same experiment can be performed using a Mach-Zehnder interferometer. (e) Four-fold coincidence is plotted while ϕ_{MZI} is varied. Absolutely indistinguishable sources will have four-fold coincidence with 100% visibility compared to the 33% visibility of the totally distinguishable photons [47, 48]. Partially indistinguishable sources have visibilities between these two values.

Naively, it may appear that indistinguishability between two independent sources requires that $f(\omega_s, \omega_i)_{source1} = f(\omega_s, \omega_i)_{source2}$. Considering the latter is true, but the purity is not unity then the heralded photons have multiple spectral modes as mentioned in the previous section (Sec. 2.2.4) and shown in Fig. 2.8. Different spectral modes are orthogonal to each other as obtained through orthogonal Schmidt decomposition and shown in Fig. 2.9. Figure 2.12 depicts the situation of measuring quantum interference with such impure

sources. As the first spectral mode of source S1 is orthogonal to the second spectral mode of source S2, they will not interact in the beam-splitter and not bunch together. This will result in this residual value of 4-fold coincidence count rate and the sources will not be considered indistinguishable. Therefore, the purity of the sources has an intimate relationship with indistinguishability. If both of the sources are pure and have identical spectral composition, only then will their identical bi-photon functions result in 100% indistinguishability. One way to include all the above figures of merit into one attribute is

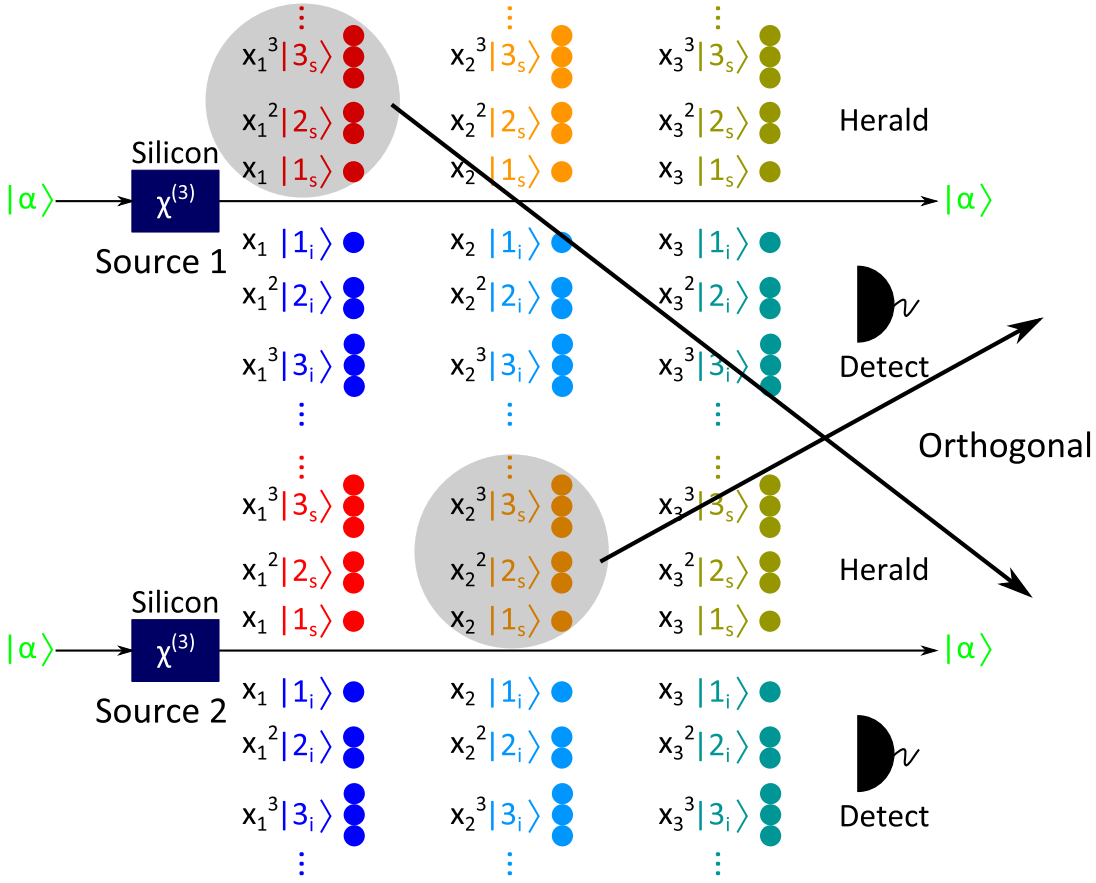

Figure 2.12: Orthogonality of the different optical modes of impure sources shows the potential cause for reduced interference in an indistinguishability measurement of sources. Therefore, indistinguishability measurement is intimately related to the spectral purity.

to introduce coefficient of PIM,

$$\mathbb{C}_{\mathrm{PIM}} = \mathrm{B}_{4\mathrm{F}} \times \mathrm{PIM}_{\mathrm{raw}} \div \mathrm{T}_{\mathrm{int}}. \tag{2.55}$$

The raw visibility of PIM, $\mathrm{PIM}_{\mathrm{raw}}$ takes into account multi-pair and multi-mode effect on the indistinguishability while the raw 4-fold brightness $\mathrm{B}_{4\mathrm{F}}$ and integration time $\mathrm{T}_{\mathrm{int}}$ together take into account the intrinsic photon generation efficiency (γ_{eff}), heralding efficiency (η_H) and collection efficiency (e.g. VGC loss). Comparing $\mathbb{C}_{\mathrm{PIM}}$ of different sources, we can evaluate the scalability of heralded single-photon sources. A source is more scalable if it has higher brightness ($\mathrm{B}_{4\mathrm{F}} \uparrow$) and higher raw visibility ($\mathrm{PIM}_{\mathrm{raw}} \uparrow$) for the same integration time ($\mathrm{T}_{\mathrm{int}}$).

2.3 Recent advances with HSPS

In the past few years, there has been tremendous progress with the development and performance of single-photon sources. Although practical sources are still far from ideal,

the present SPDC based multiplexed HSPSs [49] and quantum dot based high brightness DSPSs [50] have shown great promise. The HSPSs based on silicon photonics have also progressed significantly in the last few years. In the following sections, some of these results are reviewed from the point of view of an ideal HSPS.

2.3.1 HSPS in silicon photonics

There are three structures in silicon photonics which have been used often as SFWM based HSPSs in the last few decades. They are waveguides (strip and ridge), micro-ring resonators and photonic crystals (PhC) (waveguides and cavities). The brightnesses of these HSPSs have been investigated extensively and Tab. 2.1 shows the relative comparison of the brightness values from selected experiments. In contrast, purity, specifically spectral purity, has been investigated in fewer experiments [44, 51–55]. Most of these experiments have investigated the purity of the micro-resonator HSPSs. Only a few measured the purity of the waveguides [44, 53][10] but not in the context of achieving higher purity with or without spectral filtering. Thus, systematic investigation of the spectral purity of the SOI waveguide HSPSs have not been performed till now. In fact, in most waveguide experiments, narrow spectral filters are employed and it is assumed that the spectral purity is achieved. Lastly, among all the experiments, only three experiments to date have investigated indistinguishability as 4-fold coincidences by performing a triggered HOM interference (Sec. 2.2.5). All three of these experiments were performed with nanowire waveguides. Therefore, indistinguishability data for other structures such as micro-ring resonator or PhC waveguides do not presently exist in the literature.

[10] reconstructing JSI & JSP using stimulated four wave mixing

Lit.	Power (μW)	R (MHz)	γ_{eff} ($Mcts/s/mW^2$)	CC_2 ($kcts/s$)	CAR	η (dB)	Purity (%)	Indist. (%)
[56] Wg	2185	500	**5.72**	5	–	**1.9**	-	71
[57] Wg	–	10	–	0.6	7	-	-	69
[58] Wg	200	50	–	0.6	50	2.5	-	**88**
[38] Rg	59	-	$\mathbf{149 \pm 6}$	5.5	532	3.5	-	-
[59] Rg	700	-	1.62 ± 6	–	500	2.5	-	-
[60] Rg	–	-	–	–	12	10	-	-
[55] Rg	8	10	–	–	–	5	$\mathbf{97 \pm 9}$	-

Table 2.1: Figures of merits of SOI HSPSs. In addition to figures of merits, experimental conditions are also tabulated. Wg: waveguide HSPS; Rg: micro-ring resonator HSPS; R: repetition rate of the pulsed laser; CC_2: raw coincidence counts; η: collection loss from the HSPS. The brightness of a moderate Q-factor resonator is orders of magnitude higher than a waveguide HSPS. The purity of a resonator is high without spectral filtering. The reported highest indistinguishability for waveguide HSPS is $88 \pm 8\%$, while for resonator HSPSs it is not measured yet. These indistinguishability values are achieved with spectral filtering.

The very first of the aforementioned waveguide experiments, has been done by Harada et al [56] (2011). It shows 71% raw indistinguishability between nanowire HSPSs. It is argued that the visibility reduction is solely due to multipair emission as very narrow spectral filters ($0.2\ nm$) were used. Another result of $69 \pm 3.4\%$ raw indistinguishability has been reported in an active temporal multiplexing scheme [57]. A higher value of visibility $88 \pm 8\%$ has been reported by also employing narrow spectral filtering [58]. However, the nature of spectral filtering and its impact on the visibility has not been investigated in

these experiments.

Other four-fold experiments with silicon HSPS have been reported very recently [61, 62]. In these experiments a silicon nanowire has been used as HSPS in the context of wavelength-division and time-division multiplexing schemes, and the properties of the single-photons were not in a focus. All of the mentioned experiments used the fundamental spatial waveguide mode. Recently, photon-pairs generation using SFWM involving multiple spatial waveguide modes has been experimented [63] with the promise of higher spectral purity without narrowband filtering.

Similar to the waveguides, the micro-ring resonator and the PhC waveguides have been investigated extensively to optimise the brightness. Theoretically, the micro-ring resonators are much brighter than the waveguides. A significantly higher CAR value 532 (12000) was obtained for a input power $59\ \mu W$ (at much lower power) in a regular micro-ring resonator [38] along with 99.5% photon-number purity ($g_H^{(2)} = 0.005$) for $20\ \mu W$. To date, this is the highest CAR values for a low CW input power with the highest brightness as a SOI HSPS. Therefore, in a multi-photon experiment with 2-fold, 4-fold or higher order coincidences it will facilitate higher count rates with much lower backgrounds.

It has been shown theoretically that the resonant enhancement of the micro-ring resonator HSPSs cause intrinsic purity of 92%, without performing any spectral filtering [34]. Experimentally, purity $P = 97 \pm 9\%$[11] of the micro-ring resonator HSPSs ($Q \sim 4 \times 10^4$, $FWHM = 38\ pm$, $5\ pm$ spectral resolution) has been also measured by reconstructing the JSI using stimulated four wave mixing [55]. In another experiment, single-photons generated from counter-propagating pump pulses in a micro-ring resonator have been interfered in HOM interferometer with a raw visibility of $88.1 \pm 3.1\%$. As the interfered photons were from the same resonator, this value implies the spectral purity and close to the ideal value 93%. Although it has not been shown either theoretically or experimentally, similar outcomes can be expected from cavities based on PhC waveguides. Very recently, schemes have been proposed to further increase the spectral purity of the micro-ring resonator to near unity. One of these proposals employs pump pulses with adjustable temporal shape to excite the resonator [66]. In other proposals, adjustable cavity-coupling for signal and idler photons have been used to increase the purity of the photons [64, 65]. These results imply that the indistinguishability between single-photons from micro-ring resonator HSPSs should be very high, which has not been experimentally demonstrated yet, and is one of the experiments performed in this thesis.

[11] estimated from the quoted Schmidt number $K_{Schmidt} = 1.03 \pm 0.1$

The photon-number purity of either of the waveguide or micro-resonator sources is not usually quoted in experiments. Loss in collecting the photon-pairs off-chip is still too high (best VGC in SOI is $-0.36\ dB$ [67]) to have any decent value of the heralding efficiency. Theoretical calculations on the micro-ring resonator shows that in the presence of loss, heralding photons' rate and heralding efficiency cannot be optimised simultaneously [41]. Increasing the heralding efficiency significantly reduces the heralding photons' rate. This calculation suggest the best achievable heralding efficiency for a micro-ring resonator to be 80%.

Indistinguishability experiments or other quantum algorithms involving multiple sources require stable resonant position of the resonators. Stabilising the resonance position of a micro-ring resonator is non-trivial due to its high sensitivity. Thermal stabilisation of micro-ring resonators with phase locked loop for stable frequency comb generation has been studied already for pulsed configuration [68]. More recently, re-injecting signal-idler pairs of the resonator as amplified spontaneous emission, CW lasing is achieved without any external laser [69, 70]. This technique is also used for frequency comb stabilising.

Micro-disc resonator sources in SOI with very high Q-factor (near a million) have been

demonstrated with pair generation rate of $100\ kcounts/s$ at near telecom wavelengths with $22\mu W$ CW pump power [71]. This is the highest raw brightness observed in an SOI HSPS though this source was not fully integrated as tapered optical fibre was used to collect the photons. Theoretical simulation of SFWM photon-pairs generated inside a photonic band gap Bragg cavity has been shown to choose only specific phase matching condition to be fulfilled which increases the CAR of the process [52]. A review of photon-pair generation and photon-storage buffers in photonic crystal designs in SOI chips can be found in [72].

A full integration of source and detectors in a quantum photonic circuit also requires high extinction on-chip pump rejection filters. As the pump powers that we use to generate photon-pairs are about $0\ dBm$, an excess of $100\ dB$ pump extinction filter is required. Usual filter structures in SOI involves cascaded AMZIs, micro-ring resonators and Bragg filters. It has been shown that imperfect filters due to the fabrication tolerance results in reduced extinction than designed [73]. In that experiment, using a MZI to mimic perfect beam-splitter resulted in $60\ dB$ extinction, compared to the imperfect component with $\sim 30\ dB$ extinction. In another experiment, single etch step Bragg filter grating of 1.1 nm bandwidth with $40\ dB$ rejection has been shown [78]. As Bragg filters are comparatively longer than the AMZIs or resonators, there is the possibility of generating spurious SFWM photon-pairs inside the filters. This has been studied both theoretically and experimentally in [79].

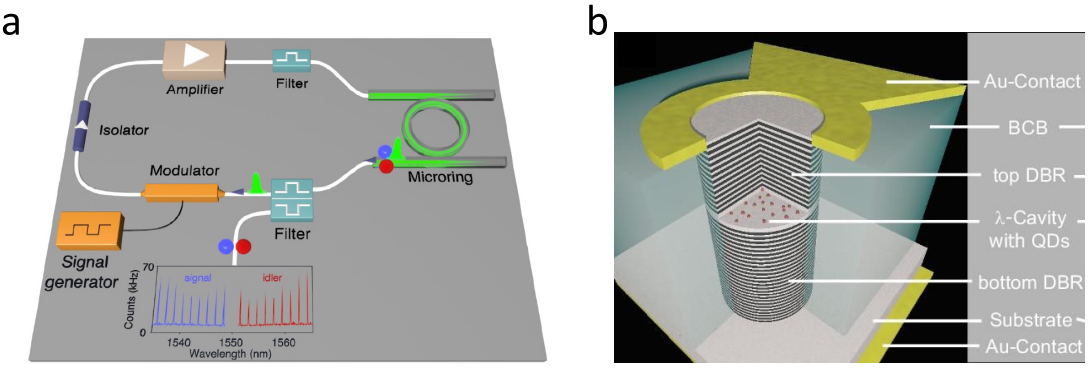

Figure 2.13: Single-photon sources without external lasers. (a) Shows the configuration of a harmonically mode-locked laser using a micro-ring resonator. This configuration is similar to the standard active mode-locked laser such as the commercially available fibre-ring laser: ultrafast optical clock (UOC) from *PriTel, Inc.*. This figure is adapted from *Roztocki et al, Opt. Express 25, 18940-18949 (2017)* [54]. In that experiment an unheralded $g^{(2)}(0) = 2.00 \pm 0.11$ was also observed. (b) Shows quantum LEDs, using all electrical excitations. This figure has been adapted from *Heindel et al, Appl. Phys. Lett. 96, 011107 (2010)* [80] demonstrating $g_H^{(2)}(0)$ value of 0.13 ± 0.05 at a rate of $8.5\ MHz$ with 34% overall efficiency of $220\ MHz$ electronic excitations. In a later experiment [81], with similar structure, similar $g_H^{(2)}(0) = 0.152$ for $400\ MHz$ repetition rate has been demonstrated.

2.3.2 SPS in other platforms

DSPSs: Quantum dots, LEDs & organic molecules

Quantum dot experiments are usually characterised by three attributes: brightness, photon-number purity and indistinguishability. The brightness is measured by the probability of generating photons per excitation pulse. The photon number purity is measured using standard conditional $g_H^{(2)}(0)$ experiments. The indistinguishability measurements for quantum dots and similar structures are different from the HSPSs. For HSPSs, photons are inter-

fered from two independent HSPSs. For quantum dots, photons which are generated in different times but from the same quantum dots are interfered, which is essentially a temporal indistinguishability (spectral purity) measurement among photons from the same source. The idea here is to temporally de-multiplex photon-stream of a single quantum dot into multiple photon-streams such that each stream behaves as an independent single-photon source. Therefore, high temporal indistinguishability and simultaneous high brightness determines how many independent photon-streams can be achieved from a single quantum dot [50]. Table 2.2 shows recent performance in the quantum dots and similar structures. This is a rapidly developing research area and the aforementioned metrics (brightness, $g_H^{(2)}$) are not fully characterised (especially in terms of laser power and such) in many platforms. Among all the platforms, the *InGaAs* quantum dots have excelled both in brightness and Spectral purity. A comprehensive review on DSPSs can be found in [82].

Lit.	Temp.	R (MHz)	$\bar{n}(\%)$	$g_H^{(2)}$	Purity (%)	τ_{bin}	Indist.(%)
[83] InGaAs	cryo	80	14	0.03	71 (NR), 96 (R)	32	–
[84] InGaAs	cryo	81	15	0.03	–, 99 (R)	–	–
[85] InAs/GaAs	cryo	76.4	6.6	0.007	–, 92 (R)	1120	–
[86] InAs/InP	cryo	–	–	0.06	–, –	–	55
[87] DBT	room	–	75	0.2	–, –	–	–
[26] Col. cent.	room	–	–	0.3	–, –	–	–

Table 2.2: Figures of merits of DSPSs. $Col.Cent.$ refers to colour centre; $Temp.$ refers to operating temperature and τ_{bin} refers to the n^{th} time bin used for interference. Purity refers to the spectral purity usually quoted as indistinguishability by quantum dot community. Other metrics have their usual meanings.

Quantum dots are unique structures. To date, scalable fabrication of quantum dots has not been demonstrated experimentally [82]. Only in one of the two most recent experiments a HOM interference is performed between two independent InGaAs/GaAs quantum dots [88] estimating the visibility to be 80%[12] due to non-zero $g_H^{(2)}(0)$ with average 18% collection efficiency. It also uses low loss silicon oxynitride waveguide circuit as hybrid integration with quantum dots at cryogenic temperature. Although the photons are generated in this experiment using non-resonant excitation, it is not electroluminescence. In the other experiment [86], the indistinguishability between photons emitted from two independent quantum dots has been estimated as 55% without background corrections.

[12] or 50% depending on the correction method

In a recent experiment [83], absolute brightness of $3.5\ MHz$ has been achieved, which is 14% of the total excitation pulses. At this brightness the photon number purity was higher than 97%. The temporal indistinguishability of the photons were 70% for non-resonant excitation and 96% for resonant excitation. In another report, 99% temporal indistinguishability with state-of-the-art extraction efficiency of 15% brightness for a photon-number purity of 99% ($g_H^{(2)} \sim 0.0028$) [84] has been achieved. A similar result has been reported in [88, 89]. In all of the above results, the use of the optical cavity enhances the Purcell factor which prohibits sideband emissions and ultimately increases temporal indistinguishability of the photons. A more exotic result shows photon triplet generation from a quantum dot positioned inside an epitaxially-grown photonic nanowire [90]. A triplet is a sequential emission of three photons with strong correlations. Also, plug-and-play fibre coupled quantum dots has been shown recently [91].

The point defect solid state single-photon sources have the obvious advantage of operating temperature over the quantum dots. While the quantum dots structures need to be operated in cryogenic temperature, the point defect sources operate at room temper-

ature [26]. Some of these sources have also shown wavelength tuneability of the emitted photons such as Boron nitride point defects [92] ($g_H^2(0)$ is 0.39 and 0.34 for 633 nm and 714 nm respectively), nitrogen vacancy (NV) centres in a GaP-on-diamond platform [93] which is useful for indistinguishability experiment.

Significant progress has been made recently with organic molecules as single-photon sources in terms of brightness. DBT molecules at room temperature can yield 75% steady population inversion, while cooling it down to liquid nitrogen predicts more than 99% yield [87]. Another bio-molecule terrylene can reach 96% efficiency at room temperature [87] and already demonstrated 68% quantum yield by [25]. In these experiments, the photon collection efficiency is not optimised.

Comparing Tab. 2.1 and Tab. 2.2, we can see that the brightness and temporal indistinguishability (spectral purity) is higher for quantum dot SPSs than SOI HSPSs. However, indistinguishability measurement among multiple HSPSs is high while for quantum dots it presently scarce. Moreover, quantum dots require cryogenic operating temperature.

Work	Power (mW)	R (MHz)	$\bar{n}$	CC_2 ($kcts/s$)	η_H (%)	Purity (%)	Indist. (%)
[94] ppKTP	80	81	0.0007	24.3	64 ± 2	–	82 ± 2
[95] ppKTP	–	100	–	–	77 ± 3	90.6	91 ± 4
[96] ppKTP	700	–	–	–	40	95 ± 3	–
[97] aKTP	10	80	0.0005	–	53	90.7	89.7 ± 0.2
[98] ppLN	0.014	4	0.0042	0.2	12	–	–
[99] ppLN	0.03	1	0.01	–	46.2	66	–
[100] KDP	–	76	–	–	42	–	94.4 ± 1.6
[49] ppKTP	–	0.5	0.18	–	66.7 ± 2.4	92 ± 3	–

Table 2.3: Figures of merit of periodically poled SPDC HSPSs. The indistinguishability values here are obtained without any spectral filtering.

SPDC based on crystalline systems

The periodically poled crystalline waveguides, such as ppKTP, ppLN or KDP usually have high brightness and spectral purity simultaneously. It has been reported that, trade-off exists among heralding efficiency, spectral purity and brightness of the generated photon-pairs from ppKTP HSPSs at telecom wavelengths [101, 102]. In [94], it is discussed that the side lobes of the phase-matching function ($sinc$) in the JSA, limit the purity below 84% corresponding to $82 \pm 2\%$ indistinguishability which, if spectrally filtered, achieves indistinguishability of $100 \pm 5\%$. In another report, using different ppKTP constructions, the 90% purity is achieved using both JSI and unheralded $g^{(2)}(0)$ measurements [95]. Recently, apodised KTP has been introduced using domain engineering techniques [97] and without (with) any spectral filtering, $90.7 \pm 0.2\%$ (92.7%) indistinguishability and 53% (52%) heralding efficiency have been achieved.

Lithium niobate (LN) on insulator platform has emerged as integrated platform (topcial review [103] & [104]) and hybrid integration of femto-second glass waveguide with PPLN has also been reported [106, 107]. Recently, in this platform, high speed electro-optic modulators has also been demonstrated [105].

Among all the previously mentioned single-photon sources in Tab. 2.1, Tab. 2.2 and Tab. 2.3, the SPDC sources have shown comparable performance with quantum dots in terms of brightness and purities. At the same time, SPDC HSPSs have the best raw indistinguishability data (94.4 ± 1.6) among all the platforms without any spectral filtering.

III-V and compound semiconductor platforms

AlN micro-ring resonators have shown second order non-linearity and SPDC with almost unity purity from second order correlation function ($P = 1.07 \pm 0.12$) [108]. Photons were pumped at 775nm TM(2,2) mode and collected from 1550 nm TM(0,0) mode. AlN has electro-optic coefficients 10 times smaller than lithium niobate which has been compensated in this work with a 2×10^5 Q-factor micro-ring resonator. This work is an excellent demonstration of challenging fabrication of multi-mode (polarisation modes) waveguide SPDC process with high spectral purity.

GaAs emerged with the possibility of electrically self-pumped platform [109]. This results show type-I spontaneous parametric down-conversion of laser light from a $2.2\ mm$ long Bragg-reflection waveguide, with estimated internal pair production efficiency 2×10^{-8} (pairs/pump photon) or $8.57 \times 10^7 cts/s/mW$. However, this structure has a high linear propagation loss ($4.3\ dB/cm$).

UV-written silica waveguides

Recently UV written Ge doped silica waveguides (total 18) on a silicon substrate has been demonstrated to produce near identical photons at visible wavelengths. The waveguide lengths were $2.3\ cm$ each and $4.8\ \mu m$ thick with lateral Gaussian profile. The coupling efficiency is more than 80% from waveguide to the fibres. The raw purity is $\sim 87\%$ and with a gentle filtering (92% photon transmission) the purity increased to 97%. The maximum attained raw indistinguishability was 92.2%. With $80\ mW$ injected average power at visible wavelength (700 nm), 250 four-folds per second was observed, although the brightness of the photon-pairs of the different waveguides varies less than 4% [110, 111]. In terms of brightness, purity and raw indistinguishability, these silica waveguides have shown comparable performances with SPDC HSPSs.

Work	Power (mW)	R (MHz)	$\bar{n}$	CC_2 ($kcts/s$)	η_H (%)	Purity (%)	Indist. (%)
[111] Wg	80	80	–	200	31.6 ± 0.3	87	92.2
[112] Wg	–	0.25	–	–	–	–	–

Table 2.4: Figures of merit of other SFWM based HSPSs. The indistinguishability value here are obtained with spectral filtering. [111] is in visible wavelength while [112] is in $1550\ nm$.

Optical fibres

SFWM photon-pair generation has been proposed in standard polarisation maintaining fibres using dual-pump scheme [113]. In this scheme, SFWM photon-pair spectra can be tailored to achieve 99% purity albeit a trade off with spectral proximity with the pump spectra. With narrowband spectral filtering, 88% raw indistinguishability has been experimentally observed in micro-structured fibre [114]. JSI using stimulated four wave mixing was first measured in optical fibre by [115], and later [116] demonstrated near factorability ($P \sim 0.98$) with a bow-tie birefringent fibre.

2.3.3 Multiplexed SPS

The idea of multiplexing multiple single-photon sources was introduced to increase the photon number purity of the HSPSs, and to make the single-photons' stream more regular

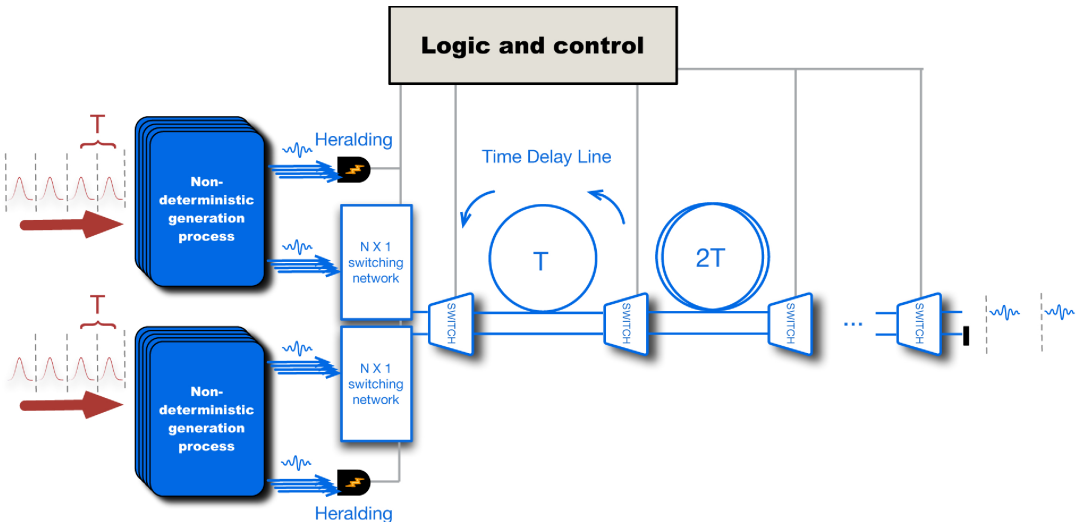

Figure 2.14: A scheme of spatial and temporal multiplexing of HSPSs adapted from *Mendoza et al. Optica 3, 127-132 (2016)* [117]. Here $N \times 1$ spatial switches are connected to N sources for spatial multiplexing. At the same time the output stream of the spatial multiplexing is regularised in time with a time interval T which is called temporal multiplexing.

[118, 119]. Together, these two effects can transform probabilistic HSPSs to deterministic on-demand single-photon sources. Figure 2.14 describes a spatial and temporal multiplexing scheme [117]. Laser pulses with time-period T generate signal-idler photon-pairs in N sources (shown by the blue squares) separated in space. The idler photons from the sources are being detected for heralding and the signal photons from each sources are connected to an input port of a $N \times 1$ switch. Detection of a heralding photon from any of these HSPSs will result in a single photon at the output of the switch. Combining single-photons from N sources to one output stream is called spatial multiplexing. Now the photons from these streams can be time delayed by integer multiple of T to make the photon stream regular in time such that at each time period T there are single-photons. This is called temporal multiplexing.

Multiplexing multiple single-photon sources, whether deterministic or heralded is popular due to its promise of increased brightness with lower CAR values (increased photon number purity). A multiplexed source can achieve high enough brightness to carry out multi-qubit algorithms or high bit rate QKD protocols. The proof of principle of this idea has already been demonstrated in time multiplexed sources such as in SOI, optical fibre and crystal based platforms (ppKTP, ppLN). [120] used a frequency conversion technique for multiplexing. [121] multiplexed PCF (total no 4) with average 86% (raw 71%) purity at telecom wavelength. With coupling loss to SMF-28 as -5.3 dB and the switch loss 0.94 dB, it results into a factor of 1.71 effective improvement of count rates for a fixed CAR value of 40. [49] multiplexed 40 time bins from the same ppKTP source with an average 92% spectral purity, and predicted 30 ten-fold coincidence per seconds and 1 thirty-fold coincidence per seconds which is 5 orders of magnitude higher than the recent 10 photon entanglement experiment by [122].

2.3.4 Characterisation of HSPS

Previously mentioned purity experiments mostly consists of using stimulated method to reconstruct JSI such as [115]. Recently, joint spectral phase (JSP) has been measured using phase-sensitive amplification [44]. Also time-lens technique has been used to measure

joint temporal amplitude (JTA)[13] and manipulate temporal correlation and therefore JSA [45]. Similar technique has been used to measure JSA at different position in the HOM interference [123]. In a recent report, Schmidt modes are selected experimentally by noticing that for a Gaussian JSA, the eigenmodes are Hermite-Gauss polynomials [124]. Using a sum-frequency generation technique and shaping the pump to match the eigenmode spectra, the upconverted photons have been detected which project the signal photons only to that eigenmode due to orthogonality conditions.

[13] Fourier transform of JTA ≡ JSA

An experimental overview of PIM methods has been presented in [125] for BBO crystal and optical fibres. The measurements include JSA, JSP, unheralded $g^{(2)}$, HOM measurements and a relative comparison of implied purity. It shows a good agreement between $g^{(2)}$ and HOM.

When measuring brightness and $g_H^{(2)}$, we assume perfect instruments. That is not necessarily valid for any experiments and for a high count-rate experiment the effect of counting logic system plays a role [126]. These types of effects can be mitigated using renormalisation of the measurement results. In a related experiment, pseudo photon-number resolving detector is used for heralding to investigate the effect of loss or noise on heralding along with determining the squeezing parameter [127]. This method will be very useful to correctly estimate the brightness of a HSPS.

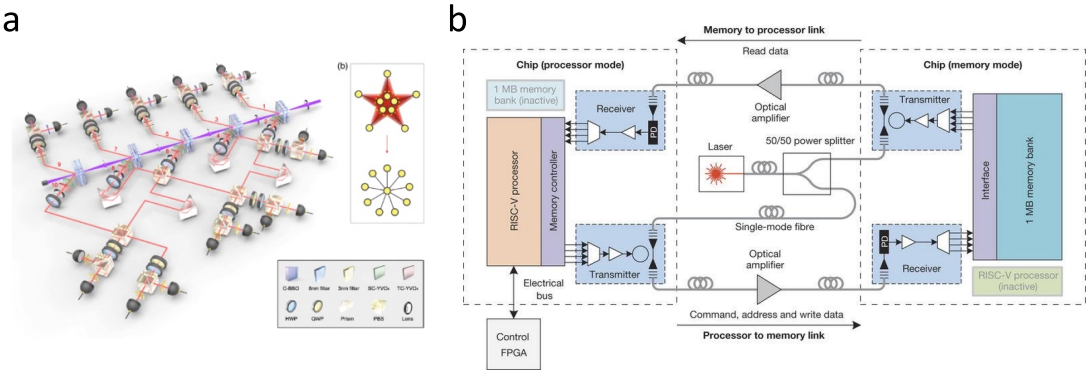

Figure 2.15: State of the art experiments. (a) 10 photon entanglement experiment. This figure is adapted from *Wang et al, Phys. Rev. Lett. 117, 210502 (2016)* [122]. (b) Electronic and photonic integration on the same chip using commercial $45\ nm$ CMOS compatible SOI platform. This image is adapted from *Sun et al, Nature 528, 534-538 (2015)* [17].

2.3.5 State of the art experiments with SPSs

One of the most challenging multi qubit experiments performed in recent years with practical HSPSs is the demonstration of the ten-photon entanglement [122]. The ability to herald ten single-photons requires stable 20-fold coincidence counts from HSPSs. Another experiment related to the state of the art HSPSs is the 18 qubit entanglement using three degrees of freedom [128]. Such experiments inspire the realisation of scalable optical quantum computing or other technologies with non-ideal single-photon sources in near future.

The primary reason to develop a near ideal single-photon source is to perform flawless quantum photonic experiments. The two most detrimental effects on a multi-photon experiment based on quantum interference are multi-mode and multi-pair effect due to an imperfect source. Usually, spectral filtering and (pseudo) photon-number resolving detection are used to mitigate those two effects when using an imperfect source. Recently, using time-lens techniques to the heralded photons, correlation of the SPDC photon-pairs from

anti-correlated to positively correlated has been demonstrated [129]. Also, there has been proposal to use post processing the outcome of a quantum experiment and reconstruct it for ideal sources [130, 131] or use methods such as counter-factual quantum erasure (remove the need for entanglement sharing) [132] or use weak coherent light [133] or thermal state [134].

Apart from being single-photon sources, micro-ring resonators have also been used for single-photon level quantum frequency conversion with 60% conversion efficiency [135] with the prediction of increasing it to 95% [136], and table top optical frequency combs [137].

Not all the quantum computing schemes are related to linear optical quantum computing or measurement induced nonlinearity. Single-photon induced phase shift is a holy grail of quantum logic circuits as it means deterministic photon-photon gate. In a recent experiment, a single photon pulse imprints a π phase shift on a second light beam using Rydberg blockades combined with electromagnetic induced transparency in an optical dipole trap [138]. In terms of quantum memory, three microsecond storage of weak coherent pulses with a Prussium doped crystal at 3.5 k for spin wave solid state quantum memories has also been shown [139].

2.4 Synopsis & outlook

In this chapter, we viewed the figures of merit (FOM) of a single-photon source: brightness, photon-number purity, spectral purity and indistinguishability. Using these FOMs, the SOI HSPSs are compared with state of the art SPDC HSPSs and DSPSs in different platforms. In terms of brightness, heralding efficiency, purity and indistinguishability the multiplexed SPDC HSPSs are the best single-photon sources available although none of the single-photon sources so far have shown more than 95% raw indistinguishability through quantum interference visibility [100]. Quantum dots DSPSs have demonstrated significant progress recently and have become comparable and even better than SPDC regarding brightness and indistinguishability (spectral purity) of photons from the same dot [50]. Using active demultiplexing such a high brightness and spectrally pure DSPS acts as multiple sources of indistinguishable single-photon streams. Quantum dots are unique and only very recently single-photons from two independent quantum dots has been interfered with 55% visibility [86] thus limiting the possible integration of multiple quantum dots in the same circuit. In contrast, using a high degree of multiplexing SPDC sources are achieving high brightness, purity and indistinguishability of single-photons [49]. Once a near ideal SPS is demonstrated in any of these platforms, we can scale up the linear optical circuit to perform sufficiently complex quantum algorithms. Such scaling up approach also requires a system that favours integration and SOI is one such platform.

The SOI photonic HSPSs have shown comparable intrinsic brightness to SPDC sources, but due to the low collection efficiency, the raw brightness is still low. The recent proposals [41, 64–66] with micro-ring resonator HSPSs promise near unity (99.99%) spectral purity with near unity indistinguishability and high heralding efficiency which are essential to build a multiplexed SPS.

Chapter 3

Silicon photonics

Contents

The silicon industry is the technological revolution that started a few decades ago in California in silicon valley. Emerged as the electronics industry, it has changed many aspects of our lives, in particular, by introducing computers for personal and professional uses. Over the last few decades, it has also opened pathways to implement light manipulations in the nano-scale regime in the very same silicon based platform. This study and application of optics in silicon is called silicon photonics. The term *photonics* is similar to the word *electronics*, inducing similar connotations such as integration of light manipulating structures. Albeit, *photonics* is neither limited to silicon structures nor to the integrated chip technologies. Photonics is also used to denote fibre based technologies and even large crystal based structures used as lasing materials. Thus, loosely defined, photonics is the science and engineering of photon-based phenomena. Specifically, in recent years, the study of quantum phenomena with photons, commonly known as quantum photonics, emerged as a quantum-based technology (e.g. quantum computing and quantum metrology). There are a vast number of material platforms used for quantum photonics: *Silicon on Insulator* (SOI), *Lithium Niobate waveguides* and *femtosecond laser written waveguides*, to name a few. We have chosen SOI platform for its versatility and mature fabrication technology.

This chapter begins with a brief description of the SOI photonic components used in this thesis for the photon indistinguishability measurements (PIMs). Any deviation from

the desired behaviour of these components can alter the PIM significantly. Therefore, it is necessary to understand the underlying physics of the SOI photonic components and the possible source of imperfections. Among those components, waveguides and micro-ring resonators are used as HSPSs in this thesis. The physical principle and design parameters of these two components are discussed in the next section. Afterwards, a short overview of the design software used is presented along with the foundry used for fabrications.

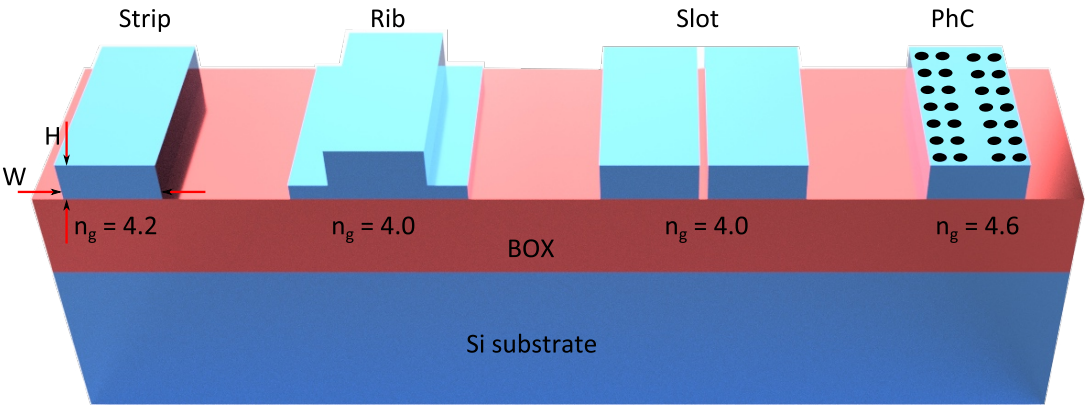

Figure 3.1: Silicon on insulator photonics waveguides. The layers of a silicon chip are shown. The silicon wafer or the silicon substrate is the bottom layer. The insulating SiO_2 material is grown by thermal oxidation on top of the substrate and commonly known as the buried oxide (BOX) layer. The actual high quality silicon layer used for device fabrication is bonded on top of the BOX [140]. Generally used thicknesses values are for substrate $200\ \mu m$ to $700\ \mu m$, for the BOX $3\ \mu m$ and for the deposited silicon $220\ nm$. Some broadly used waveguide structure in SOI are strip, rib, slot and photonic crystals (PhC) with respective group indices of (n_g) 4.2, 4.0, 4.0 and 4.6 at $1550\ nm$ telecom wavelength with standard dimensions [141, 142].

3.1 Silicon on Insulator platform

A Silicon on Insulator (SOI) chip consists of layers of different materials as shown in Fig. 3.1. The substrate is a silicon wafer of about $700\ \mu m$ thickness which varies depending on the application. On top of that $3\ \mu m$ (this amount may vary) SiO_2 is grown through oxidation, which is often called as buried oxide (BOX). High quality crystalline silicon of $220\ nm$ (the number varies) is bonded on top of the BOX [140]. Patterning the top layer of this silicon with different physical and chemical processes are usually termed as fabrication steps. Often, a cladding material such as SiO_2 is deposited on top of the silicon layer.

SOI is popular for a few reasons, most notably, because of the mature fabrication technology and the existing road map to electronic integration. In addition, photonic circuits designed and made in a standard foundry following standard fabrication process will give the consistent performance of the components. That makes an experiment widely repeatable. Therefore, the SOI platform, in principal, can produce commercial grade and foundry independent photonic components. Commercially, the most popular photonic component is the optical interconnect that facilitates the high bandwidth of data transmissions. A brief description of the components that we have used for our quantum photonics experiments follows.

3.1.1 Photoinic components

A photonic component is a nano scale structure, which is designed to manipulate light similar to a regular free space optical component. Among these components, the waveguide is the most important. It not only guides light through the photonic circuit but it also can change properties of the propagating light. For example, a waveguide with certain dimensions changes the dispersion properties of light many times more than the material dispersion. We begin our description with waveguides in the SOI photonic platform.

Waveguides

In free space, light is focussed, collimated or reflected to facilitate point-to-point communication with large components such as lenses and mirrors. In nano-scale regime, unlike the macro-optics components, the wavelength of the light is comparable to the dimension of the components. Therefore, the design and dimensions of a light guiding structure is non-trivial. One of the simplest light guiding structure in nano-scale regime is a slab waveguide. Figure 3.2 (a) shows the formation of slab waveguide where a slab of higher refractive index material (n_1) is sandwiched by slabs of lower refractive index materials (n_2, n_3) on either sides. The slab is confined in the vertical x-direction but infinite on the transverse y-direction and propagating z-direction. The physical principle behind guiding light in the slab waveguide is total internal reflection. While propagating, the light undergoes total internal reflection in the x-direction, and becomes confined in the x-direction inside the high index slab. Imposing self-consistency condition, waveguide modes are defined by the fields that maintain the same transverse direction and polarisation at all distances along the waveguide axis (i.e. eigenmodes) [143][14].

[14] Chap. 7 of the reference

The behaviour of light inside the slab is qualitatively represented by the dispersion diagram in Fig. 3.2 (b). Dispersion diagram is the relation between the energy ($\hbar\omega$) and momentum ($\hbar\beta$) of the light, or between angular frequency ω and wave-vector β. In the bulk medium, this relation results in a line called the *light line*. The slope of the *light line* is the group velocity v_g of the light in that medium:

$$v_g = \frac{d\omega}{d\beta} \tag{3.1}$$

As refractive index is defined by the ratio of the velocity of the light in that medium to the speed of light in the vacuum (c), the group index is defined by,

$$n_g = \frac{c}{v_g} \tag{3.2}$$

and the wave-vector can be expressed as $\beta = k_0 n_g$, where k_0 is the wave-vector of light in free space. Thus the slope of the light-line of a material can be uniquely represented by the refractive index n_g. A quantitative use of the light-line can be found in [144]. In this section a qualitative use of the light line is applied to explain the guided waveguide modes. Figure 3.2 (b) represents the light-lines of the slab waveguide's materials n_1, n_2 and n_3. As $n_1 > n_2 > n_3$, the slope of the n_3 medium's light line is the highest. The slab waveguide confines the light between the high index (n_1) and low index n_2 material and the light responds to both of the materials at the same time. Therefore, intuitively, the refractive index of the propagating light has to be in between these two values (e.g. n_1 and n_2). This index of the propagating light is called the effective refractive index n_{eff}. It means that the dispersion relation of the confined guided mode of light has to be somewhere in between those two light-lines. Based on this idea, the waveguide modes can be defined into three categories: guided modes, propagating radiative modes and evanescent radiative modes. The strict definition of the guided modes is that the electromagnetic fields of the guided

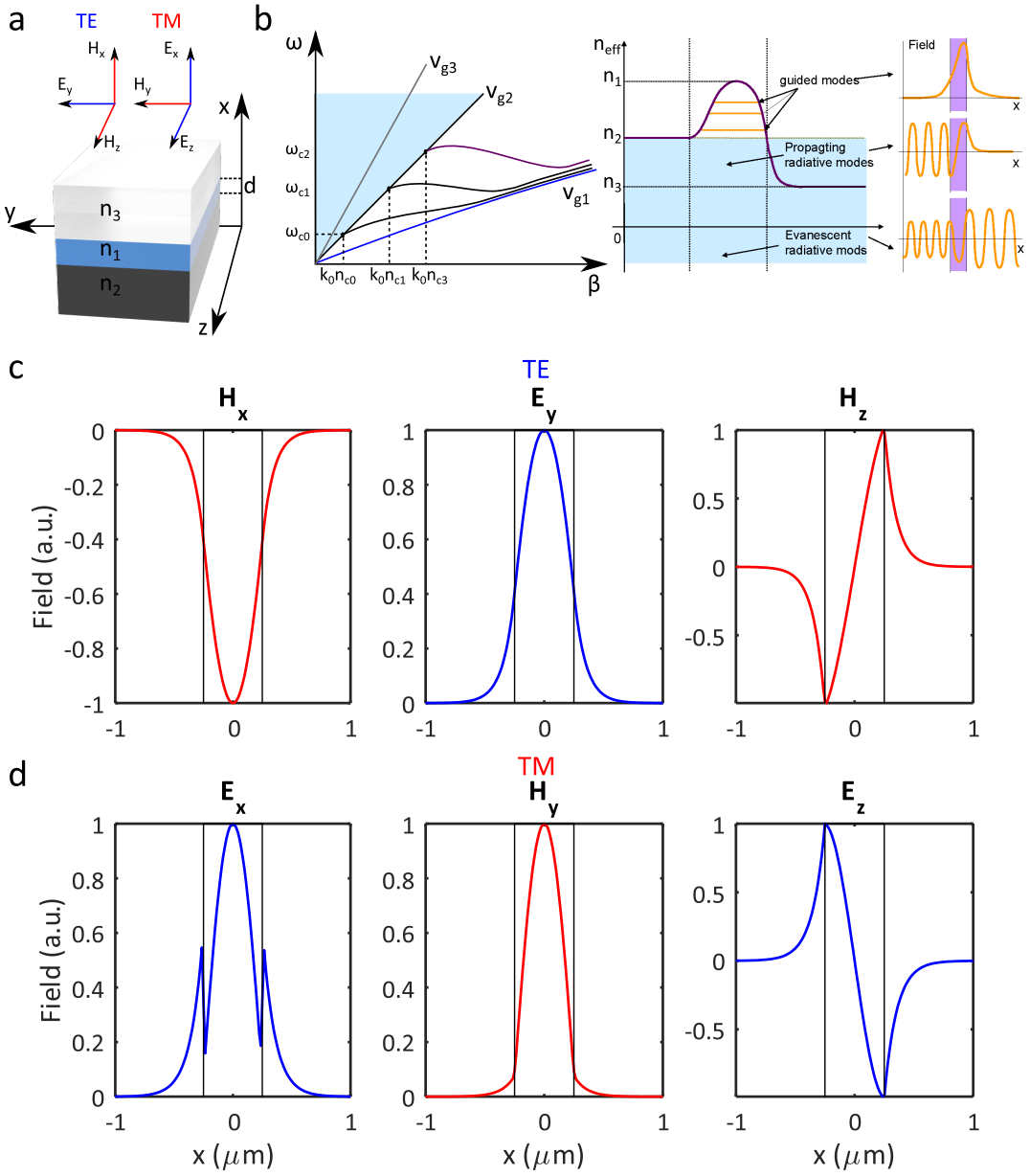

Figure 3.2: Slab waveguide and dispersion relation. (a) In a slab waveguide, a slab of high index material (n_1) is sandwiched by low index materials (n_2 and n_3). The TE and TM optical modes of propagation contain the electromagnetic field components (H_x, E_y, H_z) and (E_x, H_y, E_z) respectively. (b) The dispersion relations of the propagating waveguide modes have to be in-between the light-lines of the high index (v_{g1}) and low index (v_{g2}) materials. Due to the light confinement, a discrete set of waveguide modes (eigenmodes) exist, each with its own cut-off frequency (ω_c). The plot on the right shows the propagating eigenmodes form discrete energy levels while the radiative modes form a continuous band. These plots are adapted from Microphotonics course notes of Universiteit Gent and the textbook by Saleh and Teich [143] (Fig. 7.28). (c) Shows the mode profiles of the field components of TE mode obtained using *Lumerical Mode Solver*. (d) Shows the mode profiles of the field components of TM mode. The black vertical lines in these plots refer to the extent of the n_1 slab.

modes decay exponentially from the core and no oscillatory field exists at infinite distance from the core. For propagating radiative modes, the fields decay exponentially only on one of the interfaces of the waveguide, while for evanescent radiative modes fields are oscillatory on both interfaces.

The basic wave-theory indicates that when the light-wave is confined in the *x-direction*, it will only allow standing waves with certain wavelengths. Therefore, the confined light in this slab waveguide will have discrete standing wave modes, each with its own dispersion relations. These are called the eigenmodes of propagations. For each of the eigenmodes, there is a minimum frequency that the standing wave pattern can sustain for that particular dimension of the waveguide. Figure 3.2 (b) denotes them by ω_{ck} which are also known as cut-off frequencies of the modes k. Light with lower frequencies will not be guided and will radiate optical energy to the surroundings. These are called radiative modes. The preceding discussion indicates that the waveguide changes the total dispersion of the light. Also, this dispersion is related to the waveguide geometry, and therefore can be engineered.

The dependence of the total internal reflection on the wave-vector (β) of light also explains the existence of cut-off frequency of a guided mode. If we start with the lowest possible β and then continuously increase it to plot the dispersion profile, we see the following behaviour: at a certain frequency the light energy experiences only the n_2 cladding material and starts propagating at the boundary of n_2 and n_1. This is the minimum $\beta_{c0} = k_0 n_{c0}$, where the total internal reflection can take place inside the waveguide core n_1. The notion of this cut-off wave-vector exists because the total internal reflection starts at a certain angle, which strongly depends on the frequency of the light. Thus, the dispersion relation starts at the n_2 light line. At a higher β, more light starts to propagate inside the n_1 material, and the dispersion relation moves towards n_1. It can asymptotically reach n_1 if the light is completely confined inside n_1.

The quantitative description of the above is acquired by solving Maxwell's equations of electromagnetic wave propagation inside the slab waveguide. The solutions are essentially eigenmode solutions and reveal there are two broad category of eigenmodes that propagate inside the waveguide. They are related to the orientation of the electric field of the light with respect to the geometry of the waveguide. When the electric field vector is perpendicular to the direction of propagation of light in the waveguide, it is called transverse electric field mode of propagation or in short *TE*. The second mode is the transverse magnetic filed propagation mode or *TM*, indicating the magnetic field of the light being perpendicular to the propagation direction. Figure 3.2 (c), (d) shows the non-zero components of the fundamental TE and TM modes of propagation inside a slab waveguide.

Figure 3.1 shows a few types of waveguides used in practical SOI platforms: strip or nanowire, rib, slot and photonic crystal waveguides. In the rest of the thesis, only nanowire waveguides will be discussed. The nanowire waveguide can be viewed as the modification of the slab waveguide. It resembles a box which is the core to guide light and the surrounding air/glass materials are the cladding to employ the total internal reflection. As mentioned before, the geometry of the waveguide, such as the width (W) and the height (H) of the nanowire waveguide play an important role in determining the dispersion of the light. The total dispersion profile (material + waveguide) of a waveguide mode is usually represented by the effective refractive index $n_{eff}(\lambda)$ as a function of the wavelength. While the group index n_g of the light is related to the real part of the effective index, the linear loss α of the propagating light is related to the imaginary part

(from *Optical Materials* course notes of Universiteit Gent):

$$n_{eff}(\lambda) = n_{effR}(\lambda) + i n_{effI}(\lambda) \tag{3.3}$$

$$n_g = n_{effR} - \lambda \frac{dn_{effR}}{d\lambda} \tag{3.4}$$

$$\alpha(\lambda) = n_{effI}(\lambda) k_0 \tag{3.5}$$

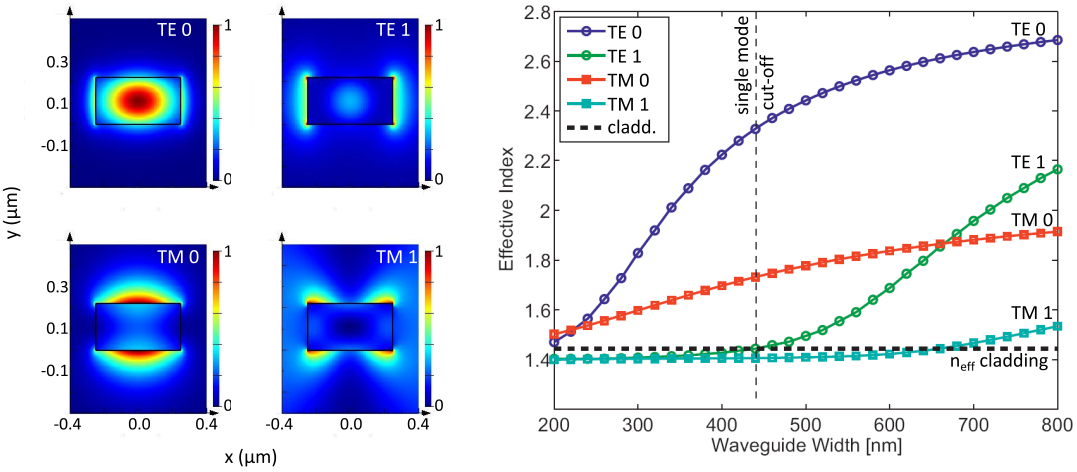

Figure 3.3: Modes in a strip waveguide. The left side of the figure shows the electric field intensity profiles of the first 4 TE and TM optical modes. These are obtained using *Lumerical Mode Solver* for a waveguide dimensions of $500\ nm \times 220\ nm$ at wavelength $1550\ nm$. Different electric field intensity profile results in different effective indices. As shown in the plot on the right side, the width of the strip waveguide determines the number of propagating spatial modes and their effective indices. A waveguide with $220\ nm$ height is single mode (fundamental TE and TM only), for width $< 450\ nm$. For a width of $500\ nm$ it still contains only fundamental TE mode. The right-hand side plot is adapted from [145].

The real and imaginary parts of the effective index are not independent of each other but connected through Kramers-Kronig relations. This plays a role in the employment of the phase shifters as a photonic component, as we only wish to change the phase without introducing losses.

An important design criterion of our PIM experiment is to carry light in a single spatial mode for a certain range of wavelengths. The single mode nature ensures the spatial mode purity of the generated SFWM photon pairs. Figure 3.3 (b) depicts a simulation result (numerical mode solver solving Maxwell's equations following the usual boundary conditions) of effective index as a function of waveguide width W for height $H = 220\ nm$. This figure has been taken from [145]. As can be seen from the figure, a single mode waveguide carries at least one single mode at TE mode and one single mode at TM for for $W = 500\ nm$. Usually, the height is specified by the foundry. That leaves us to choose the width only. The dispersion relation strongly depends on the width of the waveguide. By choosing the correct width, we can restrict the number of spatial modes that can propagate in the waveguide while engineering some aspects of the dispersion. In the next chapter (Sec. 4.2.1), a more detailed analysis of the dispersion profile of this waveguide geometry will be discussed in the context of the phase matching bandwidth of the Spontaneous Four Wave Mixing (SFWM) process.

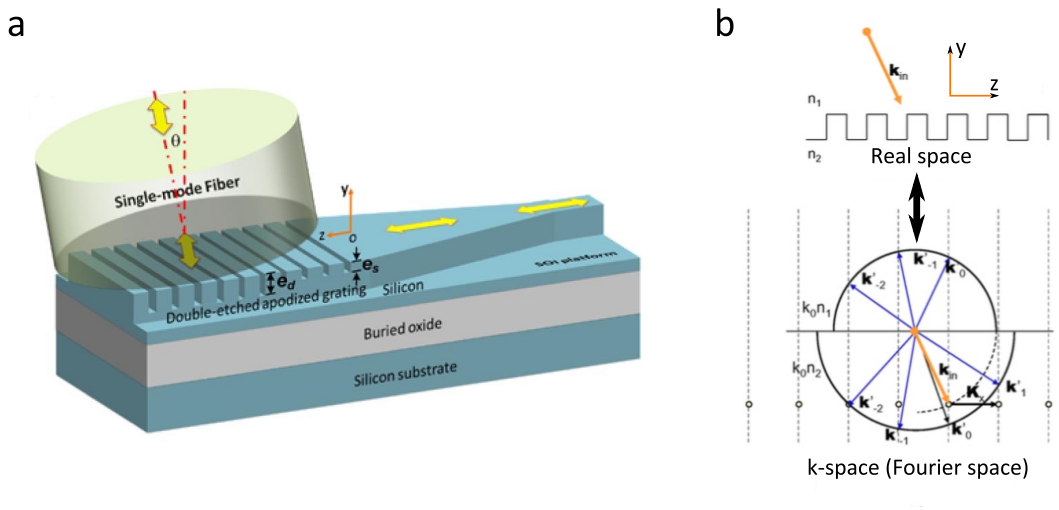

Figure 3.4: Vertical grating coupler in SOI. (a) represents schematic and cross-sectional view of a VGC in SOI with $1.5\ dB$ coupling loss with $54\ nm$ 3-dB bandwidth at $1560\ nm$. This image is adapted from *Li et al, Optics Express 21(7), 7868 (2013)* [146]. (b) represent Bragg conditions in k-space due to refractive index periodicity in real space (spatial dimensions) with period Λ. Due to the periodic refractive index in z-direction, k_z only take discrete values $m(2\pi/\Lambda)$. Therefore, an incident light beam (k_{in}) will couple to specific k vectors of light allowed by the Bragg condition. The closer the k_{in} is to an allowed k vector, the higher the coupling efficiency. This image is adapted from the *Microphotonics* course notes of Universiteit Gent.

Vertical grating couplers (VGC)

The next important photonic component is the coupler that couples light in and out of a SOI photonic chip. As every photon counts in a quantum photonic experiment, an efficient coupling, usually to an optical fibre, is desirable. The main challenge is to match the optical mode field diameter (MFD) of the optical fibre with the waveguide. While the typical core diameter of a single mode optical fibre (SMF-28 Corning) is $8.2\ \mu m$ (MFD $= 10.4\ \mu m$) for $1550\ nm$ wavelength, our choice of nanowire waveguide has a core width of $0.5\ \mu m$ as explained in the last section. Therefore, the numerical apertures of these two structures have to be matched through the use of the coupler.

There are two well known ways of coupling light in and out of a SOI photonic chip: tapered waveguide for edge coupling and grating coupler for vertical coupling. A edge coupling of $0.1\ dB$ loss (97.8% transmission) in coupling efficiency in silicon-nitride on insulator photonic circuit has been proposed by Sandia National Lab in US for visible wavelength (about $700\ nm$). A similar value ($0.7\ dB$ loss per facet) has been shown [147] with silicon waveguides at $1550\ nm$, although the total efficiency was limited ($\sim 3.5\ dB$) due to the loss of the collecting lensed fibre. Both of the preceding examples have used a deep reactive-ion etching method called Bosch etching. The pre-existing edge coupling photonic devices in our group have about $8\ dB$ loss per tapered coupler.

The vertical grating couplers (VGC) has been proven to be the more popular method of coupling light in and out from the silicon nano-photonic chip to the optical fiber network. The size of a VGC is relatively large, therefore easy to align. Also, a VGC does not have to be placed at the edge of the chip, and can be positioned almost anywhere in the design space. The physical principle of the VGC follows from the *Bragg condition*[15] of the periodic structures: periodicity of the refractive index in the spatial domain (e.g. $n(x)$ periodic in x-direction) results into a discretisation of the wave-vector (e.g. k_x is discretised) in the

[15] more generally, Floquet-Bloch Theorem

Fourier domain (k-space). Therefore, the component of the wave-vector k is only allowed to take certain values at the direction of periodicity. In one dimension it reduces to the response of light passing through N number of slits/openings. The light after the slits will be only focussed to a certain spatial location following the interference. These locations fulfil a relation with the distance between two slits that stems from the Bragg condition. The spatial locations of the interference are called the diffraction orders.

Figure 3.4 shows an example of VGC based on the periodicity of the refractive index. If the 3D periodic structure is designed with certain periodicity, the light will propagate at a certain direction out of the plane of the photonic chip. By varying the period, height and width of the periodicity, it is possible to control the peak wavelength transmission, the bandwidth of the transmission, the angle between the chip and the propagation direction. At the moment, the state of the art efficiency of coupling light in/out through this structure is about 88% transmission (less than $0.58\ dB$ loss) [148] and an apodised design with 92% transmission ($0.36\ dB$ loss) [67].

Directional couplers (DC)

A direction coupler is analogous to a beam splitter cube for macro-optics. The physical principal of a directional coupler is the evanescent wave tunnelling phenomena between two closely placed waveguides (Fig. (a), (b)). As explained in the previous sections, the total internal reflection at the boundary of the waveguide confines the light in the waveguide. Although most of the light energy is confined in the core of the waveguide, the tails of the electric and magnetic field extends in the cladding surrounding the core, as shown in Fig. 3.2 (c), (d). These fields decay monotonically in the cladding and are called the evanescent fields. If another waveguide is brought closer to the first waveguide, then the evanescent fields of the light propagating in the first waveguide will intersect the second waveguide. That has a non-zero probability of exciting propagating optical mode into the second waveguide, and transfer energy from the first waveguide. This phenomenon is called wave-tunnelling, or more generally frustrated total internal reflection. If the waveguides are close together for a long enough distance then this interaction will cause the energy of the light in the first waveguide to completely transfer to the second waveguide. Moreover, further increasing the interaction length can cause the light energy to oscillate between the two waveguides. Therefore, choosing a certain length of the interaction region we can choose the amount of splitting of the optical energy from one waveguide to the other.

The ability to control the energy transfer makes DC irreplaceable in micro-ring resonator or other whispering gallery mode resonators. There are two primary design parameters of a DC: length (L) of the interaction region and the gap (g) between these two waveguides. Figure 3.5 (c) shows the effect of the parameters on the cross-transmission (κ) of the optical fields. The outcome of a directional coupler is usually expressed as a four-port scatter matrix, relating the inputs and the outputs:

$$\begin{bmatrix} E_{out1} \\ E_{out2} \end{bmatrix} = \begin{bmatrix} \kappa & \tau* \\ \tau & -\kappa* \end{bmatrix} \begin{bmatrix} E_{in1} \\ E_{in2} \end{bmatrix} \tag{3.6}$$

Here, τ is the self-coupling coefficient satisfying the energy conservation rule,

$$|\tau|^2 + |\kappa|^2 = 1 \tag{3.7}$$

According to the *super mode* analysis [145], if the effective index difference between the

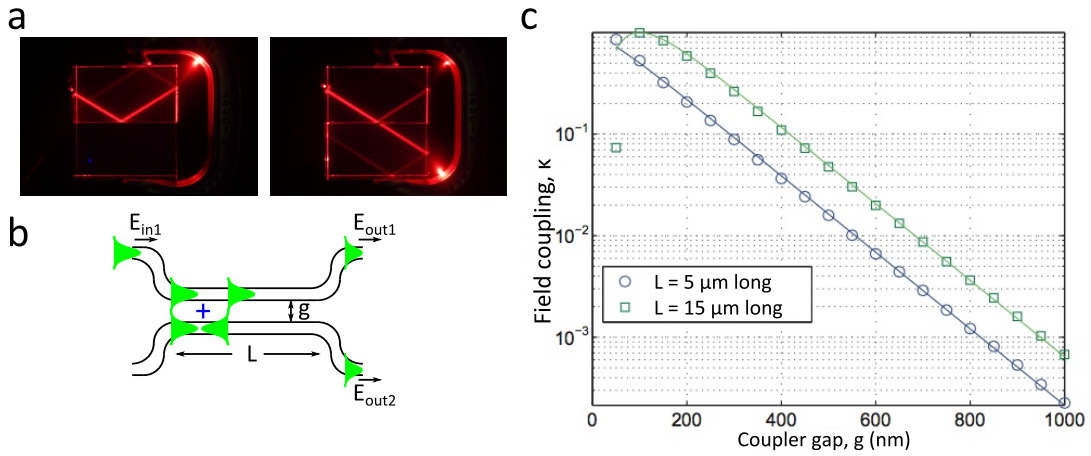

Figure 3.5: The physical principle behind directional coupler (DC). (a) Photographs of the frustrated total internal reflection (FTIR) or wave tunnelling with refraction blocks. The left photograph shows the total internal reflection (TIR) at the top block. In the right photograph, the presence of the bottom refraction block causes most of the light transmitting through it. Thus, wave tunnelling causes TIR to become FTIR. The photographs are taken from the website: `http://www2.oberlin.edu/physics/catalog/demonstrations/modern/ftir.html`. (b) The principle of wave tunnelling applied in terms of *super mode theory* explains the working of the DC. An optical mode propagating in a waveguide feels the presence of a nearby second waveguide. The evanescent field of that optical mode excites super modes propagating through the waveguides and transfers optical powers. Depending on the interaction length L and gap g between the waveguides, optical modes leave both of the waveguides with varying proportions of the intensities. (c) A graph showing optical field coupling coefficient κ between two waveguides as a function of g for two different L (adapted from [145] for a strip waveguide: $500\ nm \times 200\ nm$, obtained using *Lumerical Mode Solver*). It shows that the total optical field transmission ($\kappa = 1$) for the shorter length L ($= 5\ \mu m$) occurs at a larger gap g ($= 150\ nm$).

modes of the waveguides is Δn then,

$$\kappa = \sin\left(C_g \frac{\pi \Delta n}{\lambda} L\right) \tag{3.8}$$

$$\tau = \cos\left(C_g \frac{\pi \Delta n}{\lambda} L\right) \tag{3.9}$$

Here, $C_g = Aexp(-Bg)$ is a constant that depends on the gap g and the particular geometry of the two waveguides through the constants A and B. As from the equation, it can be seen that the coupling coefficients κ and τ depends on the wavelength of the propagating light. Using certain fabrication techniques, the directional coupler can be made broadband, such that it maintains the same splitting ratio over a broad range of wavelength. In contrast it can be made very narrow band as a filter, such that all the light at certain wavelength can only be output from one specific waveguide. In general, we have used a commercial software *Lumerical Mode Solver* to simulate our designs of DC. Using a parametric simulation on the DC geometry, L and g are chosen for a resonator HSPS.

Multi-mode interferometer (MMI)

Multi-mode interference (MMI) coupler is a photonic component based on the interference among multiple spatial modes of a wide waveguide. The MMI connects single mode waveguides to a multimode waveguide region. In the multi-mode region, several spatial optical modes are excited. These modes propagate inside this multi-mode region and interfere

with each other. Based on the device geometry, it can form N images of the input single mode at N locations of the MMI. Those locations, if connected to single mode waveguides, can propagate each of those single modes. Therefore, MMI can be used as $m \times N$ splitter for m single mode inputs. A MMI has larger device geometry compared with DC and is usually symmetric. That makes a 2×2 splitter MMI a more tolerant choice to fabrication imperfections over the DC for an even beam-splitter design. Figure 3.6 shows an MMI with two inputs and two outputs and the interference pattern inside the device. The inputs and outputs of the MMI are also related by Eq. 3.6.

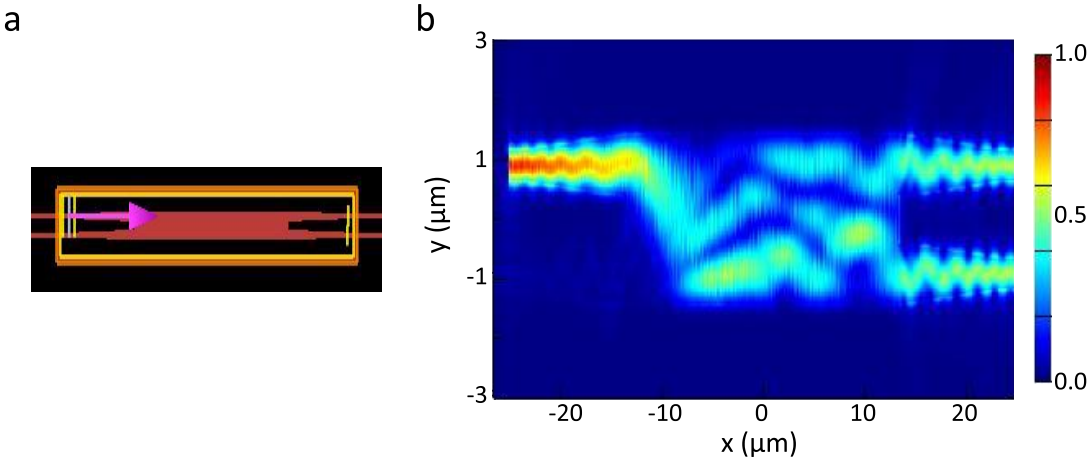

Figure 3.6: MMI energy density. (a) Shows the simulation area of the *Lumerical FDTD solutions* corresponding to the geometry of a MMI design pre-existing in our group. (b) Shows the energy density of the MMI in terms of the spatial dimensions. The incoming light excites multiple spatial modes which interfere. At the end of the MMI, light is re-coupled to the output single mode waveguides.

Thermo-optic heater

Reconfigurable photonic circuits require photonic elements that induce phase shifts on the propagating optical mode of light. Unlike macro-optics, SOI photonics cannot change the length of the waveguide at will to introduce phases to the propagating light. Instead, the real-part of the effective refractive index of the material is modified to change the optical length of the light $L_{opt} = n_{effR}L$ to induce a phase shift $\phi = k_0 L_{opt}$. According to *Kramers-Kronig* relationships, the real and the imaginary part of the n_{eff} are related such that one could not be changed without affecting the other [20]:

$$Re\{\chi(\omega)\} = \frac{1}{\pi}\int_{-\infty}^{\infty} \frac{Im\{\chi(\omega')\}}{\omega' - \omega} d\omega' \tag{3.10}$$

$$Im\{\chi(\omega)\} = \frac{1}{\pi}\int_{-\infty}^{\infty} \frac{Re\{\chi(\omega')\}}{\omega' - \omega} d\omega' \tag{3.11}$$

Here, the susceptibility of the material $\chi(\omega) = n_{eff}^2(\omega) - 1$. It is interesting to note that, according to these relations, if a material is dispersion-less (i.e. n_{effR} is constant), then it is also lossless ($\alpha = 0$). The key to introduce a phase shift with negligible loss is to modify n_{eff} much further away from the resonant response of the material which will induce negligible loss.

Silicon is a centro-symmetric ($\chi^{(3)}$) material and therefore it does not have any electro-optic coefficient. It means applying an external electric field will not distort the structure of the silicon and therefore the light will see the same material, and the effective index of the light will be the same. Therefore, for silicon, localised heat is used which does not

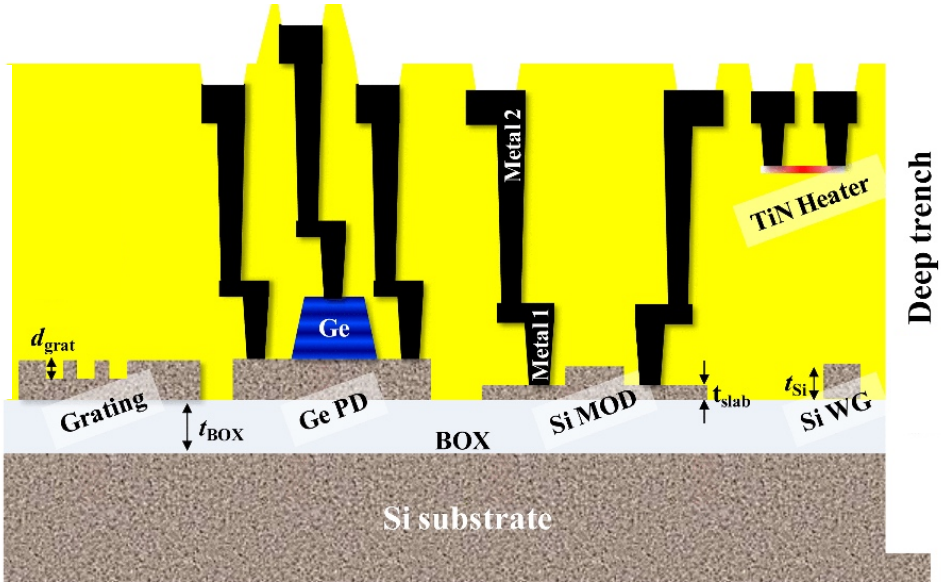

Figure 3.7: The material layers of a thermal phase-shifter fabricated by the IME foundry. The image is adapted from *Lim et al, IEEE JSTQE 20(4), 405-416 (2014)* [149].

depend on the symmetry. Heating a concentrated region of a silicon waveguide distorts the material structure sufficiently to induce a phase shift. A typical heater used in our fabricated SOI chips requires about 30 mW of electrical power dissipation as heat to induce a π phase shift. These heaters are formed with fabrication techniques depending on the foundry. Figure 3.7 shows heaters connected through vias in the chips we received from IME foundry. Simpler tri-layer metallisation process also exists which we received from ANT foundry and also made ourselves (App. D). The heater material is usually a highly resistive material such as titanium nitride which can efficiently convert the electrical energy into heat. The heaters are electrically connected through the gold tracks to the bond-pads and then to the outside world.

Mach-Zehnder interferometer (MZI)

A Mach-Zehnder interferometer is the most common interferometer for chip based photonics. The light entering through one of the input ports will be split evenly by a directional coupler (or an MMI) and then propagate without any interaction in separate waveguides. One of the waveguides may have a thermo-optic phase shifter which can change the phase of the light in one of the waveguides. After a certain propagation length these two waveguides are brought together in another directional coupler (or an MMI) where they interfere constructively or destructively based on the relative phase difference. The outcome of the MZI is expressed by the following equation:

$$\begin{bmatrix} E_{out1} \\ E_{out2} \end{bmatrix} = \begin{bmatrix} \sqrt{\eta} & \sqrt{1-\eta} \\ \sqrt{1-\eta} & -\sqrt{\eta} \end{bmatrix} \begin{bmatrix} e^{i\Phi_{MZI}} & 0 \\ 0 & 1 \end{bmatrix} \begin{bmatrix} \sqrt{\eta} & \sqrt{1-\eta} \\ \sqrt{1-\eta} & -\sqrt{\eta} \end{bmatrix} \begin{bmatrix} E_{in1} \\ E_{in2} \end{bmatrix} \tag{3.12}$$

where, $\kappa = \sqrt{\eta}$ is the splitting ratio of the DC or the MMI, and Φ_{MZI} is the phase induced by the heater. If the top (bottom) waveguide has a propagation constant β_t (β_b) and length L_t (L_b), then,

$$\Phi_{MZI} = \beta_t L_t - \beta_b L_b \tag{3.13}$$

A balanced MZI has $L_t = L_b$, where an asymmetric MZI (AMZI) may have $\beta_t = \beta_b$. An AMZI has different waveguide lengths on the top and bottom arms. Depending on the

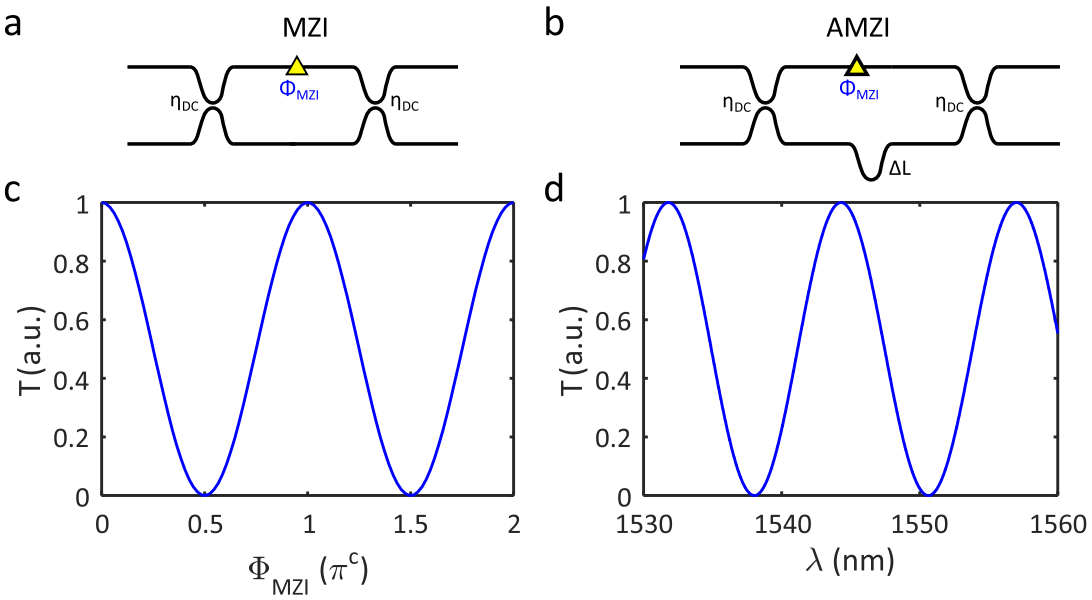

Figure 3.8: Schematics and general responses of MZI and AMZI. (a), (b) show the schematics of the MZI and AMZI. (c), (d) show the typical transmission through one of the output ports. MZI does not depend on the wavelengths of the light, while AMZI strongly depends on them.

lengths, some wavelengths will acquire more relative phase in the top waveguide than the bottom. Thus, the dispersion property of the effective index of the light together with the path length difference of the two waveguides, contribute to the position of the constructive and destructive interferences of light with wavelength dependance. The free spectral range (FSR) of the interference dips (or maxima) are related to the path length difference $\Delta L = L_t - L_b$,

$$FSR = \frac{\lambda_0^2}{n_g \Delta L} \tag{3.14}$$

Figure 3.8 shows typical responses of such structures when the paths are balanced (MZI) and when they are imbalanced (AMZI). One of the waveguides has a heater on top of it such that we can change the phase of the light propagating through that waveguide and change the interference outcome.

Micro-ring resonator

A micro-ring resonator can be viewed as an interferometer with a cavity. An ideal cavity can be seen as a physical structure similar to a closed box, which is unperturbed by and un-connected to the surrounding environments. Therefore, it is hard to access what is inside the cavity. Similarly, anything inside the cavity does not communicate with the outside world. In reality, a cavity has a weak connection to the outside world. A micro-ring resonator has two main structures. The first one is a waveguide loop which closes upon itself thereby free from any external influence, and therefore, acts as a cavity. Any light trapped inside the cavity will propagate around forever, ideally, for lossless waveguides. The second one is the bus waveguide which is put very close to this loop. It facilitates wave tunnelling through directional coupler (DC) mechanisms. This bus waveguide is the connection of the loop waveguide cavity to the outside world.

The two aforementioned structures, loop and the bus waveguides, contribute to the major responses of the micro-ring resonator cavity. The loop waveguide can only sustain light with wavelength that forms standing wave patterns. The length of the loop (L_{Rg}) has to be such that after a round trip of light propagation, it contributes constructively with the

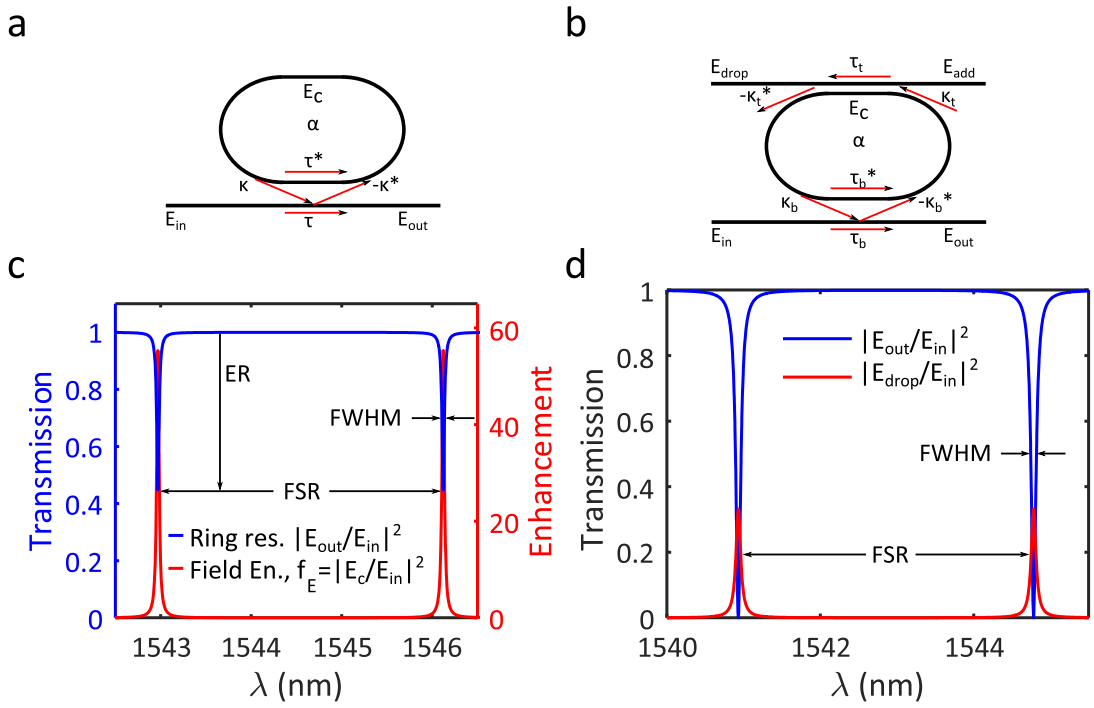

Figure 3.9: Schematics of single-bus and double-bus micro-ring resonators and their typical responses. (a), (b) show the schematics while (c), (d) show the responses with usual characterisation properties. ER: extinction ratio; FWHM: full width half maximum; FSR: free spectral range.

phase. In other words, it accumulates integer multiple of the phase 2π. That is the same resonance criteria in any cavity sustaining a standing wave motion: the integer multiple of the wavelength has to be equal to the length of the loop ($L_{Rg} = m\lambda_{res}$). These wavelengths that sustain in the cavity are called resonance wavelengths, λ_{res}. Therefore, there will be resonance wavelengths at regular intervals which is called the free-spectral-range (FSR), related by the same equation as an AMZI:

$$FSR = \frac{\lambda_{res}^2}{n_g L_{Rg}} \tag{3.15}$$

Now, in an ideal cavity with no internal loss, light can travel forever without decaying. But any real cavity will have some finite loss a_e per unit length, which results in a non-unity round-trip transmission, $\alpha_{Rg} = exp(-a_e L_{Rg}) < 1$. Thus, a pulse inside the resonator completes finite number of round trips. This metric of the cavity is called the internal quality factor, Q_{int}. When the DC mechanisms is used, it enables the bus waveguide to control the amount of light extracted from the cavity to this bus waveguide. The additional extraction of light can be viewed as additional loss which results into a lower quality factor. This is called the loaded quality factor Q_{load} of the resonator. In the rest of the thesis, unless explicitly mentioned, the quality factor Q will represent Q_{load}. In the loaded scenario, the DC parameters are called the cross-coupling coefficient κ and the self-coupling coefficient τ which satisfy the energy conservation principle:

$$|\kappa|^2 + |\tau|^2 = 1 \tag{3.16}$$

As shown in Fig. 3.9 (a) and (c), the response of the micro-ring resonator can be viewed as an MZI. For example, at the beginning of the coupling section, the input light (E_{in}) is being injected into the cavity (κE_{in}) and mixed with the light that is already in the cavity (E_C). Depending on the phase (θ) accumulated by E_C, at the end of the coupling/interaction

region, at the output of the bus waveguide (E_{out}), E_C and E_{in} interfere to form E_{out} with either of the two possible interference outcomes. The corresponding equations are:

$$E_C = -\kappa^* E_{in} + \tau^* \alpha_{Rg} e^{i\theta} E_C \tag{3.17}$$

$$E_{out} = \tau E_{in} + \kappa \alpha_{Rg} e^{i\theta} E_C \tag{3.18}$$

$$= \frac{\tau - \alpha_{Rg} e^{i\theta}}{1 - \alpha\tau^* e^{i\theta}} E_{in} \tag{3.19}$$

There is constructive interference or destructive interference, depending on the round trip phase $\theta(\lambda)$ for that particular wavelength of light. When the light wavelength is non-resonant in the loop waveguide, it cannot sustain the standing waves. It will then simply pass to the bus waveguide without any change, as if the loop waveguide does not exist. For the resonance wavelengths (λ_{res}) of the loop waveguide, there is constructive interference inside the cavity, sustaining more round trips in the cavity. The total energy is conserved through the total destructive interference outside the cavity in the bus waveguide. Therefore, if we see the response of the ring-cavity at the end of the bus waveguide as a function of wavelength, we see dips at the resonance wavelengths (Fig. 3.9 (c)). The depth of a dip with respect to the non-resonant response is called the extinction ratio (ER). The full width of the resonance line-width (dip) at half the value of the ER is called the full-width half-maximum ($FWHM$) of the resonator. Extinction ratio is related to the quality factor (Q_{load}) and denotes the degree of destructive interference at the resonance wavelengths. Inside the cavity, the recurring constructive interferences of light in each round trip add the optical field of the light at the resonance wavelength. This can be seen as an effective enhancement of light's optical field inside the micro-ring resonator compared to the input light. It is denoted as field-enhancement:

$$f_E = \frac{E_C}{E_{in}} \tag{3.20}$$

$$= \frac{-\kappa^*}{1 - \alpha\tau^* e^{j\theta}} \tag{3.21}$$

There are three modes of operations in a resonator, based on the interplay between the coupling constant and the loss inside the cavity, as shown in Fig. 3.10:

① Under-coupling regime. When we couple in much less light in steady state than that is lost in the round trip loss inside the cavity, then this is called under-coupling ($\tau > \alpha_{Rg}$). Here, the field enhancement (f_E) as well as the extinction ratio (ER) of the light is low as shown in Fig. 3.10 (a).

② Critical-coupling regime. If the coupling is just matched with the internal round trip loss, then the ER is the highest and the mode of operation is called critical coupling ($\tau = \alpha_{Rg}$). The field enhancement of light in critical coupling is the highest as shown in Fig. 3.10 (b).

③ Over-coupling regime. If we couple more light into the loop waveguide than lost in the round trip, then the destructive interference is also not as high as in the critical coupling and the extinction lowers eventually. This mode of operation is called over-coupling ($\tau < \alpha_{Rg}$). It also has lower field enhancement than the critical coupling as shown in Fig. 3.10 (c). Increasing the coupling will further reduce the f_E and the FWHM of the resonance line-width will further increase as shown in Fig. 3.10 (d).

The micro-ring resonator is a versatile device. It can be used as a spectral filter by adding a second bus waveguide as shown in Fig. 3.9 (b), (c). This configuration made the resonator a four-port device. Depending on the coupling of the second waveguide, the total loss in the loop waveguide can effectively increase. This can significantly lower the

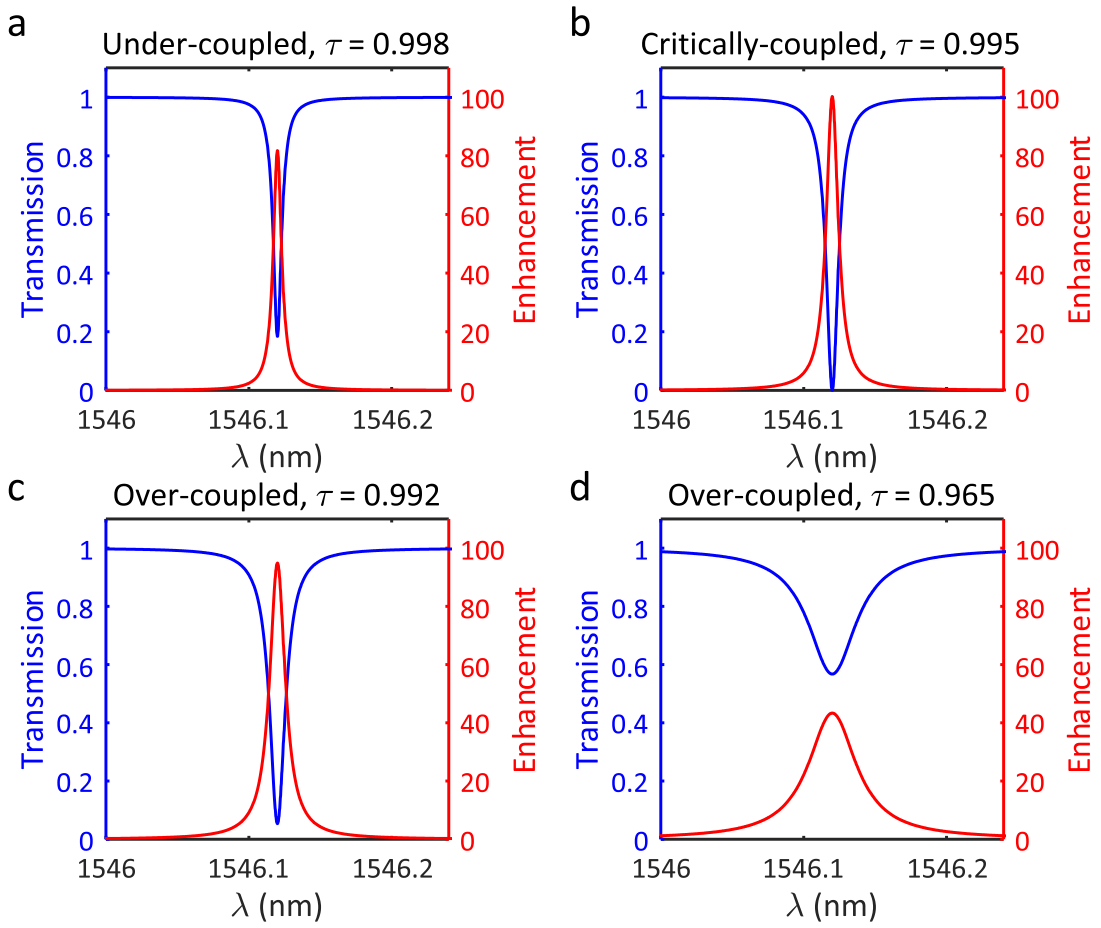

Figure 3.10: Coupling regimes of a single-bus micro-ring resonator. The output transmission of the resonator is denoted by the blue curve, while the field enhancement inside the cavity is denoted by the red curve. For the round-trip transmission coefficient $\alpha_{Rg} = 0.995$, (a) represents under-coupling, (b) represents critical-coupling, (c) and (d) represent over-coupling regimes. The extinction ratio ER and field-enhancement f_E is highest for the critical-coupling.

extinction (quality factor) and increase the *FWHM* at the resonance wavelengths. Due to the presence of the second waveguide the resonance light which destructively interfered in the first bus waveguide and cannot escape, will now escape through the second bus waveguide. The amount of light escaping through the second waveguide will be determined by the coupling (κ_2) of the second waveguide to the loop waveguide. Therefore that side of the second waveguide is called the *drop port*. If we inject light from the other end of the second bus waveguide and if it fulfils the resonant condition, then it will be coupled in to the cavity and output through the first bus waveguide. This adds new signals to the original input to the structure. Therefore, this port of the second bus waveguide is called the *add port*.

Passive and active circuits

The components discussed above are passive semiconductor components. It means they do not have any active regions such as n-type doped or p-type doped region to make p-n junctions or carrier injection modulators. The PIM experiments performed in this thesis used only the passive components.

Active components such as *p-i-n* diode across a resonator can be used with resonator

HSPS to reduce free-carrier induced loss and to increase the brightness [150]. Active components are also important for fast switching (e.g. carrier depletion modulators) for multiplexed sources. Based on the experiments presented in this thesis, in further work, PIM experiments will be performed with active components.

3.1.2 Fabrication techniques and tolerances

The previously described components were discussed from the point of view of the ideal structures without any practical imperfections. The actual physical process of patterning structures in a thin layer of silicon is called the fabrication process. This process for silicon nano-photonic components has been improved and developed extensively in the last few decades primarily benefitting from the semiconductor electronics industry. Nevertheless, depending on the method of employment, practical structures are still far from the textbook idealisations.

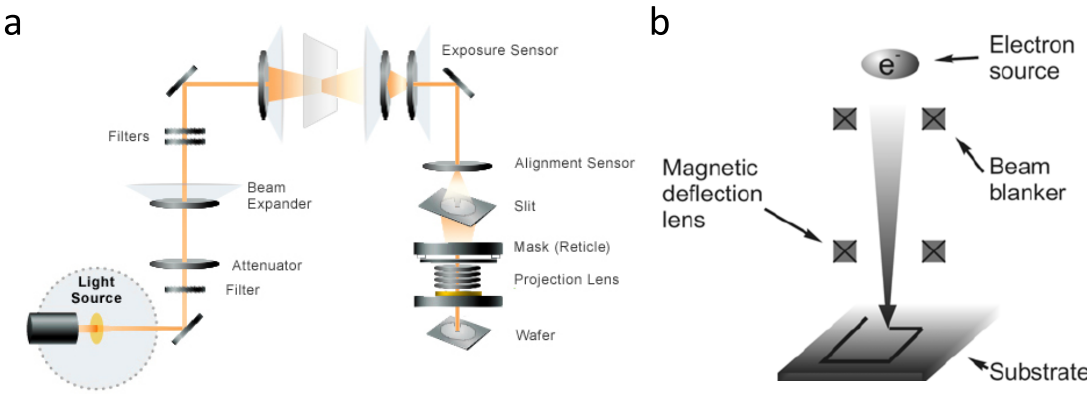

Figure 3.11: Fabrication process of nano-photonic components. (a) Shows the different components of the optical lithography process. The image has been adapted from `https://www.anandtech.com/show/10097/euv-lithography-makes-good-progress-still-not-ready-for-prime-time`. (b) Shows the schematic diagram of electron beam lithography system.

The two main methods of fabrications are deep ultra-violet photo-lithography and electron beam lithography. As the main idea of patterning is to imprinting an image on the surface of the silicon layer, the mentioned two methods are actually sophisticated imaging technique in nano-scale. The first one, deep UV photolithography, imprints the image of the component using optical projection using deep UV light similar to a photographic shot with a camera. The physical principle behind this lithography technique is very similar to developing paper photographs with chemical developers. Due to the very short UV light (248 nm or 193 nm depending on the process), the minimum feature size corresponds to the diffraction limit and the projection techniques. Using immersion lithography technique the feature size can be as low as $65\ nm$. The minimum feature or tolerance in the design of a photonic component has to comply with this value.

Electron beam lithography (EBL), uses the De Broglie wavefunction of the electrons by choosing the right energy of the electrons to imprint an image on the resist. Here, the electron beam can be raster scanned starting from the top right corner and going to the left and then continuing to the next line at the right etc. This is very similar to the old *cathode ray tube* based television. Using 100 keV energy electron beams, a minimum feature size of $6\ nm$ can be achieved. Therefore, it appears that EBL has a clear advantage over photolithography in terms of minimum feature size.

The EBL does not necessarily make the fabricated components superior than the photolithography process. The actual quality of the fabricated device also depends on the subsequent physical processes such as etching, depositions etc. Once a waveguide pattern is imprinted on the silicon, the surrounding silicon layer has to be etched away to form the sidewalls of the waveguides. This etching determines the sidewall roughness related to the scattering loss and back-reflections. The roughness that exists in the sidewall of the waveguides scatters forward propagating light in the backward direction. It can be expressed as:

$$\alpha = \alpha_{scat} \frac{(\Delta n)^2 E_S^2}{P} \tag{3.22}$$

Where, α_{scat} is a constant related to the etching process, Δn is the index contrast at the interface, E_S is the strength of the electric field at the edge of the waveguide and P is the power in the optical field. Surface roughness not only increases the linear loss but also sometimes contributes to unpleasant effects in some photonic components. For example, resonance splitting due to back scattering is a major problem in a ring-resonator cavity. Sometimes, this will result in a directional coupler with splitting coefficients deviating only after 3rd significant digits from the designed splitting coefficients. But that is enough to change the extinction ratio of an AMZI filter from 60 dB to 30 dB [73]. The combination of cladding and depositing heater elements and metal layers may also affect the quality of the final state of the components.

Tolerances and reproducibility

The fabrication tolerance limit of $6\ nm$ in EBL compared to $65\ nm$ in photolithography appears to be in favour of choosing EBL. However as the photolithography takes the whole image of the imprinting at one go, it is much faster than the electron beam lithography that does a much slower raster scan. Another important reason in choosing photolithography is the reproducibility of the photonic components. Photolithography process that happens specifically in a foundry follows standard procedure that gives standard components comparable to other foundries. In contrast, the EBL is usually not commercially mass producible scheme and thus not standardised. That makes it less viable for reproducible components with the same performance. The number of samples delivered in a photolithography process is usually few times higher than the EBL.

3.2 Design software and foundries

A successful implementation of a nano-photonic design in SOI requires various types of simulations to make the geometry, determine the design parameters or to estimate the performance of the devices. Often, a final file in the *GDSII* format is produced. It contains all the geometrical definition of the components for each fabrication steps to be used by the foundry that fabricates the devices.

3.2.1 Software

The design parameters of the photonic components are determined with commercially available softwares such as *Lumerical*. *Lumerical* contains standard design tools: *Eigenmode Expansion* as waveguide *Mode Solver*, *FDTD* tools to accurately determine the coupling ratio of a DC etc. Often, a new photonic component, or specific design physics cannot be simulated in any commercial softwares. In such scenarios, *MatLab* or other similar numerical simulation tools are required to simulate the performance of the devices.

Once the design is finalised, it is implemented by a python based software package called *IPKISS*. This essentially contains a large library of geometry packages to draw layer by layer geometrical shapes. The final output of the IPKISS is the *GDSII* file. This file contains all the information of the different material layers, shapes of the components at different layers and the position of each component with respect to each other.

3.2.2 Foundries

Most of the SOI photonic chips mentioned in this thesis were fabricated in the *Institute of Microelectronics* (IME) of Singapore. These are referred with the prefix IME. IME chips are fabricated using photolithography process. Therefore, many of the device constraints and imperfections in our photonic chip are due to the constraints of the IME foundry service.

One of the experiments has been performed with a chip fabricated using EBL in *Danmarks Tekniske Universitet*. This chip is referred to as DTU-tele in the rest of the thesis.

3.3 Synopsis & outlook

SOI is one of the many photonic platforms. It has a myriad number of well designed photonic components suitable for carrying out a quantum algorithm. Although SOI does not have the best components in every single aspect, it is the most mature, commercial-grade platform. It not only has high optical nonlinearity required for waveguide or micro-ring resonator HSPSs but it also has low loss optical delay lines [74, 75], high-speed electro-optic modulators [76] and even the possibility of multi-layer photonic chip [77], all of which are necessary to accommodate very large scale integration to design a sufficiently complex quantum computer.

In this chapter, a set of photonic components have been briefly described. These components are used to design the photonic circuits for the photon indistinguishability measurements (PIM) in the subsequent chapters. Each of these components has the ability to affect the PIM as we will see in Chap. 6 and Chap. 7. Therefore, it is essential to understand their ideal behaviour and the design parameters. Two of these components are the waveguides and the micro-ring resonators which also act as HSPSs. Also, the component directional coupler (DC) is very sensitive to its design parameters and fabrication imperfections and plays an important role setting the performance of the resonator HSPSs and the MZI. In the next chapter, the design procedures to identify the optimum parameters of all these components are illustrated. These design parameters play an important role in the performances of the PIM circuits, particularly on the HSPSs.

PART II

PIM circuits in SOI: design, modelling and simulation

Implementing on-chip PIM circuits in SOI platform requires choosing appropriate design parameters for each photonic component used in the circuit. Modelling a new component using FDTD and the expected spectral response of the whole circuit facilitates the choice of the optimum design parameters (including HSPSs) as discussed in Chap. 4. Subsequent simulations have been done in Chap. 5, to estimate the purity of the on-chip HSPSs, and to estimate the effect of the device imperfection on indistinguishability measurements. These give an estimate of the performance of the designed PIM circuits and necessary tools to analyse the experimental data.

Chapter 4

Designing and modelling PIM circuits

Contents

In this chapter, we will design and model on-chip and off-chip photon indistinguishability measurement (PIM) circuits. A common PIM method is to use Hong-Ou-Mandel (HOM) [46] interference, as described in Sec. 2.2.5. Usually, in a HOM interference the single-photons' wavepackets are delayed in time and then gradually overlapped on an even beam-splitter. An integrated circuit does not have an analogue time-delay (analogue path variation); therefore, it is not ideal for such experiments to be performed on-chip. At the same time, the immobility of the waveguides makes the relative phase difference between two optical paths in an integrated circuit very stable. Thus, a highly stable Mach-Zehnder interferometer (MZI) can be implemented in an integrated platform and used for PIM (Sec. 2.2.5). This stability is the primary strength of an integrated quantum photonic platform. The interference data collected using on-chip MZI (Chap. 6) is much less noisy than the off-chip HOM interference (Chap. 7). A stable MZI fringe is not only important for a PIM but also readily useful in quantum metrology. In general, such stability is necessary to perform long and complex quantum photonic experiments, which is immensely important for scalable quantum photonic circuits (e.g. quantum computer).

Prior to fabrication, it is necessary to agree on the design parameters of a photonic component as most of them cannot be changed afterwards. In addition, the delivery time of an SOI multi-project-wafer (MPW) fabrication is about six months—one-quarter of the

lifetime of a PhD. Both of these points indicate the necessity of extensive simulations to ensure that the right circuit is sent for fabrication.

Fabricating a PIM circuit requires simulations of the photonic components (e.g. waveguides, HSPSs), the circuit designs for PIM, and the spectral response to determine the correct reconfigurability. The very first simulation is performed to choose the appropriate waveguide dimensions. Waveguides interconnect the photonic components in the circuit and guide the light through them. Therefore, the loss has to be low, and the minimum bend radius for optical guiding has to be known. We also need to ascertain the single spatial mode for spatial mode purity of the HSPSs and estimate the dispersion in the waveguide. Specifically, the group index (n_g) and the group velocity dispersion (GVD) need to be known. The n_g determines the free spectral range (FSR) of the resonator HSPSs and the filters. The GVD parameter determines the phase matching bandwidth of the SFWM photon-pairs generation.

This chapter begins with the proposed design of the PIM circuit. Then it continues to the modelling of the photonic components including compact waveguide model and its relation with the HSPS. Afterwards, the spectral response of one of the PIM circuits is presented which shows the role of different components in the circuit. Finally, the images of the *GDSII* files of the implemented designs are shown.

4.1 Design proposal of the PIM circuits

A PIM circuit design needs at least two HSPSs for single-photon generation and an interferometric component for the indistinguishability measurements among them. For an off-chip PIM, only two on-chip HSPSs are required, since the interference can be performed with an off-chip beam-splitter. An on-chip PIM requires not only on-chip HSPSs but also on-chip filters to separate signal-idler photons and an on-chip MZI for quantum interference. These components can be arranged in a few ways as described in the following sections.

4.1.1 Schematics of the on-chip PIM circuit

The schematics are arranged under two tag-names based on the MPW fabrication run they have been sent to: IME01 and IME03. IME is a foundry in Singapore who fabricated our SOI photonic chips. IME01 and IME03 are the chips fabricated in the years 2014 and 2016 respectively. IME01 chips contain the most basic on-chip and off-chip PIM circuits. IME03 chips contain some major modifications based on our experience with IME01 chips. In addition to IME01 and IME03, on-chip PIM has been performed with a reconfigured DTU-tele chip. DTU-tele is designed by Dr Jianwei Wang in our research group for multi-photon experiments, and fabricated by a research group in *Danmarks Tekniske Universitet* (DTU).

Figure 4.1 (a) and (b) show the IME01 designs for both off-chip and on-chip PIM respectively. The premise of the off-chip PIM is simple: a laser pulse (green pulsed shape in the figure) will be split equally by an on-chip directional coupler (DC); laser pulses will generate photon pairs in source 1 and 2; photon-pairs will be coupled out of the chip and interfered in a HOM experiment. The on-chip PIM has three additional components: two filters and a MZI. The filters separate signal and idler photons. Idler photons are sent for detection to herald the signal photons. Signal photons from these two independent HSPSs are then interfered on the MZI.

Figure 4.1 (c) and (d) show the IME03 designs for on-chip PIM. IME03 designs are modified version of IME01 chips, based on the following observations:

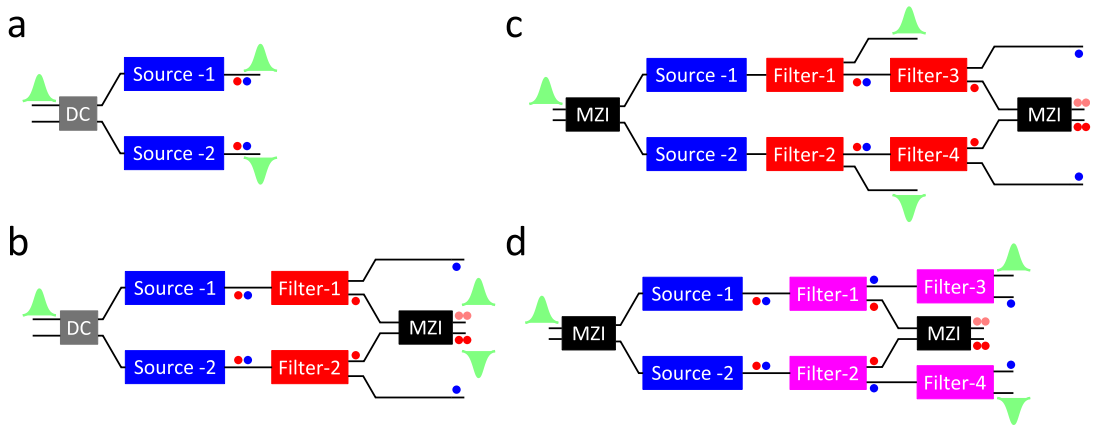

Figure 4.1: Schematics of the design proposals of on-chip and off-chip PIM circuits. The input pump pulses in the circuits are represented by green pulse shapes. Signal-idler photons are represented by red and blue dots respectively. (a) contains only two on-chip sources which are used for off-chip PIM. (b) represents an on-chip PIM, where the photon-pairs are first generated by HSPSs 1 and 2, then signal-idler photons are separated by filter 1 and 2, idler photons are sent out for detecting the presence of signal photons and lastly, the signal photons are interfered on an MZI. (c) is a slightly modified version where the first two filters (1 & 2) are used for pump rejection to limit the spurious four wave mixing. The rest of the circuit remains the same. (d) contains slightly different filters designed for narrowband spectral filtering to increase the spectral purity, and it is specifically designed for waveguide HSPSs. First two of these filters (1 & 2) spectrally filter only the signal photons which then interferes in the MZI. The last two filters (3 & 4) can spectrally filter the idler photons if needed. (a), (b) are implemented in IME01 chips, while (a), (c), (d) are implemented in IME03 chips.

① Due to fabrication tolerances, the directional couplers (DC) in the IME01 chips did not have even splitting ratios, which resulted in unequal pumping of two HSPSs and imperfect MZIs. Therefore, the input DCs have been replaced with MZIs in Fig. 4.1 (c) and (d) to ensure equal pumping. Also, the DCs in the MZIs have been replaced by MMIs. As described in the last chapter, MMIs have larger dimensions compared to DCs, therefore more tolerant to fabrication imperfections. The symmetric geometry of a 2×2 MMI for even splitting also makes it more tolerant to fabrication imperfections.

② Spurious four wave mixing (Sec. 6.3.3) is an issue with the IME01 chips due to the long input waveguides and the propagation of the pump through the whole circuit. Photon-pairs generated by spurious four wave mixing in the circuit other than in the HSPSs can reduce the quantum correlations. Therefore, the input waveguides have been shortened in IME03 circuits. Also, filter 1 and 2 are used to filter out the pump pulses just after the HSPSs. This stops spurious four wave mixing in the rest of the circuit.

③ Off-chip spectral filtering to increase spectral purity is challenging as it is difficult to find a narrowband spectral filter which is tuneable in wavelength with low insertion loss. The on-chip filters in Fig. 4.1 (d) are narrowband spectral filters used to increase spectral purity of the waveguide HSPSs. This design is low loss and tuneable in both the wavelength and the filter bandwidth. The first two filters (1 & 2) separate and also spectrally narrow the signal photons, while the last two filters (3 & 4) only spectrally filter idler photons if they are reconfigured (Sec. 4.2.6).

4.1.2 Proposed designs

Based on the above schematics, the following designs were implemented:

① IME01 off-chip PIM design contains waveguide HSPSs based on the schematic of Fig. 4.1 (a).

② IME01 AMZI design contains single-bus micro-ring resonator HSPSs and asymmetric MZIs (AMZIs) as filters based on the schematic of Fig. 4.1 (b).

③ IME01 RF design contains single-bus micro-ring resonators as HSPSs and double-bus micro-ring resonators as filters based on the schematic of Fig. 4.1 (b). RF stands for ring filter which is used to separate signal and idler photons.

④ IME03 RF design contains single-bus micro-ring resonators as HSPSs, asymmetric MZIs (AMZIs) as first two pump-rejection filters (1 & 2), and double-bus micro-ring resonators as the last two filters (3 & 4) based on the schematic of Fig. 4.1 (c).

⑤ IME03 Wg design contains waveguide HSPSs, a special resonator based photonics component (described in Sec. 4.2.6) as spectral filters based on the schematic of Fig. 4.1 (d).

All of the above designs are first modelled on a component by component basis, then the spectral response of the whole circuit is simulated.

4.2 Modelling photonic components

The main purpose of the following modelling is to ensure the optimum performance of the components in the photonic circuit. Each component mentioned in the preceding section will be modelled according to the experimental considerations: a compact waveguide model to determine n_g and dispersion; FDTD simulations of directional coupler (DC) designs for optimum resonator parameters and the correct FSR for filters. All our circuits are designed for the transverse electric (TE) mode.

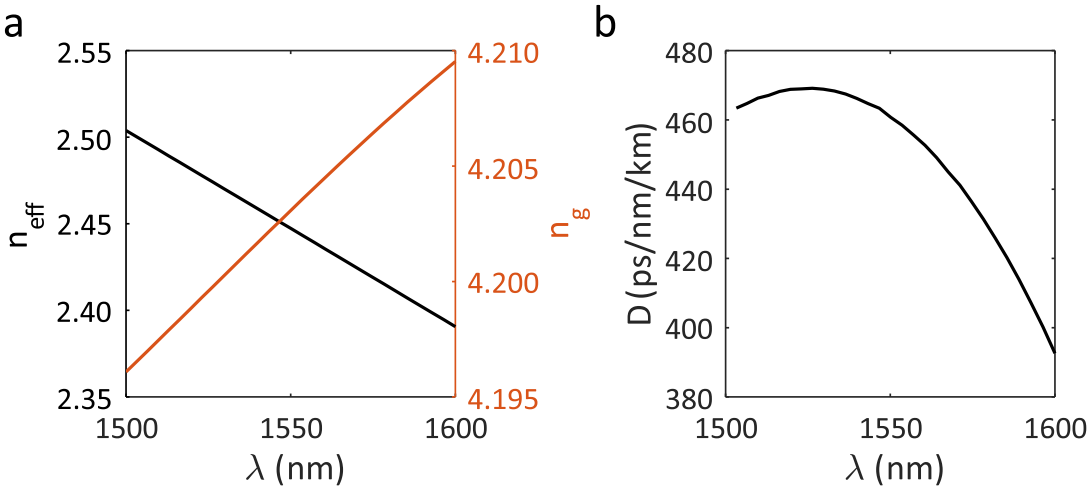

Figure 4.2: Dispersion using compact waveguide model for a $500\ nm \times 220\ nm$ silicon nanowire waveguide calculated using *Lumerical Mode Solver* for TE mode. (a) Effective index n_{eff} and group index n_g as a function of the wavelength of the light. (b) The dispersion parameter D_λ as a function of the peak wavelength of the pulsed light in the waveguide.

4.2.1 Compact waveguide model

In this section, we will only model the nanowire waveguide. In designing photonic circuits, it is useful to estimate effective index and the linear loss (imaginary part of the effective index) as close to the practical values as possible. The value of the effective index as a function of the wavelength, expressed as a Taylor series expansion up to the second order term, is used as a practical model of the dispersion in the waveguide. This model is called the compact waveguide model [145]:

$$n_{eff}(\lambda) = n_1 + n_2(\lambda - \lambda_0) + n_3(\lambda - \lambda_0)^2 \tag{4.1}$$

$$n_g(\lambda) = n_{eff}(\lambda) - \lambda \frac{dn_{eff}}{d\lambda} \tag{4.2}$$

A commercial software, *Lumerical Mode Solver*, can simulate the light propagation inside the nominal waveguide design, following Maxwell's equations of the electromagnetic wave propagation. It outputs the eigenmode propagation of light and the effective index for each mode for a particular wavelength. A simulated compact waveguide model for a standard $500\ nm \times 220\ nm$ nanowire waveguide for TE mode is presented in Fig. 4.2. From this figure, we extract the value of $n_g = 4.16$ and the dispersion parameter $D = 460\ ps/nm/km$ at $1550\ nm$.

Fabricating a AMZI based on this model, and measuring the response of the device we can also estimate the actual value of effective index and the dispersion to match with the modelled value. Such an experiment is presented in App. A.

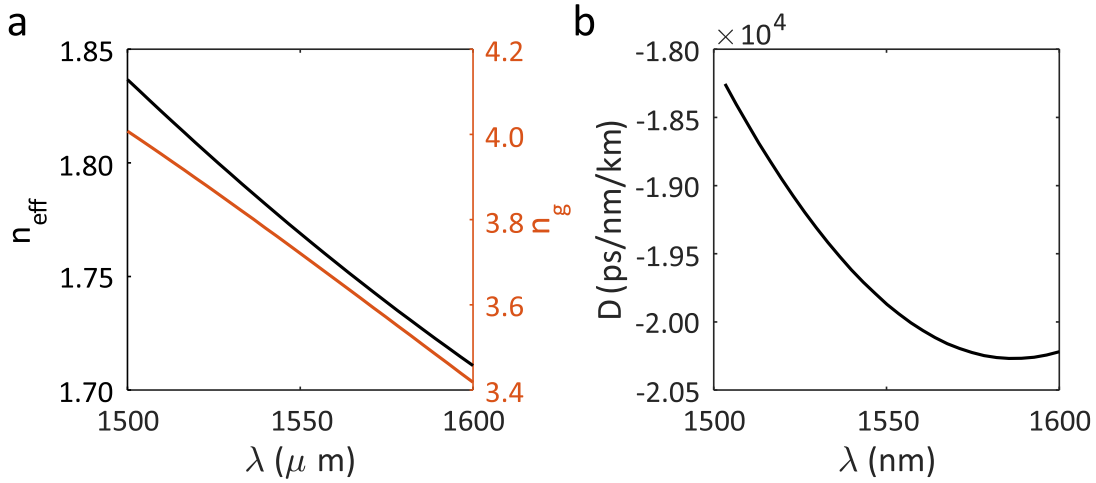

Figure 4.3: Dispersion using compact waveguide model for a $500\ nm \times 220\ nm$ silicon nanowire waveguide calculated using *Lumerical Mode Solver* for TM mode. (a) Effective index n_{eff} and group index n_g as a function of the wavelength of the light. (b) The dispersion parameter D_λ as a function of the peak wavelength of the pulsed light in the waveguide.

4.2.2 TE vs TM

It is mentioned before that the transverse electric (TE) mode of propagation is chosen over the transverse magnetic (TM) mode of propagation. That is based on the following reasons effectively captured by the compact waveguide model of TM light in Fig. 4.3:

① It can be seen from Fig. 4.3 (a) that the value of n_g at $1550\ nm$ is about 3.7 for a fundamental TM mode. This is lower than the $n_g = 4.16$ of fundamental TE mode. Low n_g value translates into lower intensity due to lower confinement, larger bend radius for low loss guiding, and larger footprint of the same component.

② Figure 4.3 (b) shows that the value of the dispersion parameter D is few orders of magnitude higher than the TE mode. A higher dispersion will make the phase-matching bandwidth of SFWM smaller. This will result in photon-pair generation near the pump pulse wavelength, resulting in the need of more strict constraints on pump filtering.

③ The TM modes are more sensitive to temperature variation as explored in App. A. A small fluctuation in the temperature results into a large variation in the TM effective index compared to TE. Therefore, a resonator with TM mode will be more challenging to stabilise compared to TE.

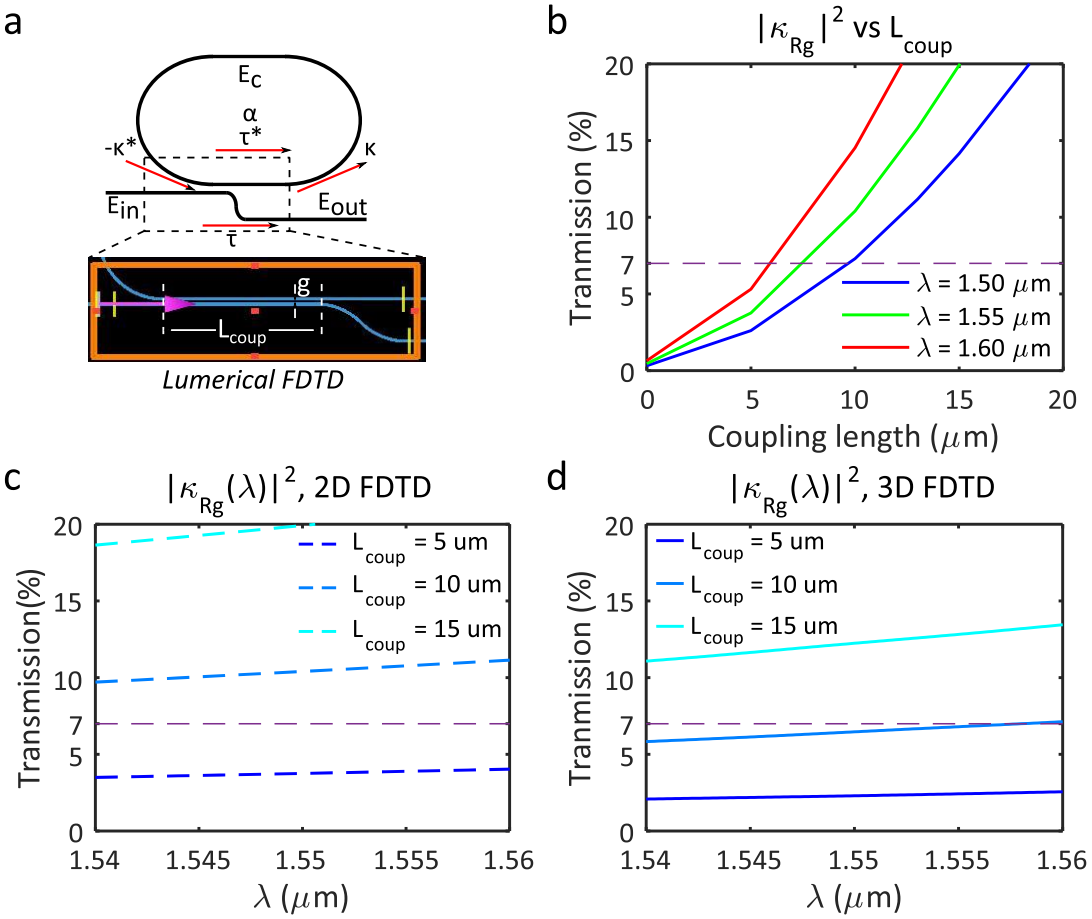

Figure 4.4: FDTD simulation result on the coupling of the ring-resonators by varying the coupling length L_{coup}. (a) shows the device geometry simulated in *Lumerical FDTD simulation*. (b) represents 2D simulation to determine the L_{coup} for $|\kappa_{Rg}|^2 = 0.07$. (c) shows wavelength dependence of the DC for three different values of L_{coup}. (d) shows 3D FDTD simulation to estimate the L_{coup} for $\lambda = 1.55\ \mu m$.

4.2.3 FDTD simulations of directional-couplers (DC)

The analytic expressions of the splitting ratio of the DC mentioned in the last chapter are used to determine the design parameters of a DC with low accuracy but closer to the desired values. Subsequently, a Finite Difference Time Domain (FDTD) simulation is performed to refine it to a more accurate version of the component behaviour for a specific device geometry. Such accuracy is required, for example, to design the coupling section of a ring-resonator. As we know from the Eq. 3.19 that the response of the resonator

depends critically on the parameter values of the coupling region, namely, the coupling length L_{coup} and the gap g. An inaccuracy of a few percent in the coupling $\kappa(L_{coup}, g)$ can change the resonance from over coupled to critically coupled regime. Considering the round-trip transmission inside the resonator is $\alpha_{Rg} = 0.995$, the $|\kappa_{Rg}|^2 = 0.07$ is chosen for slightly over-coupled resonators (Sec. 4.2.4).

All the simulations and fabrication here are done with a comparitvely large gap between the waveguides ($g = 300\ nm$) to achieve higher fabrication tolerance on the length L_{coup}. A larger gap (g) results in a larger length L_{coup} to achieve the same field coupling (Fig. 3.5), and a larger L_{coup} has larger tolerance limits. Fig. 4.4 (a) shows the simulation geometry of the resonator—known as the racetrack resonator with an S-bend in the coupling region. Fig. 4.4 (b) shows the 2D FDTD simulation results of the transmission $|\kappa_{Rg}|^2$ in the ring region as a function of the coupling length for different wavelengths. For a $|\kappa_{Rg}|^2 = 0.07$, the L_{coup} is between $5\ \mu m$ and $10\ \mu m$. Fig. 4.4 (c) shows that for this geometry the coupling constant κ strongly depends on the wavelength of the interest. For example, fixing the coupling length L_{coup} to achieve over-coupling the resonator in the pump wavelength may result in under-coupling in shorter wavelength signal photons. Fig. 4.4 (d) shows the more accurate but resource-hungry 3D FDTD simulations of the same parameters. Using these simulations as a guide, the $L_{coup} = 12\ \mu m$ is determined for the micro-ring resonator HSPSs mentioned in the next section.

4.2.4 Optimum design parameters for waveguide and micro-ring resonator HSPSs

Following the literature and the simulation presented previously, the photon-pairs generation in the waveguide and resonator HSPSs is optimised in this section. This parameter set will be verified by experiments presented in Chap. 6 and Chap. 7. We will first discuss the optimum parameters for the waveguide structure and then the micro-ring resonator structure.

Waveguides

Once the waveguide cross section of the PIM circuit is chosen from the dispersion calculations, the primary parameter for a waveguide source that we can modify while maintaining single mode operation is the length of the waveguide, L_{Wg}. According to the photon pair generation theory, the generation rate γ_{eff} is proportional to the square of the length of the waveguide without considering any self-phase modulations (Eqn. 2.10). At the same time the total linear loss $\alpha_T = \alpha_{Wg} L_{Wg}$ increases with the length of the waveguide. As these two effects contribute simultaneously,

$$\gamma_{eff} \propto L_{Wg}^2 exp(-2\alpha L_{Wg}) \tag{4.3}$$

there will be an optimum length that will maximise the photon-pair generation rate as shown in Fig. 4.5 (a). It is assumed in these figures that we know the actual value of the linear losses (propagation and bending losses) for a certain waveguide structure that we use. For a loss $\alpha_{Wg} = 3\ dB/cm$ for IME01 chip, the optimum length is found to be $14.5\ mm$.

Another important parameter is the dispersion parameter D, which is extracted from the compact waveguide model, to determine the SFWM phase matching for this chosen wavelength. The length and the dispersion parameter are related to the phase mismatch

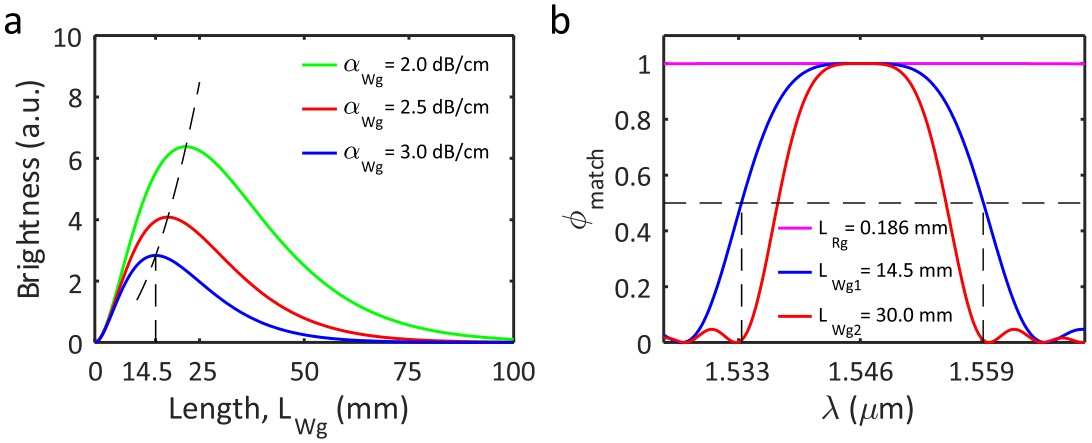

Figure 4.5: Optimum waveguide parameters. (a) shows the relative brightness values for three different linear loss α_{Wg} as a function of the waveguide HSPS length L_{Wg}. For a $\alpha_{Wg} = 3\ dB/cm$, the optimum $L_{Wg} = 14.5\ mm$. (b) The phase-matching function plotted for three different values of waveguide length L_{Wg}. It shows that for the chosen length the $3\ dB$ bandwidth of the phase-matching is $28\ nm$.

Δk of the phase matching function through the following equations:

$$\phi_{match} = sinc^2\left(\frac{\Delta k\ L_{Wg}}{2}\right) \tag{4.4}$$

$$\Delta k = -2\pi c^2\left(\frac{1}{\lambda} - \frac{1}{\lambda_0}\right) GVD(\lambda_0) \tag{4.5}$$

$$GVD(\lambda) = \frac{\lambda}{2\pi c} D(\lambda) \tag{4.6}$$

Figure 4.5 (b) shows that for our chosen values of length and pump pulse (at $1546\ nm$), the $3\ dB$ phase matching bandwidth is broad enough ($\sim 26\ nm$) to collect the generated SFWM photon-pairs in most of the telecom C-band. The figure also shows that, for the geometrical length ($L_{Rg} = 0.186\ mm$) of a typical resonator, the phase matching function ϕ_{match} is almost unity for the whole of C-band.

Micro-ring resonators

Figure 4.6 (a) shows the different attributes which need to be optimised for a resonator HSPS: free spectral range (FSR), extinction ratio (ER), full-width at half-maximum (FWHM) of the resonance line-width.

The first of these attributes is the FSR. Figure 4.6 (b) shows FSR as a function of the geometrical length of the resonator using the expression

$$FSR = \frac{\lambda_0}{n_g(\lambda_0) L_{Rg}} \tag{4.7}$$

Although ring resonators of any FSR can be used as HSPSs, in reality FSRs, which are multiples of $\sim 0.8\ nm$ ($100\ GHz$) are desirable. That value $0.8\ nm$ corresponds to the channel spacing of the International Telegraphic Unit (ITU) grid (shown in Fig. 4.7) in the telecom C-band. The value of the FSR is chosen to be $3.1\ nm$ ($400\ GHz$) which corresponds to the resonator's geometrical length of $L_{Rg} = 185.37\ \mu m$.

Secondly, to maximise the brightness, the field enhancement f_E needs to be maximised (Eqn. 2.12). f_E is related to the extinction ratio (or the intrinsic quality factor) of the resonator. These are related to the relative amplitude of the self-coupling coefficient τ and intrinsic cavity loss α through the equation as mentioned in the previous chapter:

$$f_E(\lambda) = \frac{-\kappa^*}{1 - \alpha\ \tau^* \exp(i\theta(\lambda))} \tag{4.8}$$

Figure 4.6 (c) shows the ER as a function of τ for a lossy ($\alpha = 0.900$) and a low loss ($\alpha = 0.995$) cavity. To maximise the intrinsic brightness of the photon-pairs generation inside the cavity we would have chosen critical coupling $\tau = \alpha$. It turns out that the heralding efficiency or the photon-number purity (ratio of heralding an actual photon and the vacuum) is at most 50% at critical coupling [41]. The reason behind the 50% photon-number purity is related to the non-unity escape probability of both signal and idler photons [32]. A slightly over-coupled regime can maximise the heralding efficiency to 68% [41]. Therefore, for our low loss cavity $\alpha = 0.995$, we chose $\tau = 0.965$ for a slight over-coupling. This corresponds to the transmission to the ring, $|\kappa|^2 = \sqrt{1 - |\tau|^2} = 7\%$.

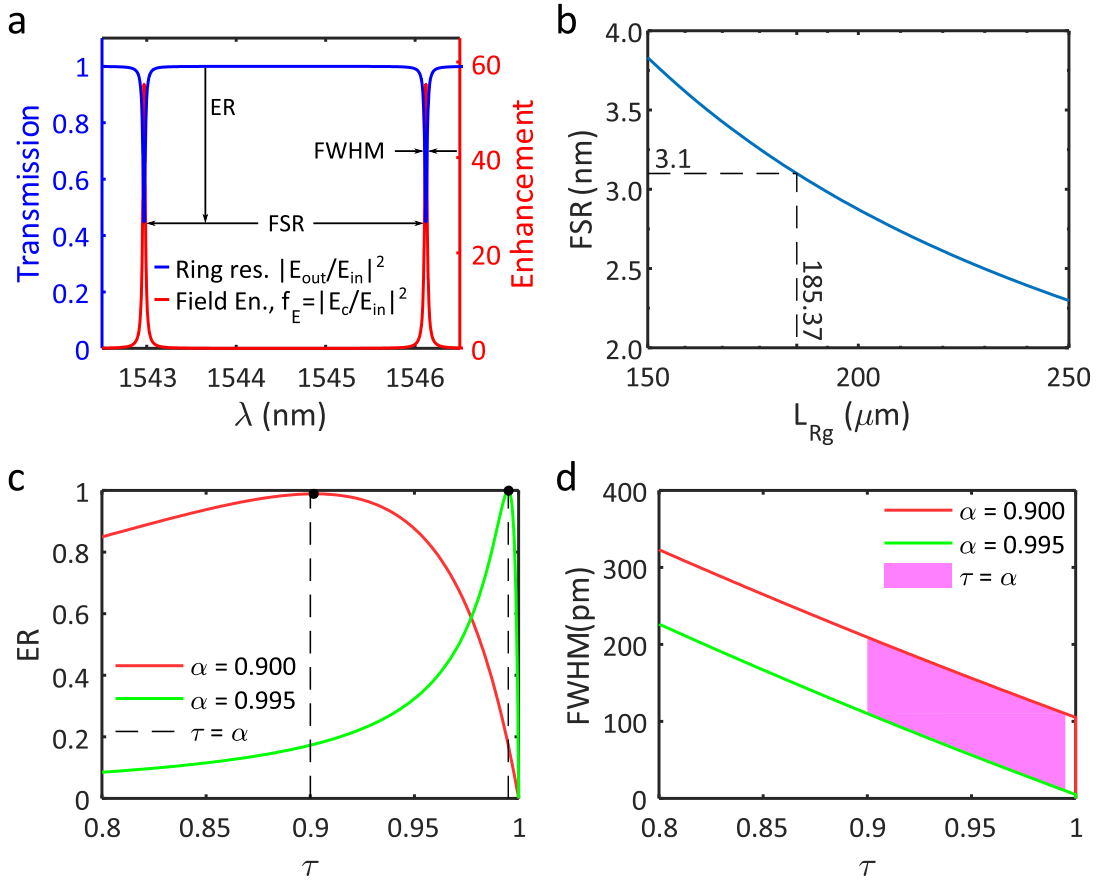

Figure 4.6: Optimum design parameters for micro-ring resonator HSPS. (a) A typical response and field enhancement of a resonator. Here the definitions of different attributes of a micro-ring resonator are shown: free spectral range (FSR), extinction ratio (ER) which is related to the intrinsic quality factor Q, full-width at half-maximum (FWHM) of the resonance line-width. (b) The FSR as a function of geometrical length of the resonator. For a FSR of $3.1\ nm$, the length is $185.37\ \mu m$. (c) The extinction ratio ER (and f_E & Q) is highest at critical coupling ($\tau = \alpha$) for both high and low loss resonators. (d) The FWHM of a resonator shortens monotonically from over-coupling to under-coupling regime. The shaded region represents the area between high ($\alpha = 0.900$) and low ($\alpha = 0.995$) loss resonators critical-coupling region.

The chosen value of $|\kappa_{Rg}|^2 = 7\%$ is used in Fig.4.4 to choose the correct coupling length of the directional-coupler region of the resonator. For a gap of $300\ nm$ between the waveguides, the coupling length is found to be $L_{coup} = 12.2\ \mu m$ at $\lambda_0 = 1550\ nm$.

Lastly, the purity of these resonators needs to be related to the source geometry. According to the literature [32, 34], if the FWHM of the resonance line-widths are narrower than the pump-pulse bandwidth, such that the resonance effectively sees a flat-top pump,

then the optimum purity of the resonator (93%) can be achieved. As we use $0.8\ nm$ bandwidth broadband ITU grid DWDM filters to clean the pump spectrum, the pump pulses used have bandwidth narrower than that. If we choose a factor of 10 to divide $0.8\ nm$ to get $80\ pm$ for the FWHM of the resonance line-width, then it will fulfil the flat-top pump condition to achieve high spectral purity. Figure 4.6 (d) shows the value of FWHM as a function of τ. For our choice of $\tau = 0.965$ for the over-coupling condition, the FWHM$= 30\ pm$. Later in Sec. 5.1.2, the JSA of such a configuration is computed and found to be in agreement with our choice.

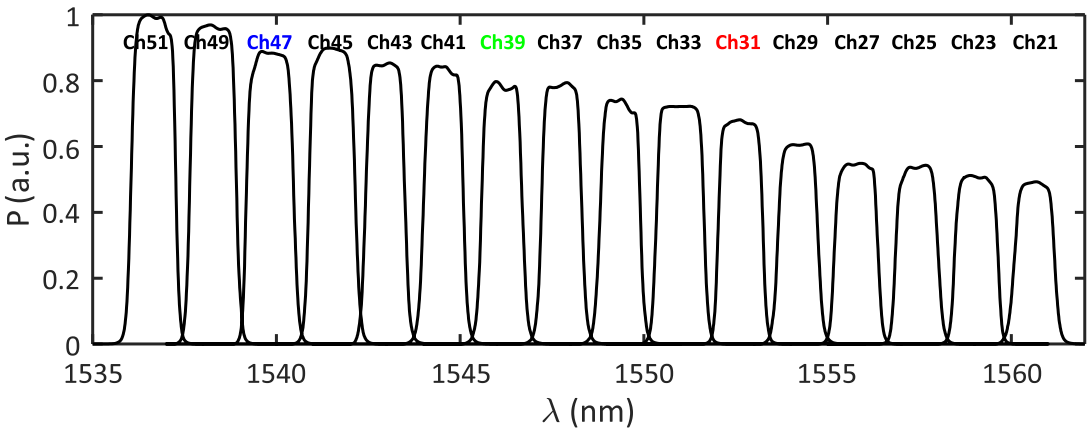

Figure 4.7: Typical response of an *Opneti* Dense Wavelength Division Multiplexer (DWDM). The chosen signal, pump and idler channels are 47, 39 and 31 respectively.

4.2.5 Optimum filter parameters

There are two types of filtering important for our quantum photonic experiments. The first of those is the off-chip filters from *Opneti*, which filter the pump spectral leakage at the signal-idler photons' spectra. These filters have high suppressions ($> 50\ dB$ for non-adjacent channels) of the pump photons at signal-idler wavelengths. The filter's channel spacings ($200\ GHz$) follow the ITU grid for only odd-numbered channels. A typical filter response from the channels are shown in Fig.4.7.

The other filters are on-chip filters to separate the signal-idler photons. As mentioned in the last section, the resonator HSPSs have a FSR matching the ITU grid. These filters are asymmetric MZI (AMZI) filters and the double-bus resonators (DbR) filters. The path length difference (ΔL) of the AMZI filters are chosen to be $149\mu m$ for $1550\ nm$ wavelength of light, using the compact waveguide model and the FSR of the signal-idler using the following equations:

$$FSR_{filter} = \frac{4}{5} FSR_{source} \tag{4.9}$$

$$\Delta L = \frac{\lambda_0^2}{n_g(\lambda_0) FSR_{filter}} \tag{4.10}$$

The above relation of the FSRs results in the filter's transmission to be maximum at the idler photons' collection channel and minimum at the signal photons' collection channel, therefore, spectrally separating the signal photons from the idler photons. The geometrical length of the DbR filters has been chosen by the same above equation of ΔL. A DbR filter has two self-coupling (τ_b, τ_t) and two cross-coupling (κ_b, κ_t) coefficients for the top and the bottom bus waveguides as shown in Fig. 4.8 (a). The through-port and the

drop-port transmissions of a DbR filter are expressed as,

$$\frac{E_{out}}{E_{in}} = \frac{\tau_b - \tau_t^* \alpha e^{i\theta}}{1 - \tau_b^* \tau_t^* \alpha e^{i\theta}} \tag{4.11}$$

$$\frac{E_{drop}}{E_{in}} = \frac{-\kappa_b^* \kappa_t \sqrt{\alpha} e^{i\theta/2}}{1 - \tau_b^* \tau_t^* \alpha e^{i\theta}} \tag{4.12}$$

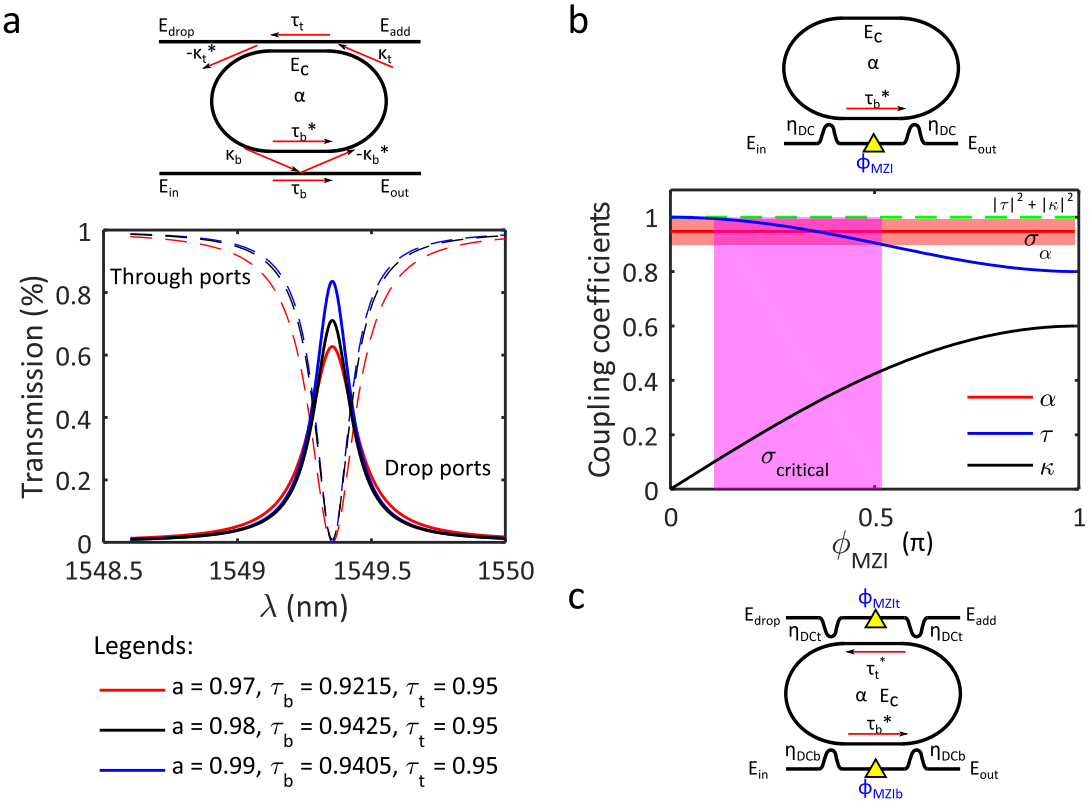

Figure 4.8: Choosing the parameters of the spectral filters. (a) The coupling coefficients of the DbR were chosen to obtain a FWHM $\sim 200\ pm$. (b) Replacing the coupling section of the bottom bus with a MZI gives control over the coupling-regimes of the resonator. (c) Replacing the top bus with another MZI adds control over the filter parameters (*FWHM*) and transmission.

where θ is the roundtrip phase. Our goal is to choose the coupling coefficients such that the drop-port transmission is near unity for a specific *FWHM*. For an intrinsic cavity loss of $\alpha = 0.98$, the values $\tau_b = 0.9425$ and $\tau_t = 0.9500$ were chosen using Fig. 4.8 (a) to achieve a *FWHM* $\sim 200\ pm$ with a transmission of $\sim 70\%$.

4.2.6 Narrowband spectral filters to increase purity

Replacing the fixed coupling section of the resonator with a MZI, we have more control over the coupling regimes. As shown in Fig. 4.8 (b) by choosing the phase of the MZI, κ (or τ) can be chosen to match the α. As α strongly depends on the fabrication process of the foundry, this design makes the resonators more robust. A device based on this principle is shown in Fig. 4.8 (b) and was designed by Dr Damien Bonneau.

The aforementioned structure (Fig. 4.8 (b)) can be modified by adding a second MZI coupling section for the top bus as shown in Fig. 4.8 (c). The transmission of this modified structure is also expressed by Eq. 4.11 and 4.12 where τ_b and τ_t are fully adjustable. Here, both the *FWHM* and transmission of the filter and can be chosen as a narrowband

spectral filter to increase the purity of the single-photons. These filters are used for IME03 waveguide design.

4.2.7 Component variations and modelling feedback

In order to design a photonic component in a specific foundry, a significant amount of simulation is required to get close to the practical value. For reproducibility, it is important to design that specific component with several copies on the same chip and also with a gradual variation of the parameter most susceptible to fabrication tolerance. For example, to get a reproducible directional coupler made by a specific foundry, we need to put many designs of that directional coupler with different values of gaps and lengths. This will help capturing the trend of the design that is susceptible to width and height variation of the waveguide along with the reproducibility of the minimum feature size of the design which is the gap between the two waveguides here. The measurement outcomes of these devices can then be fed back to the model to adjust it to give more accurate designs for the next fabrication process. We have followed this procedure specifically for the directional couplers and the resonator HSPSs from the first designs in IME01 to the next designs in IME03. Thermal crosstalk investigation and resonator phase estimation were two circuits that we have designed based on the modelling feedback as shown in App. B.

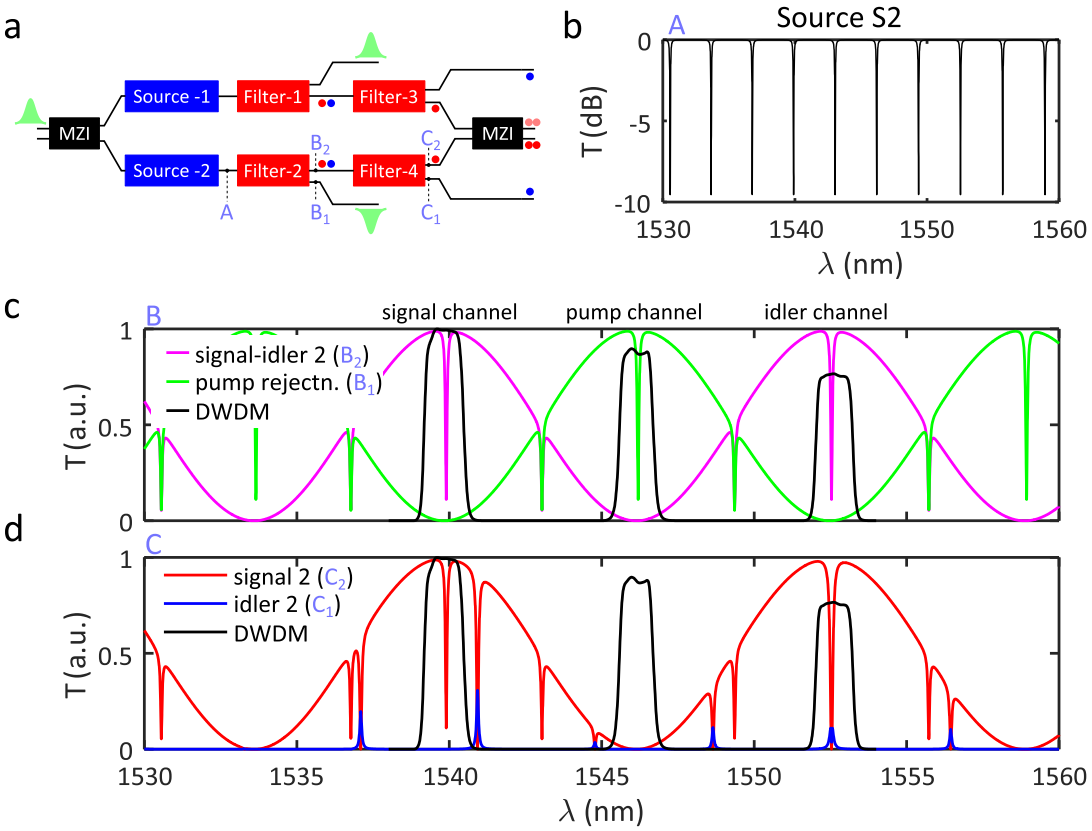

Figure 4.9: Modelling the spectral response of a photonic circuit with the schematic in (a). (b) Shows the HSPS spectrum at point **A** of the schematic. (c), (d) The spectra of the resonators need to be well-matched with the on-chip AMZI (point **B**) and double-bus resonator filters (point **C**).

4.3 Simulating the spectral response of the PIM circuit

Once all the parameters of the individual photonic components are chosen, they are all connected together to form a circuit corresponding to the schematics in Fig. 4.1. If the circuit contains wavelength sensitive devices such as filters or resonator HSPSs, then it is customary to simulate the final spectral response of the circuit. Such a simulation: ① checks if all the different FSRs of different components are calculated correctly, ② helps anticipating the possible reconfigurability of the PIM circuits for experiments. In this section, the circuit corresponding to the IME03 RF design (Fig. 4.1 (c)) is used to show the final spectral response of the PIM circuit in Fig. 4.9.

Let's consider, light from a broadband source is coupled into the photonic circuit from the left through the grating couplers. It first encounters a MZI with reconfigurable phase Φ_{MZI-in}. This phase is chosen such that the MZI splits the incoming light into equal proportions. The outputs of this MZI are connected to two identical micro-ring resonator HSPSs 1 and 2. If the MZI is configured to even-splitting, then both of the resonators will have the spectral responses to the broadband light as shown in Fig. 4.9 (b) with many resonant dips spaced as regular interval with $FSR = 3.1\ nm$. This is the point **A** in the schematics.

Each of the resonators are connected to asymmetric MZIs (AMZI) filters 1 and 2. The spectral responses of an AMZI connected to a resonator are shown in Fig. 4.9 (c). These are the points $\mathbf{B}_1$ and $\mathbf{B}_2$ in the schematics. The AMZI has one output $\mathbf{B}_1$ which is coupled out of the photonic circuit to dump the pump spectra. This is the green curve with highest transmission at the pump channel. The other output $\mathbf{B}_2$ has maximum transmission at the signal-idler channels to separate them from the pump channel.

Finally, the $\mathbf{B}_2$ is connected to a double-bus ring-resonator (DbR), configured as an add-drop filter. The two outputs of these filters are denoted by $\mathbf{C}_1$ and $\mathbf{C}_2$ and shown in Fig. 4.9 (d) by the blue and red curves respectively. The blue curve $\mathbf{C}_1$ transmits only in the idler channel, therefore filtering the idler for heralding the signal. The red curve transmits in the signal channel which is connected to the final MZI for PIM.

4.4 The implemented PIM circuits

The GDSII images of the implemented PIM circuits are shown in Fig. 4.10 and tabulated in Tab. 4.1. The long input waveguides for the IME01 AMZI and IME01 RF designs can be seen in Fig. 4.10 (a) and (b).

Figure	Design
Fig. 4.10 (a)	IME01 AMZI
Fig. 4.10 (b)	IME01 RF
Fig. 4.10 (c)	IME01 off-chip PIM
Fig. 4.10 (d)	IME03 waveguide
Fig. 4.10 (e)	IME03 off-chip PIM
Fig. 4.10 (f)	IME03 RF

Table 4.1: GDSII images of the implemented schematics.

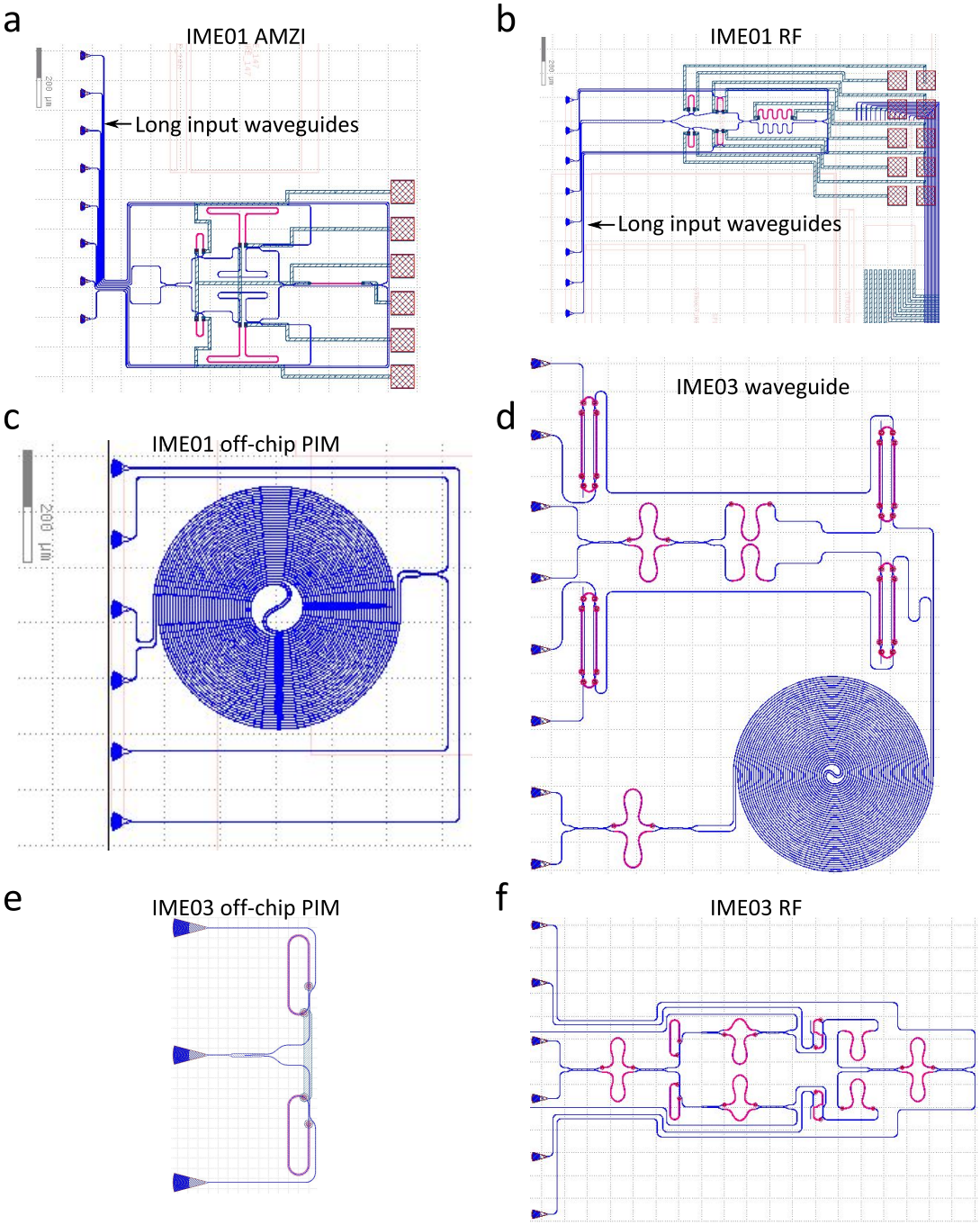

Figure 4.10: GDSII images of the implemented PIM circuit designs. (a) IME01 AMZI design. The long input waveguide can be seen on the left. (b) IME01 RF design. The long input waveguide can be seen at the left. (c) IME01 off-chip PIM design. (d) IME03 waveguide design. (e) IME03 off-chip PIM design. (f) IME03 RF design. Different colours represent different material layers: blue hash is the silicon waveguide layer, pink hash is the thermo-optic heater layer, red hash is the metal connector layer etc.

4.5 Synopsis & outlook

At the beginning of this chapter, we have presented four on-chip and off-chip PIM schematics. In order to implement the schematics, we have first performed simulations to choose the correct waveguide dimensions for an appropriate dispersion and single spatial mode propagation. The dispersion governs the phase matching condition during the SFWM photon-pair generation process. The single mode propagation ensures spatial mode purity. Next, the HSPSs are optimised: the optimum interaction length of the waveguides is chosen to maximise the brightness; coupling coefficients of the micro-ring resonators are estimated using *Lumerical 3D FDTD* simulations to maximise the brightness and heralding efficiency. To implement on-chip PIM schematics, we have also calculated the parameters of the spectral filters. With the aforementioned designs of the components, the spectral response of the whole circuit is simulated to check the appropriate parameters of the components.

Among all of the components, the directional couplers were the most fundamental simulations as it sets the performances of both the resonator HSPSs and the double-bus resonator filters. The cross-coupling coefficient (κ) plays a significant role in determining the FWHM, quality factor and the transmittance of the resonances which affect the HSPSs and signal-idler demultiplexers: brightness and heralding efficiency of a resonator HSPS can change significantly and the bandwidth and transmittance of a resonator filter can reduce immensely. Therefore, if the final chip has slightly wrong directional couplers, whether due to imprecise design or fabrication imperfections, it affects the performances of the resonator based PIM.

The GDSII images show the actual implementation of the designs from the early schematics in Fig. 4.10 as tabulated in Tab. 4.1. Fig. 4.10 (a) and (b) also show the long input waveguide responsible for spurious SFWM discussed in Sec. 6.3.3. The experimental data on the IME01 designs are presented in Chap. 6 and Chap. 7. As we will see in Chap. 8, for a complex circuit a suitable on-chip PIM circuit directly indicates the performance of the quantum protocol that depends on the indistinguishability of the HSPSs.

Chapter 5

The effect of purity and device imperfections on PIM

Contents

In the previous chapter, the PIM circuits were designed in SOI using classical device simulations. The designs were expected to obtain ideal PIMs and the optimum performance of the waveguide and resonator HSPSs regarding brightness and purity. These optimum values were estimated based on the existing literature, and simulations considering ideal components. In reality, the HSPSs have imperfections which can be analysed in the context of a PIM before an actual experiment is performed. These component imperfections usually stem from the SOI fabrication process. SOI device fabrication is a complex many-step process. The actual fabricated devices may be unavoidably different from the original designs. Therefore, PIM simulations with imperfect HSPSs and imperfect PIM circuits help us anticipating the experimental outcomes. These simulations also enable us to review the designs for the future PIM circuits.

In this chapter, we will first analyse the limiting factors of a practical HSPS in the view of experimental conditions (e.g. laser pulse-width) and component imperfections. Afterwards, a model is described to simulate PIM with imperfect circuits and practical HSPSs.

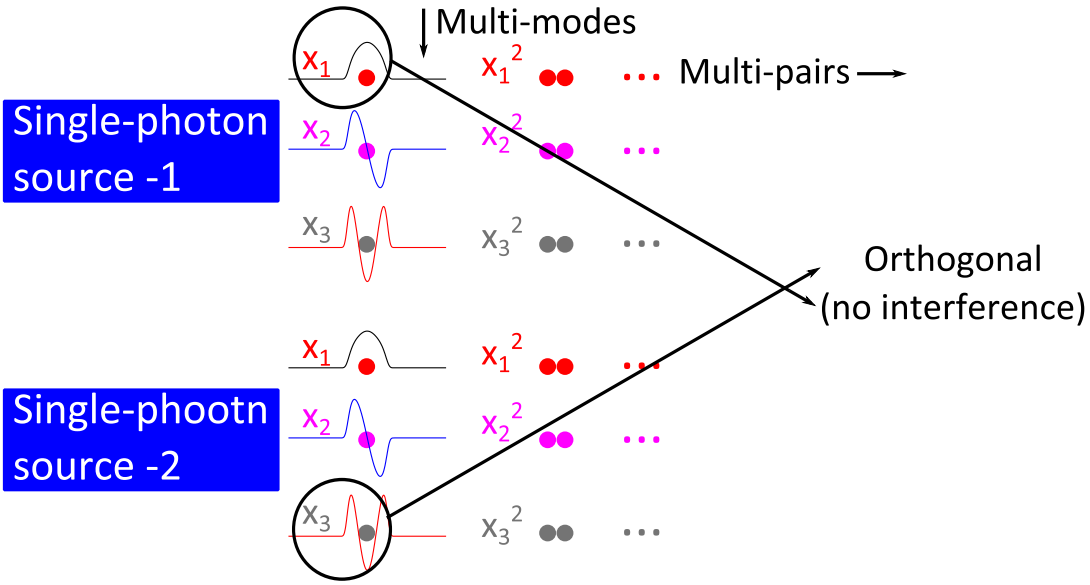

Figure 5.1: Orthogonality of the different optical modes of impure HSPSs shows the potential cause of reduced interference in a PIM. As the value of the strength of the squeezers (x_k) has to always be $x_k < 1$, the multi-pairs always have lower probabilities of emission than the single-pair.

5.1 Spectral purity of the HSPSs

The spectral purity of a HSPS refers to the proximity of the heralded signal photons to be in a single spectral mode. A HSPS is a twin-beam squeezer [28], and more generally a multi-mode twin-beam squeezer [30], as mentioned in Sec. 2.2.4. The modal structure strongly depends on the signal-idler spectral correlation which stems from the energy and momentum conservations. Generally, a SFWM based HSPS has multi-mode spectral structure and multi-pair effects, as mentioned in Sec. 2.2.4 and depicted as a cartoon in Fig. 5.1. While the latter effect is an intrinsic property of a HSPS, the former is closely related to the design parameters. The multi-mode spectral structure is quantified as spectral purity of the HSPS (i.e. single mode $\rightarrow$ unity purity).

As mentioned in Sec. 2.2.4, the spectral correlation of a HSPS is captured by the bi-photon wavefunction $f(\omega_s, \omega_i)$ in the interaction Hamiltonian H_{int} in Eq. 2.8. The JSA of our SFWM HSPSs are simulated using the following equation [28],

$$f(\omega_s, \omega_i) = \int d\omega_p \alpha(\omega_p)\alpha(\omega_s + \omega_i - \omega_p)\phi_{match} \tag{5.1}$$

Here, $\alpha(\omega_p)$ is the pump envelope, and the momentum conservation or phase matching function and can be expressed as

$$\phi_{match} = sinc^2\left(\frac{\Delta k\ L}{2}\right) \tag{5.2}$$

where, Δk is the phase or momentum mismatch, and L is the SFWM interaction length. Neglecting the non-linear phase shift for low pump power the phase mismatch can be calculated using the dispersion relation presented in Fig. 4.2,

$$\Delta k = n_g(\omega_p)k_0(\omega_p) + n_g(\omega_s + \omega_i - \omega_p)k_0(\omega_s + \omega_i - \omega_p) - n_g(\omega_s)k_0(\omega_s) - n_g(\omega_i)k_0(\omega_i) \tag{5.3}$$

The graphical representation of the bi-photon function in terms of ω_s and ω_i is commonly known as Joint Spectral Amplitude (JSA). The spectral purity is achieved when the heralded photon is in a single mode, that is JSA: $f(\omega_s, \omega_i) = h(\omega_s) \times g(\omega_i)$. This represents

separable signal and idler spectra. Thus, if a heralding idler photon is detected, the heralded signal photons is projected into a single spectral mode, independent of the spectrum of the detected idler photon.

In general, the $f(\omega_s, \omega_i)$ (JSA) is expressed as a sum of separable functions in signal and idler spectra using Schmidt decomposition, $f(\omega_s, \omega_i) = \sum_{k=1}^{\infty} \lambda_k \, h_k(\omega_s) \times g_k(\omega_i)$, where λ_k are the Schmidt coefficients. Thus the HSPSs wave-function can be expressed as a multi-mode squeezer, which can be rewritten as a tensor product ($\otimes$) of the k single mode twin-beam squeezer with strength λ_k [30, 37],

$$|\Psi\rangle = \bigotimes_k \sqrt{1 - x_k} \sum_{n_k=0}^{\infty} (-e^{j\theta_{\lambda_k}})^{n_k} \sqrt{x^{n_k}} \, |n_k, n_k\rangle \tag{5.4}$$

where k is the number of optical modes, x_k is the squeezing strength of k_{th} mode and $|n_k, n_k\rangle$ represents n number of signal and idler photons in the k_{th} mode. The λ_k is related with the squeezing strength x_k depicted in Fig. 5.1 by the relation $x_k = |tanh^2(\lambda_k)|$. As the value of the strength of the squeezers (x_k) always has to be $x_k < 1$, the multi-pairs always have lower generation probability than the single-pair. This equation shows that spectral correlation invokes several optical modes, and detecting a idler photon projects the heralded signal into multiple modes. The purity will be calculated according to Eq. 2.44, in terms of the Schmidt coefficients, purity $P = \sum \lambda_k^4$. The squeezing strength x_k is related to the average photon-number per pulse through Eq. 2.31,

$$\bar{n}_k = \frac{x_k}{1 - x_k} \tag{5.5}$$

In this section, using the aforementioned equations, the JSA of the waveguide HSPS is analysed first, and then the resonator HSPS is investigated. From each of the JSA the values of the Schmidt coefficients λ_k and the squeezing strength x_k are extracted using Schmidt decomposition and used to calculate the purity.

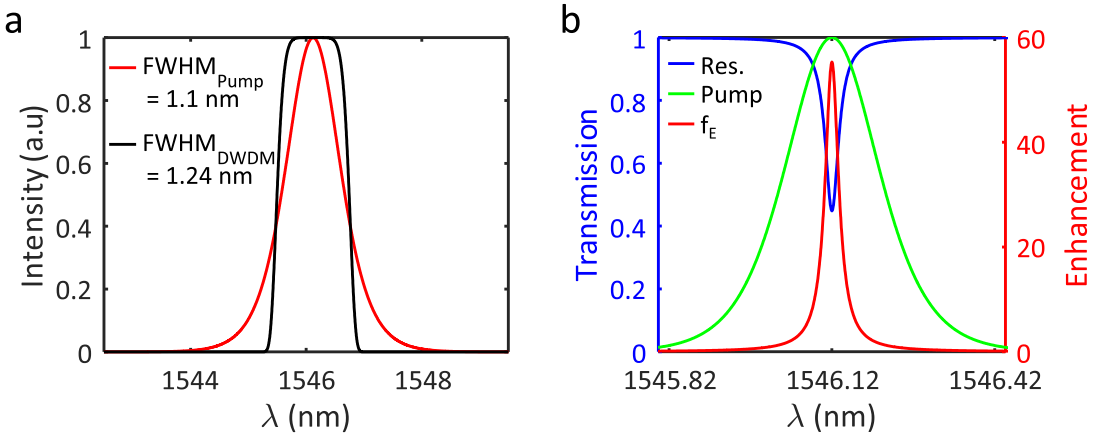

Figure 5.2: Pump-pulse and filter functions. (a) Pump envelope of a $sech^2$ pulse with FWHM $= 1.1\ pm$, in contrast to DWDM filter with FWHM $= 1.24\ pm$. (b) The response and field enhancement (f_E) from a resonator of FWHM = $30\ pm$. It sees the pump-top almost flat for pump FWHM = $200\ pm$ within the resonance line-width.

5.1.1 Waveguide JSA and spectral filtering

For our chosen waveguide length $L = 14\ mm$, the phase matching is near unity ($\phi_{match} \approx 1$) for the signal-idler wavelengths of interest (Fig. 4.5). Our pump envelope is a solitonic $sech^2$ pulse, generated from the fibre ring-laser (*PriTel FFL*) at a telecom wavelength

(1546 nm), as shown in Fig. 5.2. The pump is expressed by the equation:

$$I_{pump} = I_0 \; sech^2 \left(\frac{\lambda - \lambda_0}{\sigma_{pump}} \right) \tag{5.6}$$

Here, $FWHM_{pump} = 2sech^{-1}(1/\sqrt{2})\sigma_{pump} = 1.1 \; nm$ is used. The JSA of our waveguide HSPS with this pump pulse and without any spectral filters is plotted in Fig. 5.3 (a) using Eq. 5.1 resulting in purity, $P = 0.22$.

If we use the spectral filters depicted in Fig. 5.2 for signal, pump and idler wavelengths, then the JSA becomes,

$$f(\omega_s, \omega_i) = \int d\omega_p \alpha(\omega_p) F_p(\omega_p) \alpha(\omega_s + \omega_i - \omega_p) F_p(\omega_s + \omega_i - \omega_p) F_s(\omega_s) \; F_i(\omega_i) \phi_{match} \tag{5.7}$$

where the filter functions are expressed by:

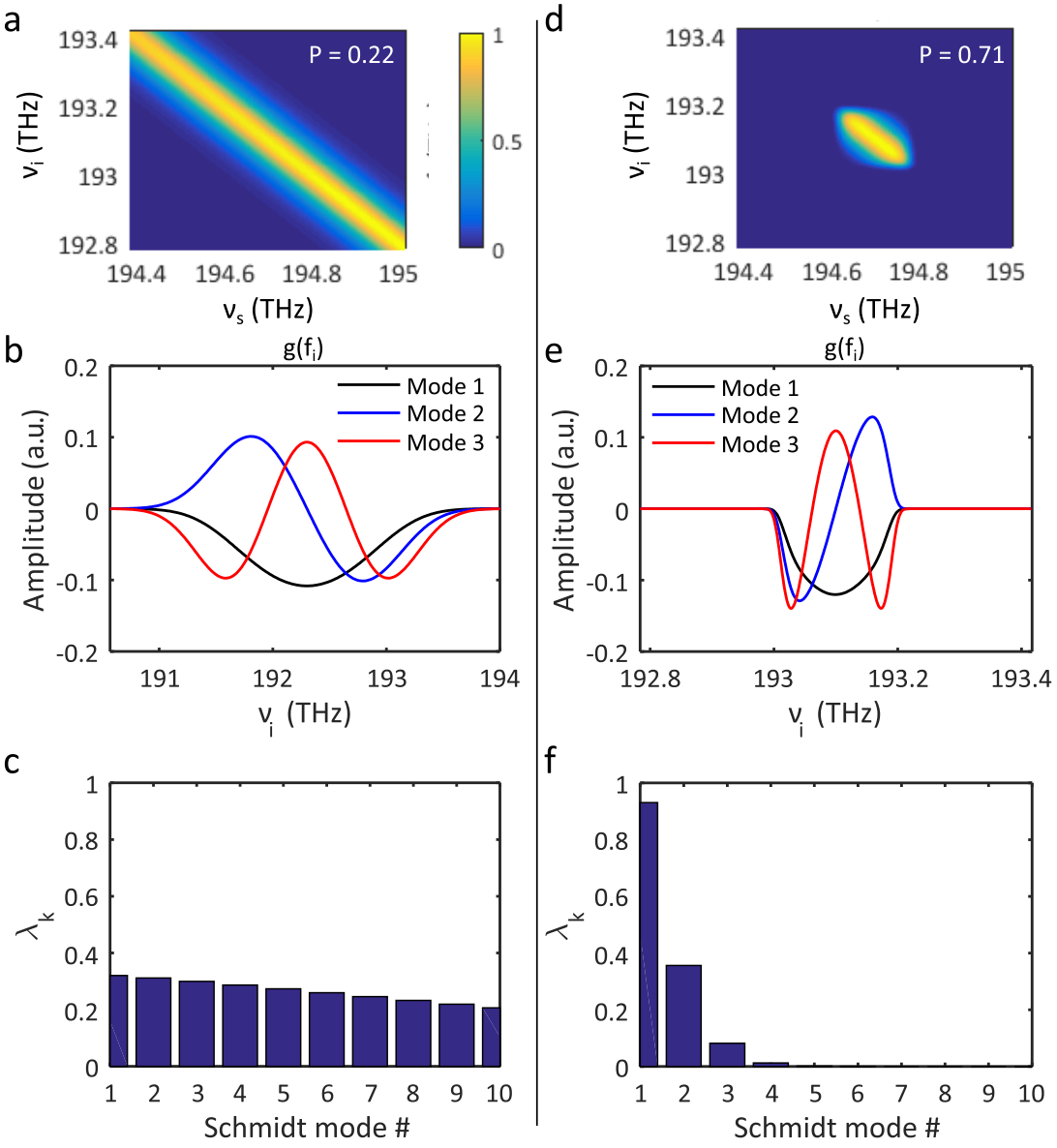

Figure 5.3: JSA of a nanowire waveguide. (a) JSA without any spectral filtering. (d) Improvement of JSA using spectral filtering with a top-hat like (higher order Gaussian shape with finite roll-off) functions (Eq. 5.10). (b), (e) Shows the spectra of the first three Schmidt modes. (c), (f) Show the relative strengths of these modes with respect to each other.

$$F_p = I_0\, e^{-(\frac{\omega-\omega_{p0}}{2\sigma_{DWDM}})^8} \tag{5.8}$$

$$F_s = I_0\, e^{-(\frac{\omega-\omega_{s0}}{2\sigma_{DWDM}})^8} \tag{5.9}$$

$$F_i = I_0\, e^{-(\frac{\omega-\omega_{i0}}{2\sigma_{DWDM}})^8} \tag{5.10}$$

and $FWHM_{DWDM} = 2\sqrt[8]{2ln(2)}\sigma_{DWDM} = 155\ GHz$ corresponding to $1.24\ nm$. The DWDM (dense wavelength division multiplexer) is a commercial filter from *Opneti* which does not provide any analytic function to express the filter shape. The above functions match with 99% correlation with the experimental data and will be used as representatives of these filters. The centre wavelengths of these filters correspond to the ITU grid channels of Ch 47, 39 and 52, such that $\lambda_{s0} = 1552.18$, $\lambda_{p0} = 1546.12$ and $\lambda_{i0} = 1539.48$ respectively. The JSA with the spectral filtering is plotted in Fig. 5.3 (b) showing the calculated purity, $P = 0.71$. The corresponding Schmidt decomposition is used to plot the spectral structure of the first three modes of these JSAs in Fig. 5.3 (c), (d) which show their mutual orthogonality as expected. Their respective relative strengths (λ_k) are plotted in Fig. 5.3 (e), (f).

Before analysing the JSA of the resonators in the next section, the following points can be drawn from this section and Fig. 5.3:

① Using the above method, the purity and squeezing strengths x_k of each mode k are determined. These values will be useful in the next section to estimate the indistinguishability between two HSPSs. Also, this method will be used to fit the experimental purity data estimated from unheralded $g^{(2)}(0)$ measurements in Chap. 7.

② Spectral filtering improves the purity. As we filter more, we discard a portion of the spectrum of the heralded photons, which results in an effective frequency dependent loss in the signal channel. Thus, this purity improvement comes at a cost of degraded heralding efficiency [151].

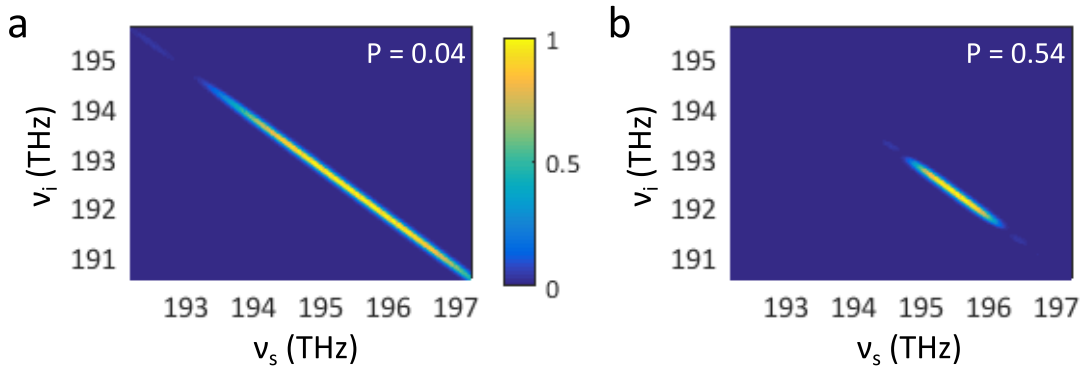

Figure 5.4: Effect of phase matching on a waveguide JSA. (a) JSA for $L = 14\ mm$. (b) JSA for $L = 140\ mm$. It shows that a strong phase matching can change the JSA significantly.

③ The effect of the phase matching function in these JSAs is not noticeable. This is due to the assumption that it is unity for waveguide of length $14\ mm$ and the dispersion estimated for the waveguide dimensions (height $220\ nm$, width $500\ nm$). The phase mismatch can also be expressed by $\Delta k = (\omega - \omega_{p0})^2 \times GVD(\omega_{p0})$ using Taylor series expansions of the k-vectors. The group velocity dispersion, $GVD(\omega_{p0})$ has wide range of values that can be found in the literature determined both experimentally and theoretically. The *GVD* in the waveguide differs from material's *GVD*, and strongly depends on the waveguide's dimensions. In this simulation, the *GVD* is chosen to be a conservative value of $460\ ps/nm/km$ as suggested by *Lumerical Mode Solver* simulation mentioned in Fig. 4.2. If the length is increased 10 times to $L = 140\ mm$,

then the effect of phase-matching is visible in the JSA as depicted in Fig. 5.4. In this particular example, the phase matching has increased the purity at the expense of the brightness (long $L \propto$ high linear loss). Depending on the dispersion, it can also prohibit phase matching. Therefore, in future, a rigorous experimental method is required to determine the dispersion in these waveguides.

The Joint Spectral Phases (JSPs) of these waveguides are not plotted as they are flat (i.e. factorable) if the pump is considered chirp-less and free from any phase profile caused by self or cross phase modulation.

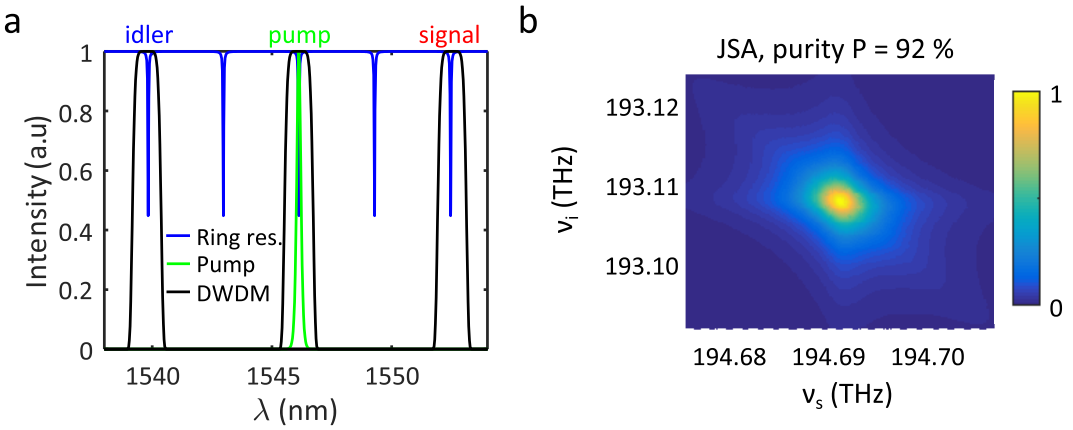

Figure 5.5: JSA of a ring resonator for a broad bandwidth pump pulse. (a) The spectral alignment of the resonance positions of a micro-ring resonator with respect to a pump and broadband filters. (b) The resulting JSA has about 92% purity.

5.1.2 Micro-ring resonator JSA and design parameters

The bi-photon function of a micro-ring resonator is a modified version of the waveguide JSA expression to take into account the resonance field enhancement ($f_E(\omega)$) of the pump, signal and idler frequencies [32, 34]:

$$f(\omega_s, \omega_i) = \int d\omega_p \; \alpha(\omega_p) \; \alpha(\omega_s + \omega_i - \omega_p) \; \phi_{match} \\ f_E(\omega_p) \; f_E(\omega_s + \omega_i - \omega_p) \; f_E^*(\omega_s) \; f_E^*(\omega_i) \tag{5.11}$$

The $f_E(\omega)$ expression is the same expression for a single-bus all-pass micro-ring resonator mentioned in Chap. 3:

$$f_E(\omega) = \frac{-\kappa^*}{1 - \alpha \; \tau^* \exp(i\theta(\omega))} \tag{5.12}$$

where, κ is the cross coupling coefficient, α is the round trip loss, τ is the self-coupling coefficient, and $\theta(\omega) = \omega L / v_g(\omega)$ contains the dispersion relation through group velocity $v_g(\omega)$. L is the geometrical length of the resonator and determines the FSR of the resonance to match the DWDM filter channels. These DWDMs are broadband filters and mainly rejects the pump spectral leakage into the signal-idler photons' spectra.

As we know from the last chapter, the designed ring-resonator HSPS has $L = 186 \; \mu m$. This value corresponds to $400 \; GHz$ ($3.1 \; nm$) FSR and $3.6 \; GHz$ ($30 \; pm$) FWHM of resonance line-widths at telecom wavelengths. The phase matching function for such a resonator is near unity ($\phi_{match} = sinc^2(\Delta k \; L/2) \approx 1$) for the wavelengths of interest as shown in Fig. 4.5 (b). For a secant hyperbolic pump envelope with $25.1 \; GHz$ ($200 \; pm$) FWHM, we obtain the JSA shown in Fig.5.5. In this configuration, all the signal, idler and pump resonances are filtered with a broadband filter (DWDM) corresponding to Ch 47, 39 and 31. The purity

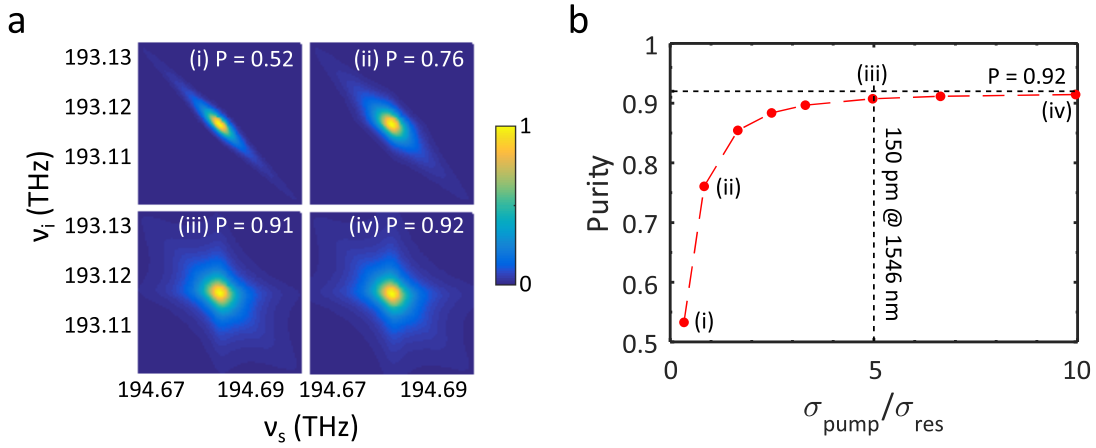

Figure 5.6: Purity as a function of the ratio of the pump to resonance bandwidths (FWHMs). (a) From top-left, clockwise, the pump FWHM is broadened from $1.25\ GHz$ ($10\ pm$) to $37.60\ GHz$ ($300\ pm$) while keeping the ring FWHM fixed at $3.60\ GHz$ ($30\ pm$). (i) FWHM = $1.25\ GHz$, (ii) FWHM = $3.15\ GHz$, (iii) FWHM = $18.80\ GHz$. (iv) FWHM = $37.60\ GHz$. (b) The plot shows that at $150\ pm$ pump FWHM, the purity reaches a plateau ~ 0.92.

of this JSA is, $P = 0.92$ without performing any narrowband spectral filtering. This is in contrast to the waveguide JSA which needs narrowband filtering to increase the purity.

As reported in [32, 34], if the pump-pulse in Eq. 5.11 is broad enough compared to the resonance line-width, the purity will approach to its maximum value 0.93. In order to verify: ① that for our choice of resonator, a broad pump gives high purity (close to 0.93) and ② to determine the optimum value of the pulse-width when the purity value starts to change significantly, the pump FWHM is varied and purity is calculated from the JSA as shown in Fig. 5.6. ② is important, specifically, to reduce the spurious four wave mixing without compromising the purity as mentioned in the Sec. 6.3.3. Here the JSA is calculated, keeping the ring-resonance fixed at $3.60\ GHz$ ($30\ pm$) FWHM, while the pump-spectra is varied gradually from $1.25\ GHz$ ($10\ pm$) to $37.60\ GHz$ ($300\ pm$). With a narrow pump FWHM $10\ pm$, there is a strong correlation between signal and idler spectra. This correlation gradually reduces resulting in higher purity with broader pump FWHM and reaches a plateau at about $150\ pm$ ($18.80\ GHz$) as shown in Fig. 5.6 (d). Hence we can say that the optimum pump pulse-width (FWHM) is $\sim 150\ pm$.

5.1.3 Imperfect micro-ring resonator

Often, a spectral scan of a micro-ring resonator shows imperfections in the resonance spectra with split resonance dips or split field enhancements. It can be assumed, sidewall roughness of the waveguides due to fabrication imperfections causes back reflection inside the resonator. The back reflection causes backward propagating mode inside the same resonator. Figure 5.7 (a) shows a modification of the original resonator model by adding a second coupled resonator that contains mode propagating in the opposite direction. The cross-coupling coefficient κ_3 is the amount of back-reflected mode expressed as a fraction of the original propagating mode in the cavity. The final output mode contains at least two optical modes or two super-modes which are orthogonal to each other. The field enhancement of an imperfect micro-ring resonator with back reflections can be expressed by the following equation:

$$f_{E-split} = \frac{-\tau_1\kappa_1^2\alpha_1 exp(i\theta_1)(\tau_3\alpha_2 exp(i\theta_2) - \tau_2)}{1 - \tau_2\tau_3\alpha_2 exp(i\theta_2) - \tau_2\tau_1\alpha_1 exp(i\theta_1) + \tau_1\tau_3\alpha_1 exp(i\theta_1)\alpha_2 exp(i\theta_2)} \tag{5.13}$$

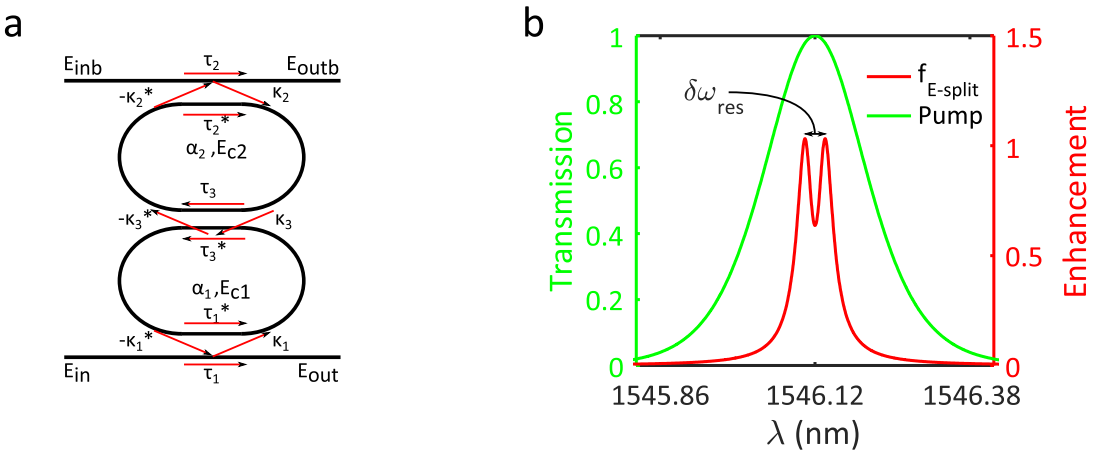

Figure 5.7: The split-resonance model of a micro-ring resonator. (a) Modification of the original resonator configuration by adding a second coupled resonator that contains a mode propagating in the opposite direction describing back-reflection. κ_3 is the amount of back-reflected mode expressed as a fraction of original propagating mode in the cavity. (b) The field enhancement inside such a structure is plotted for $\kappa_3 = 0.03$. The notation $\delta\omega_{res}$ is used to specify the value of splitting. In this example, $\delta\omega_{res} = 33.79\ pm$ $(4.24\ GHz)$. The pump envelope has a FWHM = $200\ pm$.

where the symbols have their usual meanings. Figure 5.7 (b) plots the above equation for the same parameter values of all the parameters of a single-bus ring, except the κ_3 is chosen as 0.03, resulting in, $33.79\ pm$ resonance split. The pump envelope for FWHM $= 200\ pm$ is also plotted to put this into perspective. By varying the κ_3, the splitting of

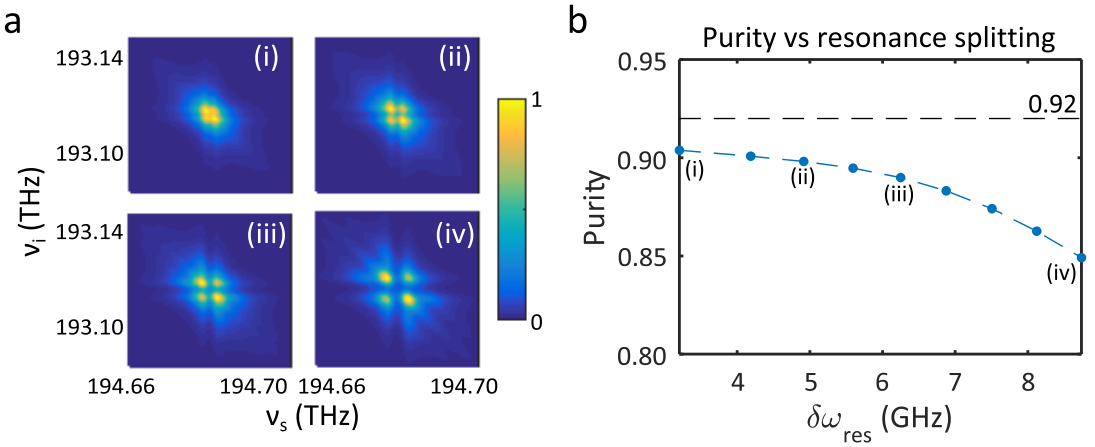

Figure 5.8: Purity as a function of resonance splitting of a ring-resonator. The splitting is varied from $3.20\ GHz$ $(25.5\ pm)$ to $8.74\ GHz$ $(69.7\ pm)$. (a) (i) $\delta\omega_{res} = 3.20\ GHz$, $P = 0.90$, (ii) $\delta\omega_{res} = 4.92\ GHz$, $P = 0.89$, (iii) $\delta\omega_{res} = 6.25\ GHz$, $P = 0.88$, (iv) $\delta\omega_{res} = 8.74\ GHz$, $P = 0.85$. (b) Purity plotted as a function of resonance splitting. Even a splitting of $8.74\ GHz$ does not change purity significantly.

the resonances can be varied and the JSA can be calculated for a fixed pump FWHM $500\ pm$ as shown in Fig. 5.8. In these JSAs, all the other parameters of the resonators are kept the same as Fig. 5.5, which corresponds to a slightly over-coupled resonator ($|\kappa_1|^2 = |\kappa_2|^2 = 7\%$). The corresponding purity is plotted in Fig. 5.8 (d). In our micro-resonators from the IME-chips, we have observed the split resonances below $10\ pm$. It is evident that for a splitting of $10\ pm$ the purity value does not change more than a few percent from its' optimum value $P = 0.92$.

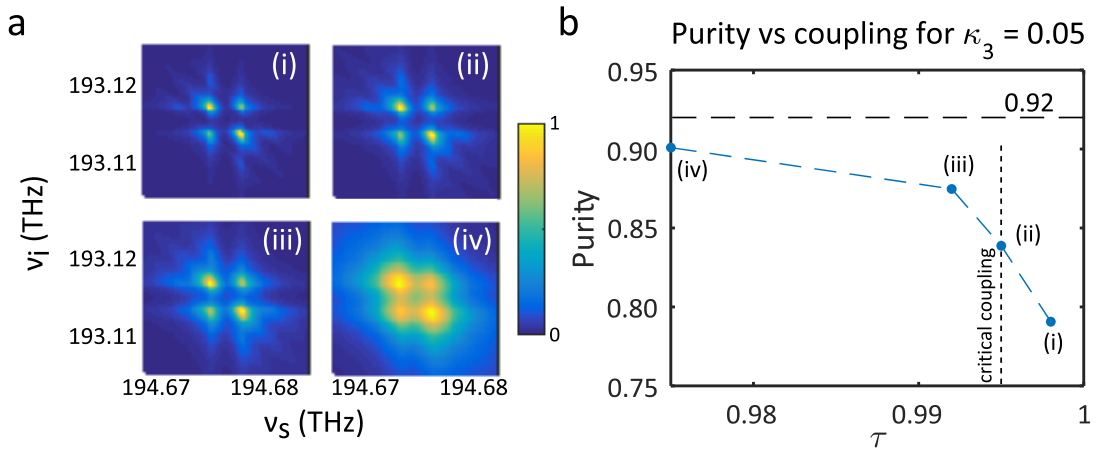

Figure 5.9: Purity as a function of coupling for a chosen resonance splitting ($\delta\omega_{res} = 6.88\ GHz$) of a ring-resonator. (a) (i) Under-coupled ($\tau = 0.998$), $P = 0.79$, (ii) Critically coupled ($\tau = 0.995$), $P = 0.84$, (iii) Over-coupled ($\tau = 0.992$), $P = 0.87$, (iv) Over-coupled ($\tau = 0.975$), $P = 0.90$. These JSA imply that the different couplings at split resonances reduce the purity. (b) Purity is plotted as a function of different coupling regimes.

The JSAs of a practical micro-ring resonator can also be plotted for different coupling regimes to see if there is any effect of coupling on the purity. For a chosen splitting of $6.88\ GHz$ ($\sim 55\ pm$), the coupling is varied from the under-coupled to the over-coupled regime and the JSA is plotted in Fig. 5.9. It shows that the different coupling regime does change the appearance of the JSA. The JSA with over-coupling regime smears the details of the resonance splitting and may hide the backward propagating mode. Thus, the purity calculated from the JSA reaches a higher value for the over-coupled regime than in the under-coupled regime for an imperfect resonator.

5.2 The effect of device imperfections on PIM

Indistinguishability refers to the degree of identicalness among the heralded single photons emitted from multiple sources. As mentioned in Chap. 2 (Fig.2.11, Fig. 5.1), often the heralded photons from multiple sources are interfered in a HOM configuration or MZI configuration to perform a PIM. This measurement will be affected by the multi-pair and multi-mode characteristics of a practical HSPS as mentioned in the last section.

In addition to imperfect sources, the imperfections in the photonic circuit can also affect the PIM. The directional couplers in the MZI can have un-even splitting ratio due to fabrication imperfections which will distort the MZI fringes. Moreover, experimental considerations such as non photon number resolving detectors (PNRDs) also influence the PIM. For example, the multi-pair effect can be mitigated if we had 100% efficient PNRD.

Figure 5.10 represents schematic of the experimental configuration, which will be used to simulate the PIM. The sources in this figure are practical HSPSs with multi-pair and multi-mode effects as described in Fig. 5.1. The heralded photons are transformed through a unitary matrix (U) for PIM. The creation operators of the heralded signal photons before and after the unitary are denoted by $a^\dagger$, $b^\dagger$ and $c^\dagger$, $d^\dagger$ respectively. Using this notation, a single photon state from HSPS 1, can be expressed as $|1\rangle_{s1} = a_{s1}^\dagger|0\rangle$, where $|0\rangle$ represents vacuum. Similarly, a two-photon state is represented by $|2\rangle_{s1} = (1/\sqrt{2})(a_{s1}^\dagger)^2|0\rangle$ and so on. The outcome of the PIM in the output modes $c^\dagger$, $d^\dagger$ are related to the input modes $a^\dagger$, $b^\dagger$ by,

$$\begin{bmatrix} c^\dagger \\ d^\dagger \end{bmatrix} = \begin{bmatrix} U_{11} & U_{12} \\ U_{21} & U_{22} \end{bmatrix} \begin{bmatrix} a^\dagger \\ b^\dagger \end{bmatrix} \tag{5.14}$$

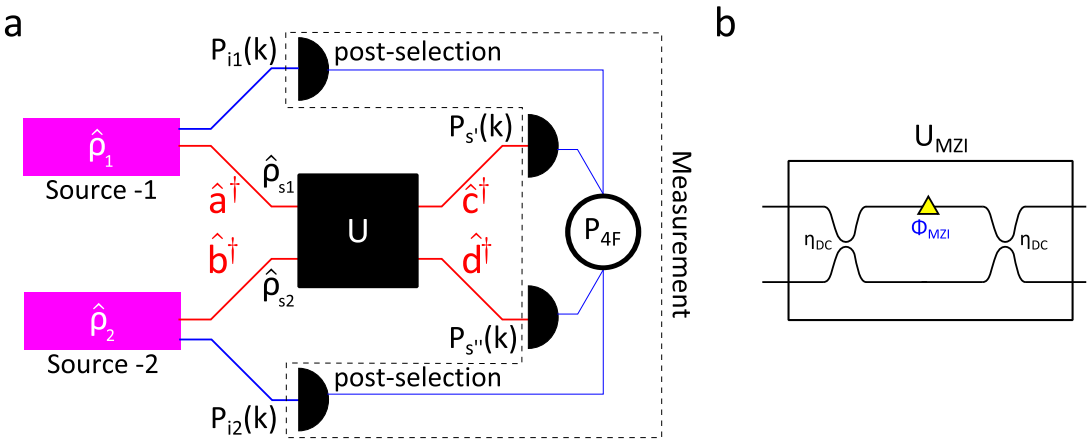

Figure 5.10: Configurations to simulate device imperfections. (a) Represents the PIM configuration, where all the losses are lumped with the detectors. (b) Represents the unitary of the MZI.

For the simplest case, without any multi-pair or multi-modal effects and with perfect detection efficiency, the transformation for the PIM for distinguishable photons ($s1 \neq s2$) and indistinguishable photons ($s1 = s2 = s$) become,

$$a^\dagger_{s1} b^\dagger_{s2}|0\rangle \xrightarrow{U} \left(U_{11}U_{21}c^\dagger_{s1}c^\dagger_{s2} + U_{11}U_{22}c^\dagger_{s1}d^\dagger_{s2} + U_{12}U_{21}d^\dagger_{s1}c^\dagger_{s2} + U_{12}U_{22}d^\dagger_{s1}d^\dagger_{s2}\right)|0\rangle \tag{5.15}$$

$$a^\dagger_{s} b^\dagger_{s}|0\rangle \xrightarrow{U} \left(U_{11}U_{21}(c^\dagger_{s})^2 + U_{11}U_{22}c^\dagger_{s}d^\dagger_{s} + U_{12}U_{21}d^\dagger_{s}c^\dagger_{s} + U_{12}U_{22}(d^\dagger_{s})^2\right)|0\rangle \tag{5.16}$$

The corresponding probabilities of four-fold coincidences are,

$$\begin{aligned} P_{4FD} &= P(i_1, i_2, s', s'') = P(c^\dagger_{s1}d^\dagger_{s2}) + P(c^\dagger_{s2}d^\dagger_{s1}) \\ &= |U_{11}U_{22}|^2 + |U_{12}U_{21}|^2 \end{aligned} \tag{5.17}$$

$$\begin{aligned} P_{4FI} &= P(i_1, i_2, s', s'') = P(c^\dagger_{s}d^\dagger_{s}) \\ &= |U_{11}U_{22} + U_{12}U_{21}|^2 \end{aligned} \tag{5.18}$$

This section will begin with the model on the effect of device imperfections in the PIM circuits, then the effect of lossy detection is included in the model. Afterwards the effect of source imperfections while performing PIM is included. Finally, a comparison between HOM and MZI PIM is presented using this model.

5.2.1 Indistinguishability measurement with imperfect devices

The transformations of photons during PIM through a MZI or an HOM interferometer are often expressed by unitary matrices.

Unitary matrix of imperfect HOM

For an HOM experiment, the unitary matrix is the beam-splitter matrix with splitting ratio η_{DC}:

$$U_{DC} = \begin{bmatrix} \sqrt{\eta_{DC}} & \sqrt{1-\eta_{DC}} \\ \sqrt{1-\eta_{DC}} & -\sqrt{\eta_{DC}} \end{bmatrix} \tag{5.19}$$

The visibility of the HOM interference is defined as,

$$V_{HOM} = \frac{P_{4FD} - P_{4FI}}{P_{4FD}} \tag{5.20}$$

where P_{4FD} and P_{4FI} are calculated using Eq. 5.17 and Eq. 5.18 for an ideal source. Thus, for a perfect beam-splitter ($\eta_{DC} = 1/2$) and ideal sources, Eq. 5.18 gives $P_{4FI} = 0$ and $V_{HOM} = 100\%$, as expected for completely indistinguishable sources.

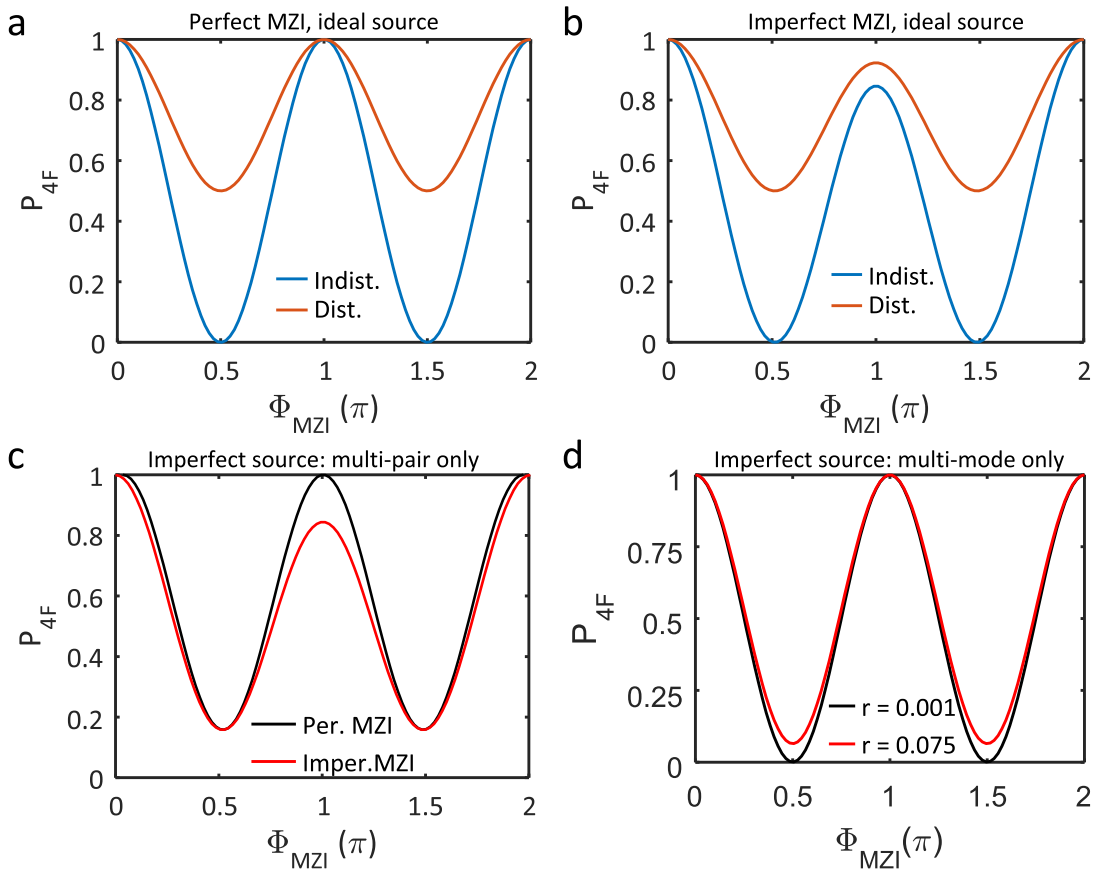

Figure 5.11: MZI fringes for (a) perfect ($\eta_{DC} = 50\%$) and (b) imperfect ($\eta_{DC} = 40\%$) MZI. The blue (red) line represents fringes with indistinguishable (distinguishable) photons. (c) Inclusion of multi-pair effect on the indistinguishable fringe reduces the visibility. Adding device-imperfection (imperfect MZI) distorts the fringe while keeping the visibility definition unchanged. (d) Inclusion of multi-mode effect without any multi-pair emission reduces the fringe visibility for perfect MZI. Here, r represents the ratio of first two Schmidt modes. $r = 0.001$ means, there is effectively one Schmidt mode (spectrally pure).

Unitary matrix of imperfect MZI

On-chip indistinguishability is measured using a MZI which is implemented with two directional couplers (Sec. 15) and a thermal phase shifter (Sec. 15) in between to change the phase. The directional couplers act as beam-splitters and due to imperfections may have uneven splitting ratio η_{DC}. The unitary transfer matrix of the MZI can be expressed as a function of the reflectivity of the directional coupler η_{DC}, and MZI phase Φ_{MZI},

$$
\begin{aligned}
U(\eta_{DC}, \Phi_{MZI}) &= \begin{bmatrix} U_{11} & U_{12} \\ U_{21} & U_{22} \end{bmatrix} \\
&= U_{DC} \begin{bmatrix} e^{i\Phi_{MZI}} & 0 \\ 0 & 1 \end{bmatrix} U_{DC} \qquad (5.21) \\
&= \begin{bmatrix} \sqrt{\eta_{DC}} & \sqrt{1-\eta_{DC}} \\ \sqrt{1-\eta_{DC}} & -\sqrt{\eta_{DC}} \end{bmatrix} \begin{bmatrix} e^{i\Phi_{MZI}} & 0 \\ 0 & 1 \end{bmatrix} \begin{bmatrix} \sqrt{\eta_{DC}} & \sqrt{1-\eta_{DC}} \\ \sqrt{1-\eta_{DC}} & -\sqrt{\eta_{DC}} \end{bmatrix} \qquad (5.22)
\end{aligned}
$$

With no multi-pair or multi-mode effect, and for a perfect MZI, if the four-folds for totally indistinguishable photons ($s1 = s2$) are expressed as $P_{4F.I}$, and the four-folds for totally distinguishable photons ($s1 \neq s2$) are expressed as $P_{4F.D}$, then using Eq. 5.17 and Eq. 5.18,

they can be expressed in terms of the MZI phase (Φ_{MZI}):

$$P_{4F.I} = |cos(\Phi_{MZI})|^2 \tag{5.23}$$

$$P_{4F.D} = |cos^2(\Phi_{MZI}/2)|^2 + |sin^2(\Phi_{MZI}/2)|^2 \tag{5.24}$$

The visibility V_{MZI}, is expressed by,

$$V_{MZI} = \frac{(P_{4F})_{max} - (P_{4F})_{min}}{(P_{4F})_{max} + (P_{4F})_{min}} \tag{5.25}$$

where P_{4F} can be completely distinguishable (P_{4FD}), completely indistinguishable (P_{4FI})

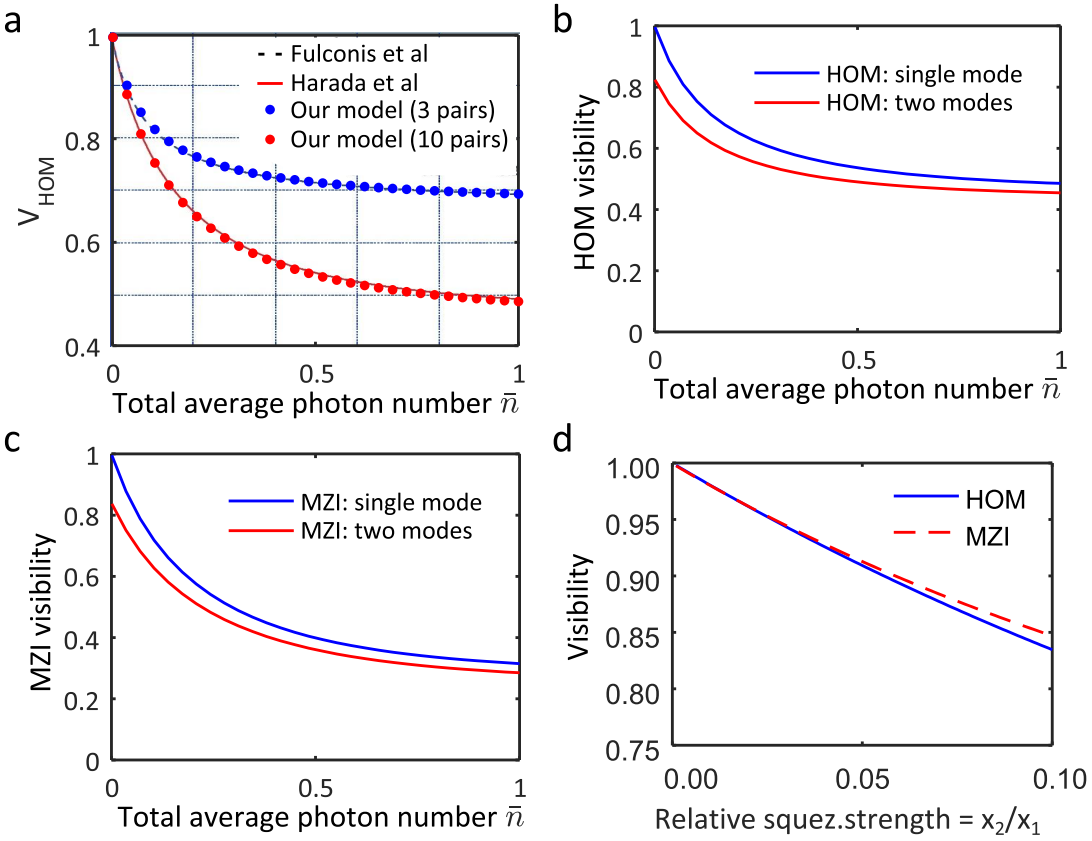

Figure 5.12: Visibility of HOM and MZI interference as a function of average photon-number $\bar{n}$ generated by each HSPS. (a) Our method for single-mode squeezer agrees with results obtained from the literature with multi-pair emissions. Fulconis et al [114] (black dashed line) includes total 3 photon-pairs at a time and Harada et al [56] (red solid line) includes total 10 photon-pairs at a time. Our results, shown by red and blue dots, agrees with the literature. (b) HOM visibility for both single-mode and multi-mode case: total mode # = 2, purity = 83%, relative strength between the squeezers $4:1$, detection efficiency in all channels $\eta = 0.01$. The multi-mode case starts from a reduced visibility even at the absence of multi-pair emissions due to lower purity. (c) The same analysis is performed for the visibility of the MZI as a function of average photon number. The MZI graphs have steeper slopes than the HOM interference graphs. (d) Shows the relative comparison of the absolute visibility values of a PIM using HOM and MZI as a function of the HSPSs' purity. High values of purity constitutes effectively two Schmidt modes, and can be expressed by the ratio of them, x_2/x_1.

or partially indistinguishable (P_{4F}). Figure 5.11 (a) plots the MZI fringes for both distinguishable ($V_{MZI} = 33\%$) and indistinguishable ($V_{MZI} = 100\%$) photons from ideal sources with perfect MZI. Now, as shown in Fig. 5.11 (b), if the MZI is imperfect with splitting

ratio $\eta_{DC} = 0.39$, then the equation of the visibility still remain the same albeit the fringe distorts due to the imperfect destructive interference at certain phases. This shows the robustness of the measurement using a stable integrated MZI. An imperfect MZI does not change the raw visibility, while an imperfect beam-splitter used for HOM changes the raw visibility value.

5.2.2 Lossy detection

In our experiments, the photon collection efficiency is less than 100%. If there is loss in collecting photons before the interference, then there has to be an analysis of the photon-number state of the surviving photons. For example, a two-photon state can become a single-photon state after passing through a lossy channel. That behaviour needs to be accounted for a correct analysis.

If there is no loss of photons before the quantum interference (generally the case in the photonic circuits for on-chip PIM), then all the losses can be lumped together. If the lumped detection efficiency of a idler photon channel is η_i, then for a generic non-photon-number-resolving detector [153], the probability of detecting k idler photons is,

$$P_i(k) = 1 - (1 - \eta_i)^k \tag{5.26}$$

This relation is also used for signal photons. For the rest of the analysis in this section, we will assume that the above equation holds.

5.2.3 Inclusion of the imperfect HSPS

Single-mode twin-beam squeezer

A single-mode twin-beam (referring to signal and idler beams) squeezer, which contains the multi-pair emissions but not multi-mode effect, can be expressed by the following wave-function in terms of number state basis ($|n, n\rangle$) [28],

$$|\Psi\rangle = \sqrt{1-x} \sum_{n=0}^{\infty} (-e^{j\theta_r})^n \sqrt{x^n} \, |n, n\rangle \tag{5.27}$$

After the detection of idler photons in each source, the resulting heralded density matrix $\hat{\rho}_s$ can be calculated for the single-mode squeezer as,

$$\begin{aligned} \hat{\rho}_s &= tr_i(P_i(k)|\Psi\rangle\langle\Psi|) \\ &= (1-x) \sum_{k=0}^{\infty} P_i(k)|k\rangle\langle k| \end{aligned} \tag{5.28}$$

Here, the photon collection and detection efficiency (Eq. 5.26 for k idler photons) has been taken into account in the heralded density matrix $\hat{\rho}_s$. After the unitary transformation, $\hat{\rho}_s \xrightarrow{U} \hat{\rho}'_s$, the probability of detecting a four-fold event for the single mode squeezed state with multi-pair emission and lossy detection will be,

$$\begin{aligned} P_{4F} = N_1 N_2 \sum_{\substack{n_{c_1},\dots n_{c_k}=0 \\ n_{c_1}+\dots n_{c_k}\geq 1}}^{\infty} \sum_{\substack{n_{d_1},\dots n_{d_k}=0 \\ n_{d_1}+\dots n_{d_k}\geq 1}}^{\infty} & P_s(n_{c_1}+\dots n_{c_k}) P_s(n_{d_1}+\dots n_{d_k}) \\ & \langle n_{c_1}|\langle n_{d_1}|\dots\langle n_{c_k}|\langle n_{d_k}|\hat{\rho}'|n_{c_1}\rangle|n_{d_1}\rangle\dots|n_{c_k}\rangle|n_{d_k}\rangle \end{aligned} \tag{5.29}$$

where $P_s(k)$ is the probability of detecting k signal photons considering a lump detection efficiency η_s, and c_k and d_k are output optical modes of the U. In a MZI, the phase Φ_{MZI} is scanned to get the minimum and maximum four-fold coincidences which are used to estimate the visibility and in subsequently indistinguishability using Eq. 5.25. The

fringe shape for single mode squeezer with multi-pair emissions is plotted in Fig. 5.11 (c). It shows that the fringe visibility reduces due to multi-pair emissions even though the photons are identical to each other. The same scenario for an imperfect MZI shows the distortion of the fringe shape while the fringe visibility remains the same.

The average photon-pairs ($\bar{n}$) generated by each HSPS is related to the squeezing strength x by Eq. 2.31 as,

$$x = \frac{\bar{n}}{1+\bar{n}} \tag{5.30}$$

Increasing the value of $\bar{n}$ by turning up the input laser power implies increasing the value of the squeezing strength x, which in turn increases the probability of multi-pair emission. This will reduce the visibility. In literature such model including only multi-pair emission exists for HOM interference visibility: *Fulconis et al* [114] has calculated V_{HOM} including total 3 photon-pairs at a time, while *Harada et al* [56] used upto 10 photon-pairs at a time. Figure 5.12 (a) shows the visibility as a function of $\bar{n}$, from the above two literature: *Fulconis et al* [114] by black dashed line and *Harada et al* [56] by red solid line. The calculated HOM interference visibility using our model (from the above equations) are superposed on the aforementioned literature using blue dots (total 3 photon-pairs emissions) and red dots (total 10 photon-pairs emissions). It can be seen that our multi-pair model agrees with the literature.

Unitary evolution and multi-mode quantum interference

The inclusion of multiple optical modes will change the above single-mode equations to the multi-mode twin-beam squeezers as a tensor product of the k single-mode twin-beam squeezers with strength x_k [30, 37] as mentioned at the beginning of this chapter,

$$|\Psi\rangle = \bigotimes_k \sqrt{1-x_k} \sum_{n_k=0}^{\infty} \sqrt{x^{n_k}} \, |n_k, n_k\rangle \tag{5.31}$$

The reduced density matrix ρ_s of the heralded signal photons for multi-mode twin-beam squeezer can be expressed by detecting at least one idler photon in at least one of the Schmidt modes k, with the normalisation constant N,

$$\hat{\rho}_s = N \sum_{\substack{n_1,\ldots n_k=0 \\ n_1+\ldots n_k \geq 1}}^{\infty} P_i(n_1+\ldots n_k)\langle n_1|\ldots\langle n_k|\hat{\rho}|n_k\rangle\ldots|n_1\rangle \tag{5.32}$$

Considering the input optical modes of U from source 1 and source 2 are $\hat{a}_{1i}$ and $\hat{a}_{2j}$ respectively with i and j as i^{th} and j^{th} Schmidt modes, and the output optical modes of the transformation are $\hat{c}^\dagger_{ij}$ and $\hat{d}^\dagger_{ij}$, then the transformation for distinguishable photons will be (only two Schmidt modes shown for simplicity),

$$\hat{a}^\dagger_{11} \rightarrow U_{11}\hat{c}^\dagger_{11} + U_{12}\hat{d}^\dagger_{11}; \qquad \hat{a}^\dagger_{12} \rightarrow U_{11}\hat{c}^\dagger_{12} + U_{12}\hat{d}^\dagger_{12} \tag{5.33}$$

$$\hat{a}^\dagger_{21} \rightarrow U_{21}\hat{c}^\dagger_{21} + U_{22}\hat{d}^\dagger_{21}; \qquad \hat{a}^\dagger_{22} \rightarrow U_{21}\hat{c}^\dagger_{22} + U_{22}\hat{d}^\dagger_{22} \tag{5.34}$$

For the indistinguishable case, we can assume that both first and second Schmidt mode of source 2 will be the same as source 1 in the above equations: $\hat{c}^\dagger_{21} \rightarrow \hat{c}^\dagger_{11}$ and $\hat{c}^\dagger_{22} \rightarrow \hat{c}^\dagger_{12}$ and the same treatment for mode $\hat{d}^\dagger$. Therefore, the probability of detecting two heralding idler photons, and heralded signal photons at both of the output modes of the unitary can be recorded as a four-fold coincidence event P_{4F} describing heralded two-photon quantum interference. Thus, after the unitary transformation of the heralded signal photon density matrix, $\hat{\rho}_s \xrightarrow{U} \hat{\rho}'_s$, the probability of detecting a four-fold event for the single mode squeezed state can be calculated by an equation similar to Eq. 5.29, expanded to contain two modes

for each HSPS, and the same visibility defined by Eq. 5.25,

$$P_{4F} = N \sum_{\substack{\forall n_{c_{sk}}=0 \\ \sum_k n_{c_{sk}} \geq 1}}^{\infty} \sum_{\substack{\forall n_{c_{s'k}}=0 \\ \sum_k n_{c_{s'k}} \geq 1}}^{\infty} \sum_{\substack{\forall n_{d_{sk}}=0 \\ \sum_k n_{d_{sk}} \geq 1}}^{\infty} \sum_{\substack{\forall n_{d_{s'k}}=0 \\ \sum_k n_{d_{s'k}} \geq 1}}^{\infty} P_s\left(\sum_k n_{c_{sk}}\right) P_s\left(\sum_k n_{c_{s'k}}\right) P_s\left(\sum_k n_{d_{sk}}\right) P_s\left(\sum_k n_{d_{s'k}}\right)$$

$$\langle n_{c_{s1}}|\langle n_{c_{s'1}}|\langle n_{d_{s1}}|\langle n_{d_{s'1}}|...\langle n_{c_{sk}}|\langle n_{c_{s'k}}|\langle n_{d_{sk}}|\langle n_{d_{s'k}}|\hat{\rho'}|n_{c_{s1}}\rangle|n_{c_{s'1}}\rangle|n_{d_{s1}}\rangle|n_{d_{s'1}}\rangle...|n_{c_{sk}}\rangle|n_{c_{s'k}}\rangle|n_{d_{sk}}\rangle|n_{d_{s'k}}\rangle \tag{5.35}$$

PIM using HOM

The inclusion of multi-mode analysis is important to compare a PIM experiment with a less than unity purity HSPS. It shows that the visibility cannot get higher than the purity of the sources, even if there is no multi-pair effect, as shown in Fig. 5.12 (b). Here the HOM visibility is calculated for both single-mode and multi-mode (2 modes) twin-beam squeezer as a function of average photon-number $\bar{n}$. The multi-mode case is calculated for a purity of 83% with the relative strength between two modes as $4:1$. The detection efficiencies are $\eta_s = \eta_i = 0.01$, typical for our experiments.

PIM using MZI

The above analysis can also be performed for MZI, and the four-fold coincidence as a function of Φ_{MZI} (MZI fringe) can be analytically evaluated for partially indistinguishable (P_{4F}) sources. The corresponding visibilities as a function of average photon number is plotted in Fig. 5.12 (c) with detection efficiency $\eta_s = \eta_i = 0.01$. The multi-mode is calculated for a purity of 83% with the relative strength between two modes as $4:1$.

It can be seen that both the single-mode and multi-mode visibility graphs for MZI falls off steeply with increasing average photon-number (increasing multi-pair effect), compared to the HOM interference visibility.

Relation between HOM and MZI PIM

The above analysis (Fig. 5.12 (b), (c)) shows that for the same purity values (same strength of the x_k), the visibility values of the MZI and HOM interference are different at a higher average photon-number $\bar{n}$ values. As the higher value of $\bar{n}$ represents more pronounced multi-pair effect, it can be understood that they will behave differently passing through different unitaries corresponding to MZI and HOM interference. A few points can be drawn from Fig. 5.12:

① In the single-mode case (100% pure photons), without any multi-pair effect ($\bar{n} \approx 0$), for indistinguishable sources, both the HOM and MZI visibility is 100%.

② The inclusion of the multi-pair effect (high values of $\bar{n}$) shows that for the same indistinguishability of the HSPSs, the absolute values of V_{HOM} and V_{MZI} differs for the same value of $\bar{n}$.

③ Further inclusion of multi-mode effect shows that the upper bound of the visibility values for both HOM and MZI are the same and less than 100% depending on the value of the purity. As shown in Fig. 5.12 (d), for indistinguishable sources, without any multi-pair effect, for purity relatively close to 100%, the two visibility values start to differ once the purity starts to decrease. In this plot, the relative strength of the squeezer, $r = x_2/x_1$ is the ratio of the strength of the first two Schmidt modes. Using r to express purity is valid only for high purities, where there is effectively not more than two Schmidt modes.

Alternative calculations with photon-number resolving detectors

If we have photon-number resolving detectors (PNRD) or use them in future experiment, it will be interesting to know if they can make the above analysis simpler. Considering the use of PNRD, we arrive at the simplest multi-mode twin beam squeezer: two-Schmidt modes for each source with maximum one photon-pair in each optical mode. The wave-function for source 1 with two Schmidt modes of squeezing strength x_{11} and x_{12} can be expressed in the Fock basis as,

$$|\Psi_{s1}\rangle = \sqrt{1-x_{11}} \sum_{n=0}^{\infty} (-e^{j\theta_{r11}})^n \sqrt{x_{11}^n}\, |n,n\rangle \otimes \sqrt{1-x_{12}} \sum_{m=0}^{\infty} (-e^{j\theta_{r12}})^m \sqrt{x_{12}^m}\, |m,m\rangle \tag{5.36}$$

Heralding at most one idler photon in each mode and total one photon from each source, the reduced density matrix for signal photons from source 1 becomes,

$$\hat{\rho_{s1}} = N_1 P_i(1) \left[x_{11} \left(|1\rangle\langle 1|_{11} \otimes |0\rangle\langle 0|_{12}\right) + x_{12} \left(|0\rangle\langle 0|_{11} \otimes |1\rangle\langle 1|_{12}\right)\right] \tag{5.37}$$

Here, N_1 is the normalisation constant and $P_i(1)$ is the detection probability of one idler photon. Similarly, the reduced density matrix for signal photons form source 2 with squeezing strengths x_{21} and x_{22} can be expressed as,

$$\hat{\rho_{s2}} = N_2 P_i(1) \left[x_{21} \left(|1\rangle\langle 1|_{21} \otimes |0\rangle\langle 0|_{22}\right) + x_{22} \left(|0\rangle\langle 0|_{21} \otimes |1\rangle\langle 1|_{22}\right)\right] \tag{5.38}$$

Therefore, the combined density matrix for the whole system can be written as $\hat{\rho} = \hat{\rho}_{s1} \otimes \hat{\rho}_{s2}$. Any term in this density matrix can be rewritten using creation and annihilation operators, such as,

$$|1\rangle\langle 1|_{11} \otimes |1\rangle\langle 1|_{22} = \hat{a}_{11}^{\dagger} \hat{a}_{22}^{\dagger} |0\rangle\langle 0|_{11} \otimes |0\rangle\langle 0|_{22} \hat{a}_{11} \hat{a}_{22} \tag{5.39}$$

Here, $\hat{a}_{jk}^{\dagger}$, $\hat{c}_{jk}^{\dagger}$, $\hat{d}_{jk}^{\dagger}$ are creation operators and $\hat{a}_{jk}$, $\hat{c}_{jk}$, $\hat{d}_{jk}$ are annihilation operators for jk optical modes at the input/output of the unitary. The system can evolve according to the unitary transformation U as $\hat{\rho} \xrightarrow{U} \hat{\rho}'$ for completely distinguishable case, and the probability of four-fold coincidence for temporally distinguishable events becomes,

$$P_{4F.D} = N_1 N_2 P_i(1)^2 P_s(1)^2 \left(|U_{11}U_{22}|^2 + |U_{12}U_{21}|^2\right) (x_{11}x_{21} + x_{11}x_{22} + x_{12}x_{21} + x_{12}x_{22}) \tag{5.40}$$

For indistinguishable sources, there are two options:

① Source 1 and source 2 are completely indistinguishable. It means that the primary Schmidt mode 11 and 21 of source 1 and 2 respectively will result into the same optical mode, and similarly the secondary Schmidt modes 12 and 22 of source 1 and 2 respectively will transform into the same optical modes ($\hat{a}_{21}^{\dagger} \rightarrow U_{21}\hat{c}_{11}^{\dagger} + U_{22}\hat{d}_{11}^{\dagger}$; $\hat{a}_{22}^{\dagger} \rightarrow U_{21}\hat{c}_{12}^{\dagger} + U_{22}\hat{d}_{12}^{\dagger}$). Therefore, the four-fold coincidence probability will be,

$$\begin{aligned} P_{4F} =& N_1 N_2 P_i(1)^2 P_s(1)^2 \Big(\left|U_{11}U_{22} + U_{12}U_{21}\right|^2 (x_{11}x_{21} + x_{12}x_{22}) \\ &+ \left(|U_{11}U_{22}|^2 + |U_{12}U_{21}|^2\right) (x_{11}x_{22} + x_{12}x_{21}) \Big) \end{aligned} \tag{5.41}$$

② Source 1 optical modes can be decomposed into orthogonal Schmidt modes of Source 2. It means that the primary Schmidt mode of source 1 can be expressed in terms of primary Schmidt mode of source 2 (only change from distinguishable case in $\hat{a}_{21}^{\dagger} \rightarrow U_{21}\hat{c}_{11}^{\dagger} + U_{22}\hat{d}_{11}^{\dagger}$). The sub-Schmidt modes of both sources, modes 12 and 22 are orthogonal to each other and all other optical modes. If the purity of source 1 is P_1 and source 2 is P_2, then the weighting factors can be expressed as: $x_{11} = \eta_{ov}\sqrt{P_1}$, $x_{12} = 1 - \eta_{ov}\sqrt{P_1}$, $x_{21} = \sqrt{P_2}$ and $x_{22} = 1 - \sqrt{P_2}$. Then the density matrices for both sources can be relabeled as,

$$\hat{\rho_{s1}} = N_1 P_i(1) \left(x_{11}\hat{\rho}_I + x_{12}\hat{\rho}_{Ds1}\right) \tag{5.42}$$

$$\hat{\rho_{s2}} = N_2 P_i(1) \left(x_{21}\hat{\rho}_I + x_{22}\hat{\rho}_{Ds2}\right) \tag{5.43}$$

If we take the inner product of the density matrices of both sources, we get $tr(\hat{\rho}_{s1}\hat{\rho}_{s2}) = x_{11} \times x_{21} = \eta_{ov}\sqrt{P_1}\sqrt{P_2}$. Therefore, with $x_{11}x_{21} = \eta_{ov}\sqrt{P_1}\sqrt{P_2}$ and $x_{11}x_{22} + x_{12}x_{21} + x_{12}x_{22} = 1 - \eta_{ov}\sqrt{P_1}\sqrt{P_2}$, the four-fold coincidence probability will be,

$$P_{4F} = N_1 N_2 P_i(1)^2 P_s(1)^2 \Big(\eta_{ov}\sqrt{P_1}\sqrt{P_2} \times |U_{11}U_{22} + U_{12}U_{21}|^2 \Big(1 - \eta_{ov}\sqrt{P_1}\sqrt{P_2}\Big) \times \big(|U_{11}U_{22}|^2 + |U_{12}U_{21}|^2\big) \Big) \tag{5.44}$$

This is a much simpler equation and depends primarily on the purity values (P_1, P_2) as expected. Comparing it to Eq. 5.17 and Eq. 5.18, it can be seen that this multi-mode equation is a weighted equation of single-mode distinguishable and indistinguishable cases. The overlap parameter η_{ov} determines how much of the indistinguishable part of the density matrix $\hat{\rho}_I$ contributes to the fringe, and it gives an estimate of the indistinguishability of the sources.

It must be noted that this analysis is valid in the presence of PNR detector, hence, ruling out the multi-pair emission effect. Non-PNR detection will invalidate this analysis and we need to take into account the full model numerically calculated in the previous sections.

5.3 Synopsis & outlook

In this chapter, the imperfections of the waveguide and resonator HSPSs, designed in the previous chapter, are numerically investigated. Specifically, the spectral purity of the HSPSs and the effect of impurity in an indistinguishability measurement (e.g. PIM circuit) has been numerically investigated. The spectral purity is investigated by simulating the Joint Spectral Amplitude (JSA) of signal-idler photons and then using Schmidt decomposition to estimate the amount of multiple optical modes. Each spectral (i.e. optical mode) is then assumed to be an independent HSPS with the probability of multiple pair productions.

We started the investigation with our current waveguide HSPS design, which is optimised in the previous chapter only for the waveguide's length for high brightness. The JSA simulation shows that our choice of spectral filtering can achieve high purity photons, at the expense of the brightness. It is also found that the waveguide length plays an important role in shaping the JSA through the phase matching function. For our particular design, increasing the length (10 times) of the waveguide enforces a stricter phase matching, which improves the purity at the expense of the brightness. The Phase matching function strongly depends not only on the waveguide length but also on the dispersion. For a highly confined waveguide mode, the dimensions of the waveguide's cross-sectional area dominate the dispersion properties. Optimising all the dimensions of the waveguide for both purity and brightness can, in future, relax the spectral filtering condition. That will increase the brightness of the high purity photons without reducing heralding efficiency.

In contrast, the calculated JSA for the designed micro-ring resonator HSPS shows high brightness and also high purity (92%) photons without any need for spectral filtering. In recent experiments, it is seen that a practical resonator may show split resonances indicating the presence of additional modes which can potentially reduce purity. This can happen due to the imperfections in the fabrication quality which manifests as the sidewall roughness of the waveguides. Thus, it meditates back-reflections and introduces a backward propagating mode. However, JSA simulations have been performed for such scenarios, and they show that the purities do not degrade unless the splitting is severe (more than the line-width of the resonances). It is also found that an over-coupled resonator smears such resonance splitting indicating 92% purity. Therefore, in future, an

experimental investigation can explain whether the over-coupling reduces the splitting, or the JSA overlooks the presence of multiple modes.

The aforementioned JSA simulations extract the relative squeezing strengths of the multiple spectral (i.e. temporal or optical) modes of our designed HSPSs using Schmidt decomposition. Therefore, each HSPS can be assumed to be composed of k independent HSPSs, each representing a temporal mode with varying brightness determined by the previously obtained squeezing strength of that mode. Each of these modes also includes the multi-pair emission effects. The density matrix of each HSPS is then propagated through the PIM circuit with device imperfections to estimate the indistinguishability in both HOM and MZI configurations. Such a model for PIM has already been developed in the literature but only for single mode case in HOM configuration and including multi-pair effects. Our methods fully agree with the solutions extracted from these literature [56, 114]. Moreover, our model includes the multi-mode effect, which is essential to investigate a practical HSPS with non-unity spectral purity. This model quantifies the reduction of HOM or MZI visibility in a PIM with impure sources with and without multi-pair effects. Another important aspect of this implementation is its ease of generalisation. The PIM in HOM or MZI configuration for two independent HSPSs can be viewed as a 2×2 unitary matrix ($U_{2\times2}$). This is used to transform the density matrix of the sources as it propagates through the PIM circuit and then the outcomes are post-selected to correspond a measurement. As most quantum computing or communication protocols can be expressed by an unitary transformation, the outcome of those implemented in an imperfect photonic circuit with practical HSPSs can be readily simulated using our method. Such possibility is envisaged (but not presented in this thesis) for the quantum teleportation protocol mentioned in Chap. 8 with a $U_{4\times4}$ with four independent HSPSs. This model can be further generalised by including losses after the HSPS for macro-optical circuits. Although Schmidt decomposition of HSPSs and unitary representation of quantum protocols are prolific in the literature, to best of our knowledge, the two have not been combined before as presented here.

The simulations performed in this chapter form the basis of the analysis of the experimental PIM data presented in the next chapters. These simulations are also used to design the future SOI HSPSs that improve both purity and brightness.

PART III

PIM circuits: experimental results

The experimental verifications of our designed PIM circuits are presented in the following two chapters. Chap. 6 details the first experimental demonstration of PIM with micro-ring resonator HSPSs (in any platform) fitted with the theoretical expectations. Chap. 7 describes experimental off-chip PIM with simpler waveguide HSPSs to achieve high purity and indistinguishable single-photons for multi-photon experiments.

Chapter 6

On-chip PIM with micro-ring resonator sources

Contents

A large-scale quantum photonic circuit, such as modular cluster state generation [18] for quantum computing, requires an array of indistinguishable SPSs. Indistinguishability between two SPSs is measured (i.e. PIM) by interfering the single-photons generated from them. PIM has not been performed on micro-ring resonator HSPSs in SOI or any other platform, despite the fact that the resonant enhancement in the resonator naturally offers spectrally purer and brighter heralded single-photon generation (Sec. 5.1.2). An on-chip PIM also paves the way for future scalable on-chip indistinguishability measurements among many HSPSs. As shown by the cartoon diagram Fig.6.1, the primary goal of this

chapter is to estimate the degree of indistinguishability between the micro-ring resonator HSPSs by using on-chip PIM. Also, we will quantify the effect of spectral purity and multi-pair contribution on PIM and compare with our numerical predictions of Sec. 5.2.1.

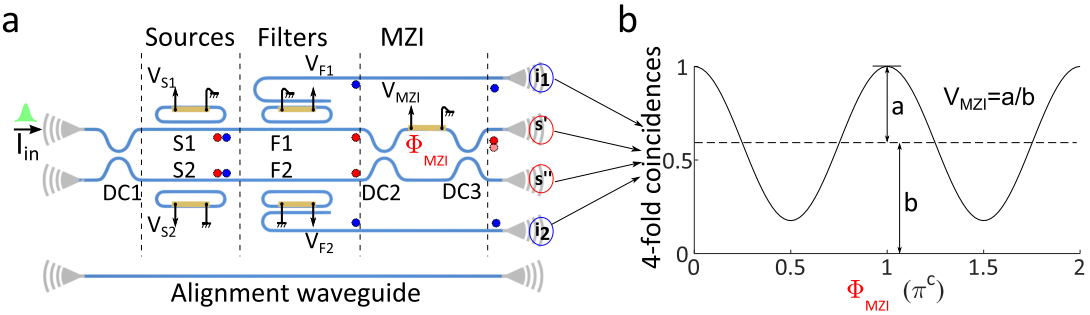

Figure 6.1: A cartoonish depiction of the final outcome of an on-chip PIM. (a) Signal and idler photon-pairs are generated in HSPSs S1 and S2, signal and idler photons are separated by on-chip filters F1 and F2, signal photons from both sources are interfered in the on-chip MZI. (b) The heralding idler photons from both sources (i_1, i_2), and the outcomes of the interference (s, s') are recorded as 4-fold coincidence (P_{4F}) as a function of the MZI phase, Φ_{MZI}. The visibility V_{MZI} of the P_{4F} fringe is directly related to the source indistinguishability as described in the last chapter.

IME01 RF design and IME03 RF design are the two circuits implemented specifically for on-chip PIM (Sec. 4.4). DTU-tele was the third design which is reconfigured for the on-chip PIM. Setting up a PIM requires two particular preparations: building the optical setup and determining the operating configurations. The optical setup is briefly introduced in the next section and the details are in App. B.

Each PIM requires the circuit elements to be configured (e.g. spectrally aligned) which are called the *Operating Points*. Operating configurations or operating points is a technical term often used in electronics. It refers to the different settings of the reconfigurable elements, such as a transistor's gate voltage, to perform a particular experiment. A PIM circuit with more than one micro-ring resonator cavities has non-trivial operating points set by the voltages on the thermal phase-shifters. The determination of the operating points of the PIM circuit is inextricably related to the experimental considerations related to the optical setup. In the forthcoming sections, at first, the classical characterisation method of the operating points of the PIM circuit is explained. Next, the effects of experimental considerations on the operating points are discussed. Finally, the on-chip PIMs with only IME01 RF design chip and DTU-tele chip are presented with closing remarks.

6.1 The optical setup

All the experiments presented in this chapter and the next share a common experimental assembly. The one used for IME01 chip is shown in Fig. 6.2. It has three major constituents:

① A *Nanomax* stage (*Thorlabs*) which holds an angle bracket that holds the optical fibre array to couple light in/out of the chip.

② The *chip holder* where the chip sits. At the top of the chip-holder sits a Peltier to control the temperature, and on top of that the Printed Circuit Board (PCB) where the chip is attached with thermally conductive glue.

③ The *PCB* facilitates the electrical connection between the chip and the driving electronics. The on-chip thermal phase-shifters for MZI and micro-ring resonators are

connected by gold tracks to the on-chip bond-pads. The electrical connections from the PCB are then wired to the electronics (Qontrol System PLC). The electronics control the electrical powers dissipated by the thermal phase-shifters.

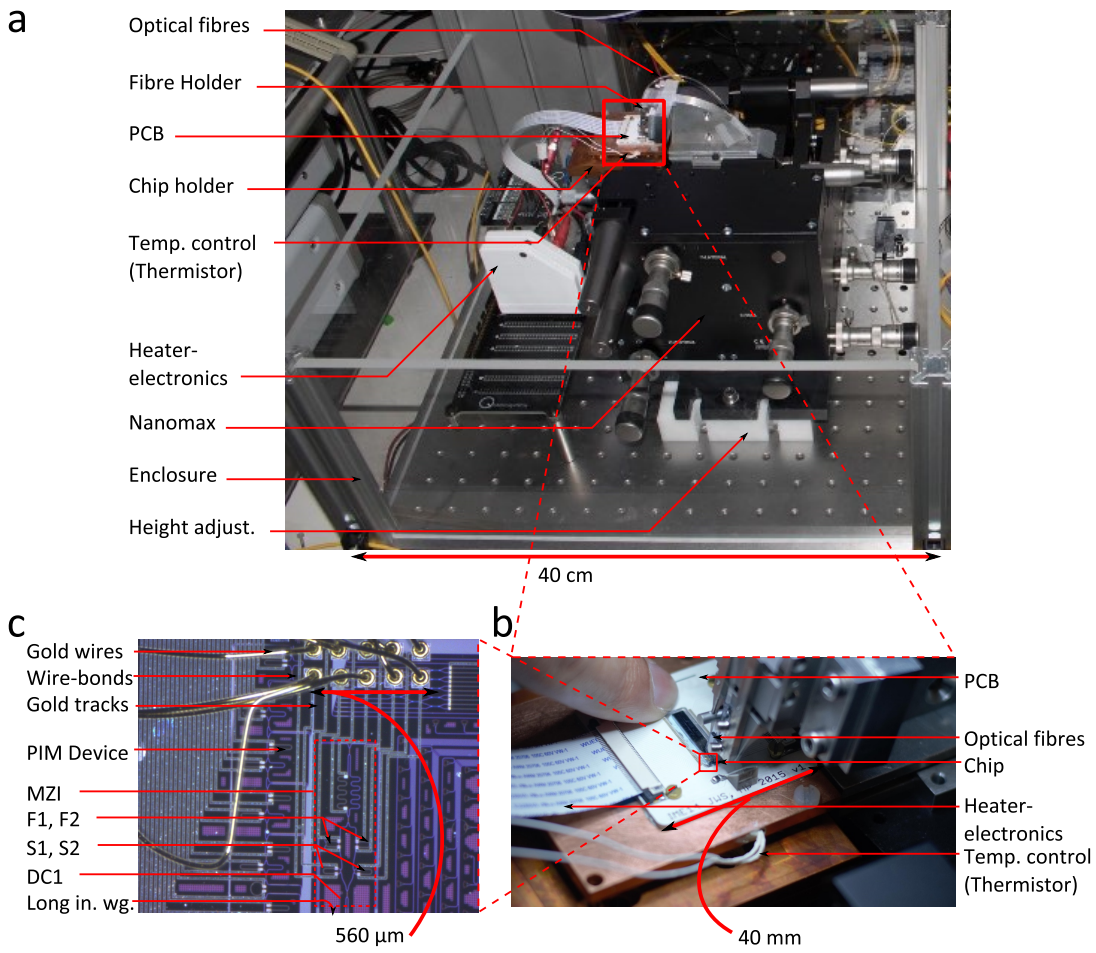

Figure 6.2: Optical setup for the PIM experiments. (a) The *Nanomax* stage and the *chip holder* labelled with the relevant parts of the setup. (b) The PCB, optical fibre arrays and electronic connections from the chip. (c) A zoomed photo of the PIM circuit in the IME01 chip showing different photonic components and gold wire-bonds of the IME01 RF design.

Once ① the Nanomax stage and ② the chip-holder heights are adjusted, and the correct ③ PCB is glued to the chip according to the chip dimensions, then the optical ports—vertical grating couplers (VGC) are aligned with the V-groove fibre array. The optical alignment procedure is elaborated in App. B.

6.2 Operating configurations of the PIM chip

One of the perks of a quantum photonic circuit is that the operational configurations of the circuit can be determined with classical laser light. A classical measurement requires relatively commonplace equipment such as a continuous wave laser and optical power meters. In addition, a classical measurement is much quicker than a quantum measurement which requires more time to accumulate single photons. Here, the task is to tabulate the operating points of the PIM circuit using classical measurement techniques. For our experiment, these are the voltages applied on the thermal phase-shifters (Fig. 6.1) for spectral alignments of all the different components in the photonic circuit. The alignments are performed by only looking at the spectral response from the MZI outputs (s', s'') of the

photonics circuit while using the electronics to control the thermal phase shifters. The simulations of the spectral response of our circuit (Sec. 4.3), helps us in anticipating the measured response.

The first experimental step is to measure the insertion loss of the photonic chip. By measuring the total loss along a very short waveguide, the insertion loss of the Vertical Grating Couplers (VGC) is determined. The insertion loss at each VGC for the IME01 chip is about $-4.5\ dB$ (transmission $\sim 36\%$), while for the DTU chip is about $-1\ dB$ (transmission $\sim 80\%$). A precise measurement of this value is required to correctly estimate the power inside the HSPS while measuring brightness (in Sec. 6.4.1).

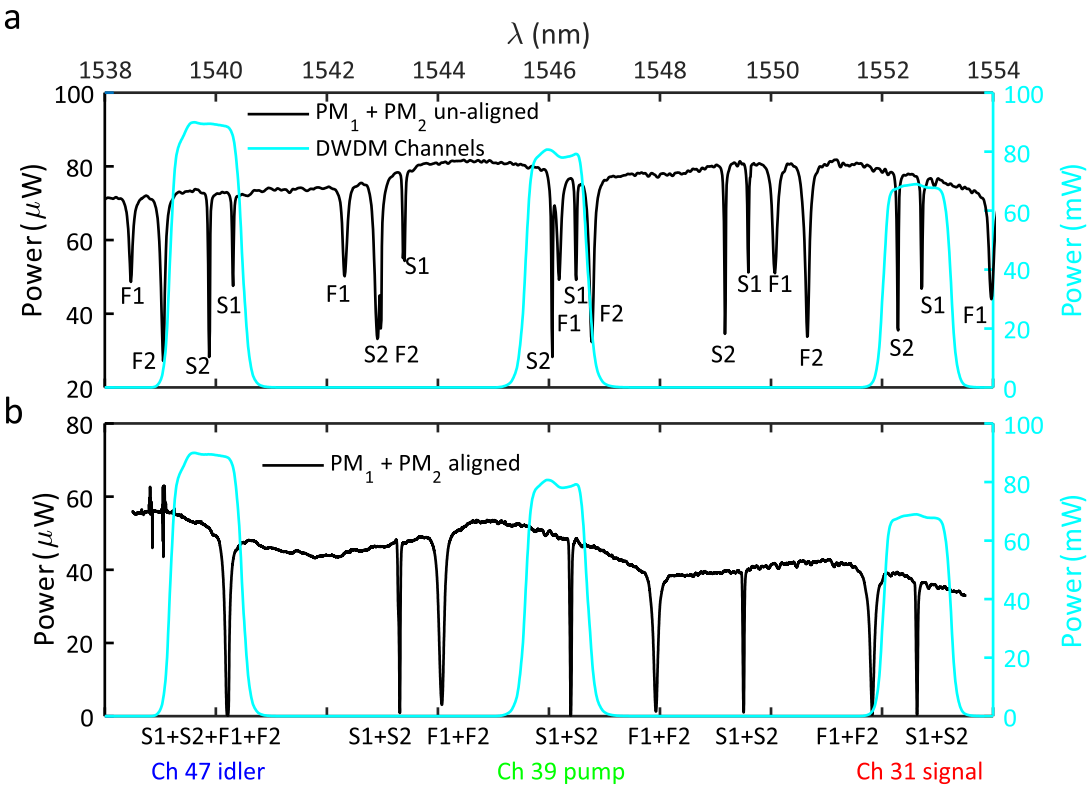

Figure 6.3: Classical characterisation and operating configurations of the PIM circuit. (a) The non-tuned spectra of the source (S1, S2) and filter (F1, F2) resonators. (b) Operating points of the resonators for $\Phi_{MZI} = 0$ ($V_{MZI} = 0.36\ V$), superposed with the DWDM filter spectra. Ch 47, 39 and 31 represents idler, pump and signal photons channels respectively. For our experiment, the operating points refer to the alignment of all the resonances as shown in the figure.

To measure the spectral response, a tuneable wavelength CW laser is injected into the input optical port (I_{in}) of the chip (Fig. 6.1). The light from the MZI output ports (s', s'') are recorded by power-meters PM_1 and PM_2 respectively. Plotting PM_1 and PM_2 while scanning the wavelength of the CW laser forms the spectral response of the chip. The spectral responses of the IME01 RF design circuit, as shown in Fig. 6.3 (a) & (b), are obtained by adding the power-meter values ($PM_1 + PM_2$). That makes the variation of the MZI phase indifferent due to the energy conservation (before and after the MZI), and avoids any unwanted phase effect on the resonator spectra. The responses show that the micro-ring resonator HSPSs are easily identifiable due to their narrower line-widths compared to the filter micro-ring resonators.

The free spectral range (FSR) of our micro-ring resonator HSPSs and filters are designed to match the spectral responses of our pump rejection filters (*Opneti*). These filters sup-

press the noise floor of the pump leakage or any stray photons, at signal-idler wavelengths, to single-photon level ($\sim 120\ dBm$ extinction). That helps achieving high signal to noise ratio ($SNR > 50\ dB$ for non-adjacent channels) for the generated signal-idler photons at the cost of reduced brightness ($\sim 3\ dB$ insertion loss). The different channels of these filters follow spectral responses centred based on the ITU grids. The channels 47, 39 and 31 are chosen respectively for idler, pump and signal photons for our experiment. The spectral response of these channels are superimposed on the spectral response of the PIM circuit (Fig. 6.3 (b)) to check the alignments of the resonators. The resonators are aligned by applying voltage across the heaters. Therefore, the operating points are the voltages on the heaters of the two source micro-ring resonators and two filter micro-ring resonators. For the configuration shown in Fig. 6.3 (b), these values are tabulated in Tab. 6.1.

$V_{S1}\ (V)$	$V_{S2}\ (V)$	$V_{F1}\ (V)$	$V_{F2}\ (V)$
0.35	1.82	3.28	2.97

Table 6.1: Operating points for IME01 PIM chip

6.3 Experimental considerations

As the PIM circuit is optically aligned and the operating points for PIM are determined, the next step, to perform actual PIM appears to be straightforward. In actuality, micro-ring resonators are well known for their use as sensors. The resonators, being cavities, are very sensitive to surrounding environment. Therefore, due to the surroundings, they can be also unstable while performing long experiments. Nevertheless, the enhanced optical field and high single-photon brightness in the cavities make them a suitable choice for quantum applications. Our naive expectation is that these two cavities are stable enough to emit heralded photons which are sufficiently indistinguishable with respect to each other so that we can do PIM. The challenges to stabilise the resonators in the PIM, also turned out to be physics worth exploring.

A few of these experimental considerations involved understanding the basic cavity physics, which is influenced by the surroundings (e.g. temperature instability, thermal cross-talk etc), as explained in the coming sections. Additionally, as this was the first 4-fold coincidence measurements in our laboratory involving SOI and Superconducting Nanowire Single Photon Detector (SNSPD)s, there were technical considerations (e.g. four-fold coincidence logic unit) which are also briefly discussed.

6.3.1 Thermal stability

Thermal instability is one of the major problems in a photonic circuit containing a cavity or certain interferometric structures. It can make the resonance of the ring resonator shift more than a line-width for a high quality factor cavity ($Q > 10^5$ at $1550\ nm$ wavelength). It can also introduce a large phase accumulation to the propagating light even if it is not on resonance with the cavity. Therefore, temperature fluctuation can erase any quantum correlation from the photons/qubits.

As can be seen from Fig. 6.4 (a), a laser is injected into our PIM chip, and then collected from the outputs of the MZI by PM_1 and PM_2, while a thermistor is used to monitor the temperature (T) of the chip. Figure 6.4 (b) shows the Lorentzian fit of the intensity of the resonator's response. This fit is used to estimate the phase response of the resonator. For our resonator the phase changes $\sim 2\pi$ from on-resonance wavelength to off-resonance

wavelength. If the resonance shifts with temperature, the phase $\Phi_{S1-S2}(T)$ will change rapidly. Figure 6.4 (c) shows that the MZI output intensities (PM_1 and PM_2) fluctuate and have strong correlations with the temperature fluctuations. As the thermo-optic coefficient of silicon is very high ($\Delta\lambda_{res} = 76\ pm/K$ as measured, in Fig. 6.5), a temperature fluctuation of $0.1\ K$ (fluctuation circled as **A**) can shift the resonance $7.6\ pm$ which is about $1/4^{th}$ of our resonator HSPS's linewidth ($30\ pm$). Thus, it can make the heralded photons spectrally distinguishable. Even, when the propagating light is off-resonance with the cavity, an accumulated phase difference ($\Phi_{S1-S2}(T)$ in Fig. 6.4 (b)) arises from a shifting cavity spectra.

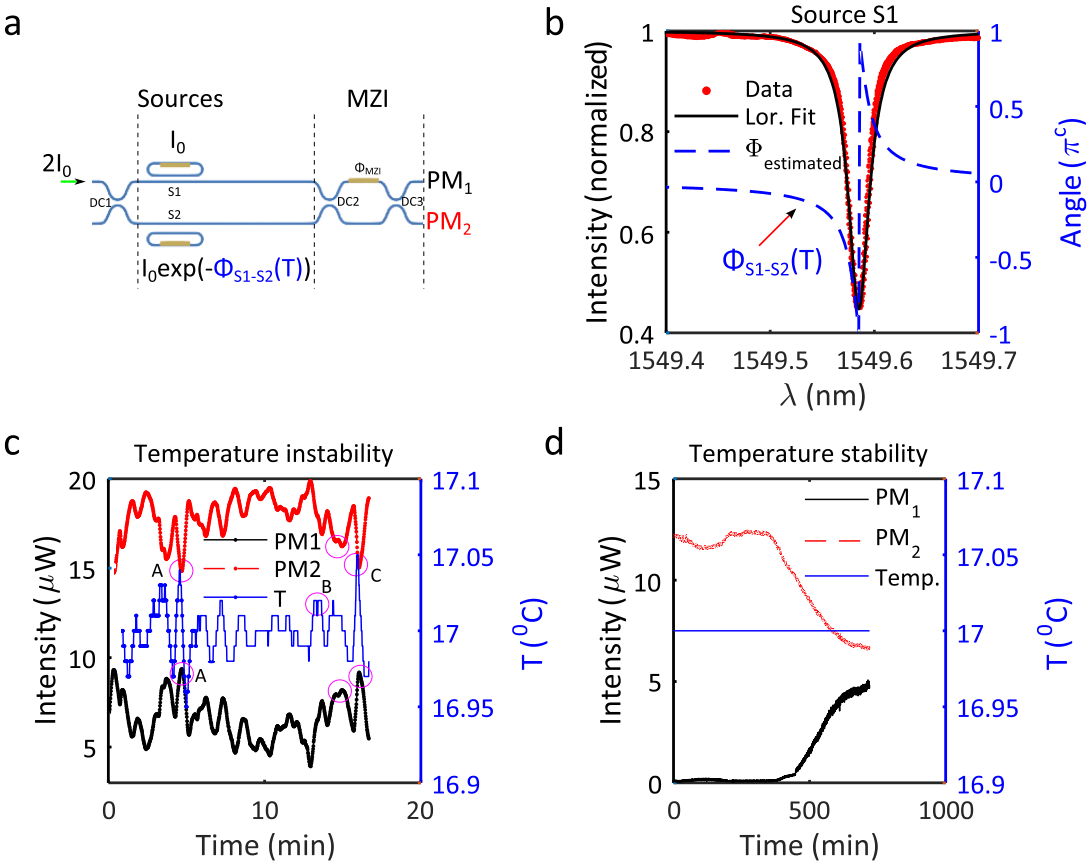

Figure 6.4: Temperature instability and unstable MZI outputs. (a) Detuning the filter rings and keeping only the source rings, the light passing through the path containing the source ring cavity S2 will obtain a phase $\Phi_{S1-S2}(T)$ with respect to cavity S1, depending on the temperature (T) of the cavity. Therefore $I_0 exp(\Phi_{S1-S2}(T))$ will interfere on the MZI with the reference light I_0 and fluctuate as the temperature fluctuates. (b) The estimated phases of the source cavities S1 and S2 have very sharp changes in phase across the resonance. (c) Temperature fluctuation monitored with a thermistor placed on the chip. Narrower cavity (Q$\sim$ 50000, FWHM$\sim$ $30\ pm$) causes very sharp phase ($\phi_{S1-S2}(T)$) change as a function of temperature T. The temperature (T) fluctuation of the cavity is strongly correlated with the MZI output power (PM_1, PM_2) as can be easily seen from the circled peaks A, B, C. Redesigning heat baths and ample thermal grease made (d) the temperature and the MZI outputs stable over 12 hours.

Figure 6.4 (d) shows temperature stability, which is obtained by using a high efficiency Peltier driven by a TEC, together with a large heat sink and a heat bath. A sample calculation on the mass of the heat bath and the placement of the temperature sensor is mentioned in the App. B.

6.3.2 Thermal crosstalk and operating points

In a photonic circuit, if there is a large heater (thermal phase shifter) present among multiple small heaters, then the heat dissipated by the large heater will start to influence the relatively small heaters (Fig. 6.5 (a)). That changes the state of the photonic component belonging to that small heater. This phenomena is termed as thermal crosstalk in this thesis. Thermal crosstalk is unavoidable in a photonic circuit containing cavities. Figure 6.5 (c), (d) shows thermal crosstalk on source ring-resonator heaters due to the large MZI heater in IME01 RF design chip. When the MZI heater dissipates heat from $0\ mW$ to $60\ mW$, the cavity spectra shifts about a linewidth ($30\ pm$) or more for our S1 and S2 HSPSs making them distinguishable in spectra. Therefore, thermal crosstalk affects the operating configuration of the PIM which requires recalculations that includes thermal crosstalk.

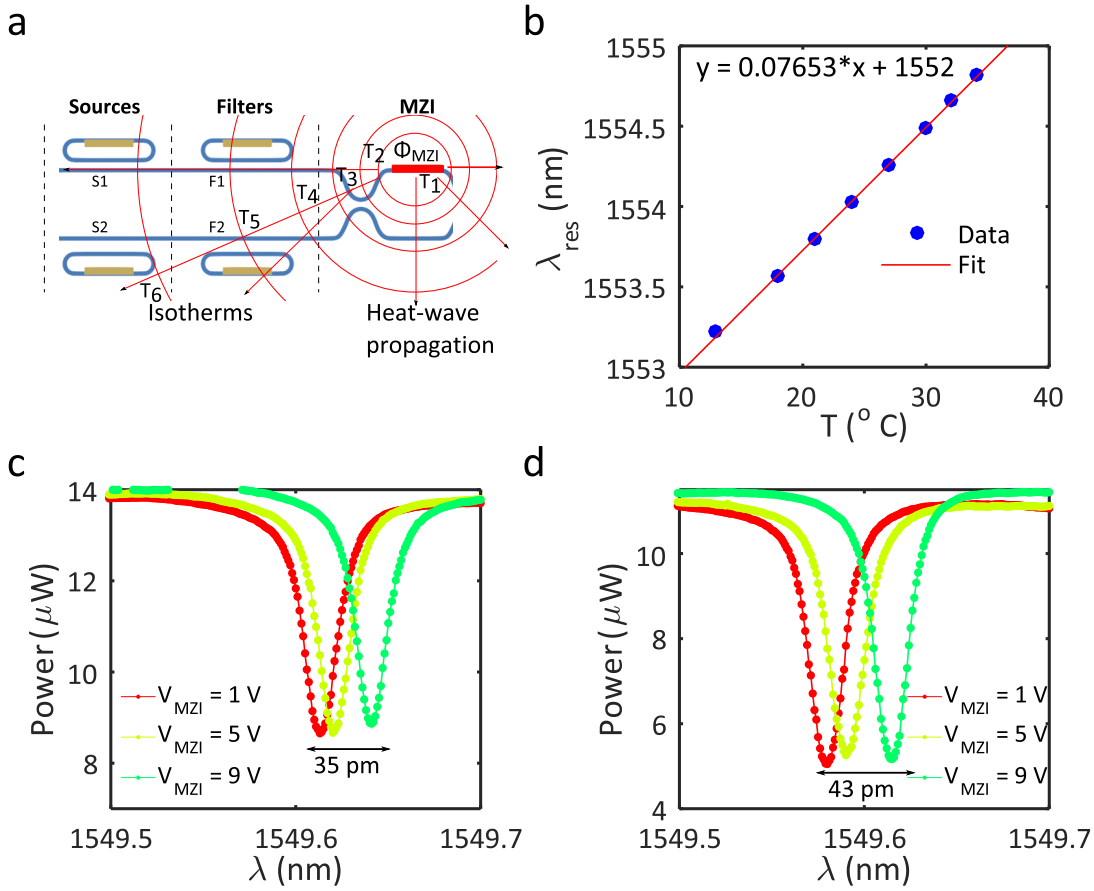

Figure 6.5: Thermal crosstalk among the MZI and high Q source-rings. (a) Heat propagation from the MZI heater to the rest of the circuit, which changes the spectral position of the resonant cavities. (b) The spectral resonance position shift per degree rise in the temperature. (c) λ_{res-S2} shifts about one FWHM amounts for $V_{MZI} = 10V$. (d) λ_{res-S1} shifts about $1.5\times$FWHM amounts for $V_{MZI} = 10V$.

One way to mitigate the thermal crosstalk is to develop a full thermal model of the chip as done by Dr Gary Sinclair and then apply a bisection algorithm for fine tuning. This approach is followed for IME01 chip. Alternatively, we can apply bisection algorithm from the very beginning to align all the resonances. This approach is followed for DTU-tele chip. Bisection algorithm is often used as a searching algorithm in computer programs and also in mathematics for root-finding. For determining operating points it is used as follows:

① The target spectral positions of the resonances are set as the response shown in Fig. 6.3 (b).

② For the maximal thermal crosstalk (MZI heater $\sim 60\ mW$), the voltage on the resonator S1 is applied to place it close to the target. If it is on the right side (V_R) of the target, the voltage is substantially lowered till we get the position to the left side (V_L) of the target. Averaging these two values of voltage, we choose a third voltage value which is closer to the target, bisection $V_b = \sqrt{(V_R^2 + V_L^2)/2}$. This procedure is reiterated until we reach the target. All the other resonators are used with the same method to get to the target.

③ The same technique is used for minimum thermal crosstalk configuration (MZI heater $\sim 0\ mW$).

④ All the other MZI phase configurations (operating points) in between are also set by using bisection algorithm using two nearest neighbouring points. For example, the phase in the middle of the maximum and minimum thermal crosstalk is determined by starting with considering maximum thermal crosstalk as V_R and minimum thermal crosstalk as V_L.

⑤ This nested bisection method carries on until all the resonances are aligned for all the MZI phase values.

A look-up table Tab. 6.2 (showing only three points here for simplicity) is used for operating points employed for the PIM at different configuration of the Φ_{MZI}. Bisection algorithm worked well as we have only one dominant heater (MZI). For a more complicated circuit, we may need a more sophisticated thermal modelling.

Φ_{MZI} (π)	V_{MZI} (V)	V_{S1} (V)	V_{S2} (V)	V_{F1} (V)	V_{F2} (V)
0	0.36	0.35	1.82	3.28	2.97
1	6.06	0.21	1.79	3.28	2.95
2	8.60	0.00	1.77	3.287	2.94

Table 6.2: Corrected operating points for IME01 PIM chip

6.3.3 Spurious four-wave mixing photon pairs

In a large photonics circuit, if photon pairs are generated through SFWM in parts of the circuit other than the HSPSs, then these are called spurious SFWM photon pairs. If the accumulated photon-pairs through spurious SFWM amounts more than the photon-pairs from the HSPSs, then, the expected quantum correlation in any measurements including PIM can be altered. Our micro-ring resonator ($Q \sim 5 \times 10^4$) HSPSs are much brighter than the waveguide HSPSs as shown in Fig. 6.6 (d), and we would not expect the spurious SFWM to affect the measurements. Also, the waveguides generate photon-pairs in a very large bandwidth while the resonators generate in a very narrow bandwidth ($\sim 30\ pm$). If the photon-pairs are collected in a very narrow bandwidth then the contributions of the resonator HSPSs far exceeds the waveguides. In contrast, as in our experiment, we collect the photons in a large bandwidth ($\sim 1200\ pm$) set by the DWDM filters, the total accumulated spurious photon-pairs from the input waveguide or the circuit is comparable to the total photon-pairs from the resonators. Specifically, the IME01 designs have long input waveguides (Fig. 6.2) of length $\sim 730\ \mu m$. This can alter the outcome of a quantum experiment in a two-fold coincidence measurement.

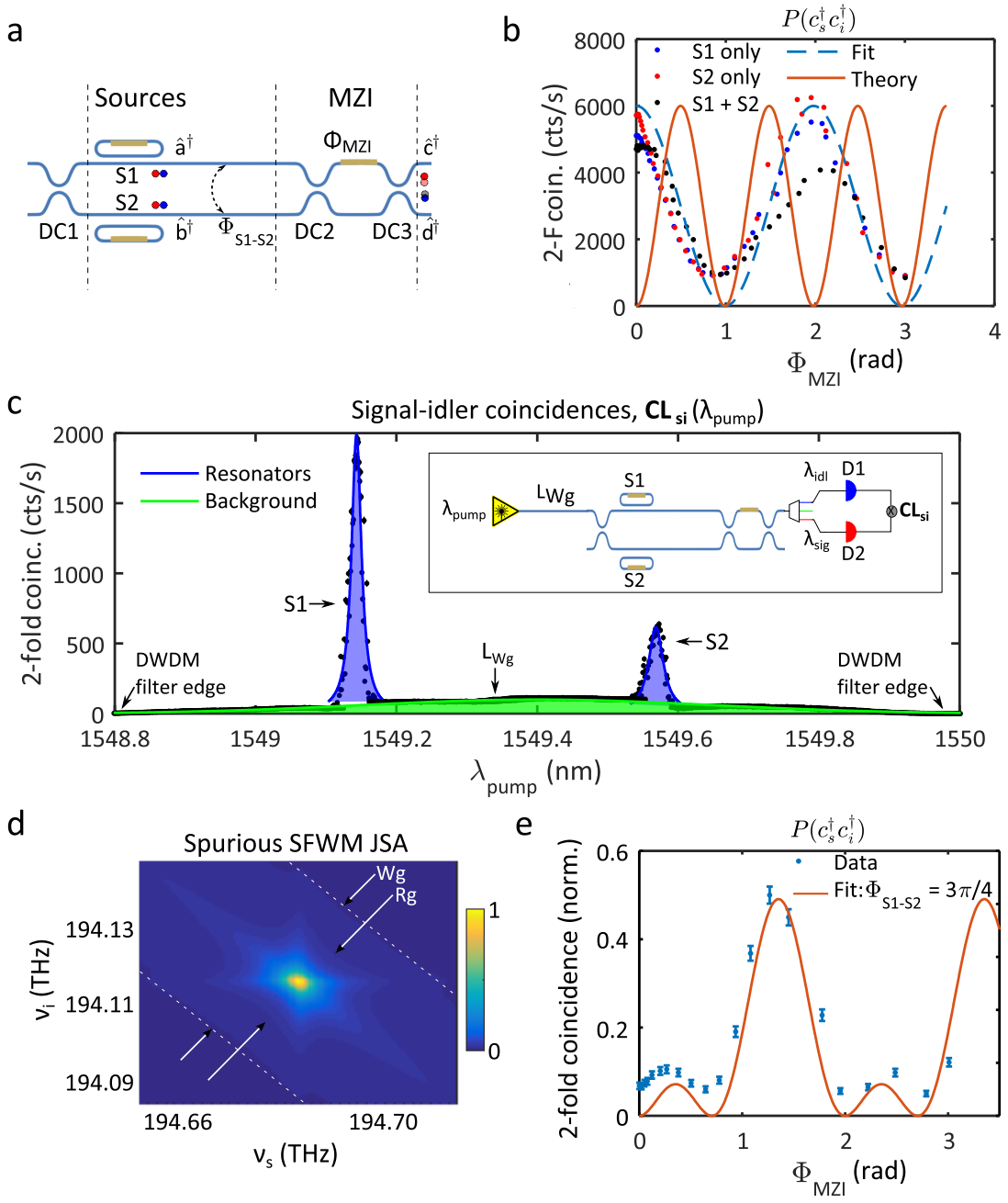

Figure 6.6: Bunching configuration and quantifying spurious SFWM. (a) The experimental setup for the measurements where the path entangled signal-idler photon-pairs from the S1 and S2 interferes. (b) Absence of any two-fold bunching ($P(c_s^\dagger c_i^\dagger)$) quantum correlation due to spurious SFWM. $P(c_s^\dagger c_i^\dagger)$ corresponds to detecting idler (blue) and signal (red) photons at output of c mode. (c) Quantifying the SFWM photon-pairs generated from the whole PIM circuit by varying CW pump wavelength λ_p. The inset shows the experimental setup. The long input waveguide ($\sim 730\ \mu m$) is responsible for most of the background (spurious) SFWM photon-pair generation. The ratios of the total coincidences from the HSPSs S1 and S2 to total backgrounds are $\frac{C_{S1}}{C_{BG}} = 0.34$, $\frac{C_{S2}}{C_{BG}} = 0.75$. These ratios can be improved by employing a tuneable bandwidth filter to narrow the pump pulse FWHM to **TF** with $200\ pm$. (d) JSA containing both resonator HSPS and the long input waveguide. The waveguide contribution is artificially weighted higher in this JSA for a better contrast. (e) Quantum correlation was recovered after employing the TF.

Figure 6.6 (a) shows the equivalent circuit of a 2-fold coincidence measurement which is affected by spurious SFWM. This circuit is obtained from Fig. 6.1 by detuning the filter resonators (F1 & F2). Considering low input pump power, signal-idler photon-pairs are generated by either in S1 or S2 at a time, forming a superposition. Following the notation introduced in Sec. 5.2.1, if the creation operators in source S1 and S2 are expressed by $a^\dagger$ and $b^\dagger$, then this superposition can be expressed by, $(a_s^\dagger a_i^\dagger + b_s^\dagger b_i^\dagger)|0\rangle$, with s & i denoting signal and idler. This superposition further propagates and interferes in the MZI. This is called the bunching configuration [154]. Considering a fixed phase difference (Φ_{S1-S2}) between S1 and S2 HSPSs, and following the same unitary transformation introduced in Sec. 5.2.1, the interference can be expressed as,

$$(a_s^\dagger a_i^\dagger + e^{i\Phi_{S1-S2}} b_s^\dagger b_i^\dagger)|0\rangle \xrightarrow{U} \frac{1}{\sqrt{2}}\big((U_{11}^2 + e^{i\Phi_{S1-S2}}U_{21}^2)c_s^\dagger c_i^\dagger + (U_{11}U_{12} + e^{i\Phi_{S1-S2}}U_{21}U_{22})(c_s^\dagger d_i^\dagger + d_s^\dagger c_i^\dagger) + (U_{12}^2 + e^{i\Phi_{S1-S2}}U_{22}^2)d_s^\dagger d_i^\dagger\big)|0\rangle \tag{6.1}$$

The probability of detecting signal and idler photons at the output c mode is denoted by $P(c_s^\dagger c_i^\dagger)$ and expressed by,

$$P(c_s^\dagger c_i^\dagger) = \frac{1}{2}|U_{11}^2 + e^{i\Phi_{S1-S2}}U_{21}^2|^2 \tag{6.2}$$

$$= \frac{1}{2}cos^2(\Phi_{MZI}) \tag{6.3}$$

In the last line, it is considered that $\Phi_{S1-S2} = 0$ and the MZI is perfect. If the photon-pairs are not generated by S1 and S2, then we will only get single-photon interference expressed as,

$$P(c_s^\dagger c_i^\dagger) = \frac{1}{2}cos^2\left(\frac{\Phi_{MZI}}{2}\right) \tag{6.4}$$

This shows that the interference period halves for a single-photon interference. The experimental data in Fig. 6.6 (b) has a fringe with half the frequency of the theoretical expectations. This is due to the strong contribution from the spurious FWHM which accumulates to the c output mode in much greater extent than the photon-pairs generated by S1 & S2.

Fig. 6.6(c) shows the quantification of the spurious background photon pairs. The generated signal-idler photon-pairs were collected by the signal-idler channels of the DWDM filters, while the CW pump wavelength is monotonically tuned across the pump channel of the DWDM. The photon-pairs generated at the resonant wavelengths of source S1 and source S2 are much higher than the spuriously generated photon-pairs in the input waveguide. In the scenario of accumulating the photon-pairs in the whole bandwidth of the DWDM channel (not just the resonant wavelength) by our wavelength insensitive SNSPDs, the ratio of the pairs generated in the waveguide (C_{BG}) is comparable with the pairs generated in the rings (C_{S1}, C_{S2}). For the data shown in Fig. 6.6(b), $(C_{S1} + C_{S2})/C_{BG} \approx 1$. In actual experiments, we use a pulsed laser to generate photon pairs, and can produce a plot very similar to Fig. 6.6(b), but using a tuneable bandwidth filter to select a $50\ pm$ (lower limit of the filter) chunk of the pump laser spectra each time.

This effect was mitigated by spectrally narrowing the pump pulse to match just the resonance linewidth. That lengthens the pump pulses in time and results in lower peak power to decimate the spurious SFWM significantly in the input waveguide. We could not narrow the linewidth arbitrarily as we know that (Sec. 5.1.2) to achieve a higher purity heralded photons, the pump spectrum needs to be flat at the resonances. In our PIM experiment of $30\ pm$ line width ring resonators, we used a $200\ pm$ bandwidth input filters for the pump. That keeps the heralded photons' purity high while reducing the spurious SFWM in the input waveguide to negligible amounts such that we recovered the bunching

effect shown in Fig. 6.6(e). The recovered fringe has the expected double period but distorted as the phase $\Phi_{S1-S2} = 3\pi/4$ is fixed in our photonic circuit and the reflectivity of the directional coupler was $\eta_{DC} \sim 40\%$.

Using TF to narrow the pump spectra is better than using spectral filtering (to discard spurious SFWM) at the end of the circuit for two reasons. The first is that the insertion loss of the filters at the input is counteracted by increasing the pump power. The second is that it reduces the SFWM in the waveguide in the same signal-idler spectra of the resonator, which cannot be separated by the output spectral filters. Also, spurious SFWM photon-pairs are generated in different parts of the circuit and therefore uncorrelated in time. As we increase the degree of coincidence from 2-folds to 4-folds, the effect of spurious SFWM becomes negligible or easily filtered out by post-selection.

6.3.4 Four-fold counting logic

As the experiment mentioned here was the first four-fold counting events experiment in our laboratory with silicon photonics sources, the counting logic system had to be built to extract four-fold event data registered by the single photon detectors. There were two major issues to resolve: ① the superconducting nanowire single photon detectors' (SNSPD) output signal compatibility with the counting logic system and ② extracting four-fold events from the accumulated time-to-digital data of the photons. Figure. 6.7 shows the outputs of the SNSPDs and their similarity with the NIM logic definition. The four-fold coincidences are extracted by modifying a software pre-existing in our group. These are elaborated in App. B.4.

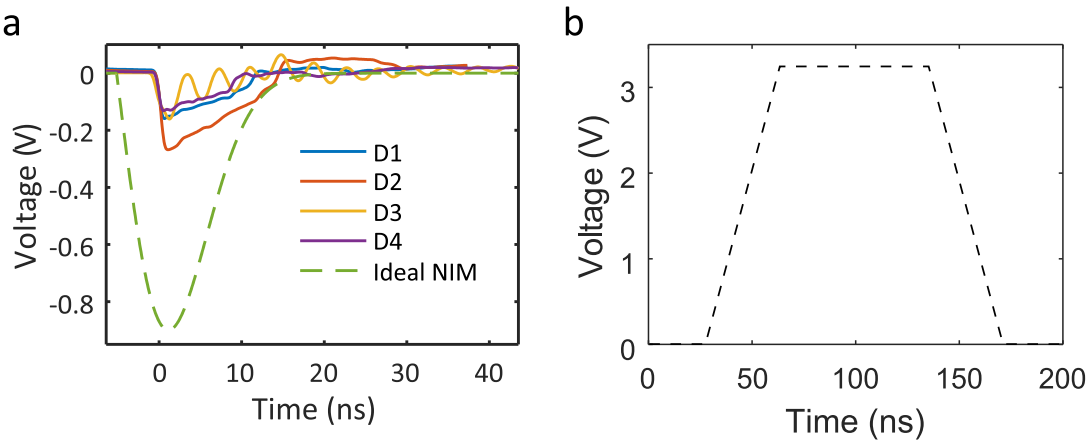

Figure 6.7: Stark contrast between NIM and LV-TTL logic levels. (a) Oscilloscope traces of the 4 SNSPDs used in the lab. It shows that the voltage levels of the detectors resemble NIM in shape but the peak voltage is 3 times lower. The ringing (oscillatory) behaviour of detector 3 shows two important things: first is the sensitivity of the low noise amplifier stage connections. The second is the need for special detection module called *Constant Fraction Discriminator* rather than LV-TTL level detections. This prevents double counting of the multiple peaks from the ringing. (b) A standard LV-TTL logic pulse is much broader and the peak voltage is positive and 3 times higher than the NIM pulses.

6.3.5 MatLab instrumentations

MatLab instrumentations has been used for all the instruments for computer control. It was necessary due to two major reasons: the previously existing C-codes for the instrumentations has lower fidelity of working when copied from one computer to the next,

and the time-tagger Hydraharp can be efficiently controlled together with all other instruments using a high level language such as MatLab. Among all the instruments, Hydraharp and the optical delay line were the more challenging ones to automate with other instruments.

6.3.6 Instrumentation mitigations

The experimental measurement described in the following sections has practical considerations that has been eluded to the performed simulations and the above discussions. These include imperfect measuring instruments.

Laser and wavemeter

A major error in measuring the classical spectra of our photonic chip was the error in absolute wavelength accuracy of the scanning laser. The sources and the filters we have used have linewidths of 30 pm to 100 pm, while the absolute wavelength accuracy of our laser is 200 pm and sensitive to the environmental temperature. That was mitigated using an wavemeter that measures the wavelength of the laser and corrects them. Later, the instrument CT400 in conjunction to the laser was used. CT400 has an acetylene gas cell inside it, which is used as a reference point to make the absolute accuracy of the laser within 2 pm.

Electronic Control of the thermal phase-shifter

One of major source of imperfections in relevant instrumentations is the electronics, that supply electrical current to the thermal phase-shifter or electronic heaters. By applying different electrical currents (i.e. different heat dissipations→different phase), these heaters act as reconfigurable photonic elements. The practical heater driver that we used has a certain accuracy/resolution in delivering the voltage across that resistance. That makes the range of continuous tuning of the reconfigurability of a particular photonic component limited to $\sim 10\,mV$ accuracy. Moreover, these heater drivers do not have any feedback loop to read out the actual electrical power dissipation, leaving a gross error in estimating the performance (i.e. phase) of the heaters. We have found that, although, the nominal applied voltages by the electronic heater-board used in the experiments are different from the actual applied voltages, the margin of error is just sufficient to perform PIM. The details of this observation are in App. B.6.

6.4 On-chip PIM with micro-ring resonators

In the previous sections, all the experimental considerations were investigated to prepare the setup for quantum measurements. In this section a PIM will be performed. A comprehensive PIM analysis requires measurements of the brightness and the purity of the resonator HSPSs. These measurements benchmark our ring resonator HSPS, and predict the performance of the PIM. Therefore, this section begins with the brightness and the purity measurements, continues to PIM and finally discusses the results and the outlooks.

6.4.1 Brightness

As the HSPSs are integrated with other photonic components, the PIM circuit requires appropriate reconfiguration for a reliable brightness measurement. In addition, the aforementioned experimental considerations non-trivially arranges the off-chip experimental

configurations. In this subsection, first, the experimental configurations for the brightness measurements will be discussed and then the results will be presented.

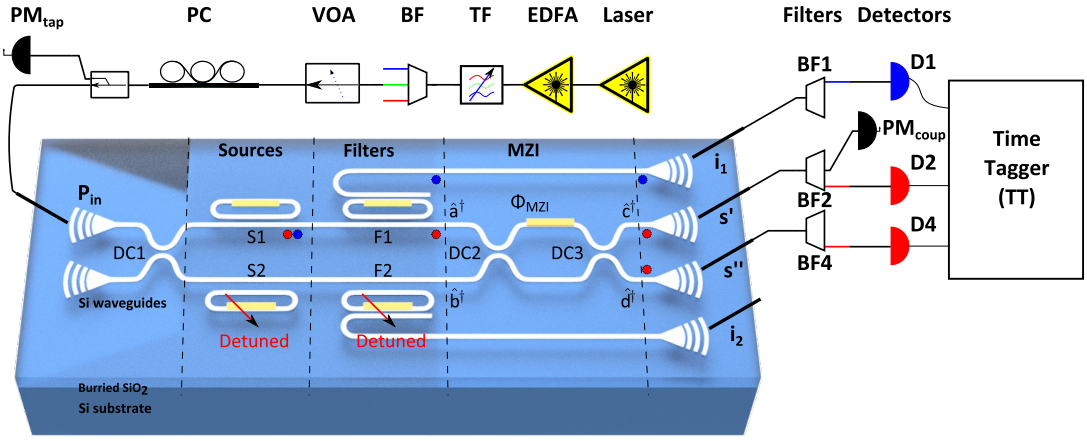

Figure 6.8: Experimental setup to measure resonator HSPS brightness of the IME01 chip. To measure the brightness of source S1, only filter F1 is tuned to separate the idler photons, while both source S2 and filter F2 are detuned. EDFA: Erbium Doped Fibre Amplifier, TF: Tuneable bandwidth Filter, BF: Broad band Filter, VOA: Variable Optical Attenuator, PM: optical Power Meter, D: single-photon Detectors.

Experimental setup

The off-chip experimental arrangements starts with a 50 MHz repetition rate input pump laser (Pritel), as shown in Fig. 6.8. The pump wavelength is spectrally tuned to Ch 39 (1546.12 nm) of ITU frequency grid using an Optical Spectrum Analyser (OSA) by measuring the wavelength. It is then passed through an EDFA to achieve the desired maximum pump power, followed by the tuneable bandwidth filter (TF). TF sets a bandwidth of $200\ pm$, which sufficiently narrows the pump spectrum but is about 7 times broader than the spectral width ($30\ pm$) of the resonances of source S1 and S2. Therefore, it limits the spurious SFWM from the input waveguide significantly (Sec. 6.3.3), while keeping the spectral purity high (Sec. 5.1.2). Then, two (only one shown in the figure) cascaded broadband filters (BF) limits the pump photon-leakage into the spectra of the generated photon-pairs. A variable optical attenuator (VOA) is used to adjust the desired optical power (P_{in}) injected into the chip. The light is then passed through a polarisation controller (PC) to control the polarisation and an 1% tap to monitor the input power to the PIM circuit. At this stage an average of $2\ mW$ input power of the laser is coupled into the photonic circuit (coupling loss $4.5\ dB$) with a suitable polarisation through the VGC.

The very left of the photonic circuit contains a directional coupler (DC1). It splits the input light with splitting ratio (η_{DC}, measured 60%) to pump source S1 and S2. Now, to avoid counting photon-pairs from both sources while measuring brightness of only one source, the other source is spectrally tuned off the pump spectrum. For example, to measure the brightness of S1, source S2 and filter F2 are spectrally tuned off the Ch 39. Only source S1 is aligned to the peak of the pump spectra in Ch 39 to generate SFWM signal-idler photon-pairs in the selected channels Ch 31 (1552.52 nm) and Ch 47 (1539.77 nm). The filter F1 is spectrally tuned to collect idler photons from Ch 47. The idler photons are coupled off chip with coupling loss $4.5\ dB \times 2$, cleaned by filter BF1 to further reject the pump, detected by the single photon detector D1 and herald the signal photons (Ch31). The signal photons are collected from both ports of the MZI, cleaned by filter BF2 and BF4, detected by single photon detectors D2 and D4. All the three detectors are con-

nected to a time-to-digital converter *HydraHarp* (from *PicoQuant*) to record the photons' arrival times. These data are post-processed to identify and sum the coincidence counts of signal-idler photon pairs generated by S1. Finally, the VOA is used to set a range of input powers P_{in}, and the coincidence counts at each power are collected. This data is plotted in Fig. 6.9 to estimate the brightness.

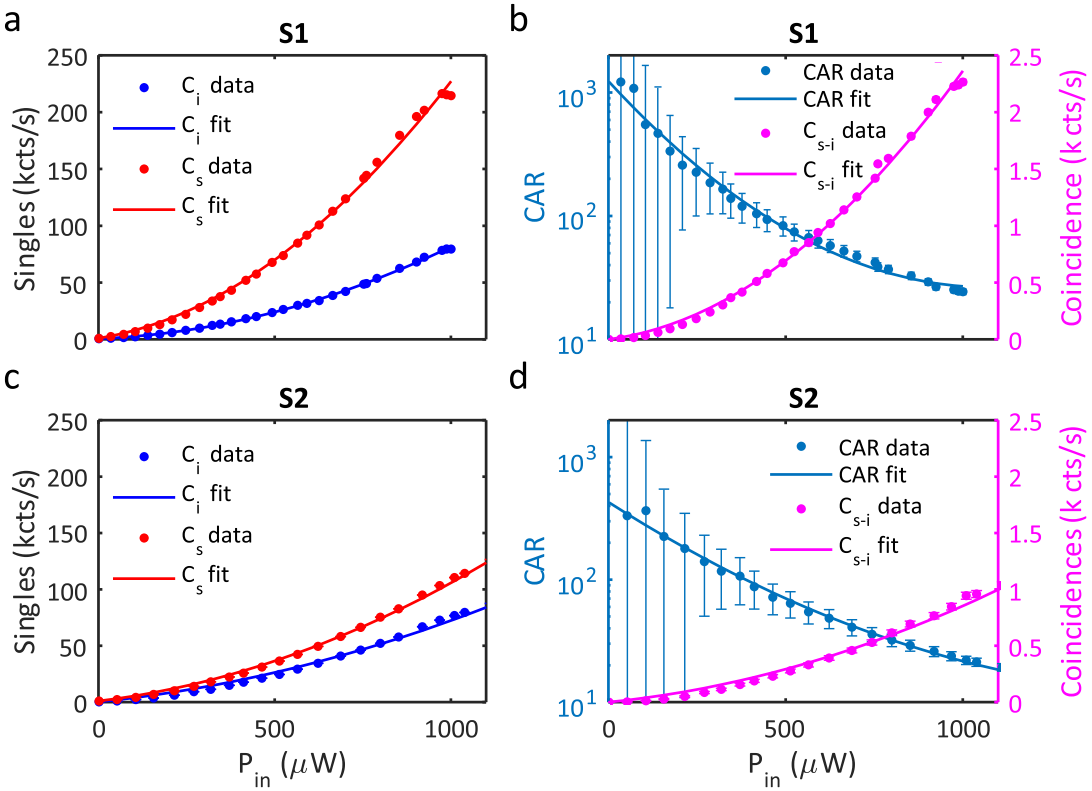

Figure 6.9: Brightness data of the resonator HSPSs of IME01 chip. (a), (c) represents the signal and idler singles counts from sources S1 and S2 resectively. (b), (d) represents the signal-idler coincidences, and the Coincidence to Accidental Ratio (CAR) for each sources respectively. Both sources achieved a CAR more than 10 even at the highest measured coincidence rate. The error-bars are calculated assuming Poissonian statistics.

Experimental results

Figure. 6.9 graphs the results obtained from the aforementioned experimental setup. Figure. 6.9 (a), (c) contains the singles counts from signal and idler photons, while (b), (d) contains coincidences and CAR (coincidence to accidental ratio) from sources S1 and S2 respectively. The data are fitted with the Eq. 2.16 from Sec. 2.2.1. The error-bars on the raw data are calculated assuming Poissonian statistics (e.g. error = $\sqrt{\text{counts}}$) and following standard error propagation methods.

As mentioned in Sec. 2.2.1, if the lumped efficiency of the four wave mixing process is γ_{eff} $(photon\text{-}pairs/s/mW^2)$, signal photons' channel detection efficiency is η_s, idler photons' channel detection efficiency is η_i, input power is P_{in} and repetition rate of the laser is R, then the average number of photon-pairs generated per pulse will be, $\bar{n} = \gamma P_{in}^2/R$ (Eq. 2.13). Our sources S1 and S2 have $\bar{n}_1 = 0.1003 \pm 0.01$ and $\bar{n}_2 = 0.123 \pm 0.01$ for $P_{in} = 1\,mW$ with 68% confidence interval as tabulated in Tab. 6.3.

There are a few points we can draw from these results:

① Table 6.4 compares the performance of our resonator with some of the best brightness values found in the literature. It shows that the brightness of our resonator has

Source	η_s	η_i	γ_{eff} $(Mcts/s/mW^2)$	$\bar{n}$
1	0.008	0.013	5.013	0.1003 ± 0.01
2	0.011	0.028	6.130	0.1233 ± 0.01

Table 6.3: Average photon number estimation of S1 and S2 of IME01 PIM chip.

similar figure of merit with the literature. It also shows that the brightness (γ_{eff}) crucially depends on the quality factor (Q) of the resonator: [38] (the best value reported so far) has about twice the Q than IME01-chip's Q, and the average power in the chip is about $1/17^{th}$ power ($59\ \mu W$ CW light) than our average pulsed power ($1\ mW$) in the chip, but it has achieved more than 30 times the brightness (value of γ_{eff}) compared to our results.

② The raw brightnesses (2-fold coincidence counts), of these two results, have only a factor of 2 difference. This emphasises the importance of having high efficiency VGCs, and good channel efficiency to the detectors, as they play more important role in actual practicality in performing a multi-photon quantum experiment. For example, with our raw brightness, we can expect a four-fold rate of,

$$\begin{aligned} CC_{4F} &= \eta_{s1}\eta_{i1}\eta_{s2}\eta_{i2}\bar{n}_1\bar{n}_2 R \\ &= 75\ cts/h \end{aligned} \tag{6.5}$$

This is much lower than a typical SPDC source of $200\ cts/s$ of four-folds with $\gamma_{eff} = 10\ Mcts/s/mW$.

Work	Power (μW)	γ_{eff}	Q	CC (k cts/s)	CAR	VGC (dB)
IME01	1000 (Pulsed)	5	5×10^4	2.265	24	4.5
[38]	59 (CW)	149 ± 6	9×10^4	4.869	532	3.5
[59]	700 (CW)	1.62 ± 6	1.5×10^4	–	500	2.5
[60]	– (CW)	–	5×10^4	–	12	10

Table 6.4: Comparing IME01 resonator HSPS's brightness with literature

The literature contain mainly the measurements of the brightness of the micro-resonator HSPS. Very few have reported spectral purity measurements: [55] measures the purity (0.97 ± 0.09) using stimulated four wave mixing process (StFWM) for a resonator HSPS with a Q of 4×10^4, similar to IME01 HSPS. There exists purity measurements such as [51] with scanning monochromators, but the margin of error is high due to high losses. In the next section, the purity measurements of IME01 HSPSs will be discussed .

6.4.2 Spectral purity

The purity of our micro-ring resonator sources can be measured in two very different ways: unheralded second order correlation function $g_{ii}^{(2)}(0)$ and using stimulated four wave mixing by measuring joint spectral intensity (JSI). The following experimental setup only discusses the purity estimated from the $g_{ii}^{(2)}(0)$. Then, the experimental results are presented and a comparison is drawn with a JSI (by StFWM) previously obtained in our group from a similar resonator in the same IME01 chip.

Experimental setup

The experimental setup for the purity measurement is very similar to the brightness measurement upto the injection of light into the chip as shown in Fig. 6.10. On the chip, to

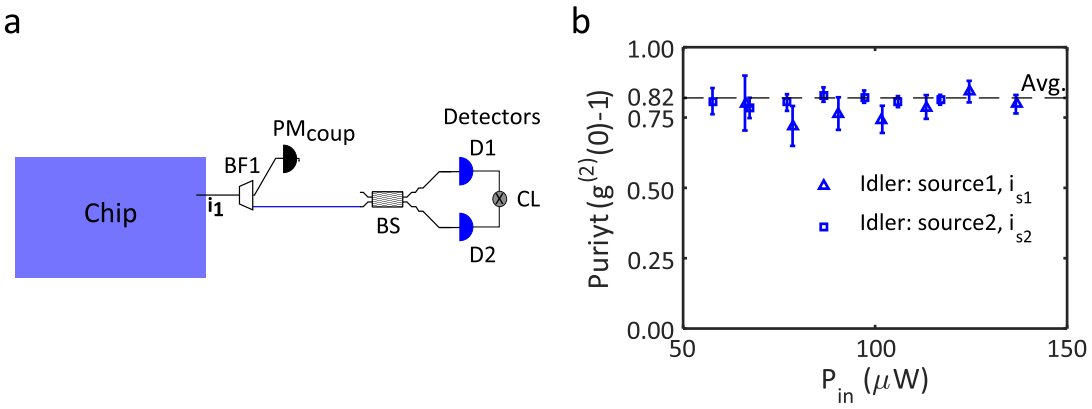

Figure 6.10: Spectral purity of the single photons are measured using self $g_{ii}^{(2)}(0)$ of idler photons. (a) The idler photons (i_1) from S1 is coupled out of the chip using F1, and then passed through a fibre beam splitter (BS with 50% reflectivity). The outcome from the BS is collected by detectors D1 and D2 connected to a coincidence logic unit (CL) for recording second order correlations. (b) Extracted purity vs input power shows that purity remains almost the same for a range of power, as expected. We did not measure purity for power lower than $58\mu W$ due to impractical integration time.

measure the spectral purity of source S1, only S1 is aligned to the pump spectra and filter F1 is aligned to collect the idler photons generated in S1. Once the idler photons are coupled out of the chip, they are incident on a fibre beam splitter (BS with 50% splitting ratio). The outcomes of the BS are collected by detectors D1 and D2 connected to a coincidence logic unit (CL) for recording second order correlation function $g_{ii}^{(2)}(0)$. The same way the $g_{ii}^{(2)}(0)$ of idler photons generated by source S2 is also measured.

In addition, the effect of the intensity of the optical input power on the $g_{ii}^{(2)}(0)$ due to any non-linear interaction has been investigated. The input optical power is varied over a $5\ dB$ range and the purity is estimated and plotted in Fig. 6.10 (b).

Experimental results

The purity of the sources has been estimated by measuring the second order correlation function $g_{ii}^{(2)}(0)$ of the idler photons from each source, and using the relation [30], purity $P = g_{ii}^{(2)}(0) - 1$ (Sec. 2.2.4). Figure 6.10 (b) plots the estimated purity values for both sources S1 and S2 as a function of the input optical power. The figure shows that the purity values of both of the sources are about the same irrespective of the input power. It suggests that the purity values are not affected by the non-linear interactions of the pump power in our range of interest. Using Schmidt decomposition, we can estimate the relative strength of the squeezers (Fig. 6.11 (c)). This plot shows that using effectively two Schmidt modes for each of our sources is a reasonable approximation for PIM simulation to match the measurements mentioned in the next section.

For our operating power, the estimated purity for both sources are $P_{S1} = 86.20 \pm 3.89\%$ and $P_{S2} = 78.69 \pm 2.44\%$. These values are lower than our expectation of 92% as predicted by the simulation (Sec. 5.1.2) for IME01 HSPSs. There is no other value in the literature that use $g_{ii}^{(2)}(0)$ to estimate the purity of a micro-ring HSPS in SOI. A value of micro-ring resonator in silicon nitride shows a $g_{ii}^{(2)}(0) = 2.0 \pm 0.11$ with high margin of error [54]. The only other value found in the literature ([55]) for SOI is obtained through StFWM process. In the next section, we compare the StFWM and $g^{(2)}(0)$ methods.

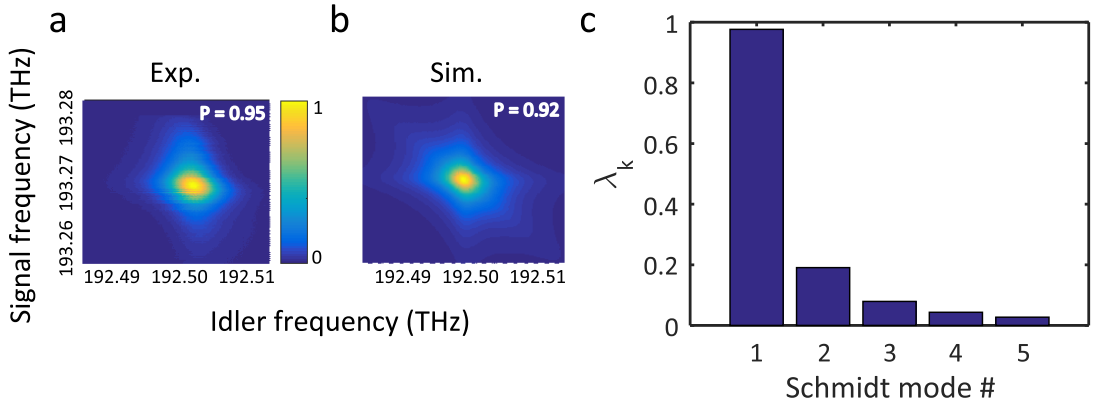

Figure 6.11: The relative strength of squeezers vs the k^{th} optical mode for multimode squeezed state obtained from simulation. (a) Experimentally estimated JSI using stimulated four wave mixing. (b) Theoretical JSA considering the linear theory (Sec. 5.1.2). (c) The relative strength of the Schmidt modes that corresponds the simulated JSA showing the strength of the primary mode.

Estimated purity from $g^{(2)}(0)$ vs simulations

Considering the general expression of the JSA (Sec. 5.1.2) for our pump pulse (secant hyperbolic) and micro-resonator, we numerically calculated the JSA as shown in Fig. 6.11 (b). The simulation predicts a purity of 0.92. Using stimulated four wave mixing we also experimentally estimated the joint spectral intensity (JSI). This experiment is performed using pre-existing codes and setup in our group on a resonator in the IME01 chip as explained in App. B and presented in Fig. 6.11 (a). The purity ($P = 0.95$) estimated from the average of 16 JSI measurements is an upper-bound, as it does not include the phase correlations of the photon-pairs.

Knowing the purity of the HSPS is crucial, as it predicts the PIM between two HSPS. The $g^{(2)}(0)$ results provides an prediction of the maximum indistinguishability between these sources as $82.36 \pm 2.25\%$ by using Cauchy-Schwarz inequality, $tr(\hat{\rho}_{s1}\hat{\rho}_{s2}) \leq \sqrt{tr(\hat{\rho}_{s1}^2)tr(\hat{\rho}_{s2}^2)}$. In contrast, the StFWM results predicts an indistinguishability of 95%. Obviously, only one of these measurements is closer to the actual purity of the resonator HSPS. The following can be inferred from our observations:

① The result from the StFWM experiment is very close to both the results reported in [55] and the performed simulation. That indicates that the IME01 resonators are of very high purity. In contrast, the simulations (Sec. 5.1.2) do not include any non linear effects inside the resonator. We know that the strong non-linearity of the silicon causes non-linear losses (e.g. two-photon absorption) or phase correlations (e.g. cross-phase modulation). If these non-linearities are included in the simulation, it may result in a lower purity.

② Due to the same reason, some [51] criticised StFWM process in measuring the purity of a resonator HSPS, as the added non-linearity due to the stimulation process inside the cavity can alter the JSA.

③ The simulations in Sec. 5.1.2 shows that the JSA can hide details of the mode structure for an over-coupled resonator. For example, if the ring is over-coupled, a split resonance due to the back-reflected mode can be hardly seen from the JSA, resulting in the appearance of a high purity.

④ The $g^{(2)}(0)$ measurements are also not devoid of criticism to measure purity of a resonator HSPS. As the relation $P = g^{(2)}(0) - 1$ holds specifically when the squeezing

(or average photon-number generated per pulse) is low. Inside a high Q resonator, due to the field-enhancement, that relation may not hold. If the total optical gain is very high, then the $g^{(2)}(0) = 2$ always as shown in Fig. 2.7 (f).

⑤ In addition, $g^{(2)}(0)$ implies the purity from the photon's arrival-time statistics of a 2-fold measurement. Noise, such as spurious four wave mixing, can easily alter that statistics, as noisy photons usually have much lower purity (Fig. 6.13 (c)). We suspect the latter happened specifically with the $g^{(2)}(0)$ measurements of the DTU-tele chip. Here, we assumed that the Raman noise in silicon has not affected our measurement as the Raman gain is about $15.6\ THz$ away from the pump with a bandwidth of $105\ GHz$ [152].

The PIM result strongly depends on the purities of the HSPSs. Therefore, the best way to measure the purity and settle the contradiction is to do a PIM.

6.4.3 Indistinguishability: PIM

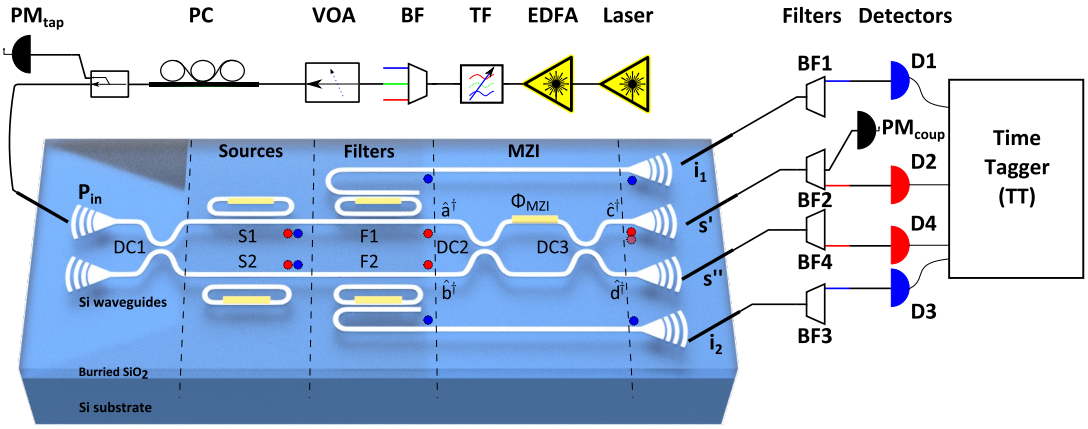

Figure 6.12: The experimental setup contains a laser which passes through a broadband filter (BF), a tuneable bandwidth filter (TF) and a polarisation controller (PC) and then coupled to the photonic circuit. The photonic circuit consists of a directional coupler (DC), micro-ring resonator sources S1 and S2, micro-ring filters F1 and F2, MZI composed of DC with reflectivity η_{MZI} (ideally $\eta_{MZI} = 50\%$). Photon-pairs generated by the sources are coupled off-chip and filtered (BF1 to BF4) and collected by single photon detectors (D1 to D4) connected to coincidence logic unit (HH).

Experimental setup

The experimental PIM setup is the same as the brightness and purity setups up to the coupling of light into the chip. The main difference in the chip is that for this measurement all four resonators S1 & S2 and F1 & F2 are aligned.

The leftmost part of the PIM circuit contains a directional coupler which splits the light coupled into the chip to pump source S1 and S2. Both sources are aligned with the pump spectrum such that resonantly enhanced SFWM produces signal-idler photon pairs in Ch31 (1552.52 nm) and Ch47 (1539.77 nm) of the ITU grid. The micro-resonator add-drop filters Φ_{F1} and Φ_{F2} are only resonant with the idler photons (Ch47) and therefore separate the idler photons through the drop port. Subsequently, the idler photons are coupled off the chip with coupling loss $4.5\ dB$ of each channel, cleaned by filter BF1 and BF3 to reject the pump, detected by single-photon detectors D1 and D3 and herald the signal photons (@Ch31).

After the MZI interference the signal photons are coupled off-chip (coupling loss $4.5\ dB$ each channel), filtered (BF2, BF4) to reject the pump and couple to the single-photon detectors D2 and D4. All four detectors (D1 to D4: average efficiency 75%, dark counts $<$ 200 counts/s) are connected to a PicoQuant time-tagger (HydraHarp). The HydraHarp records the photons' arrival times which are post processed to identify four-fold coincidence events as heralded two-photon quantum interference as a function of MZI-phase (Φ_{MZI}).

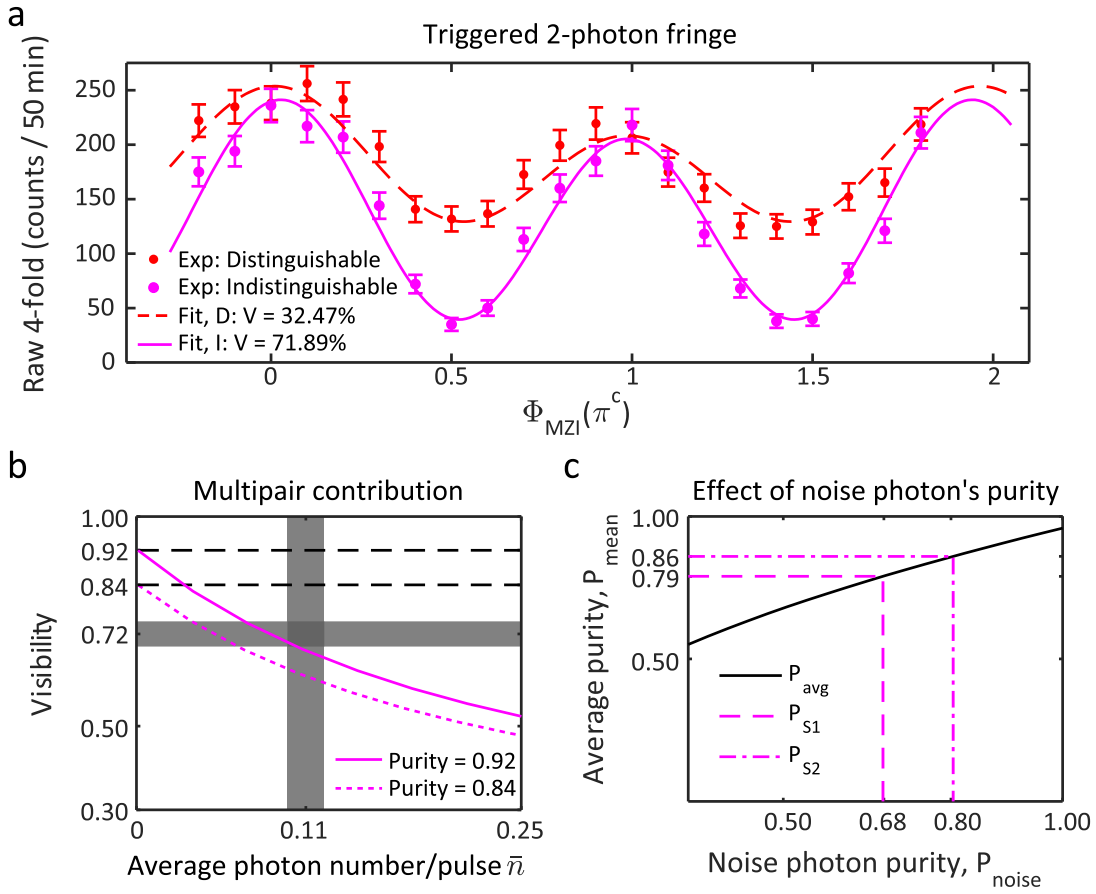

Figure 6.13: The PIM of micro-ring resonator HSPS. (a) The plot of 4-fold coincidences as a function of MZI phase Φ_{MZI}. The blue (red) events correspond to indistinguishable (distinguishable) photons with a fitted visibility of $72 \pm 3\%$ ($24 \pm 2\%$). (b) Placement of the measured visibility on the graph of the simulated visibility as a function of average photon-number per pulse. The graph shows that within the measurement errors of average photon-number, and the estimation error of the visibility, the PIM agrees more with the HSPS purity value of 92%. (c) The effect of mixing impure noise photons with the photons generated by resonator HSPSs. Considering the highest purity of resonators (0.92), the mean purity, $P_{mean} = \sqrt{0.92 \times P_{noise}}$. Purity estimated from the $g^{(2)}(0)$ implies a noise photon purity between 0.68 and 0.8 which is possibly generated in the waveguides.

6.4.4 Results: PIM in relation to purity and brightness

Figure 6.13 (a) plots the measured 4-folds as a function of MZI phase Φ_{MZI}. The magenta events correspond to the indistinguishable photons with a visibility of $72 \pm 3\%$ fitted using Eq. 5.35. Table 6.5 contains the values of the fitting parameters (App. E.2).

The red events correspond to temporally distinguishable photons with a fitted visibility of $32.47 \pm 2\%$. These values are lower than any of the predicted purities due to multi-

x	r	η_i	η_s	η_{MZI}	C_{max}	θ_{off}	S
0.11	5	1%	1%	39.191±2.977	242.7964±15.044	−0.7468±0.093	1.045 ± 0.026

Table 6.5: Fitting parameters of IME01 PIM

pair contribution as simulated in Sec. 5.2. Figure 6.13 (b) plots the visibility from the PIM as a function of average photon-pairs generated per pulse for the two purity values 0.92 and 0.837 from the simulation and the $g^{(2)}(0)$ measurement respectively as mentioned in the last section. The graph also includes the measurement errors of average photon-number ($\bar{n}$), and the estimation error of the visibility, as grey strips. As the curve with 0.92 purity passes through the intersection of these two grey strips, our PIM agrees more with this value of purity. As mentioned above, 0.92 corresponds to the theoretically predicted visibility for the resonator HSPSs. Although an experimental determination of the purity by $g^{(2)}(0)$ measurements have indicated a lower purity, this observation suggests that the true purity may indeed be closer to the theoretically estimated value. It is possible that the noise photons (e.g. from the waveguides) have altered the statistics of the $g^{(2)}(0)$ measurements as described in Fig. 6.13 (c).

The raw PIM is an important metric to integrate many sources on chip to perform a scalable multi-photon experiment. Compared to state of the art fibre HSPS or crystal HSPS which usually have more than 90% visibility, this PIM value of 72% of the resonator HSPS is not very high. However, it can be improved by tackling:

① the multi-pairs effect by

- ⓐ using photon-number resolving detectors (PNRDs) in heralding arms which will remove the multi-pair effect on the condition that the photon collection efficiency is improved to near unity,
- ⓑ improving the VGC design, such that the coupling efficiency of the device increases, and the input power can be lowered to lower multi-pair emission,

② the multimodes (impurity) effect by using interferometrically coupled resonator designs as proposed by [64, 65]. It narrows the linewidths of the signal and idler photons compared to the pump photons which increases the purity.

6.4.5 Experimental considerations and IME03 chip vs DTU-tele chip

Based on the insights gained from the PIM in IME01, IME03 chip has been designed to counteract the previously discussed experimental considerations, particularly, spurious four wave mixing. It has short input waveguides, and on-chip filters for about $20\ dB$ extinction of the pump pulse just after the photon-pairs generation in the HSPSs. One shortcoming of the IME chips is their lossy VGCs. Considering $4.5\ dB$ loss per VGC in the IME01 chips, the PIM experiments loose $18\ dB$ 4-fold counts just after the chip. With such losses we have collected just enough 4-folds to perform the experiment, despite having the HSPSs optimised for brightness.

The DTU-tele chip has been designed to perform multi-photon experiment with resonator HSPSs in our group (Chap. 8) which can also perform PIM. The primary benefit of this chip is its ultra-low loss ($\sim 1\ dB$) VGCs. These improve the collection efficiency about $3.5\ dB$ per channel resulting in a $14\ dB$ gain in the 4-fold counts (aforementioned (①-ⓑ) multi-pair effect mitigation). That allows a significantly higher 2-fold brightness, and consequently 4-fold PIM data as a function of the input power. This reveals the practicality of the HSPS in terms of the total experimental time and if it can be pushed to achieve

e.g. 8-fold coincidence counts. Also, the input pump power can be lowered more with this chip, therefore, reducing the multi-pair contribution and achieving higher raw visibility (modelled in Sec 5.2.1).

The knowledge of PIM with IME01 chip will be also used to determine what part of the photonic circuit needs to be reconfigured for a PIM. An on-chip measurement protocol is useful to understand the limitation of any multi-photon experiment. For the single qubit teleportation experiment (Chap. 8) using the DTU-tele chip, the PIM will reveal the highest achievable fidelity of the teleported states.

The DTU-tele chip has a much longer input waveguide, which brings back the spurious four wave mixing and a few other experimental considerations (e.g. thermal crosstalk). Nevertheless, for the mentioned advantages, we chose to perform the following PIM experiment with the DTU-tele chip.

6.5 Reconfiguring the DTU-tele chip for on-chip PIM

This section begins with the equivalent circuit of the DTU-chip to perform PIM; then continues to brightness, purity and multi-pair quantification measurements; afterwards measurements of multi-pair fringes and PIM fringes and concludes with PIM vs brightness measurements.

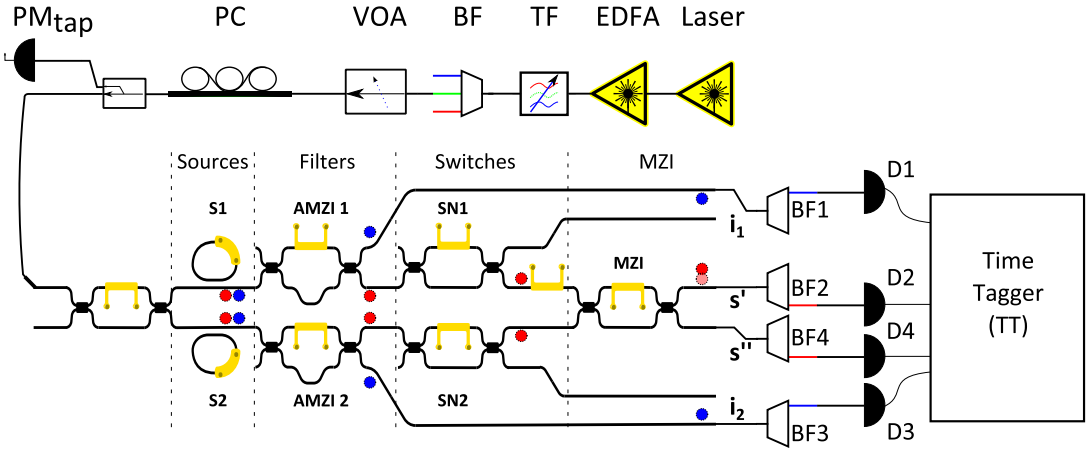

Figure 6.14: Equivalent circuit of the DTU chip for PIM. The MZI switches SN1 & SN2 are used to measure multi-pair emission fringes.

6.5.1 Equivalent circuit of the DTU-chip

The Fig. 6.14 depicts the experimental setup of the DTU-chip. The top part of pump pulse preparation is the same as the previous setups. Then the pump is injected into the part of the chip configured for PIM.

The left part of the circuit up to the switches SN1 and SN2 are configured as follows: the injected light in the chip is split equally by the input Mach-Zehnder interferometer (MZI) to pump equally the two micro-ring resonator HSPSs S1 and S2; the photon-pairs are generated inside the micro-ring resonators through SFWM such that the signal photons are in ITU grid 31 and idler photons are in ITU grid 47; an imbalanced MZI is used to separate the signal photons from the idler photons; the idler photons are coupled out of the chip and further filtered by DWDMs to clean up the stray photons from the pump spectra and detected by the single photon detectors (SNSPDs). The heralded signal photons are then passed through MZIs acting as switches for each of the photons. Based on the state of

the switches (SN1 and SN2), DTU chip is configured into four different modes of operation for the PIM:

Primary mode sets both of the switches to identity, therefore, the two signal photons are injected directly into the MZI and the outcome of the quantum interference between two signal photons are then performed as a function of MZI phase.

Secondary mode SN1 sets SN1 to identity while SN2 to swap. That allows only source S1 photons to reach to the final MZI, while source S2 photons are routed off the final MZI. Therefore, this mode measures the multi-pair fringes from source S1 only.

Secondary mode SN2 sets SN2 to identity while SN1 to swap. That allows only source S2 photons to reach to the final MZI, while source S1 photons are routed off the final MZI. Therefore, this mode measures the multi-pair fringes from source S2 only.

Background mode sets both of these switches to swap. That allows to measure 4-fold coincidence generated by spurious SFWM from the input waveguide and the rest of the circuit.

Finally, the outcome of the interference in the MZI of the two output arms are coupled out of the chip. They are then passed through another set of filters to further clean up stray photons from the pump and then to the detectors. For PIM measurements, in all four modes, the whole event is recorded as a four-fold event as a function of MZI phase Φ_{MZI}.

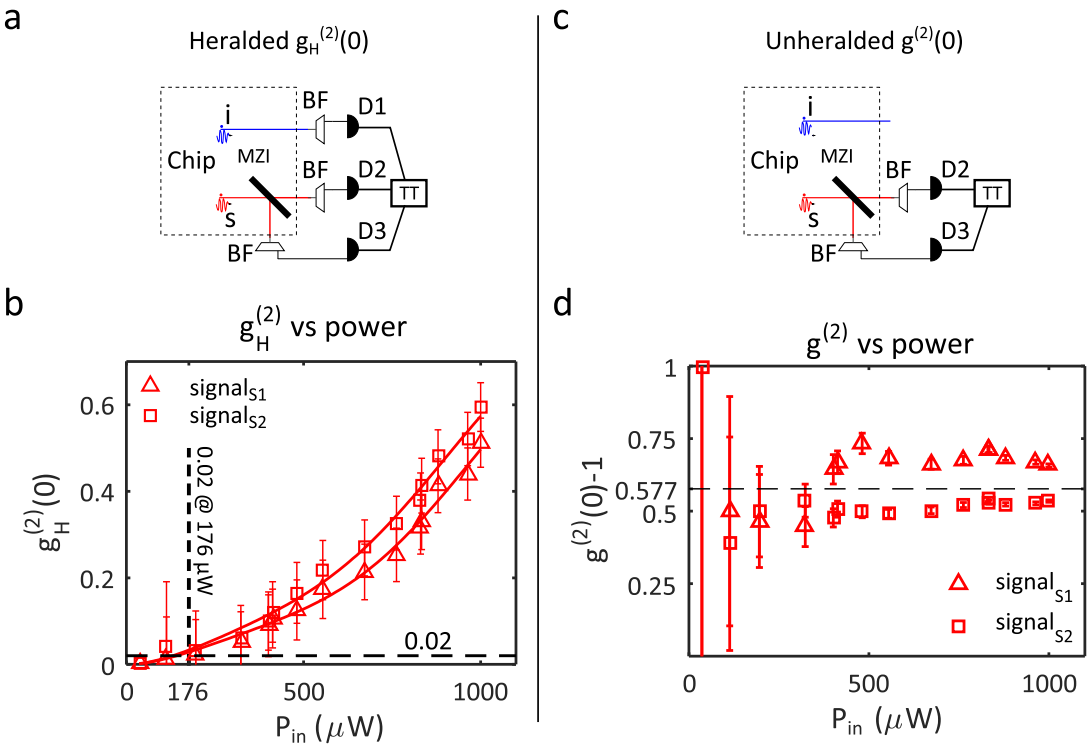

Figure 6.15: Multi-pair emission ($g_H^{(2)}$) and unheralded $g^{(2)}$ as a function of input pump power. Here the MZI phase is set as to give the maximum multi pair emission. (a) & (c) show the experimental setup, and (b) & (d) show the recorded data for source S1 & S2.

6.5.2 Brightness, multi-pair ($g_H^{(2)}$) and spectral purity ($g^{(2)}$) measurements

The measurements presented in this section use secondary operation modes (SN1 & SN2) to collect the 2-fold and 3-fold coincidences where the final MZI is set as an even splitter.

Figures 6.15 (a) and (b) show the equivalent measurements of on-chip configurations. These configurations are essentially the conditional and unheralded second order correlation measurements ($g_H^{(2)}$ & $g^{(2)}$) respectively as explained in Fig. 2.7. Only for multi-pair emissions from the sources, we can get three-fold counts. In the **Secondary mode SN1**

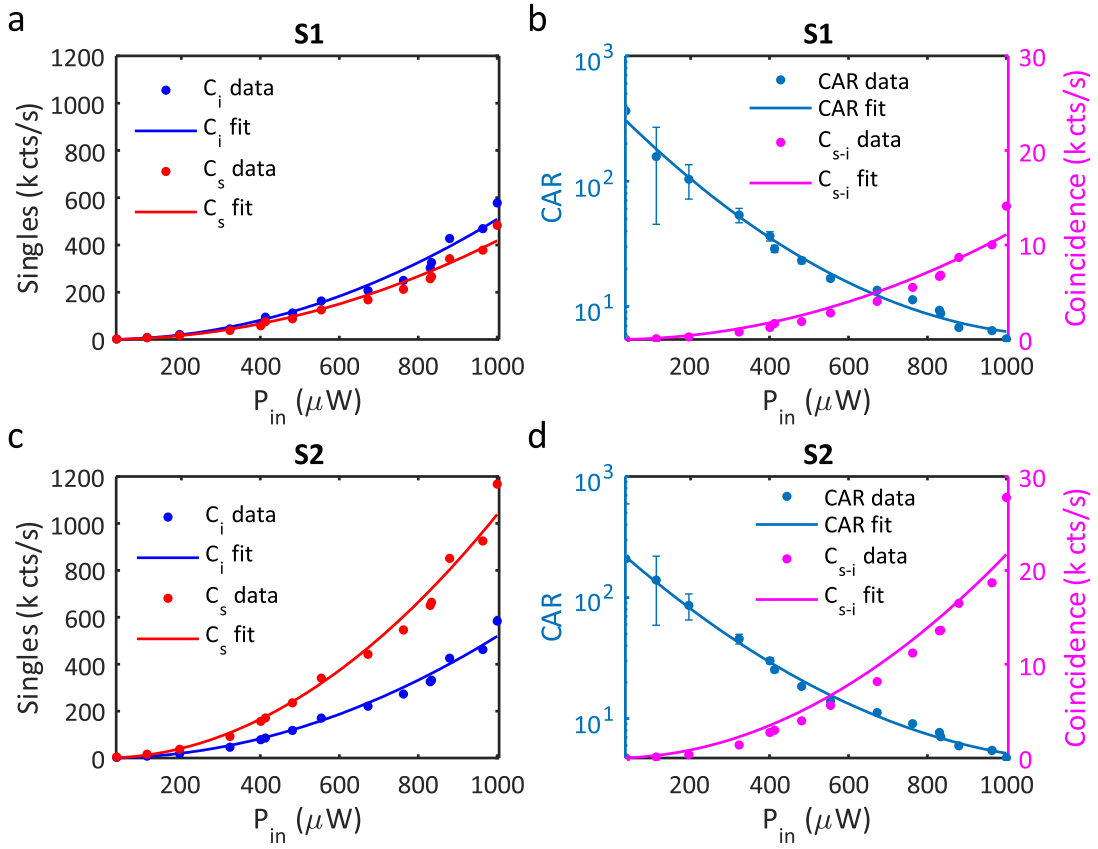

Figure 6.16: Brightness of the resonator HSPSs on DTU-tele chip. (a), (c) show the singles counts from the resonators, while (b), (d) show the coincidence counts and the CAR.

configuration, if the singles counts of each detectors are $D1$, $D2$, $D4$, and coincidence counts are D_{12}, D_{14}, then the brightness (CC), purity ($g^{(2)}(0)$) and multi-pairs ($g_H^{(2)}$) of source S1 for any input power P_{in} are:

$$CC(P_{in}) = D_{12} + D_{13} \tag{6.6}$$

$$g^{(2)}(\tau = 0, P_{in}) = \frac{D_{23}(\tau = 0)}{D_{23}(\tau \to \infty)} \tag{6.7}$$

$$g_H^{(2)}(\tau = 0, P_{in}) = \frac{D_{123} D_1}{D_{12} D_{13}} \tag{6.8}$$

where τ is the time-delay in the coincidence histogram. Similarly, using SN2, the above quantities can be acquired for source S2. The measurement error of $g^{(2)}(0)$ is calculated in App. C using the error propagation of Poissonian photon statistics.

The data plotted in Fig. 6.15 (b) represent the $g_H^{(2)}$ values for the two sources as a function of the input power. It shows that the multi-pair effect is less that 2% for a pump power less than $176\mu W$. This value is one of the best multi-pair emission value for the raw 2-fold coincident counts ($\sim 5kcts/s$) at the same power for a pulsed excitation, and comparable with quantum dot sources (Sec. 2.3). With the increment of the power, $g_H^{(2)}$ increases rapidly following a sigmoidal function [38], which is used to fit the data:

$$g_H^{(2)}(0) = \frac{\Sigma_{k\geq 2}\ a_k P^k}{1 + \Sigma_{k\geq 2}\ a_k P^k} \tag{6.9}$$

Figure 6.15 (c), (d) shows the purity estimated from an unheralded $g^{(2)}(0)$ function. It can be seen that the estimated purity values are low, about 60%. As we suspected from Sec. 6.4.4 with IME01 chip, the spurious four-wave mixing played a significant role in these measurements. Our first observation is that the DTU-tele chip is much larger than IME01 chip and also comes with long input waveguides. Therefore, the spurious SFWM in the waveguides and in the circuit of the DTU-tele chip will be higher than IME01 chip. In fact, the singles counts ($1000\ cts/s$) are much higher than the dark counts ($\sim 200\ cts/s$), even when the 2-fold coincidence counts approach zero. Also, the background mode (SN1 & SN2 swap) shows that the spurious SFWM contributes to 4-fold counts of $\sim 8cts/min$ for input power of $\sim \mu W$, thus, confirming high noise.

Our second observation is that the $g^{(2)}(0)$ measurements do not involve both the signal and idler photons of a photon-pair, and thus the advantage of uncorrelated noise reduction in the time-correlated measurements of photon-pairs cannot be employed (Sec. 6.3.3). Although, it is noted that the noise photons generated in the same time intervals as the photons from the sources cannot be reduced in time-correlated measurements. Also, any resonant source of noise in the micro-ring resonator HSPSs cannot be distinguished in these measurements. Therefore, spectral purity measured by Hanbury-Brown-Twiss (HBT) type interferometer with a single channel (e.g. only idler or only signal) in $g^{(2)}(0)$ measurements suffer severely from the noise photons (Fig.6.13 (c)).

One possible mitigation is to reduce the input power. As SFWM counts $\propto P_{in}^2$, when P_{in} reduces the CC_{Rg}/CC_{Wg} increases due to the field enhancement of the micro-ring resonators. However, as can be seen from Fig. 6.15 (d), the measurement error increases significantly at low power due to low counts and prevent any decisive agreements.

Source	η_s	η_i	γ_{eff} $(Mcts/s/mW^2)$	$\bar{n}$
1	0.022	0.027	19.185	0.384 ± 0.01
2	0.042	0.021	24.850	0.497 ± 0.01

Table 6.6: Average photon number estimation of S1 and S2 of DTU-tele chip

Figure 6.16 shows the data and the fits to obtain the brightness values of the resonators used for the PIM. Table 6.6 shows the relevant values from the fit to compare with the IME01 chip. The effective brightness values γ_{eff} are higher than the IME01 chip despite the fact that the Q-factor of the HSPSs are about the same. The previously mentioned Q-factors are estimated from the FWHM of the resonator line-widths. The Q-factor of a resonator also depends on many other parameters including linear losses in the waveguides. It is possible that the silicon waveguides of the DTU-tele chip has slightly lower loss. As the brightness goes as $\propto Q^4$, a slight change in the Q results in almost 4 times the brightness of the IME01 HSPS. With the aforementioned results of brightness and purity, we will now perform PIM.

6.5.3 PIM and multi-pair MZI fringes

Figure 6.17 shows the MZI fringe of multi-pair emissions from each source. To fairly estimate the multi pair emission for the same experimental condition, we have taken each data point of the secondary mode (SN1 & SN2) after each data point of the primary mode. The rate of multi-pair generation from source S2 is slightly higher than source S1. The raw four-fold coincidences of DTU-tele chip are almost 250 times brighter than the IME chip. This is due to the $\sim 3\ dB$ improvement of the photon collection efficiency of the each VGC (total $\sim 12\ dB$ imprvements for four-folds) of the DTU-tele chip and the slightly

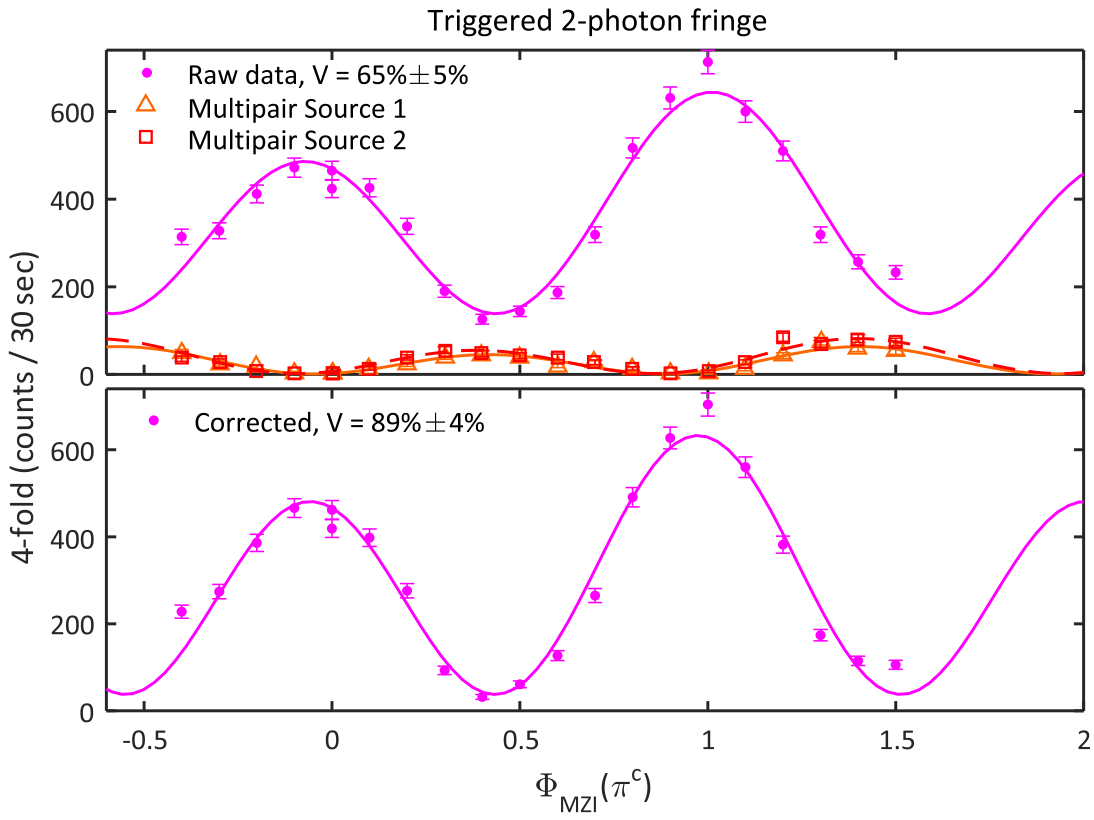

Figure 6.17: Four-fold coincidence events as a function of MZI phase. The magenta dots, fitted by the solid magenta curve (Eq. 5.35) in the top plot, represent the raw four-fold events in the primary data collection mode with a raw visibility of 65%. The triangular and square orange dots are multi-pair emissions from each source in secondary data collection modes. They are in anti-phase with the primary fringe. The corrected fringe, represented by the magenta solid line in the bottom plot, is obtained by subtracting both of the multi-pair events from both of the sources. The corrected visibility is about 89%.

higher Q-factors of the resonators. Thus, according to the coefficient of PIM (Eq. 2.55), $\mathbb{C}_{\mathrm{DTU-tele}} >> \mathbb{C}_{\mathrm{IME}}$ which implies the higher scalability of these resonator HSPSs.

We observed that the multi pair emissions are in anti-phase with the main fringe. This can be understood once we deconstruct the effect of each multi-pair term on the fringe. For simplicity, let's consider the wavefunction of each source in terms of Fock bases of signal and idler photons up to two-photon state and only with two optical (Schmidt) mode. As an example, the first optical mode of the first source is expressed as,

$$|\Psi\rangle_{11} = \sqrt{1-x_{11}}\left(|0,0\rangle_{11} - e^{i\theta_\lambda}\sqrt{x_{11}}|1,1\rangle_{11} + e^{i2\theta_\lambda}\sqrt{x_{11}^2}|2,2\rangle_{11} + ...\right) \tag{6.10}$$

As described in Fig. 6.18, if we limit our discussion by considering up to total three photon-pair emission at a time from both of the sources (S1 & S2), the effect of multi-pair emission can be categorised into three different cases:

Case 1 After heralding the idler single-photons, the terms containing vacuum can be excluded and the original fringe without any multi-pair effect is projected into the dominant: $|1\rangle\langle 1|_{11} \otimes |1\rangle\langle 1|_{21}$. This term interferes in the MZI following the unitary matrix formalism mentioned in Sec. 5.2, and the probability of detecting four-fold coincidences for a perfect MZI is,

$$P_{4F} = (1-x_{11})(1-x_{21})x_{11}x_{21}cos^2(\Phi_{MZI}) \tag{6.11}$$

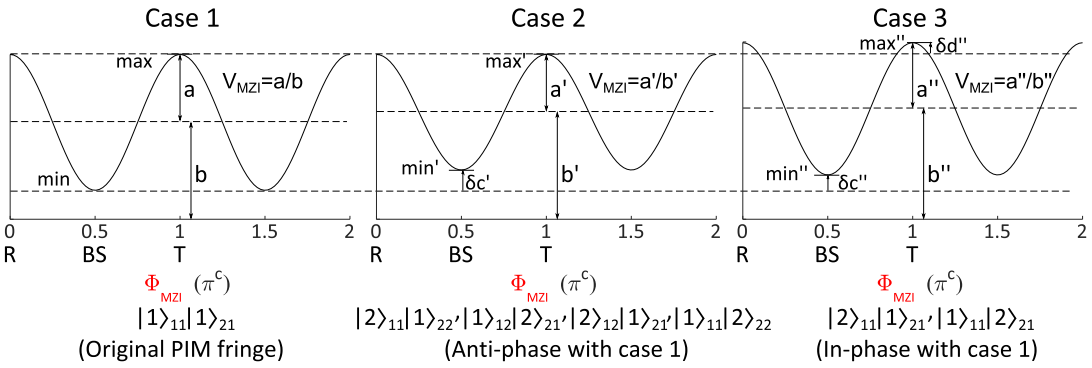

Figure 6.18: Effect of multi-pair emission on the MZI visibility.

In the figure, this term is indicated by $|1\rangle_{S1}|1\rangle\langle 1|_{S2}$ for simplicity. The order of this term can be identified by the coefficient x^2 in the probability. The visibility calculated from this term can be expressed by two parameters a and b,

$$V_{MZI} = \frac{(max - min)/2}{(max + min)/2} = \frac{a}{b} \tag{6.12}$$

Case 2 The influential multi-pair terms from orthogonal Schmidt modes are $|2\rangle\langle 2|_{11} \otimes |1\rangle\langle 1|_{22}$, $|1\rangle\langle 1|_{11} \otimes |2\rangle\langle 2|_{21}$, $|2\rangle\langle 2|_{12} \otimes |1\rangle\langle 1|_{21}$, $|1\rangle\langle 1|_{12} \otimes |2\rangle\langle 2|_{22}$. These terms have coefficients $x_{11}^2 x_{22}$ and similar and the photons in the orthogonal Schmidt modes do not interact with each other. These are the terms which contributed to our multi-pair measurements in Fig. 6.17 using secondary operating modes (SN1 & SN2) and the probability of four-fold coincidences between x_{11} & x_{22} is expressed as,

$$P_{4F} = (1 - x_{11})(1 - x_{22}) x_{11}^2 x_{22} sin^2(\Phi_{MZI}) \tag{6.13}$$

This fringe is in anti-phase with Eq. 6.13. Higher order terms will also result into a similar form but with coefficient $\sim x^4$. Figure 6.18 (case 2) shows that these terms only change the minimum position of the fringe. If the minimum value of the fringe is increased by δc, then the decreases in the visibility is expressed by,

$$V'_{MZI} = \frac{a'}{b'} = \frac{a - \delta c/2}{b + \delta c/2} < V_{MZI} \tag{6.14}$$

The fringes produced by **Case 2** is measured by our secondary modes SN1 and SN2. Therefore, subtracting the SN1 and SN2 fringes counteracts the multi-pair emission in the PIM.

Case 3 The multi-pair terms which cannot be estimated by SN1 and SN2 modes are $|2\rangle\langle 2|_{11} \otimes |1\rangle\langle 1|_{21}$ and similar. This term correspond to an in-phase four-fold coincidence probability and visibility,

$$P_{4F} = (1 - x_{11})(1 - x_{21}) x_{11}^2 x_{21} \frac{1}{4}(1 + 3cos^2(\Phi_{MZI})) \tag{6.15}$$

$$V_{MZI} = \frac{a + (\delta d - \delta c)/2}{b + (\delta d + \delta c)/2} < V_{MZI} \tag{6.16}$$

These terms are also adversely affecting the probabilities and if subtracted then the visibility will improve.

Subtracting the added multi-pair fringe from the original fringe, we obtained the corrected fringe with visibility of $\sim 89\%$, indicating the average purity of the sources are limited to about 89%. As discussed above such direct subtraction does not take into account all the different multi-pair emission effects and at worst case scenario may overestimate the visibility. A better way to estimate the effect of multi-pair emission on the PIM is to plot the visibility as a function of average photon-number as described in the next section.

6.5.4 PIM vs average photon number

The model mentioned in Sec.5.2 can be used to infer at what input power the multi-pair emissions minimally affect the PIM. Figure 6.19 shows the theoretical MZI visibility as a function of the average photon number generated per pulse $\bar{n}$. The upper bounding curve of the magenta band represents the single optical mode and the lower bounding curve represents out two Schmidt mode model for 92% spectral purity. To validate the model, we have measured the visibility at different input pump power level, as presented by the black dots. The measurement and the numerical prediction matches reasonably well within the margin of error. The graph shows that, for $\bar{n} < 0.05$, the multi-pair emission is low enough to get a raw visibility $> 80\%$.

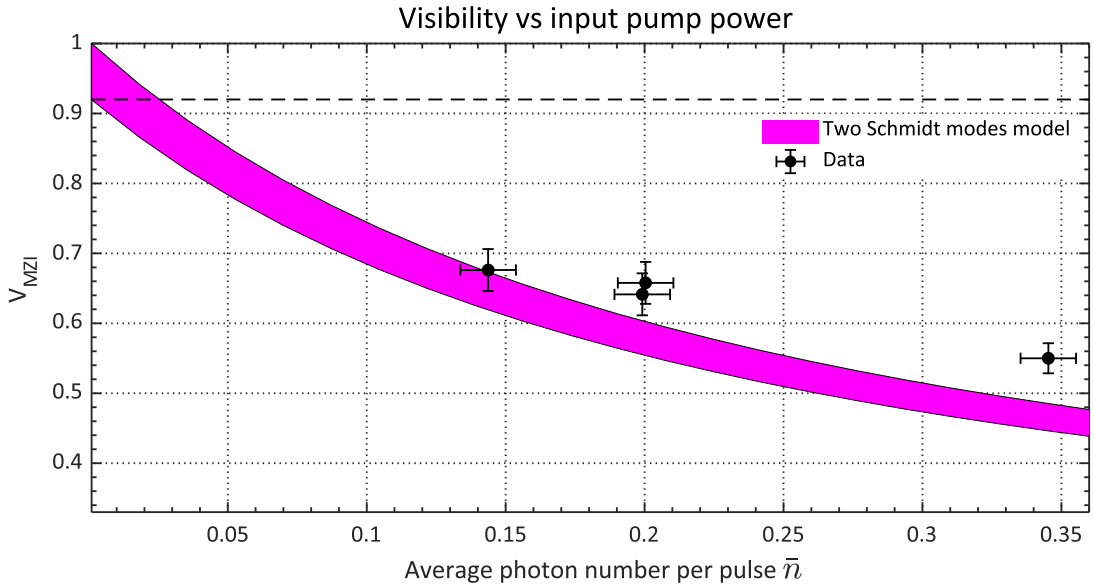

Figure 6.19: The visibility of the MZI fringe generated from two separate micro-ring resonators as a function of power showing the effect of multi-pair emission on raw visibility.

This leads to the observation that a trade-off exists between the raw indistinguishability (visibility) and the integration time. If the input power into the chip is lowered to achieve a higher raw visibility, then the time required to accumulate photons (integration time) per data point increases. Figure 6.19 shows that for the measured data points, lowering the power $1.5\ dB$ increased the visibility from 55% to 65%, while the integration time also increased from $0.5\ min$ to $2\ mins$. Table 6.7 uses the model to further show that to get a raw visibility above 90%, our integration time has to increase more than 32 times. At this rate, a multi-photon experiment involving more than 4-fold coincidences may become impractical. Considering our current setup, we will get a 6-fold coincidence per 10 mins, and an 8-fold coincidence per week.

$\bar{n}$	0.34	0.17	0.085	0.043	0.021
$T_{int}(min)$	0.5	2.0	4.0	8.0	16.0
$V_{MZI}(\%)$	~ 50	~ 60	~ 70	~ 80	~ 90

Table 6.7: $\bar{n}$ vs integration time.

This leads to the conclusion that there are two practical ways to perform multi-photon experiments with HSPS: ① using high efficiency photon number resolving detectors for heralding will naturally counteract the multi-pair emission effect with the caveat that the total photon-detection efficiency has to be near unity. ② Using a resonator cavities with

higher Q-factor. As can be seen from the literatures (Tab. 6.4), doubling the Q-factor makes the intrinsic brightness of the resonator almost 30 times higher. Although harder, it is certainly possible to stabilise a higher Q resonator for the whole period of the experiment.

6.6 Synopsis & outlook

In this chapter, we have discussed the PIM circuit and the optical setup to investigate brightness, purity and indistinguishability of micro-ring resonator HSPSs. The effect of the sensitivity of the resonators on determining the operational points and instrumentation has also been explored. The impact of noise or background photons generate by spurious SFWM in the input waveguide and/or in the circuit has been thoroughly investigated. We found that one of the advantages of resonator HSPSs is to successfully mitigate the noise photons. The noise photons can wash away the quantum correlation from resonator HSPSs in a 2-fold measurement. One way to reduce these background photons and improve the signal-to-noise ratio is to temporally lengthen (spectrally narrowing) the pump pulse. This reduces the peak power and subsequently the spurious SFWM in the waveguide while the resonant enhancement in the resonator still generates a high amount of photon-pairs. The caveat here is the effect of the spectrally narrow pump pulse on the spectral purity. The highest achievable spectral purity for our basic design, 92%, is acquired by having the pump spectra almost flat-top over the resonant response [34], which sets the minimum spectral width to about $150\ pm$ (5 times the resonant linewidth, as simulated in Chap. 5) and subsequently limits the signal-to-noise ratio. Also, as the 4-fold measurements require precise time correlation, it naturally reduces the noise photons which have a much lower probability to generate 4-fold coincidences. Therefore, the residual background is negligible for the smaller IME01 PIM circuit during 4-fold measurements. The background generated in a bigger circuit such as the DTU-tele chip is non-negligible even for 4-fold measurements (e.g. $8\ cts/min$ 4-fold noise photons). The same logic dictates that collecting photons from single channels such as only signal photons for unheralded $g^{(2)}(0)$ measurements will drastically affect the measurements. This effect of the noise photons is quantifiable when using a resonator HSPSs, unlike waveguide HSPSs, and therefore, can be post-processed or mitigated. The noise photons can be further reduced using at least two more component level engineering and one device level engineering. Firstly, using higher Q resonator along with high-efficiency grating couplers (such as in DTU chip) can improve the signal-to-noise ratio by further reducing the pump power while keeping the HSPS's brightness high. Secondly, designing short input waveguides and filtering out the pump just after the HSPSs (e.g. IME03 circuits) will keep the spurious SFWM to a minimum. The capability of quantifying and separating the background photons from the photon-pairs generated in the HSPSs makes the micro-ring resonator a good choice over waveguide HSPSs for high fidelity quantum computing and communication protocol.

In terms of brightness and purity, micro-ring resonator HSPSs have naturally higher values of brightness and purity than waveguide HSPSs (e.g. Tabs. 2.1 & 6.4). But, there are controversies in the literature on the methods to measure the purity of a resonator HSPS. The stimulated SFWM method to measure the JSI has been criticised as the resonant enhancement for higher power during stimulation may involve different non-linear dynamics absent during the spontaneous process. Also, stimulated methods has not been used to measure the JSP of a resonator which can also significantly alter the spectral purity. Alternatively, the $g^{(2)}(0)$ method can measure the spectral purity involving both amplitude and phase of the single-photons by interfering them in a Hanbury-Brown-Twiss setup. Our measurements show that the noise photons affect this measurement drasti-

cally for larger DTU-tele chips. It is also noted that any noise photon generated inside the resonator may not be distinguishable in this measurement. Although both of the methods ($g^{(2)}$ and JSI) discussed here have their own merits and demerits, the JSI values tend to agree more with our experimentally measured PIM data.

Using the PIM circuit, we have interfered heralded single-photons from micro-ring resonator HSPSs for the first time on Si or any other platform and found the raw (uncorrected) MZI visibility to be 72%. This value is lower than the theoretically achievable limit 92% for our design (Chap. 5) due to the multi-pair contribution. However, this is the first PIM with micro-ring resonators which also do not require any spectral filtering. State of the art SPDC sources (Tab. 2.3) have been researched for more than the last two decades resulting in 95% indistinguishability without spectral filtering [100], and 40 time-bin multiplexing to get proposed one 30-fold coincidence/s [49]. It is also noted that the newly proposed interferometric coupling of resonator design [64, 65] or temporal manipulation of the pump pulse [66] can increase the spectral purity to 99% in SOI.

We have used the numerical model developed in Chap. 5 to fit the aforementioned PIM data. In particular, we have fitted the raw visibility (72%) obtained from the IME01 chip and concluded that the multi-pair contribution is the major cause of the raw visibility reduction. In addition, the multi-pair emissions are measured using the reconfigurability of the DTU-tele chip and a direct subtraction results in 89% corrected visibility (i.e. indistinguishability), much closer to the theoretical limit of 92%.

In future, designing resonator HSPSs with interferometric coupling and combining it with high Q-factor cavities and temporal manipulation of the pump pulse, we plan to achieve high brightness HSPSs in SOI with near unity spectral purity and indistinguishability.

Chapter 7

Off-chip PIM with waveguide sources

Contents

The nanowire waveguides are one of the most common heralded single photon sources (HSPSs) in silicon photonics due to the ease of implementation. Although the brightness of the nanowire HSPSs has been explored extensively in many experiments, a systematic investigation of the spectral purity has not been performed. The spectral purity of the nanowire HSPSs has been investigated in [44, 53], but not in the context of spectral filtering to achieve high purity. Also, among all the waveguide experiments, only three experiments to date have investigated indistinguishability by performing a triggered HOM interference. The very first of the aforementioned waveguide experiments has been done by Harada et al. in 2011 [56]. It shows 71% raw indistinguishability between nanowire HSPSs. It is argued that the visibility reduction is solely due to multi-pair emission as very narrow spectral filters were used. Other raw indistinguishability results $69 \pm 3.4\%$ [57] and $88 \pm 8\%$ [58] have also assumed spectral purity by employing narrow spectral filtering. In these experiments, the spectral purity was assumed but not measured. Thus a systematic characterisation of waveguide HSPSs' brightness, purity and indistinguishability will illuminate on their scalable employability in future multi-photon experiments.

The primary focus of this chapter is to investigate the spectral purity as a function of spectral filtering and use the IME01 off-chip PIM design to investigate the indistinguishability of the waveguide HSPSs. The cartoon in Fig. 7.1 shows that this is an off-chip

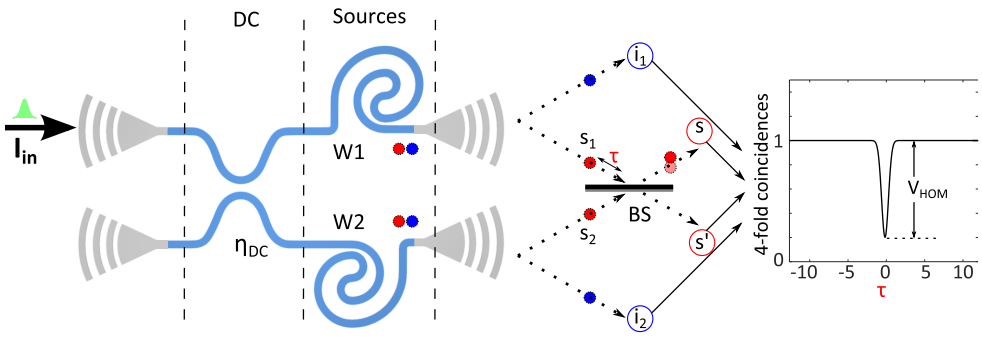

Figure 7.1: A cartoonish depiction of off-chip PIM with waveguide HSPSs W1 & W2. DC: directional coupler; D: single-photon detector; BS: beam-splitter; CL: coincidence logic unit.

quantum interference experiment similar to the original HOM experiment [46]. Despite designing an on-chip PIM for waveguide sources in IME03 chip, it was not used for measurements due to a design fault as explained at the end of the chapter. The IME01 off-chip PIM circuit design contains two waveguide HSPSs **W1** and **W2**, each with an optimal waveguide length of $14\ mm$ to maximise the brightness (Sec. 4.2.4). Benchmarking the performance of the PIM also requires the characterisation of brightness and purity of these waveguides. Here we first measured brightness and heralding efficiency of **W1** and **W2**, then estimated purity at different spectral filtering configurations. Lastly, we performed off-chip heralded quantum interference (HOM) to estimate the indistinguishability.

7.1 Brightness and purity measurements

This section begins with a description of the experimental setup to measure the brightness of the waveguide HSPSs. Subsequently, the purity of these HSPSs and its dependence on the spectral filtering has been discussed and experimentally demonstrated.

7.1.1 Brightness

The following experimental setup is similar to the brightness measurements of the micro-ring resonators mentioned in the last chapter. There are a few changes at the out-coupling section of the chip, due to the difference in the chip design and the experiment.

Experimental setup

Figure 7.2 describes the experimental setup on measuring the brightness of the waveguide HSPSs. A pulsed laser (*PriTel* FFL of 50 *MHz* repetition rate, nominal $1\ ps$ pulse width) is connected to an Erbium doped optical fibre amplifier (*PriTel* EDFA) to attain the desirable power. The output optical beam from the amplifier is then connected to two broadband pump rejection filters (DWDMs from *Opneti*) to reduce the pump leakage in the anticipated spectra of the signal and idler wavelengths. It is then connected to a Variable Optical Attenuator (VOA from *OZ optics*) to control the amount of injected power into the chip while keeping the same pulse shape. Output of the VOA is connected to a polarisation controller (PC) which chooses the polarisation of the light that can maximally couple to the transverse electric (TE) mode supported by our Vertical Grating Couplers (VGCs). A 1% tap from the output of the polarisation controller is connected to an optical power meter PM_{tap}, while the rest is connected to the input fibre that couples light into the chip. In effect, the 1% tap monitors the input power coupled into the chip, provided the coupling does not change significantly over time.

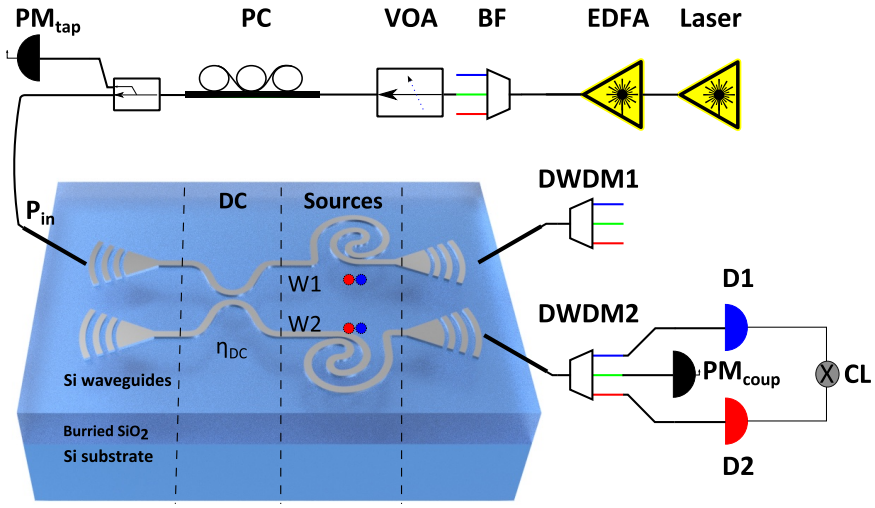

Figure 7.2: Experimental setup to measure brightness of the waveguide sources. A pulsed laser light is prepared with desired power and polarisation and coupled into the chip. A directional coupler (DC) in the chip splits the power and generate photon-pairs in both W1 & W2. Signal-idler photon-pairs are coupled out of the chip and spectrally separated using DWDM filters. Signal and idler photons are then detected by single-photon detectors D1 and D2 and coincidences are collected by coincidence logic unit (CL). EDFA: fibre amplifier; BF: broadband filter; VOA: variable optical attenuator; PM: powermeter.

The chip contains two waveguides with the same length connected by a directional coupler with splitting ratio η_{DC} (ideally, $\eta_{DC} = 50\%$). The directional coupler splits the pump light according to the splitting ratio which then propagate inside each waveguide producing SFWM signal-idler photon-pairs. The outputs of the waveguides are coupled out of the chip through fibres connected to wavelength demultiplexer DWDMs (from *Opneti*). The DWDMs separate photons at signal, idler and pump wavelengths. A DWDM output at the pump wavelength is connected to a power meter to monitor the coupling into the chip. Together, PM_{tap} and PM_{coup} give us an indication if the experimental condition has been changed due to a change in the coupling.

The signal and idler channels are connected to single photon detectors (D1, D2 SNSPDs) through fibre channels and polarisation controllers (not shown in the figure) for 2-fold measurements of the brightness. The polarisation controller is used to maximise the efficiency, as some of the SNSPDs have polarisation dependence.

The average VGC loss in this chip is $-4.5\,dB$ for each coupler at the best coupling, making the average insertion loss of the device higher than $-9\,dB$. The best coupling point drifts of within an hour and the insertion loss settles around $\sim 5.5\,dB$ per coupler for a long experiment. The measurement of the η_{DC} gives us $40\% : 60\%$ splitting ratio as described in App. C. Therefore the two waveguide HSPSs were not equally pumped.

Experimental results

Figure 7.3 contains the analysed experimental data. Fitting and solving the system of equations described by Eq. 2.16, using singles from signal and idler photons and coincidences from signal-idler photon-pairs, we obtain the value of the brightness in the form of average photon number $\bar{n}$ generated per pulse as tabulated below. Here, η_s and η_i represent detection efficiencies of the signal and idler photons respectively. It can be seen from Fig. 7.3 (a,b) that η_s and η_i for the $W2$ channels are lower than the $W1$ channels. Although our single-photon detectors have similar efficiencies, the channel efficiencies (from

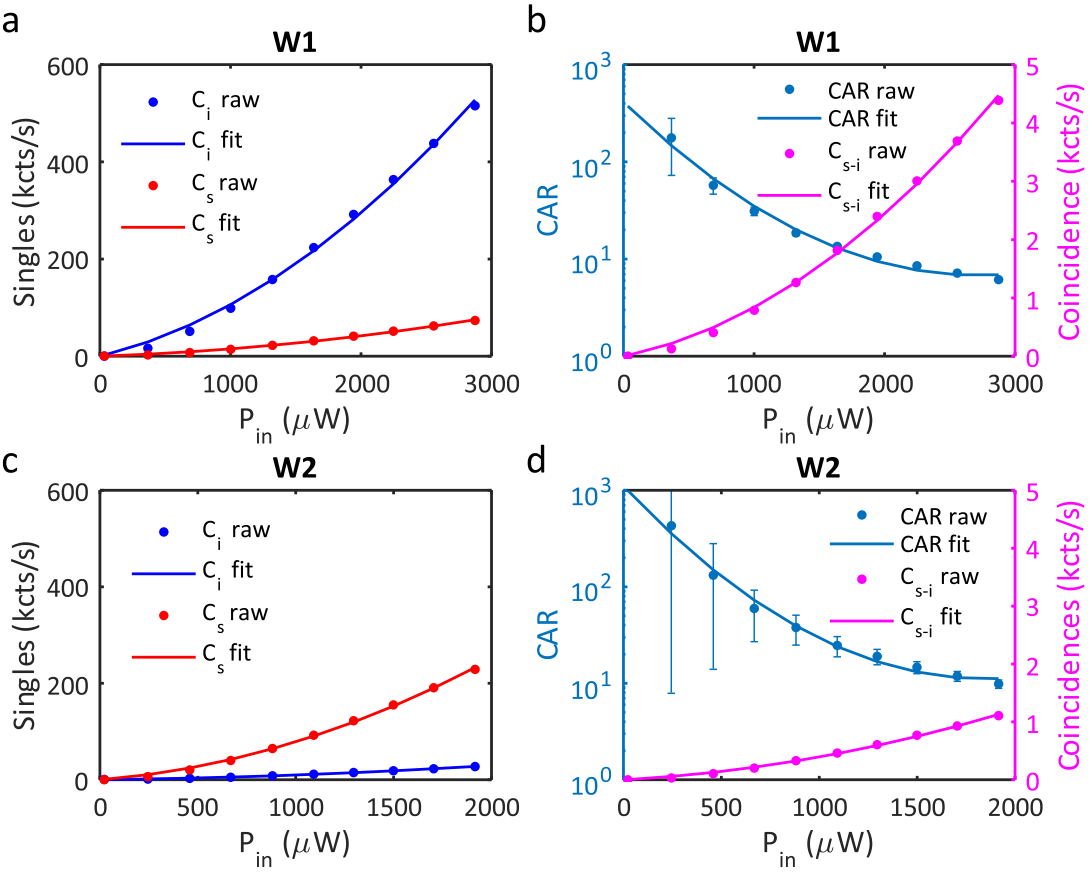

Figure 7.3: The raw signal and idler singles counts are shown in (a,c) and coincidence counts with corresponding coincidence to accidental ration (CAR) are shown in (b,d) respectively for the two waveguide HSPSs W1 & W2 respectively.

Source	η_s	η_i	γ_{eff} $(Mcts/s/mW^2)$	$\bar{n}$
$W1$	0.065	0.0093	0.637	0.012 ± 0.005
$W2$	0.0045	0.0420	1.114	0.022 ± 0.005

Table 7.1: Average photon number estimation of waveguide HSPSs

the outputs of the chip to the detectors) vary. The off-chip DWDM filtering to reduce the pump leakage together with the channel loss brought down the total detection efficiencies to an average $\eta = 1.84\%$ per signal/idler photon's detection.

In Tab. 7.1, $\bar{n}$ is calculated for $P_{in} \approx 1\ mW$ to compare with the micro-ring resonator HSPSs measured in the last chapter. We can see that the value of the $\bar{n}$ is about one order of magnitude lower for the waveguide HSPSs. This is because the intrinsic brightness (γ_{eff}) of the waveguides are also about an order of magnitude lower than the resonators. These values of the $\bar{n}$ are comparable with other waveguide experiments reported in the literature (Tab. 2.1). In contrast, the raw collection efficiencies of the coincidence counts in [35, 56] are higher as their coupling efficiencies per channel are a few dB higher than ours.

It is important to note that as we are using a high peak power pulsed laser, the appropriate use of the correct power meter is important. Most of the solid state power heads are inappropriate for a direct measurement as they have a maximum limit of $500\ mW$ to $1\ W$, while the peak power of the laser can easily exceed $1\ W$, thereby, saturating the power head and giving a wrong reading. As the two power meter readings PM_{tap} and PM_{coup} are

collected by solid state power meters at relatively low power (due to $20\ dB$ tap and $\sim 15\ dB$ insertion loss), our power meter data are reliable.

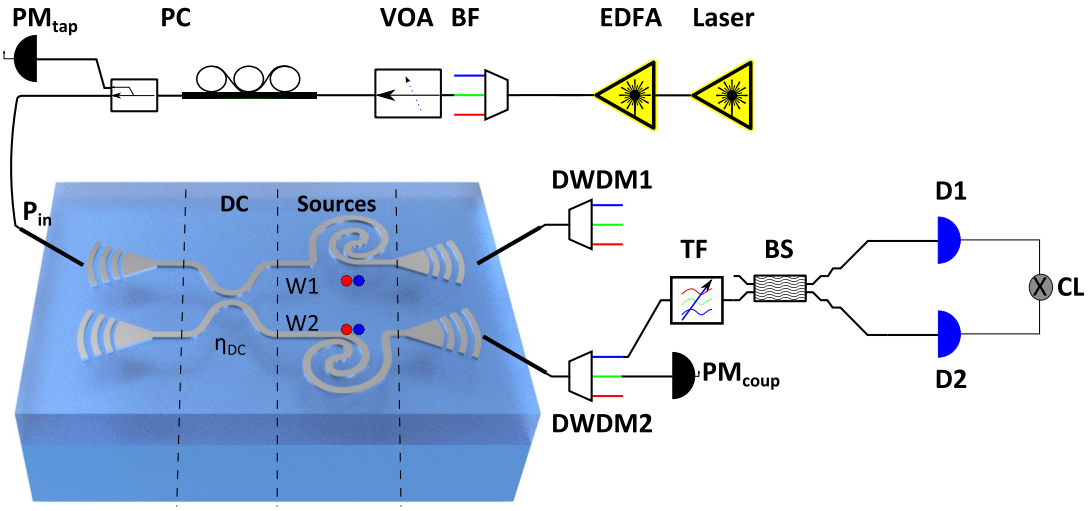

Figure 7.4: Experimental setup on purity measurements. Upto the ouput DWDM it is the same as the brightness setup. After the chip, idler photons are separated by a DWDM and passed through a tuneable bandwidth filter (TF). The output of the TF is connected to an even beam-splitter (BS) for the second order correlation ($g^{(2)}(0)$) measurements. The outputs of the BS are detected by detectors D1 and D2 and recorded by Coincidence Logic unit CL for estimating $g^{(2)}(0)$.

7.1.2 Purity

The purity of the heralded photons from the waveguide HSPS has been estimated by measuring unheralded second order correlation function $g^{(2)}(0)$ (Sec. 2.2.4) as described below.

Experimental setup

In this measurement (Fig. 7.4), the experimental setup is the same as the brightness experiment in the last section upto the output DWDM. At the output of the DWDM, only the idler photons have been chosen to be detected. It is passed through a tuneable bandwidth filter (TF), which is used to change the bandwidth of the spectral filtering. After the TF, they are passed through a fibre beam splitter with equal splitting ratio and then being collected by the single-photon detectors and recorded as two fold coincidences. This is a second order correlation measurements $g^{(2)}(0)$ between the photon flux from the two output arms of the beam splitter. The spectral filtering ratio in this experiment can be defined as,

$$r_F = \frac{FWHM_{pump}}{FWHM_{filter}} \tag{7.1}$$

where $FWHM_{pump}$ and $FWHM_{filter}$ are the Full Width Half Maximum measure of the bandwidths of the pump and the filter spectra respectively. The aforementioned measurements have been performed for a range of TF bandwidth for two different pulse-width configuration of the input pump laser (*Pritel FFL*). A filter cartridge inside the cavity of this pulsed laser can be changed to different values. When we used $2\ nm$ and $5\ nm$ filter cartridges (denoted by A and B respectively), the values of the pump spectral widths are found to be $0.4\ nm$ and $1.1\ nm$ as measured by an OSA (Fig. 7.5 (a), (b)). The narrow pulse-width is smaller (less than half) than the DWDM filter bandwidth used for signal-idler photons.

Therefore, without considering the effect of TF, in this case the DWDM acts as a broadband filter for the pump while spectrally filtering the signal and idlers. The ratio of the pump bandwidth to DWDM filters are then low ($r_F = 0.4/1.24 \approx 1/3$). In contrast, the broader pulse-width fills the DWDM channel. In this case the spectral filtering ratio $r_F \approx 1$ without considering the effect of TF.

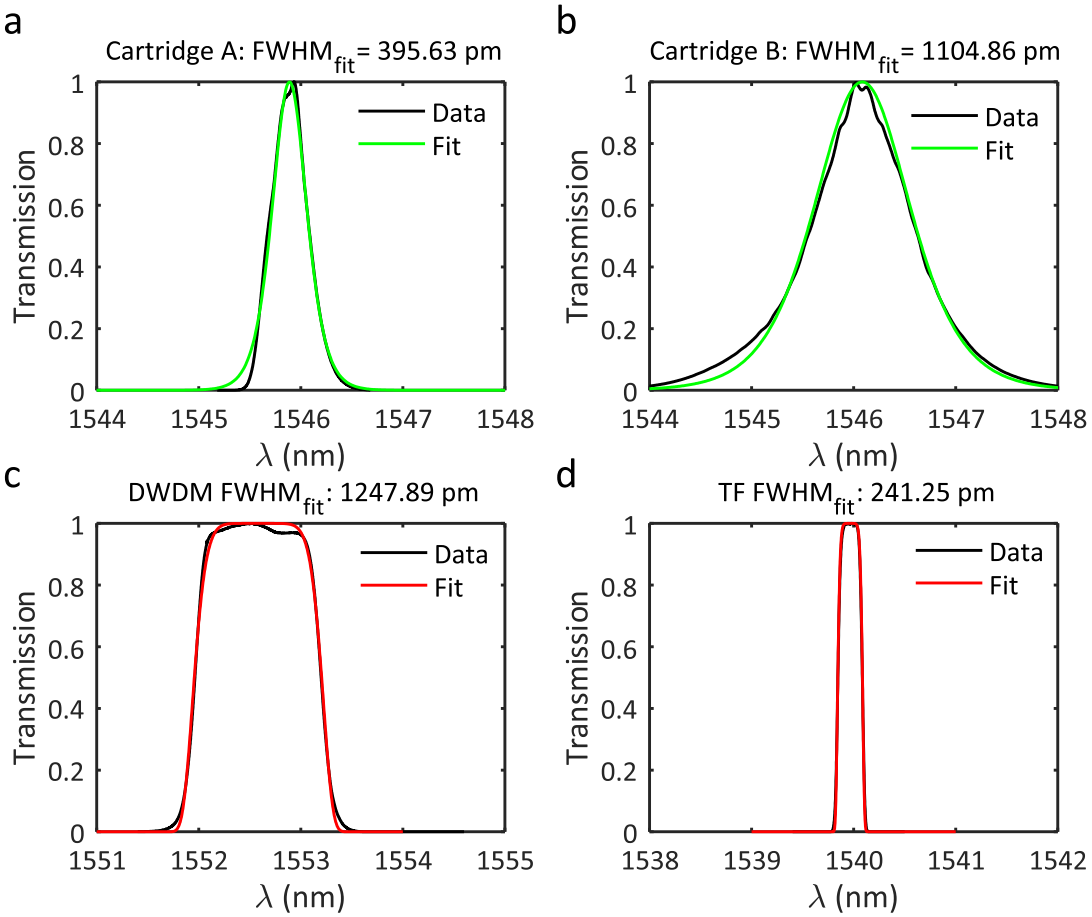

Figure 7.5: Fitting the pump (a & b) and filter (c & d) spectra of different bandwidths using Eqs 7.2, 7.3 & 7.4.

Tuneable bandwidth filter (TF)

The tuneable bandwidth spectral filter (TF) is the crucial component in this experiment to employ spectral filtering on the spectra of the idler photons. TF is used to vary the filtering ratio r_F for the above two pump pulse spectra. The TF (*Yenista X-50*) has a range of filtering bandwidth (Full Width Half Maximum (FWHM)) from $950\ pm$ to $50\ pm$ with $1\ pm$ resolution over the whole C-band of the telecom spectra. Therefore, for narrower pump configuration, r_F is varied from 0.42 to 8, while for broader pump configuration it is varied from 1.15 to 22.

This filter was not manufactured specifically for quantum applications, where loss plays an important role. The $-5\ dB$ insertion loss of this filter reduces the photon flux appreciably and increases the time required for $g^{(2)}(0)$ measurement. The $g^{(2)}(0)$ is a 2-fold coincidence measurement, while the PIM described in the next section is a 4-fold measurement. Therefore, this TF cannot be used practically for the PIM.

Experimental results

The raw measurement results of 2-fold coincidences are plotted in App. C showing the coincidence counts as a function of the arrival time between the photons (τ). Using the formulae mentioned in Sec. 2.2.4, we calculated the $g^{(2)}(0)$ from the raw data to estimate the purity ($P = g^{(2)}(0) - 1$) as a function of TF's FWHM, and plotted in Fig. 7.6 (a). The brown dots and the green dots correspond to $0.4\ nm$ and $1.1\ nm$ pump spectral width respectively. As expected, the purity of the idler photons increases with narrower spectral filtering ($r_F \to \infty$).

Fitting data with simulated JSA

In order to understand the connection between the measurement results and the purity calculated from the JSA, we need to simulate the JSA for our choice of filters and pump spectra. Figure 7.5 shows the spectral shapes of the pump measured with an OSA, and the TF and DWDM filters measured with scanning continuous wave laser. The pump spectra are fitted with an hyperbolic secant function which is a typical output of a passively mode-locked fibre-optic solitonic pulsed laser (*PriTel FFL*). As mentioned in Chap. 5, the commercial filters do not provide any analytical form to describe the transmission. We have guessed the following functions of the filter spectra which fitted the transmission with $> 98\%$ correlation.

$$\alpha_P(\lambda) = I_0\ sech^2\left(\frac{\lambda - \lambda_0}{\sigma_{pump}}\right) \tag{7.2}$$

$$F_{TF} = I_0\ e^{-(\frac{\lambda-\lambda_0}{2\sigma_{TF}})^8} \tag{7.3}$$

$$F_{DWDM} = I_0\ e^{-(\frac{\lambda-\lambda_0}{2\sigma_{DWDM}})^8} \tag{7.4}$$

Here the relations between the σ and *FWHM* are,

$$FWHM_{pump} = 2sech^{-1}(1/\sqrt{2})\sigma_{pump} = 1.763\sigma_{pump} \tag{7.5}$$

$$FWHM_{DWDM} = 2\sqrt[8]{2ln(2)}\sigma_{DWDM} = 2.083\sigma_{DWDM} \tag{7.6}$$

$$FWHM_{TF} = 2\sqrt[8]{2ln(2)}\sigma_{TF} = 2.083\sigma_{TF} \tag{7.7}$$

As we know most practical traces, especially if they are related to statistics or distributions, can be presented with a Gaussian or a modified Gaussian with reasonable amount of accuracy. In the above equations, we chose a modification of the exponent which made the function flat-top with desired roll-off of the filter.

We calculated the JSA for a particular filter settings of the idler photons using the aforementioned spectral fittings and the following equation from Sec. 2.2.4:

$$f(\omega_s, \omega_i) = \int d\omega_p \alpha_P(\omega_p) F_{DWDM}(\omega_p) \alpha_P(\omega_s + \omega_i - \omega_p) F_{DWDM}(\omega_s + \omega_i - \omega_p)$$
$$F_{DWDM}(\omega_s)\ F_{DWDM}(\omega_i)\ F_{TF}(\omega_i)\phi_{match}(\omega_s, \omega_i) \tag{7.8}$$

Here, ω is the angular frequency corresponding to that wavelength. The phase matching function ϕ_{match} is almost unity for our choice of waveguide HSPSs. It is calculated using Eq. 5.2 and Eq. 5.3. In the fitting of the experimental purity data with our numerically calculated JSA, the pump spectral widths were divided by a factor of $2\sqrt{2}$ for the best fit and remained as the only fitting parameter.

The calculated values of the purity from the simulated JSA are plotted as solid lines in Fig. 7.6 (a). The brown and green solid curves represent the narrower and wider settings of the pump pulse spectra. Both curves follow the experimental data as the purity gradually increases to 1. It is also noticeable that the green curve at wider filter width has

much higher purity values than the brown curve. According to the JSA this is due to the higher uncertainty of the energy conservation due to the wider pump envelope. Figure 7.6 (b) shows a few of the calculated JSAs for the narrower pump width ($0.4\ nm$) setting. The JSA, at a wider filter configuration, is elongated, similar to a cigar-shape at 45 degree energy conservation line showing correlation between signal and idler photons. At a narrower filter setting, the JSA resembles a box-shape (fuzzy vertical line) with almost no correlation between signal and idler photons thereby increasing the purity towards unity. The normalised relative strength of the first five Schmidt modes are also plotted in Fig. 7.6 (c) showing how the strengths of the higher mode numbers increase with the filter width.

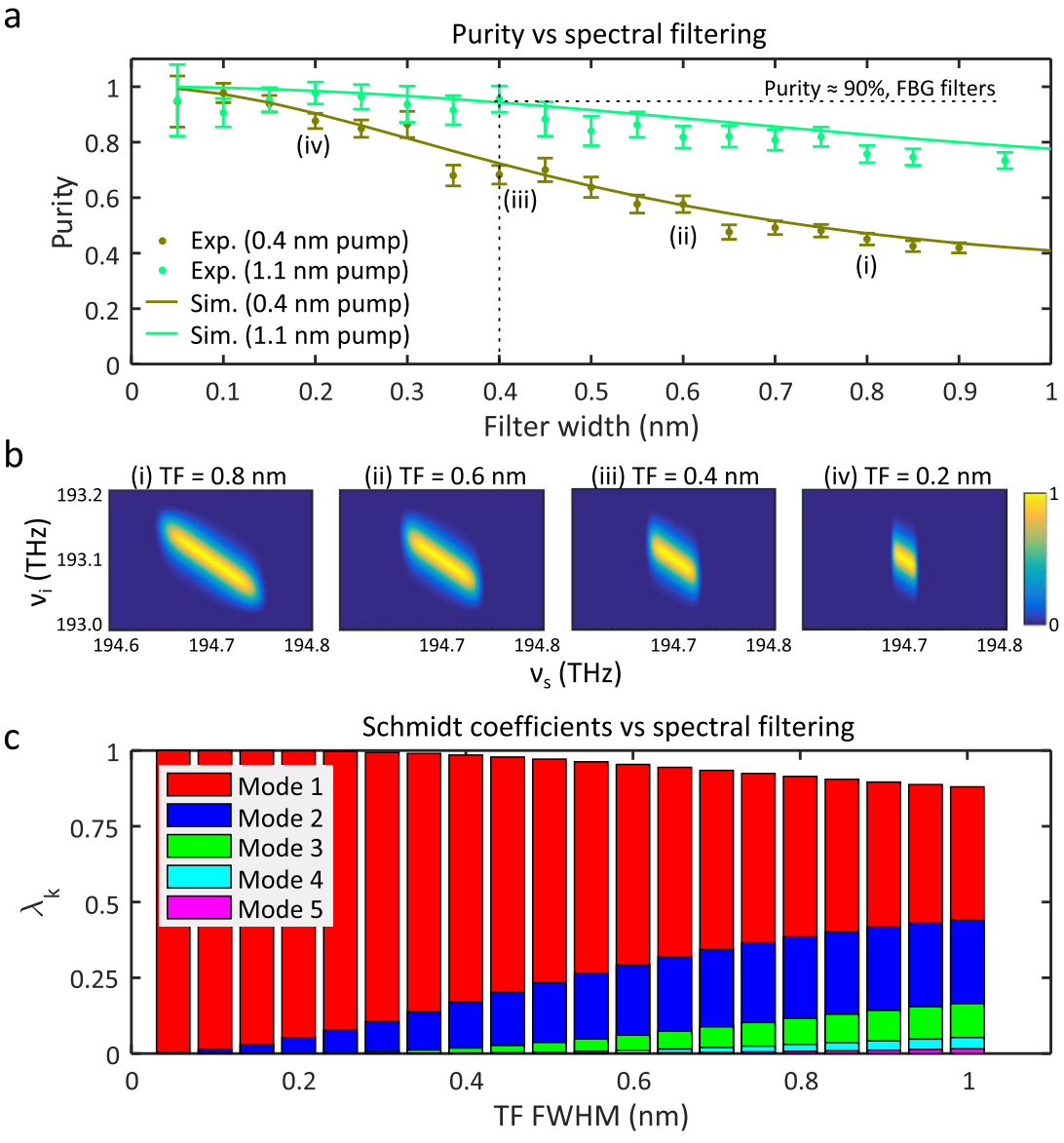

Figure 7.6: Experimental purity data of the waveguide HSPS estimated through $g^{(2)}(0)$. (a) Purity as a function of the FWHM of the spectral filtering for two different pump pulse FWHMs. The brown (green) solid line, fitting the brown (green) events corresponds to pump FWHM of $0.4\ nm$ ($1.1\ nm$). (b) Simulated JSA as a function of filter bandwidth using the spectral shapes used for the spectral fittings. From the top-left JSA to the bottom-right JSA the filter bandwidth gradually widens. (c) The relative strengths of the first five Schmidt modes for different values of purity (filter width) as calculated from the JSA.

At the right-end of the graph, at the widest filter setting ($950\ pm$), the purity is about 80% for the green curve ($r_F \approx 1$) while 42% for the brown curve ($r_F \approx 0.42$). At about, $1/3^{rd}$ of this filter setting, at $\sim 400\ pm$, the purity has significantly improved for the brown curve to $\sim 75\%$ ($r_F \approx 1$) while also improving the purity of the green curve to $\sim 90\%$ ($r_F \approx 3$). These observations will be useful in the next section when off-chip PIM will be performed using different filter settings.

It is noted that this increased purity comes at a price of heralding efficiency and brightness [151]. As the filtering is essentially modifying the JSA by filtering out part of the spectra of the photons, it will then reduce the cumulative flux of that particular photon channel for the whole wavelength range. Therefore, the photon-pair counts will drop, decreasing the brightness and the heralding efficiency of our waveguide HSPSs.

This trade off is crucial in building scalable single-photon sources with waveguide HSPSs with both high purity and high brightness for a complex photonic circuit that requires multi-photon coincidences. The duration of the multi-photon experiment will increase exponentially with the decreasing number of the available high purity photons from these parametric sources. Therefore, lowering the brightness and heralding efficiency of the HSPSs to increase the purity can even make the duration of an experiment changed from an hour to a week. In the next section, we will measure the indistinguishability of the waveguide HSPSs by using spectral filtering method to increase the purity. We will also attempt to quantify the duration of an experiment affected by spectral filtering and multi-pair emission.

7.2 Off-chip PIM using HOM interference

Once we choose the spectral filters and pump pulse bandwidth, the next step is to perform the PIM using HOM interference. First, the details of our HOM interference experiment is presented, followed by the experimental outcomes. Lastly, the effect of multi-pair emission is determined by recording HOM interference for two different settings of filter bandwidth, each with three different values of the input pump power.

7.2.1 Experimental setup

HOM interference requires precise measurement of the path length difference between the interfering photons' wavepackets with about $50\ ps$ width (depending on our filter settings), to guarantee that they will overlap in time (Sec. 2.2.5). As the speed of light is about $30\ cm/ns$ in free space, to have a pico-second resolution, the path length difference has to be calculated in a millimetre scale resolution.

One very specific reason, that makes this path length adjustment challenging, is the difference in the time delay through the two different DWDMs (#1 and#2) for the W1 and W2 sources. These DWDMs have large dispersions and often contributes $10\ ns$ (or more) time-delay difference between the same output channels in two different DWDMs. Therefore, if the path lengths are not matched, the signal photons from DWDM 1 will be nanoseconds apart from signal photons filtered by DWDM 2. Therefore, they will never overlap or interfere in our HOM measurements.

The first delay-matching calculations of this experiment was performed with free space optics together with Dr. Takafumi Ono as mentioned in the *Acknowledgements* and elaborated in the App. C. This method is similar to the methods described in the literature [56–58], but unlike using unheralded two-fold coincidences to match the time delay and detect the position of the HOM dip, we have used the coincidence logic unit to calculate the delay. The free space optical components were not stable enough to perform long HOM

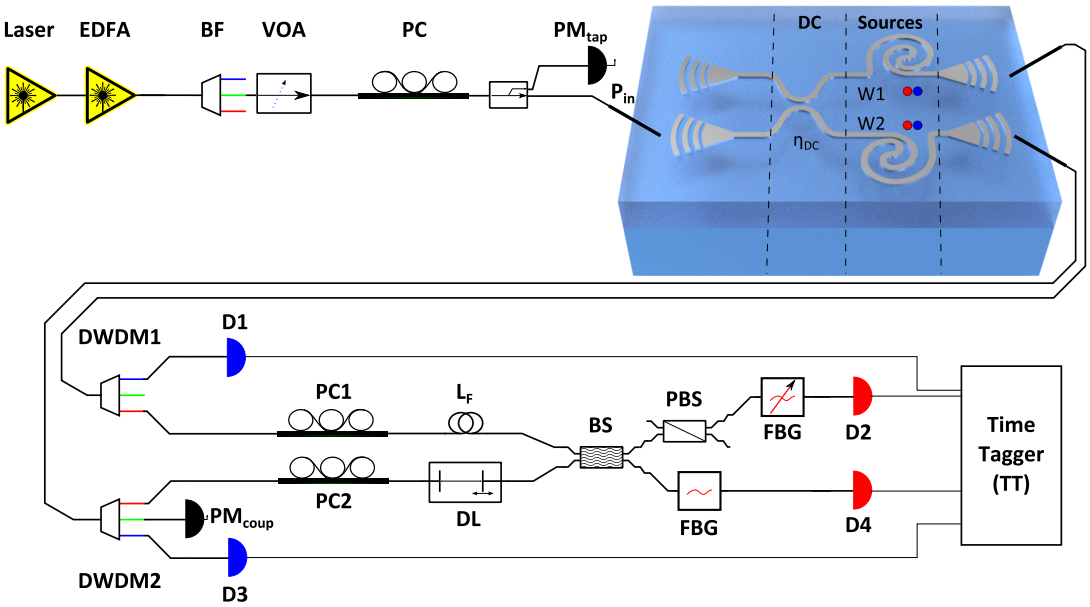

Figure 7.7: Experimental setup of off-chip PIM with waveguide sources. All the components in this setup are in enclosed packagings with fibre pigtailed connections. BF: Broadband Filter, VOA: Variable Optical Attenuator, PM: Power Meter, D: single-photon detectors, DWDM: Dense Wavelength Division Multiplexer, L_F: Length-matched Fibre, DL: Optical Delay Line, BS: Beam Splitter, PBS: Polarisation Beam Splitter, FBG: Fibre Bragg Grating.

interference, in addition to the losses introduced by coupling lenses. Eventually, in our setup all the free space elements were replaced with all fibre components. The primary benefit of using all fibre optic components was that the setup became stable and retained the same experimental characteristics, even in the course of a few months. The challenge was to prepare fibre lengths (for delay-matching) with millimetre scale precision.

All-fibre pigtailed setup

The all fibre pigtailed experimental setup for HOM measurement is shown in Fig. 7.7. The first part of the experimental setup up to the chip is the same as the last two experimental diagrams used for brightness and purity measurements. After the chip, the DWDMs separate the signal and idler photons from each waveguide HSPS **W1** and **W2**. Idler photons are then detected by single-photon detectors D1 and D3 and herald the presence of the signal photons. The signal photons off the #1 DWDMs are then passed through an extra fibre patch-cords L_F, while signal photons from #2 is passed through a fibre pigtailed delay line DL (*OZ optics*, motorised, computer controlled) to match the delay. The path length mismatch between these two paths was found to be $L_F = 25 \pm 5\ cm$. A single mode fibre patch cord (SMF28e) has been chosen as L_F and then continuously cleaved by a millimetre at one end until it matches the desired delay.

Each path is connected to a polarisation controller (PC #1 and #2) which has its output connected to the input of a fibre beam-splitter (BS). The quantum interference between the signal photons occur in the BS at the right time delay τ of the DL. One output of the beam-splitter is connected to a fibre polarisation beam-splitter (PBS) such that both photons entering the beam splitter have the same polarisation as can be adjusted by the polarisation controllers, PC #1 and #2. The photons from the PBS output and the other output of the BS are then filtered by the FBG filters and collected by single-photon detectors D2 and D4. The photons arrival time is recorded by time-tagger (TT) and post processed to

extract the 4-fold coincidences. Finally, the HOM interference as 4-fold coincidences is measured as a function of time delay (τ) and presented in the next section.

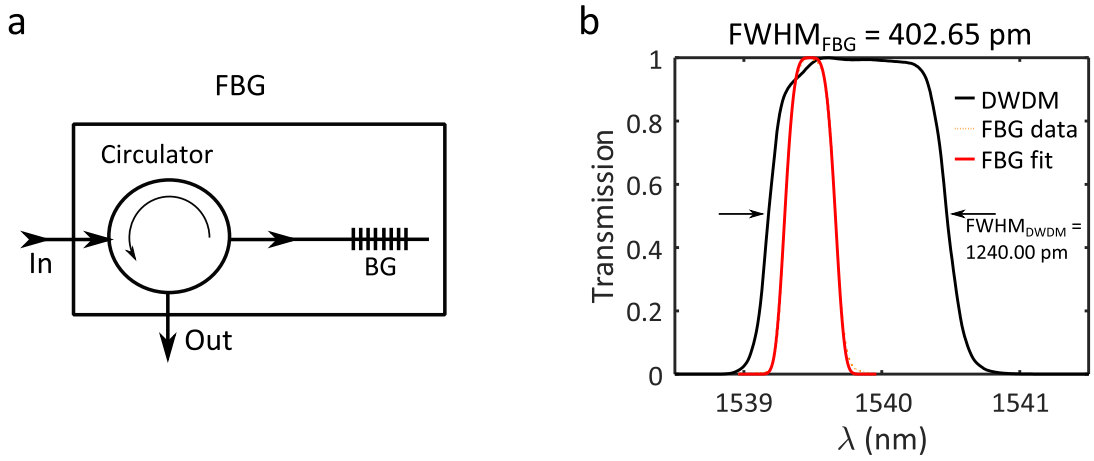

Figure 7.8: Fibre Bragg Grating (BG) spectrum in comparison to DWDM spectrum.

As mentioned earlier, due to its high insertion loss ($\sim 5\ dB$), using TF to increase the spectral purity is not suitable for a 4-fold measurement. Using two matching TFs corresponds to $\sim 10\ dB$ loss which will decimate the 4-fold counts. Instead, we have employed the narrowest commercially available Fibre Bragg Gratings (FBG) filters with $-0.5\ dB$ loss. The chosen FBGs have FWHM of $50\ GHz$ ($\sim 395\ pm$) at central wavelength $\lambda_0 = 1539.48\ nm$. Thus, the FBG spectrum is $1/3$ of the broader pump spectra. To maximally match the signal photons' spectra from two independent waveguides, two FBG filters were chosen: one fixed in the aforementioned wavelength and the other one tuneable in wavelength. Figure 7.8, shows the spectral shape of the fixed FBG. It can be seen that the roll-off of the FBG is less steep than the DWDM and fitted with the following function:

$$F_{FBG} = I_0\ e^{-(\frac{\lambda-\lambda_0}{2\sigma_{FBG}})^4} \tag{7.9}$$

7.2.2 Experimental results

We have performed HOM interferences for three different input pump powers for two different filter settings. In both settings, the broader pump pulse spectrum (green line in Fig. 7.6 (a)) was chosen where pump bandwidth approximately equals to the DWDM filter bandwidth. The filter settings were:

① The pump, signal and idler photons all have the same DWDM filters. This corresponds to the filtering ratio $r_F \approx 1$. According to Fig. 7.6 (a) the maximum achievable visibility in this configuration is $\sim 78\%$.

② The pump and the idler photons have the same DWDM filters. The FBG filters were used for signal photons. This corresponds to the filtering ratio $r_F \approx 3$. According to Fig. 7.6 (a) the maximum achievable visibility in this configuration is $\sim 90\%$.

Figure. 7.9 shows the experimental results for the aforementioned settings. As expected, higher filtering ratio ($r_F \approx 3$ with $1/3^{rd}$ narrower spectral filters) corresponds to higher HOM interference visibility. We can also see that for both settings, reducing the input pump power resulted in higher HOM interference visibility. This is due to multi-pair emission as mentioned in Sec. 5.2, and also discussed in a later sub-section. The best HOM interference visibility we have achieved was Fig. 7.9 (f) replotted in Fig. 7.10. The equations that has been used to fit all these experimental data is described below.

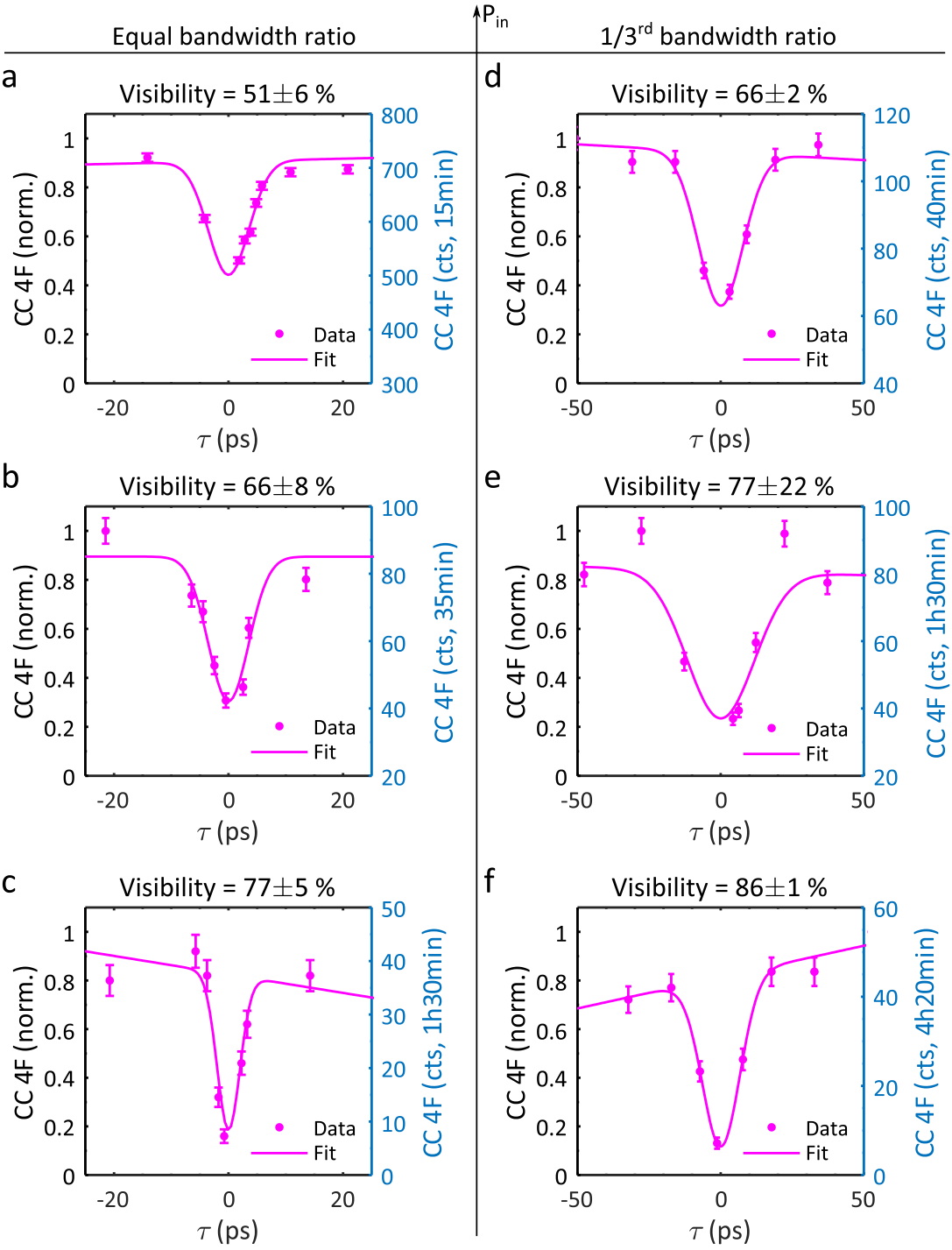

Figure 7.9: The HOM interference for two different settings of the spectral filtering. (a), (b), (c) correspond to $r_F \approx 1$ with decreasing power while (d), (e), (f) correspond to $r_F \approx 3$ with decreasing power. Eq. 7.14 was used to fit the data. The right-hand y-axes represent the actual counts in the experiments while the left-hand y-axes are normalised for comparison.

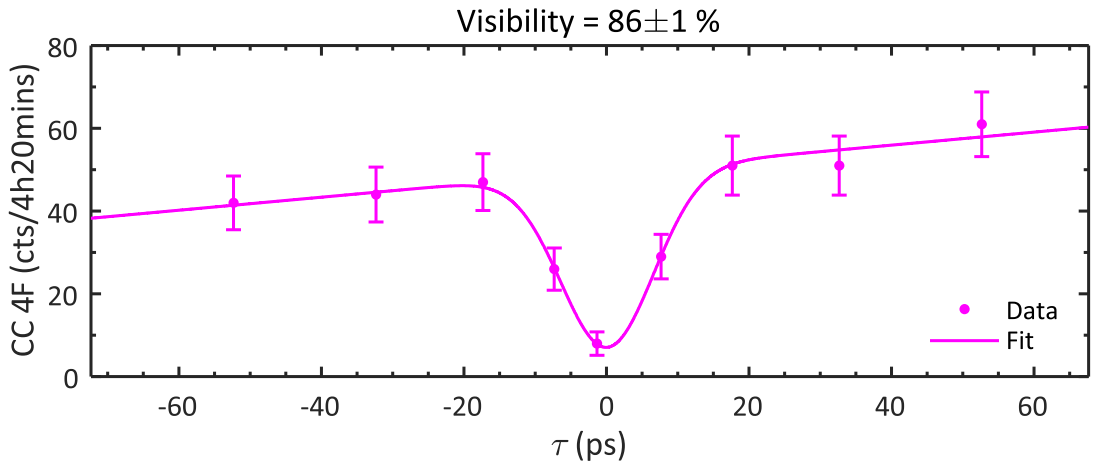

Figure 7.10: The highest HOM interference visibility (fitted with Eq. 7.14) was achieved using FBG filters ($r_F \approx 3$) with low input power. That ensured high spectral purity with low multi-pair contribution. Without multi-pair contribution, Fig. 7.6 (a) indicates that highest expected visibility is $\sim 90\%$.

HOM interference fittings

The procedure introduced in [155] for SPDC and adapted in [114] for SFWM, relates the four-fold coincidence detection probability per pulse (P_{4F}) with the brightness and the spectral purity of the interfering HSPSs. Although we will not re-derive the mentioned expression and not derive a closed form expression of HOM interference for our specific pump pulse and filter shape, the following discussion is used to understand the implication of filter functions in our experiment. If i_1 and i_2 refer to the heralding idler photons, s_3 and s_4 refer to the heralded signal photons after the interference, then P_{4F} can be expressed as,

$$P_{4F} = P(i_1, i_2, s_3, s_4) = \bar{n}_1 \bar{n}_2 \eta^4 \left(R^2 G_{13} G_{24} + T^2 G_{14} G_{23} - RT \left(G_{int}(\tau) + G^*_{int}(\tau) \right) \right) \tag{7.10}$$

Here, $\bar{n}_1$ and $\bar{n}_2$ represent average photon pairs per pulse from waveguide HSPSs W1 & W2, the average channel detection efficiency $\eta = \sqrt[4]{\eta_{i1}\eta_{i2}\eta_{s3}\eta_{s4}}$, R and T correspond to the reflection and transmission of the beam-splitter used for the interference. The functions G_{ij} and G_{int} contain the spectral information of the SFWM photon-pairs. The subscript i refers to the source (W_1 or W_2) while j refers to the detection of the interfered signal photons:

$$G_{ij} = (2\pi)^2 \int d\omega_p d\omega_s d\omega_i |\alpha_P(\omega_p)|^2 |\alpha_P(\omega_s + \omega_i - \omega_p)|^2 |F_{sj}(\omega_s)|^2 |F_{ik}(\omega_i)|^2 \tag{7.11}$$

The cross terms (e.g. $G_{13}G_{24}$) in Eq. 7.10 results into delta function (e.g. $\delta(\omega_{s1} - \omega'_{s2})\delta(\omega'_{s2} - \omega_{s1})$) which is satisfied by matching the filter spectra of our signal and idler photons (e.g. using the tuneable FBG to match the fixed FBG). Therefore, the term that is related to the visibility of the interference outcome is,

$$\begin{aligned} G_{int}(\tau) =& (2\pi)^4 \int d\omega_p d\omega'_p d\omega_{s1} d\omega_{i1} d\omega_{s2} d\omega_{i2} \alpha_P(\omega_p) \alpha_P(\omega_{s1} + \omega_{i1} - \omega_p) \alpha_P(\omega_p) \alpha_P(\omega_{s2} + \omega_{i2} - \omega_p) \alpha^*_P(\omega_p) \\ & \alpha^*_P(\omega_{s2} + \omega_{i1} - \omega_p) \alpha^*_P(\omega_p) \alpha^*_P(\omega_{s1} + \omega_{i2} - \omega_p) |F_{i1}(\omega_{i1})|^2 |F_{i2}(\omega_{i2})|^2 |F_{s1}(\omega_{s1})|^2 |F_{s2}(\omega_{s2})|^2 e^{i(\omega_{s1} - \omega_{s2})2\tau} \end{aligned} \tag{7.12}$$

The filter functions ($F_i(\omega)$, $F_s(\omega)$) play an important role in the shape of the HOM dip and fitting the HOM interferograms. For energy matched Gaussian pump pulse and filter functions, the above results in a closed form expression,

$$P_{4F} = \bar{n}_1 \bar{n}_2 \eta^4 \left(R^2 + T^2 - 2RTV_{HOM} exp\left(-\frac{(\tau - \tau_0)^2}{2\sigma_\tau^2} \right) \right) \tag{7.13}$$

Considering the power fluctuations while adjusting the time delay (τ), we used the following equation to fit the HOM interferograms,

$$P_{4F} = \bar{n}_1\bar{n}_2\eta^4(m\tau + c)\left(R^2 + T^2 - 2RTV_{HOM}exp\left(-\frac{(\tau-\tau_0)^2}{2\sigma_\tau^2}\right)\right) \tag{7.14}$$

Here, m and c are also fitting parameters. Our pump and filter functions are not Gaussians and the exact analytical solution for our experiment is not available. Nevertheless, the Gaussian approximation worked well with our data. The HOM interferences in Fig. 7.9 and Fig. 7.11 are fitted using this equation and the corresponding visibilities are extracted with 68% confidence interval.

Multi-pair effect: HOM visibility vs average photon number

The effect of multi-pair emissions on the interference visibility is best understood using Fig. 7.11 (a), where the visibility is plotted as a function of average photon number generated per pulse ($\bar{n}$). As we know from Sec. 2.2.1 that $\bar{n} \propto P_{in}^2$, by adjusting the input pump power we can adjust $\bar{n}$. Also from Sec. 2.2.1, we infer that the emission probability of two-photon state is $\propto \bar{n}^2$ and so on. Therefore, increasing the $\bar{n}$ increases the chance of multi-pair emissions and effectively reduces the visibility as derived in Sec. 5.2.

In Fig. 7.11 (a), we plotted numerically calculated visibility as a function of $\bar{n}$ for two different purity values corresponding to our aforementioned filter settings and assuming two effective Schmidt modes. We also placed the experimentally obtained visibilities on the same plot. We found that for FBG filter setting ($r_F \approx 3$), the numerical calculations agrees with the experimental data. For the DWDM filter setting ($r_F \approx 1$), the slope of the experimental data appears different from the numerical calculation. This could be due to the fact that our effective two Schmidt mode model broke down at lower purity. It can be amended if we include three or four Schmidt modes in the model. In future, expansion of the model and recording more HOM interference visibility at different $\bar{n}$ will solidify our findings.

Experimentally, further reducing the average photon number per pulse $\bar{n}$, we can achieve higher visibilities. An inspection of the integration time to accumulate 4-fold coincidence data for each settings of the time delay (τ), as depicted in Fig. 7.11 (b), reveals that the integration time increases exponentially for decreasing $\bar{n}$ and becomes impractical. Therefore, we also need to engineer brighter waveguide HSPSs (e.g. lower propagation loss, higher collection efficiency) along with the high purity (e.g. dispersion engineering). Another experimental solution is to use higher repetition rate pulsed laser, such as $R = 500\ MHz$ actively mode locked ultrafast optical clock (UOC from *PriTel*). According to Eq. 2.13 ($\bar{n} \propto (P_{avg}^2/R)$), with higher repetition rate, for the same input pump power, the $\bar{n}$ reduces, promising better count rates with lower multi-pair emission. Figure 7.11 (c) shows a HOM interferogram using UOC laser. The details of the advantage of using UOC for waveguide HSPSs such as presented in this chapter are still under investigation.

7.3 On-chip PIM with IME03 waveguide design

The experimental result and analysis with IME01 off-chip PIM design can be performed extensively with higher stability using the on-chip PIM design in IME03 chip. As mentioned in Sec. 4.1, the newly designed narrowband, tuneable bandwidth and low loss on-chip spectral filters can be used for all signal and idler channels. This effectively could have been used to map the extent of the high HOM interference visibility for all different spectral filtering configuration ($\rightarrow$ spectral purity). Unfortunately, there was a design rule in the IPKISS codes which set the minimum length of the cavity structures. That set the

minimum FSR of such filters which went unnoticed. The fabricated design with these filters have FSRs misaligned to the DWDM pump, signal and idler channels. The resonances of these filters enters both the pump and signal (or idler) channels such that the pump will also generate signal-idler photon-pairs in those filters. Therefore, these filters cannot be used without introducing spurious SFWM photon-pairs. The results obtained from this design is not presented in this thesis.

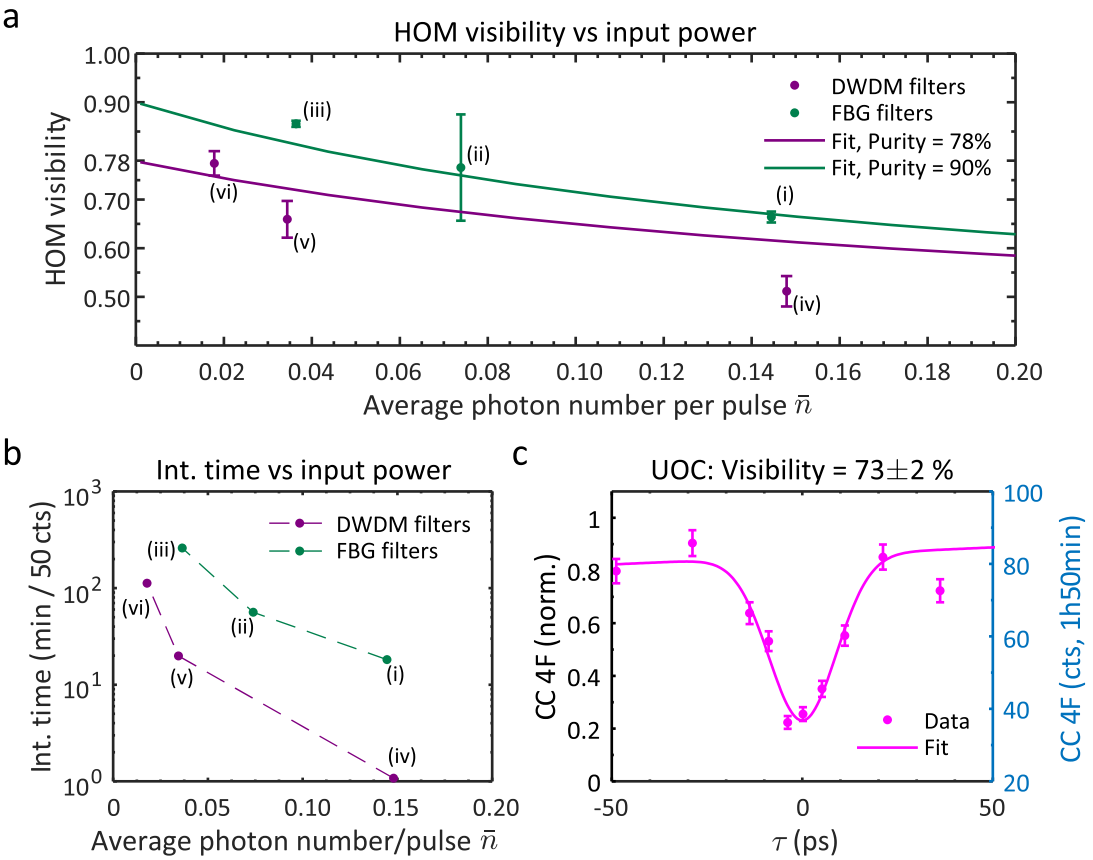

Figure 7.11: HOM visibility vs input power. (a) The HOM visibility at different input power plotted to verify the multi-mode and multi-pair emission model for FBG and DWDM filter settings. The data points marked as (i), (ii), (iii), (iv), (v) and (vi) represents respectively (d), (e), (f), (a), (b) and (c) in Fig. 7.9. (b) Exponential increase of the integration time with decreasing $\bar{n}$. (c) HOM interference using UOC laser.

7.4 Synopsis & outlook

In this chapter, we have measured the brightness, spectral purity and off-chip PIM for waveguide HSPSs. We found that our design of silicon nanowire waveguide HSPS has photon-pair generation brightness comparable to the literature. The maximum brightness from our optimum waveguide HSPSs is an order of magnitude lower than the moderately high Q-factor micro-ring resonator HSPSs of the last chapter for the same pump power. This brightness, in general, is not the fundamental limit and not the maximum achievable brightness for our design. We have observed that our specific design of waveguides which winds the long length (e.g. $14\ mm$) by spiralling in & out using a constant radius of curvature causes extra bending losses. This design results in about $4\ dB/cm$ linear loss, making our length sub-optimised (e.g. Fig. 4.5) and also loosing generated photon-pairs. In addition, using recently demonstrated lower loss rib-waveguides ($1\ dB/cm$ [38]), the

brightness can be increased to 6 times of our current value (Fig. 4.5), which, without applying any spectral filtering, is comparable to the moderate Q-factor (5×10^4) resonator HSPSs of the last chapter. A fair comparison requires those resonators to be also fabricated with the mentioned rib waveguides. That would have made the Q-factor twice ($\sim 10^5$) of our current value, resulting in more than an order of magnitude higher brightness [38]. A fair comparison also requires the brightness to be measured along with the spectral purity of the single-photons. The raw brightness can be further improved by boosting the collection efficiency, using low loss VGCs. All in all, this brightness of the waveguide HSPSs deems perfect, combined with its robustness and extremely low maintenance, for 2-fold, 4-fold or even 8-fold coincidence counts experiments which do not require high purity photons.

We have measured purity using unheralded second-order correlation function ($g^{(2)}$) as a function of spectral filtering. In this experiment, two different configurations of pump bandwidth were chosen: narrow bandwidth ($0.4\ nm$) and wide bandwidth ($1.1\ nm$) pulses. For both of these choices, purity of the heralded photons can be almost arbitrarily increased using spectral filtering. We have simulated the JSA for each of this configuration and found that the simulation agrees with the experimental result. As expected from the JSA, the wider bandwidth pump pulse causes higher purity for the same filter bandwidths. At wider filter settings, the separability of the JSA is governed by the energy conservation (pump envelope) of the SFWM photon-pairs, and wider pump translates to more separable JSA. At narrower filter settings, the purity is strongly dependent on the spectral filtering. When both settings of the pump's spectral width are normalised with respect to the filter's spectral width (Eq. 7.1), the two curve coincides. Thus, from an analytical point of view, this ratio sets the spectral purity rather than the actual values of the spectral widths. Also, this higher purity using spectral filtering comes at the cost of reduced brightness [151]. Even with the reduction of the brightness, experiments based on post-selection of two-fold coincidence events, which do not necessarily require high brightness, can benefit using the waveguide HSPSs. The obvious advantage of using a waveguide HSPS compared to a micro-ring resonator HSPS is its robustness to the environmental change and low maintenance. In contrast, a micro-ring resonator HSPS requires resonance alignment and stabilisation as mentioned in the last chapter.

We have performed off-chip PIM using HOM interferometer with the broader pump configuration for two different spectral filtering settings (narrower and broader) to observe the effect of purity on PIM. At both of these filter settings, we have varied the input pump power to see the effect of multi-pair contribution on PIM. We have observed the highest HOM interference visibility, with narrower filter settings and low input power, as expected. These data also show that spectrally filtered and reduced brightness photon flux used to increase visibility values resulted in large integration time to record one event. That makes performing a multi-photon (higher than 2-folds) experiment with waveguide HSPSs challenging. Using a higher repetition rate laser may be an experimental solution for our design of nanowire HSPSs. Yet, scaling up a quantum experiment with our waveguide HSPSs will make the duration of the data collection longer. Even with very high collection efficiency VGCs, the use of waveguide HSPSs may limit the on-chip quantum experiment up to a few fold (less than 10) coincidence events. In future, designing lower propagation loss waveguides with appropriate dispersion engineering may result in brighter and purer waveguide HSPSs.

PART IV

Applications of PIMs

The knowledge of on-chip PIM circuits can be readily useful for multi-photon experiments as described in the next chapter. The experiment considered here is quantum teleportation where the raw indistinguishability of the HSPSs limits the fidelity of the teleported state.

Chapter 8

Applications of PIM circuits

Contents

An ideal single-photon source is a requirement for many quantum photonic applications. In previous chapters, investigations of PIM on two integrated HSPSs explores the HSPSs' performance to build larger circuits. In this chapter, we will investigate a specific application: quantum teleportation from the point of view of PIM. In this experiment, three micro-ring resonator HSPSs are integrated to implement a standard teleportation protocol.

The circuit used for this experiment has been designed and fabricated jointly by Jianwei Wang and Yunhong Ding of QET Labs and DTU respectively. The circuit reconfiguration, data collection and analysis were performed by Jianwei Wang, Dan Llewellyn, Stefano Paesani, Davide Bacco and myself. The project was supervised by Mark G. Thompson (QET Labs) and Leif K. Oxenløwe (DTU).

8.1 Optimising teleportation experiment using PIM

Quantum teleportation refers to the transfer of the information of a quantum state of a qubit to another qubit using ancillary qubits in Einstein-Podolsky-Rosen (EPR) state (e.g. Bell state) [156]. Once transferred, the original qubit looses the information of the quantum states. At first instant, quantum teleportation of qubits may seem unnecessary compared to data transfer using classical bits. In classical computers, a bit can be deterministically copied from one location to another as many times as needed. According to the *No cloning theorem* [157–159], a quantum state cannot be copied with 100% certainty[16]. Therefore, quantum teleportation is the way to fully transfer a quantum state of a qubit from one party to the other. Quantum teleportation was experimentally demonstrated by [162, 163].

[16] *No broadcast theorem / Superbroadcasting* [160], imperfect copies [161]

In this section, first a basic textbook teleportation scheme is presented, then the corresponding photonic circuit diagram is described with the specific uses of PIM. Lastly, the results from this experiment are analysed.

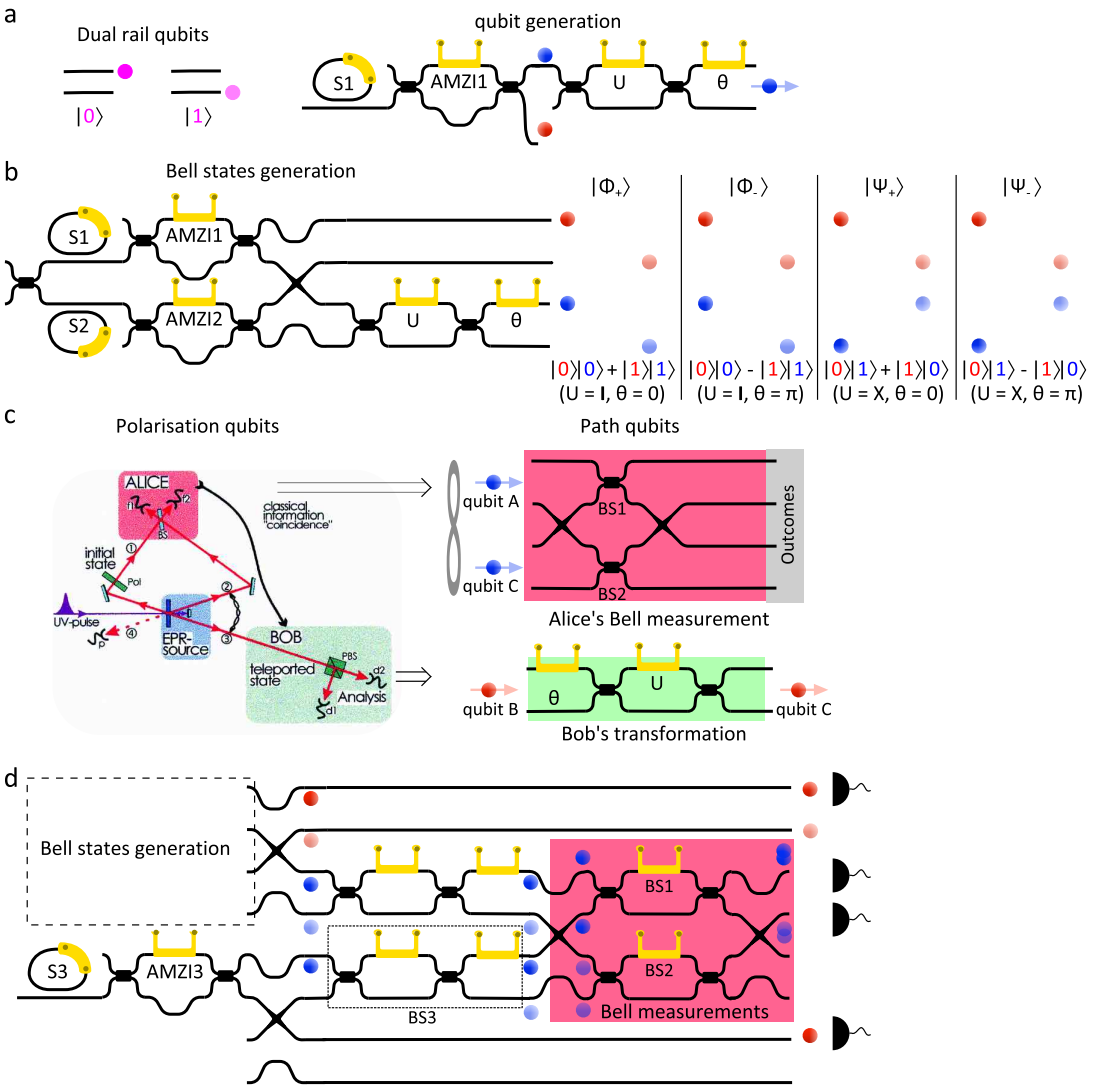

Figure 8.1: On-chip implementation of standard teleportation protocol. (a) The definition of a qubit in terms of dual rail path encoded photons. The actual position of the photons in one of the rails of the waveguides defines the value of the qubit to be $|0\rangle$ or $|1\rangle$. Signal and idler photons of a photon-pair from a micro-ring resonator HSPS produce one qubit each. (b) Maximally entangled Bell states shared by Alice (blue qubit) and Bob (red qubit). The photon-pairs are generated from micro-ring resonator HSPSs S1 and S2 and the AMZIs are used to separate the signal and idler photons. It is assumed that only one of the HSPSs will generate signal-idler photon-pairs at a time, thus making the combined signal and idler qubits entangled. Applying proper unitary operation U and phase shift θ, one of the four Bell states can be chosen. (c) Alice's Bell measurement circuit teleports the information from qubit C to qubit B. The relation between path and polarisation implementation is indicated by the arrows. The polarisation implementation diagram is adapted from [162]. (d) Alice prepares a single qubit in $|+\rangle_C$ state. Then performs a joint Bell measurement with qubit C and qubit A of the Bell state $|\Phi_+\rangle_{AB}$. The outcome is projected into $|\Phi_+\rangle_{AC}$, resulting into the teleported state $|+\rangle_B$ after an appropriate unitary operation on Bob's qubit.

8.1.1 The teleportation protocol

Let's consider that Alice will teleport the state of a quantum particle to Bob. The textbook protocol of quantum teleportation consists of the following [164]:

① Alice prepares the quantum state for teleportation, e.g.

$$|\psi\rangle_C = \alpha|0\rangle_C + \beta|1\rangle_C \tag{8.1}$$

Experimentally, such a qubit can be defined by dual rail path encoded photons as shown in Fig. 8.1 (a). In SOI circuits, using a micro-ring resonator HSPS, an AMZI spectral demultiplexer and a MZI (& a phase shifter) as a unitary, path encoded qubits can be generated for each signal and idler photons.

② Alice and Bob share one of the four maximally entangled Bell states which will be used for teleportations,

$$|\Phi_\pm\rangle_{AB} = \frac{1}{\sqrt{2}}\left(|0\rangle_A|0\rangle_B \pm |1\rangle_A|1\rangle_B\right) \tag{8.2}$$

$$|\Psi_\pm\rangle_{AB} = \frac{1}{\sqrt{2}}\left(|0\rangle_A|1\rangle_B \pm |1\rangle_A|0\rangle_B\right) \tag{8.3}$$

where the subscripts A and B represents Alice and Bob respectively. The Bell states are mutually orthogonal.

Bell states generation is enacted by the photonic circuit shown in Fig. 8.1 (b). Here two sources S1 and S2 are used to generate two qubits. Assuming only one of the sources S1 or S2 will generate photon-pairs at a time, the two qubits are superposed. This forms the basis of Bell states generation. Using a unitary and a phase shifter any of the Bell states can be prepared. Here, Alice is associated with the blue qubit and Bob is associated with the red qubit. Due to the assumption that only one or the other source will fire at a time, these two qubits become entangled and form a Bell state. If both sources generate photon-pairs at the same time, the resulting state will be invalid according to the definition of qubit.

③ Alice performs a Bell measurement on the state $|\psi\rangle_C$ together with one of the qubits from the Bell states, say qubit A from $|\Phi_+\rangle_{AB}$. In order to understand the implication of Bell measurement, let's first rewrite the status of the qubits just before the measurement,

$$|\psi\rangle_C|\Phi_+\rangle_{AB} = (\alpha|0\rangle_C + \beta|1\rangle_C)\,\frac{1}{\sqrt{2}}\left(|0\rangle_A|0\rangle_B \pm |1\rangle_A|1\rangle_B\right) \tag{8.4}$$

$$\begin{aligned} &= \frac{1}{2}\big(|\Phi_+\rangle_{AC}\,(\alpha|0\rangle_B + \beta|1\rangle_B) + |\Phi_-\rangle_{AC}\,(\alpha|0\rangle_B - \beta|1\rangle_B) \\ &\quad + |\Psi_+\rangle_{AC}\,(\beta|0\rangle_B + \alpha|1\rangle_B) + |\Psi_-\rangle_{AC}\,(\beta|0\rangle_B - \alpha|1\rangle_B)\big) \end{aligned} \tag{8.5}$$

Where the last line is only a change into Bell state basis and no measurement has been performed by Alice or Bob yet. The reason for the above decomposition is that Alice's Bell measurement uses Bell states bases. Now, Alice performs a measurement using the states A and C with one of the Bell states. As the Bell states are orthogonal, the measurement will project into only one of the above four terms with equal probability. For example, if Alice's measurement basis was $|\Phi_+\rangle_{AC}$, then Bob's state reduces to $(\alpha|0\rangle_B + \beta|1\rangle_B)$.

In terms of the photonic circuit, Alice's Bell measurement with path qubit is shown in Fig. 8.1 (c). Inside this mapping, there are two waveguide crossings representing swap operations. This indicates the assumption of indistinguishable single-photons from both of the qubits.

Let's consider that Alice will transfer the quantum state $|+\rangle_C$ to Bob, produced by the third source S3 in Fig. 8.1 (d). This is used for Bell measurement with previously generated qubit A from the Bell state $|\Phi_+\rangle_{AB}$. At the two MZIs, which are set as beam-splitters (BS1 & BS2) configuration, the blue photons from S1 and S2 undergo quantum interferences with blue photons from S3. Detecting the photons from both of the output ports of the MZI and the idler photon from the S3 projects Bob's qubit into $|+\rangle_B$.

④ Alice sends one of the four outcomes of her measurement (in our example it is $|\Phi_+\rangle_{AC}$) to Bob using two classical bits (total 4 possibilities). Once Bob knows Alice's outcome ($|\Phi_+\rangle_{AC}$), he performs an appropriate unitary operation (in this case identity) to his qubit B (that was entangled with qubit A). This operation projects his qubit to the desired state ($|+\rangle_B$). For Alice's other three measurement outcomes, he can perform appropriate unitary operations to recover the quantum state $|\psi\rangle_B$ in his basis. Here only the quantum state of $|\psi\rangle_C$ has been transferred to $|\psi\rangle_B$, the physical qubit $|\psi\rangle_C$ has not been sent to Bob.

In terms of the photonic circuit, Bob's unitary operation is shown in Fig. 8.1 (c).

8.1.2 Experimental setup

The experimental setup and the full photonic circuit is shown in Fig. 8.2. The experimental setup is essentially the same from the PIM of Sec. 6.5. The experimental considerations for making micro-ring resonators indistinguishable for a PIM has been applied in this setup for all three micro-ring resonators. We have measured the mutual indistinguishability of the three micro-ring resonators and found that their visibilities are similar to each other. The spectral responses of all three micro-ring resonators are also found to be similar to each other.

During the experiment, source S3 is used to generate $|0\rangle_C$, $|1\rangle_C$, $|+\rangle_C$, $|-\rangle_C$, $|+i\rangle_C$ and $|-i\rangle_C$ states using the part of the circuit labelled as *state preparation*. After the mixing the photons are detected by four detectors at the four output ports shown in the figure. These are recorded using the photon's arrival times and post-processed to extract the 4-fold coincidences.

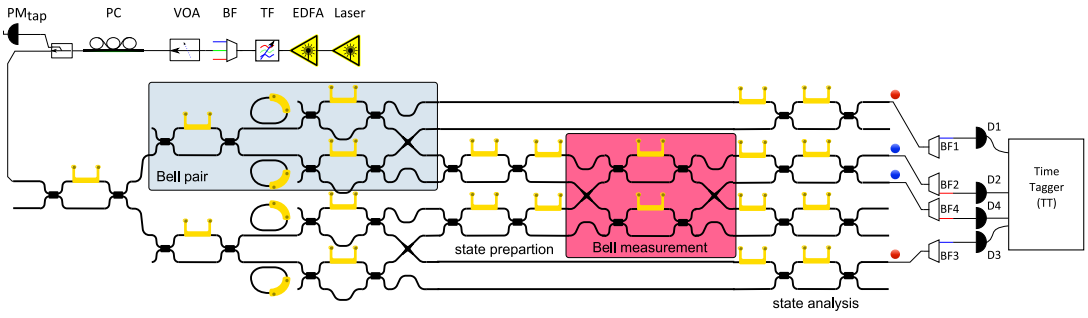

Figure 8.2: The experimental setup and the circuit diagram of the teleportation chip. The experimental setup follows the PIM setup mentioned in Sec. 6.5.

8.1.3 Result and analysis

The results of the teleportation experiment have been analysed in terms of the state fidelity. State fidelity reveals the degree of resemblance between a teleported state and the actual measured state. If our target state is $|\sigma\rangle$ (density matrix $|\sigma\rangle\langle\sigma|$) and the measured

state is $|\psi\rangle$, then fidelity (F) can be represented as an inner product,

$$F = \langle\psi|\sigma\rangle\langle\sigma|\psi\rangle \tag{8.6}$$

State	$\|0\rangle$	$\|1\rangle$	$\|+\rangle$	$\|-\rangle$
F (%)	87.4	90.4	74.5	74.6

Table 8.1: Fidelity of the teleported states.

Table 8.1 shows the fidelity of the teleported state in our experiment. The fidelity values show quantum correlations, as all of them are higher than 66%. Similarly with the PIM analysis in the previous chapters, the major reason for the reduction in the fidelity is due to the imperfect indistinguishability of the HSPSs. In particular, during the Bell measurement, the visibility of the quantum interference is reduced by the multi-pair emissions affecting the measurement outcomes. Here, high power and low power correspond to $\sim 0\ dBm$ and lowering the power tend to improve the fidelity.

8.2 Synopsis & outlook

In this chapter, the use of PIM for a quantum photonic application, teleportation, has been demonstrated. A high fidelity teleportation requires at least three highly indistinguishable HSPSs with high photon-number purity which is one step forward towards scalability from the PIM experiments with two HSPSs. In future, more quantitative analysis of the quality of PIM on this experiment will be performed.

There is a growing need to identify which source design will be the best for a specific quantum photonic experiment. While some algorithms require high indistinguishability, other algorithms may require only high brightness. The broader definition of PIM encompassing not only spectral correlation but also multiple spatial modes, polarisation mode, path modes etc. will have a positive impact on understanding higher-dimensional experiments.

Chapter 9

Conclusion

A single-photon has many physical properties. Widely used and cross-disciplinary examples of single-photons such as photosynthesis or photoelectric effect only distinguish photons based on their colour (energy of the photon). However, a quantum photonic experiment considers all the attributes of the single-photons. When single-photons, emitted from multiple emitters, are bright, in a single optical mode (pure) and indistinguishable from each other in all aspects, the emitters are called ideal single-photon sources. In particular, the indistinguishability of a single-photon source is a true measure of building a large circuit with multiple sources.

Ideal single-photon sources are a prerequisite for many of the futuristic quantum photonic applications (e.g. quantum computing). There are a few photonic platforms in the race of achieving near ideal single-photon sources. We have chosen silicon on insulator (SOI) photonics for its mature fabrication technology, plethora of standard photonic components, promise of scalability and existing roadmap to electronic integrations [18].

9.1 Summary

In this thesis, two well-known structures in the SOI platform have been chosen to investigate the attributes of heralded single-photon sources (HSPSs). One of these structures is nanowire or strip waveguide which is widely used as an HSPS. The other one is micro-ring resonator which is intrinsically brighter and purer than the waveguides due to resonant enhancement. Both of these structures generate signal-idler photon-pairs through spontaneous four wave mixing (SFWM) process. In the literature, the brightness and purity of these two structures have been investigated but the indistinguishability has scarcely been explored. In a handful of experiments, the indistinguishability of the waveguide HSPSs have been estimated but without putting it into the quantitative context of spectral purity. In contrast, the indistinguishability of heralded single-photons from multiple micro-ring resonator HSPSs has not been investigated in SOI or any other photonic platform. For a single-photon source to be ideal, it has to be bright, pure and indistinguishable with respect to each other. Therefore, to benchmark the waveguide and resonator HSPSs in SOI, we need to measure brightness, purity and indistinguishability of the single-photons simultaneously. Also, the experimental conditions that may affect these attributes need to be identified. We have termed these experiments: photon indistinguishability measurements or in short PIMs.

We aimed to perform both on-chip PIM and off-chip PIM. The off-chip PIM is the common

method to determine indistinguishability of the HSPSs. An off-chip PIM mostly involves setting up a Hong-Ou-Mandel interference experiment and interfering single-photons from multiple HSPSs as a function of the arrival time of the photons' wavepackets. Off-chip PIM design mainly requires multiple SOI HSPSs on-chip. In contrast, on-chip PIM involves interfering single-photons on an on-chip Mach-Zehnder interferometer. Thus, it also requires on-chip integration of signal-idler spectral demultiplexer and pump-rejection filters. Designing and performing on-chip PIM is also useful in understanding the characterisation procedures and the extraction of indistinguishability information of an array of HSPSs integrated into a large scale quantum photonic circuit.

We have chosen standard components in silicon photonics to design both on-chip and off-chip PIM. First, we have performed dispersion simulation to choose the waveguide cross-sectional area. The height of the waveguides (and all other photonic components) were $220\ nm$ as set by the foundry (IME) who fabricated the devices. We chose a width of $450\ nm$ that ensured a single spatial mode, and excellent very low polarisation mode mixing, thus ensuring purity in those attributes. The waveguide dimensions also influence the total dispersion such that the phase-matching function of the SFWM is near unity in the collection wavelengths of signal and idler photons. Next, based on the linear propagation loss quoted by the foundry ($\sim 3\ dB/cm$), we have performed simulations to choose the length of the waveguide HSPSs ($L = 14\ mm$) and coupling coefficients of the resonator HSPSs ($Q \sim 50 \times 10^4$). These simulations are based on the literature to maximise the brightness of our sources. Additionally, the cavity length of the resonator HSPSs and the resonator filters along with the path length difference in AMZI filters were chosen to match the free spectral range (FSR) of the off-chip high extinction pump rejection DWDM filters.

Once the HSPSs are designed for the maximum brightness, we have investigated the experimental conditions such as the pulse width of the laser light for maximum spectral purity. The spectral purity is expressed by joint spectral amplitude (JSA) and related to the energy conservation (pump pulse-width) and momentum conservation (dispersion relation) of the signal-idler photon-pairs generation. Our current waveguide HSPSs require spectral filtering to achieve adequate spectral purity. Our resonator design (linewidth: $30\ pm$ FWHM) does not require spectral filtering but requires minimum FWHM of $200\ pm$ of the pulses to achieve maximum 92% spectral purity. This value agrees with the literature [34] for our basic resonator design. Recent theoretical proposals [64–66] in the literature suggest higher than 99% purity through compound structures or pump pulse modifications. We have also simulated the effect of resonance splitting on the purity which is a common phenomenon for practical resonators. For a practical value of splitting $< 10\ pm$, the simulation suggests $\sim 90\%$ purity which is close to the optimum value.

We have simulated the imperfections that may occur in photonic circuits and affect the PIM. In this analysis, the imperfections of our waveguides and micro-ring resonators, in terms of spectral purity and multi-pair contributions were also considered. We have plotted the interference visibility as a function of average photon-number per pulse for both pure and impure HSPSs. Our simulation suggests that the interference visibility in a PIM is affected more drastically by multi-pair contributions. This model has also been used to fit the experimental PIM data.

Experimentally, we have reported, for the first time, PIM of micro-ring resonator HSPSs. Our PIM shows a MZI visibility of 72% of the resonator HSPSs fabricated by IME foundry. As expected from the simulation, we found that this value is mainly contaminated by the multi-pair contribution. If corrected for multi-pairs, we found the visibility reaches 92% where it is intrinsically limited by our basic resonator design. We have measured

the mutli-pair contributions on-chip with a reconfigurable photonic circuit (DTU-tele). A direct subtraction of the multi-pair contribution shows a visibility close to $89 \pm 3\%$. Also, the experimental plot of the visibility as a function of average photon number per pulse indicates that if the multi-pair emissions are mitigated, we can improve the visibility to 92%. Multi-pair emissions can be removed by using photon-number resolving detectors or reducing the input power in future experiments. It is worth emphasising here that our detection efficiency per signal/idler channel was between $\sim 1\%$ and $\sim 2\%$. This translates between $\sim 80\ dB$ to $\sim 70\ dB$ total loss for a 4-fold coincidence measurement. If we can improve this huge headroom of efficiency, we can lower the input power and reduce the multi-pair emission sufficiently. That will make our current resonator design comparable to the state of the art SPDC HSPSs in terms of simultaneous high brightness and high indistinguishability.

A thorough understanding of waveguide PIM has been experimentally observed. The purity as a function of spectral filtering has been investigated. Based on these purity data, off-chip PIM has been performed. The best HOM visibility we achieved was $86 \pm 1\%$ which is near the best-reported value in the literature $88 \pm 8\%$ [58]. We have also designed on-chip tuneable bandwidth low loss spectral filters. In future, on-chip spectral filtering will be employed to improve the photon counts of waveguide HSPSs while achieving high purity.

Lastly, the DTU-tele chip was used for a specific multi-photon experiment, quantum teleportation to investigate the effect of PIM on the fidelity of the teleported state. As such experiments require perfect interference among multiple qubits, we found that the indistinguishability (spectral impurity & multi-pair contribution) affects the maximum achievable fidelity.

To conclude, we have achieved a thorough understanding of the waveguide HSPSs purity and its relation with indistinguishability. We have also experimentally observed single-photon indistinguishability from micro-ring resonator HSPSs for the first time. From the point of view of multi-photon experiments, in future, we will explore the design parameter space to achieve near unity indistinguishability.

9.2 Future work

The results obtained in this thesis have opened up new possibilities and indicated a few ways to achieve near unity indistinguishability. In the near term, the following outcomes are desirable:

① Find a better expression for the PIM coefficient ($\mathbb{C}_{\mathrm{PIM}}$ of Sec. 2.2.5) for comparing any SPSs. This will enable us to compare different quantum photonic platforms.

② If the loss per signal-idler channel is improved to near unity, using photon-number resolving detectors (PNRDs) for PIM will immediately result in high brightness and high raw indistinguishable HSPSs simultaneously. PNRDs will relax the condition of reducing the power to reduce multi-pair contribution and achieve multi-photon experiments with more than two qubits interferences (e.g. 6-folds, 8-folds etc.).

③ To date, higher than 95% raw indistinguishability has not been observed in any photonic platform. In this thesis, only two SOI structures were investigated as HSPSs. Even if we put aside the two theoretical proposals of a compound structure with high purity [64, 65], there are immense possibilities with SOI to achieve near ideal single-photon sources. A few of the structures that promise higher purities are compound resonators (e.g. MZI-resonators), photonic crystal cavities, pulley micro-ring

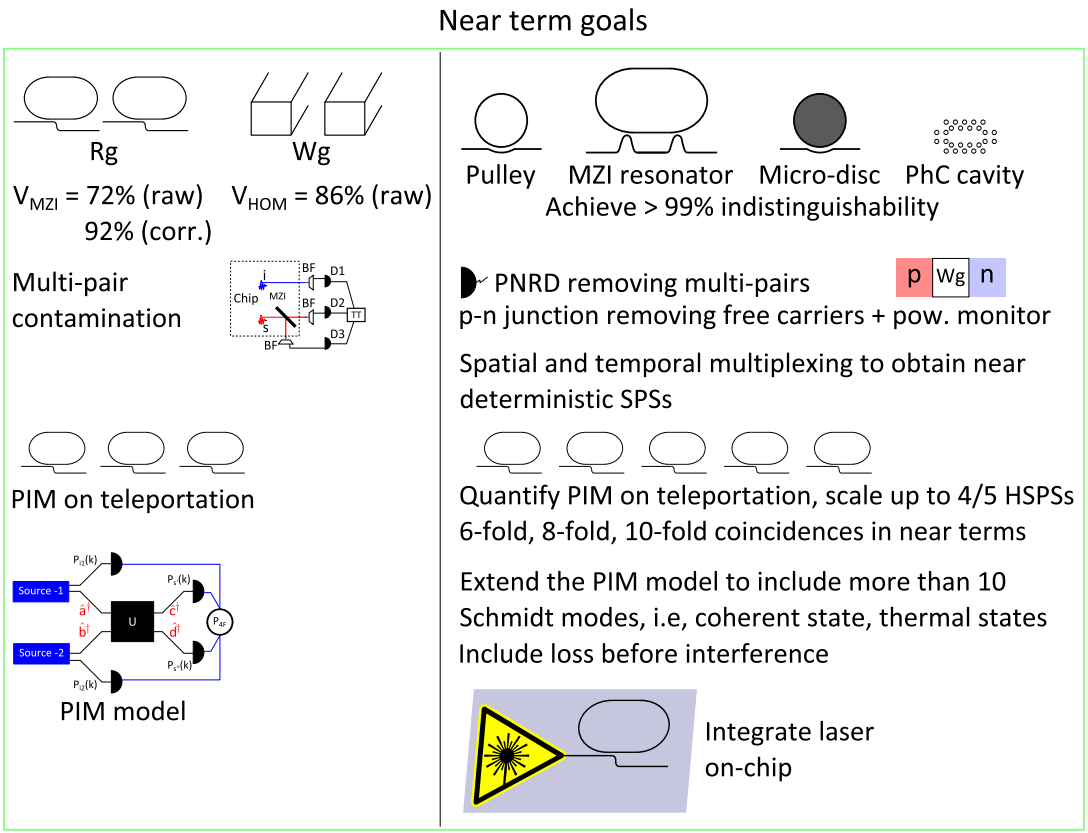

Figure 9.1: One of the important near-term goals is to use the results obtained from the presented experiments and achieve $> 99\%$ indistinguishability with high brightness.

resonators, multi-mode waveguides. We aim to achieve 99% raw indistinguishability with the aforementioned structures.

④ Once a high indistinguishability HSPSs is achieved, we can use spatial and temporal multiplexing schemes to obtain near deterministic SPSs.

⑤ The use of high repetition rate laser such as the ultrafast optical clock (UOC) will further increase the brightness while lowering the multi-pair contribution. If the slower free-carrier dispersion becomes challenging due to the high repetition rate, we can employ reverse-biased p-n junction to sweep off the carrier.

⑥ In terms of simulations, the device imperfection model presented in this thesis only considers two Schmidt modes and no loss before the interferometer. This model can be extended to an arbitrary number of modes (e.g. 10) which can then mimic any kind of quantum state such as coherent state and thermal state rather than the only two-mode squeezed state. Although for on-chip PIM, there is almost no loss before the interference, the inclusion of loss will make the model more realistic.

⑦ We have found that the $g^{(2)}$ measurements and the JSA predictions of purity for micro-ring resonators do not agree with each other. Experimental and theoretical investigation of this discrepancy, such as measuring JSA and JSP with high-resolution instruments, will help us understand the truer characterisation process of the purity. It will also reveal if there is any practical limitation in achieving high purity which is not included in the theory.

⑧ Quantifying thermal crosstalk will help us in future to develop higher density photonic circuit with multiple micro-ring resonators.

⑨ Quantifying the teleportation fidelity as a function of PIM will be useful to find the limit of such photonic circuits and indicate ways to improve the future designs.

SFWM is a $\chi^{(3)}$ process which in SOI includes non-linear losses (two-photon absorption, free carrier dispersion) and other parasitic effects. They are all inter-related through the pulse propagation equations such as non-linear Schrodinger equations (NLSEs). A basic split step simulation of the coupled NLSEs for the waveguide HSPSs has been developed. Once completed, it will give us more understanding of the device physics and its implication on the brightness, purity and indistinguishability of the waveguide HSPSs. Eventually, this model will be extended for the micro-resonator HSPSs. In recent years, Lugiato-Lefever equations have been used to explain the physics of micro-ring resonators in the context of optical frequency combs. It will be illuminating to use those equations in the context of our HSPSs.

To counteract non-linear carrier generated losses, the use of active devices such as reverse bias p-n junction across the HSPS to sweep out the carriers can be a practical solution. This method is also useful to monitor the optical power inside the HSPSs. Changing the material platform to a higher band-gap material such as silicon nitride (promising higher Q resonator with a lower loss) or changing the operating wavelength to $2\ \mu m$ have been popular choices to avoid non-linear losses. In that context, using a direct band-gap material such as GaAs or InGaAs, which also have high-performance electronic components, may also be worthy to implement indistinguishable HSPSs. In these material platforms, the laser light can also be integrated on the same chip. Some of these platforms are CMOS compatible. Also, hybrid integration of electronic platform or laser source with SOI will be a technologically sound way to put all the functionalities on the same chip.

This image is drawn by artist Milica Prokic based on our search for the perfect geometry of a resonator to achieve pure single-photons. The drawing is influenced by spectral correlations, tessellation and the word Metatron (he who sets boundaries, the measurer). The work was commissioned by QET Labs and funded by EPSRC.

Appendix A

TE vs TM: temperature dependence and phase matching

Contents

The group index (n_g) and the effective index (n_{eff}) of a waveguide mode depend on many factors, including the wavelength of the propagating light, refractive index of the material, the waveguide geometry and the orientation of electromagnetic field inside the waveguide such as *Transverse Electric* (TE) field and *Transverse Magnetic* (TM) field propagation. As the refractive index of the material depends on the temperature, TE and TM light experience different propagation responses due to temperature change and therefore the n_g and n_{eff} varies as a function of the temperature. Here, we used interferometers which only sustain either TE or TM mode, and from the temperature induced shift of the interference pattern, we quantified the effect of temperature on n_g and n_{eff} of these modes.

The analysis presented here followed the outlines of the edX UBCx Phot1x Silicon Photonics Design, Fabrication and Data Analysis course, which is supported by the Natural Sciences and Engineering Research Council of Canada (NSERC) Silicon Electronic-Photonic Integrated Circuits (SiEPIC) Program.

A.1 Introduction

A silicon photonics waveguide can have electromagnetic field of the propagating light oriented in many ways. These orientations are primarily categorised as TE and TM modes of light propagation. A pure TE or transverse electric field propagation has the electric field parallel to the wafer and continuous on the interface of the sidewall of the waveguide and the cladding (e.g, air). In contrast, a pure TM propagation has the electric field perpendicular to the wafer and does not require continuity on the sidewall interface (Sec. 3.1.1). Due to the difference in electric field orientation, the propagating light sees different

waveguide cross-sections and the environment which results in different effective index (n_{eff}) and group index (n_g) for TE and TM propagation. Moreover, as refractive index of the silicon depends on the temperature, TE and TM will respond differently to this temperature variation. Therefore any change in the environment, surrounding the waveguide, will influence the TE and TM modes which may affect the performance of the particular photonic component. As this environmental change may cause a very small change in the refractive index, a highly sensitive measurement quantity is required. For example, an interference pattern of an asymmetric Mach-Zehnder interferometer is highly sensitive to the phase of propagating light which can be affected by the environmental temperature variation. Thus by monitoring the position of the wavelength corresponding to the constructive and destructive interference of light, we can quantify the effect of temperature variation on the TE and TM light propagation.

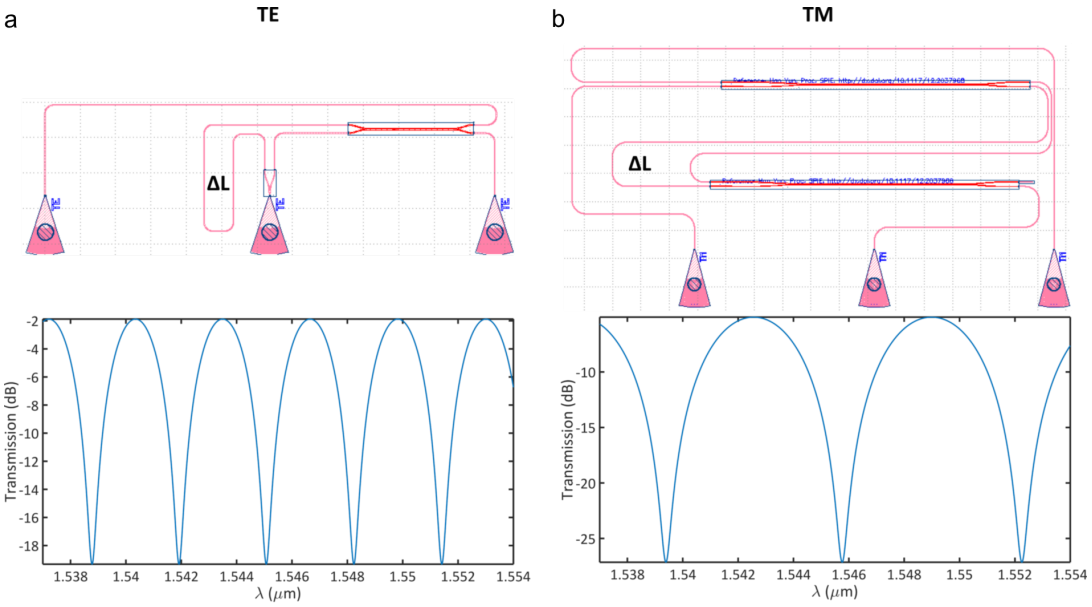

Figure A.1: At the top are typical layouts of Mach-Zehnder interferometer for (a) TE with path length difference of $\Delta L = 179.838\ \mu m$ and (b) TM modes with path length difference of $\Delta L = 105.018\ \mu m$. Below are the corresponding interference fringes generated using the compact waveguide model. With the shorter path length difference for TM-MZI, the lower group index of TM modes results into an even shorter optical length ($n_g \times \Delta L$) and therefore larger FSR compared to the TE-MZI.

A.2 Modelling and simulation

An asymmetric Mach-Zehnder interferometer has imbalanced path lengths in it's two arms as shown in Fig. A.1. Thus, different wavelength of light accumulates different phase in each arm as a function of wavelength as n_g and n_{eff} depends on the wavelength. This corresponds to the constructive and destructive interferences of light at different wavelengths.

In order to simulate the effect of temperature on the interference pattern, we first need the compact waveguide model based on n_g and n_{eff} as a function of wavelength. Afterwards, this model will be incorporated into phase accumulation of the transfer function of the interference pattern. Lastly, the effect of temperature change on n_g and n_{eff} will be calculated.

Using a typical dimension of the waveguide of $500\ nm$ of width and $220\ nm$ of height, the *Lumerical Mode Solver* can generate the appropriate effective and group index as a function of wavelength (as shown in the course [145,165]) as a Taylor expansion. Table A.1 corresponds to the compact model for the waveguide: $n_{eff}(\lambda) = n_1 + n_2(\lambda - \lambda_0) + n_3(\lambda - \lambda_0)^2$. In addition, the group index is defined using n_{eff} through a linear model: $n_g = n_{eff}(\lambda) - \lambda \frac{dn_{eff}}{d\lambda}$.

Table A.1: Compact waveguide model for TE and TM mode: $n_{eff}(\lambda) = n_1 + n_2(\lambda - \lambda_0) + n_3(\lambda - \lambda_0)^2$

Mode	n_1	n_2	n_3	n_g at 1.55 μm
TE	2.4473	−1.1327	−0.0440	4.181
TM	1.7689	−1.1259	1.9140	3.713

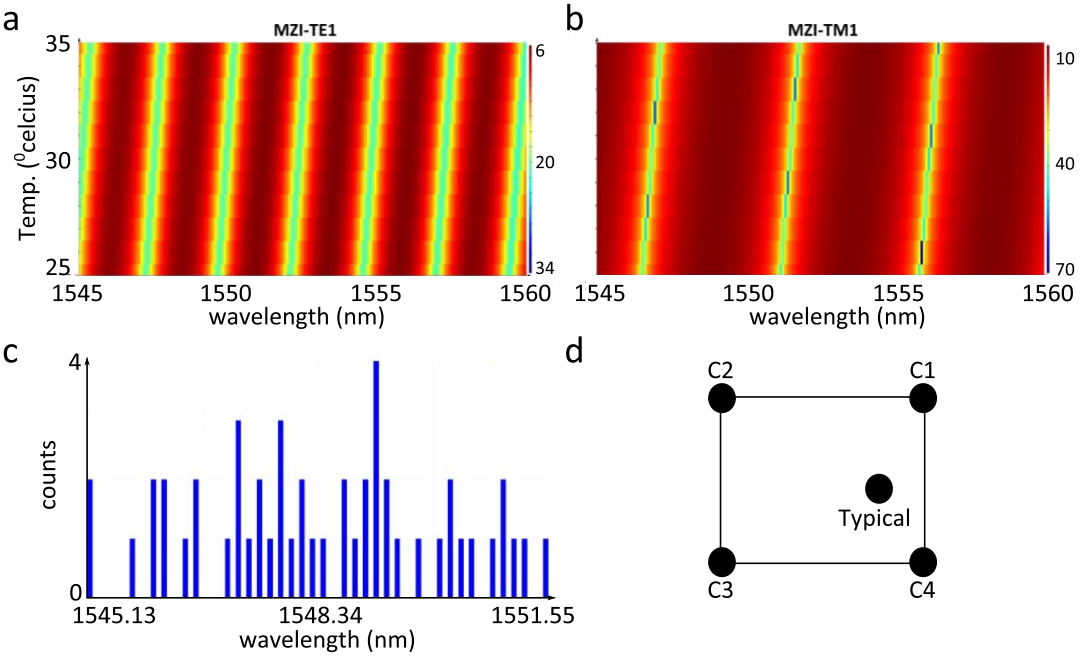

Figure A.2: TE & TM comparisons and corner analysis. (a,b) *Lumerical Interconnect* simulation of the interference fringe of devices *MZI-TE1* and *MZI-TM1* as a function of temperature. This simulation also confirms the higher temperature dependence of TM mode compared to TE. (c) Monte Carlo simulation of the MZI-TM1 device shows standard deviation of central wavelength $1.66762\ nm$ with mean $1548.41\ nm$. (d) The four corners of the *Corner Analysis* with dimensions of the waveguides: C1(470, 223.1), C2(510, 223.1), C3(510, 215.3) and C4(470, 215.3).

A.2.1 Transfer functions

Transfer function of the Mach-Zehnder interferometer used for the simulation and also to fit the data is,

$$F = 10\log_{10}\left(\frac{1}{4}\left|1 + \exp\left[-i\frac{2\pi n_{eff}}{\lambda}\Delta L - \frac{\alpha}{2}\Delta L\right]\right|^2\right) + b \tag{A.1}$$

Here, the propagation constant is $\beta = 2\pi n_{eff}/\lambda$, and the path length difference between the two arms of the interferometer is ΔL, α is the propagation loss of the waveguide while b is the extra insertion loss of the device if fitted well. The fitting of the MZI data was done

using the *findpeaks method* in matlab. A few additional Monte Carlo simulations were done for $MZI-TE1$ and $MZI-TM1$ devices to see the fabrication tolerance.

A.2.2 Simulation on temperature effect

Using *Lumerical Mode Solver*, at $1.55\ \mu m$ light-waves, the change in the value of n_{eff} and n_g for quasi-TE mode and for quasi-TM mode are plotted in Fig. A.3. The *Lumerical Interconnect* can also be used to simulate this temperature effect on the interference pattern of the MZI. Figure A.2 (a,b) contains such a plot where the movement of the wavelength positions of the constructive and destructive interferences are quantifiable.

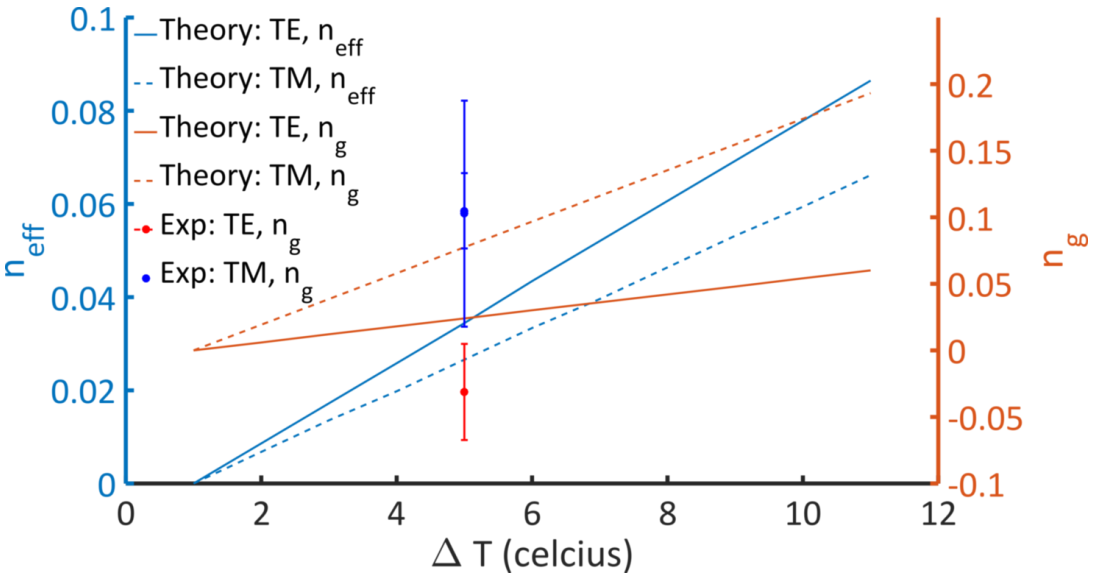

Figure A.3: A plot of effective index n_{eff} and group index n_g as a function of temperature change. The theory results are extracted from *Lumerical Mode Solver* simulations as described in the course. The experimental results are extracted from the MZI fitting of group index from the measurements at 25 degree and 30 degree celcius for TE and TM MZI.

A.2.3 Corner analysis on the waveguide model

For both TE and TM designs, 4 corners and one typical design—total of 5 waveguide models are chosen for the corner analysis. Considering the typical design is for 500×220 waveguides at 1.55 μm wavelength, the four corners are (470, 223.1), (510, 223.1), (510, 215.3) and (470, 215.3) and the outcome of the corner analysis is tabulated in Tab. A.2 below. The group index in the Tab. A.2 are at wavelength 1.55 μm.

A.3 Fabrication

The designs were fabricated in *Applied Nanotools, Inc. NanoSOI process* as described in [145]. In the rest of the report, only four devices will be discussed:

① *MZI-TE1* with $\Delta L = 179.838\mu m$,

② *MZI-TE2* with $\Delta L = 307.337\mu m$,

③ *MZI-TM1* with $\Delta L = 105.018\mu m$ and

④ *MZI-TM2* with $\Delta L = 385.416\mu m$.

Table A.2: Corner analysis for TE and TM modes: $n_{eff}(\lambda) = n_1 + n_2(\lambda - \lambda_0) + n_3(\lambda - \lambda_0)^2$

Mode	Corner	n_1	n_2	n_3	n_g	FSR-MZI-1
TE	1	2.40270	−1.19925	−0.05160	4.238	1.817
TE	2	2.47130	−1.10631	−0.04590	4.167	1.848
TE	3	2.43992	−1.11858	−0.031590	4.160	1.851
TE	4	2.37158	−1.20970	−0.03171	4.230	1.820
TM	1	1.76577	−1.28920	1.87496	3.742	2.777
TM	2	1.79755	−1.33095	1.74698	3.831	2.712
TM	3	1.74524	−1.20817	1.85858	3.560	2.919
TM	4	1.71688	−1.15964	1.94513	3.481	2.985

A.4 Experimental data and Analysis

The measurements of the devices were performed by the edX course associates as mentioned in [145] and the analysis was performed by us.

From the fitting of the measurement data, Fig. A.4 shows the graph of extracted group index n_g from experimental data as a function of wavelength in comparison to the simulation. It is evident from the graphs that the TM mode has lower group index but experience higher dispersion compared to the TE mode.

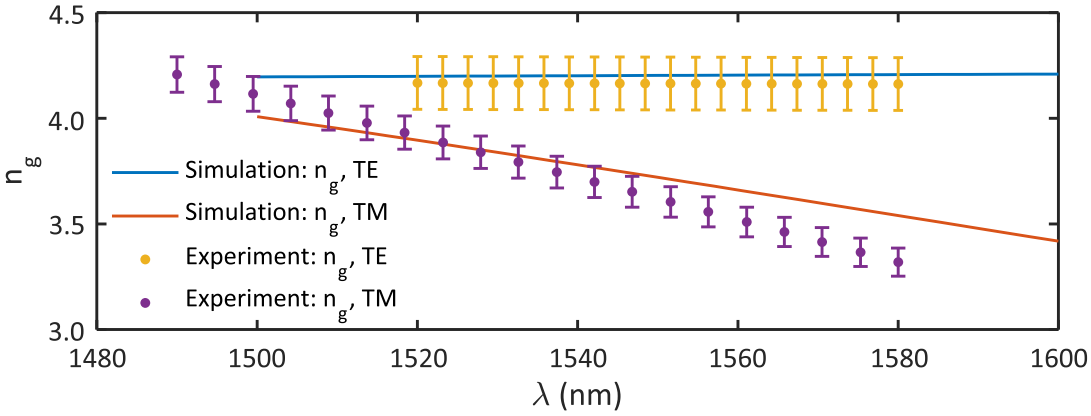

Figure A.4: Simulation vs the extracted group index for TE and TM MZI shows good agreement.

The same method is used to extract the group index from the measurement of the all four MZI devices at two different temperatures and plotted in Fig. A.3. Table A.3 shows that the measurement data for the device MZI-TE2 at 25 degree celcius was noisy with low resolution and the fitting error was large (16%) such that the n_g seems to decrease with temperature. This data point was excluded from the graph. More measurements at different temperatures would be more conclusive determining the behaviour of the optical modes.

The extracted group index n_g of all four devices are within the ranges of corner analysis performed earlier. This indicates that the usual assumption in corner analysis is reasonable in considering the imperfections of the fabricated devices.

Table A.3: Extracted group index from TE and TM MZI at different temperature

Device	Temp. (°celcius)	n_g at 1.55 μm	Fitting error
MZI-TE1	25	4.1648	3%
MZI-TE1	30	4.1661	2%
MZI-TE2	25	4.2102	16%
MZI-TE2	30	4.1795	2%
MZI-TM1	25	3.6204	2%
MZI-TM1	30	3.6242	2%
MZI-TM2	25	3.6965	6%
MZI-TM2	30	3.7003	6%

A.5 Synopsis

Observation of the simulated and experimentally extracted group index show that TM mode has higher change in group index as a function of temperature than TE mode. Therefore, environmental change can affect the TM interference based photonic component more than the TE based components. For example, resonance of the TM micro-ring resonators can be harder to stabilise against the environmental change compared to TE. Therefore, TE micro-ring resonator is a better choice as a HSPS as it is more stable in room temperatures. The same observation also suggests that TM micro-ring resonators are better sensors for detecting environmental change. As HSPSs, TM micro-ring resonators could be more useful in cryogenic temperatures as it requires less heat for a larger index gradient change for phase shifts.

Appendix B

Experimental setups and optical alignments

Contents

B.1 The experimental setups

The major three constituents of the vertical grating coupler optical setup which has been described in the Fig. 6.2 are,

① A *Nanomax* stage (*Thorlabs*) with 6 degrees of freedom (x, y, z translations and rotations). An angle (made by the Mechanical Workshop) sits on the stage and holds the optical fibre array. The optical fibre array (*OZ Optics*) couples light in/out of the chip.

② The *chip holder* where the chip sits. Its construction varies depending on the size of the chip. In general, the height of the chip should be at the pivot point of the *Nanomax* stage, to avoid cross-coupling among translational and rotational axes of the stage. Therefore, the chip-holder is constructed with an adjustable height stage, with a rotational and fine translational stages. At the top of the chip-holder sits the Peltier to control the temperature, and on top of that the Printed Circuit Board (PCB) where the chip is attached with thermal glues. An important step here is to put Peltier with correct efficiency associate with the thermal mass of the copper blocks. As shown in Fig. B.3 (a) the position of the Peltier and the size of the heat baths need to have correct sizes.

③ The *PCB* facilitates the electrical connection between the chip and the driving electronics. The on-chip thermal phase-shifters for MZI and ring-resonators are connected by gold tracks to on-chip bond-pads. These bond-pads are sufficiently large to attach a gold wire to it by applying localised heat as a form of electric spark. This process is called wire-bonding. The other end of the wire is connected to the PCB using the wire-bonding. The electrical connections from the PCB are then wired to

the electronics (Qontrol System PLC). The electronics controls the electrical powers dissipated by the thermal phase-shifters.

This optical setup and another similar to it were used to collect the experimental data mentioned in Chap. 6 and Chap. 7. In addition to these setups, a side-coupled optical setup was also built to test and characterise the HSPSs on the chips fabricated by Toshiba (SOI) and Sandia National Labs (silicon nitride). As the collection efficiencies in those chips were not high enough to perform four-fold experiments, they are not mentioned here. A photograph of the side-coupled setup is shown in Fig. B.1. In future experiments with high collection efficiency side-coupled chips, this setup will be used.

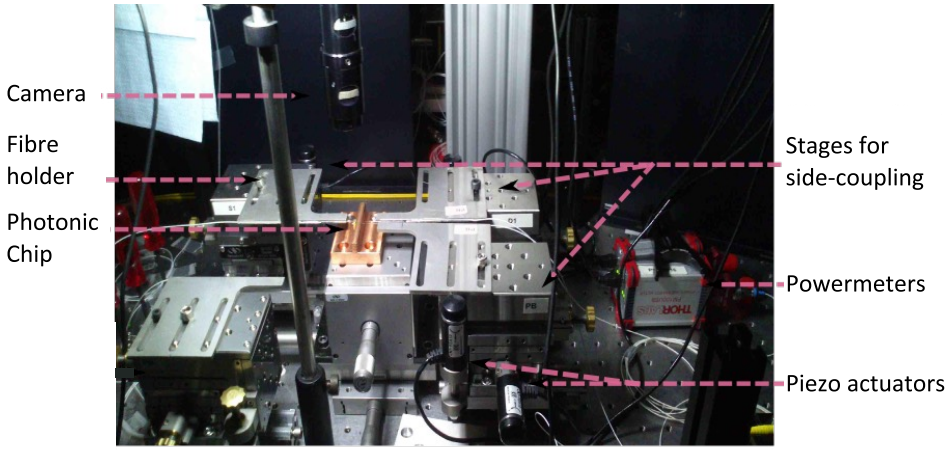

Figure B.1: Side-coupled optical setup assembled for SOI and silicon nitride chips.

B.2 Optical alignments

In our experimental setup, the fibre-array needs to be aligned with the on-chip VGCs for coupling light in/out. There are two primary alignment associated with our design. The first is the angle of the fibre-holder (① in the above discussion) and the second is the orientation of the fibre array with respect to the chip. The VGCs used in our chips require that the angle to be $10\,^{\circ}$. Appropriate orientation of the fibre array was achieved by making the flat bottom of the fibre array parallel to the PCB (hence the chip) using small mirrors which can be seen in Fig. 6.2 (c) (appearance of a miniature prism).

B.3 Thermal crosstalk and resonator phase

We have designed photonic circuit to quantify the thermal crosstalk between thermal phase shifter. This circuit will compare the heat flow through the cladding and the waveguides at various distances. A micro-ring resonator in one arm of the MZI will have the interference visibility that depends on the round-trip phase of the resonator. The data from these two circuit will indicate the phase profile of the resonators.

B.4 Counting logic for four-fold coincidence

As mentioned in Chap. 6, there were two major challanges needed to be resolved: ① compatibility between SNSPD outputs with counting logic system and ② extraction of the four-folds from the raw data.

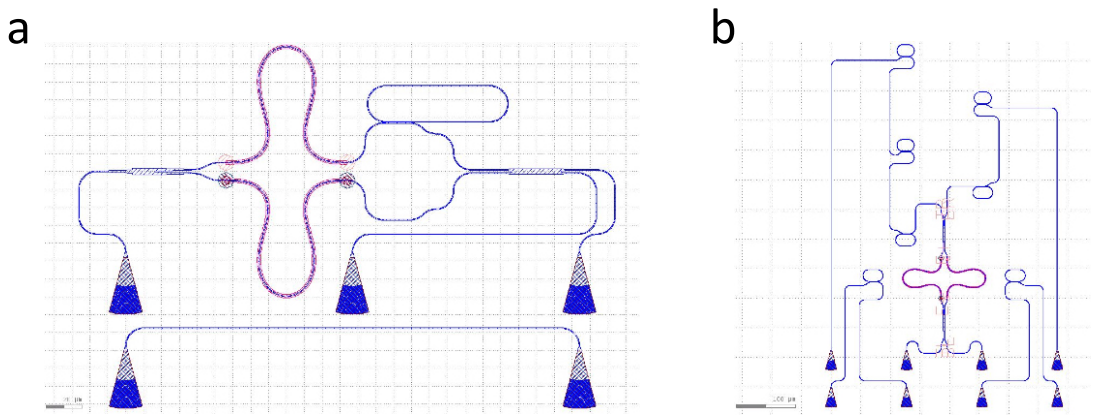

Figure B.2: Photonic circuits to quantify thermal crosstalk and resonator phase. (a) Resonator phase. (b) Thermal crosstalk.

① At the event of a single photon detection, a SNSPD emits an electrical pulse with a negative amplitude that resembles in shape the electrical standard called NIM (Nuclear Instrumentation Module) for fast negative logic on standard high temporal resolution metrology. A NIM pulse from a SNSPD resembles a negative spike falling sharply between $-150\ mV$ to $-900\ mv$ ($50\ \Omega$ termination) and decaying slowly within $200\ ps$. In terms of logic definition, that represents logic 1. In contrast, most of the counting logic with readily available computer controlled softwares operates on electronic standard LV-TTL (Low Voltage Transistor-Transistor Logic). $+3.3\ V$ represents LV-TTL logic 1 with slow rising and falling edges (e.g. $50\ ns$). Therefore, either the output pulses from the detectors needs to be converted to TTL, or a NIM compatible counting logic unit that accepts our raw output pulses needs to be used. We have tried both options. A NIM to TTL converter (from *Ortec*) was used for each of the four SNSPDs and fed into the counting logic. It turns out that it is extremely difficult to keep that setup stable over the whole duration of the experiment.

Next, we tried a counting logic module that is compatible with NIM pulses (Hydraharp from *PicoQuant*). Hydra harp does not have a readily available software to output a four-fold events. That required to write some Matlab and Python codes to expand the provided Hydraharp's library to extract the four-fold events from the time-tags. The new Matlab codes controls the Hydraharp to take data in a format called time-tags where the photon arrival times in each channel of the Hydraharp are registered.

② These data files, containing time-tags, are then copied into a computationally powerful computer. Reusing a pre-existed algorithm (from Dr. Peter Shadbolt) in our group (done by Dr Damien Bonneau) for a different counting module, and using the python modules, the four-fold events from these time-tags are extracted.

B.5 Matlab instrumentation

Most of the instruments mentioned in this thesis were connected using RS232 serial communication. RS232 protocol is one of the most well established protocol. The manufacturers of our instruments provided a set of RS232 commands to communicate with and operate the instruments. In Matlab, a serial object with correct communication port (e.g. *COM1*) is defined straightforwardly with appropriate values of *baudrate*, *start/stop bits*, *terminators* etc,

```
obj_HD = instrfind('Type', 'serial', 'Port', 'COM1', 'Tag', '');
set(obj_HD, 'Timeout', 2.0, 'Terminator', {'LF','CR'}, 'Baudrate', 115200, 'Stopbit', 1);
```

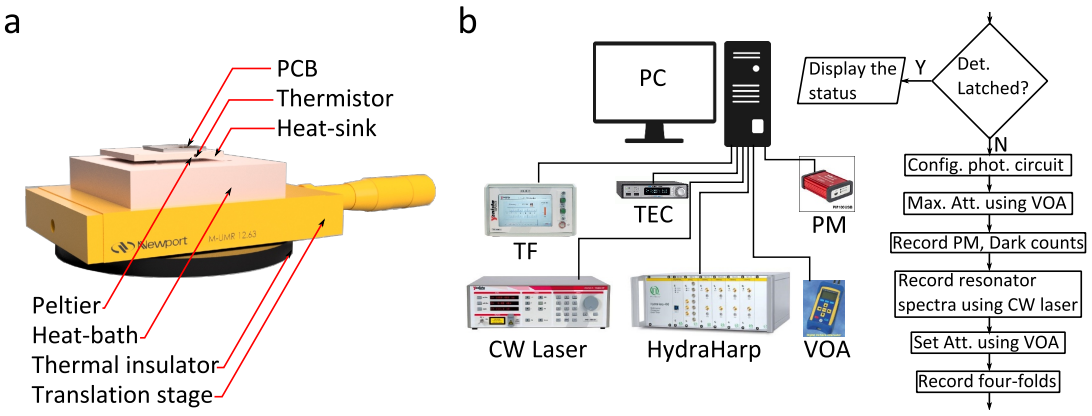

Figure B.3: Thermal stability and MatLab instrumentation. (a) The components of the thermal stability stage showing the place of the PCB and the Peltier with respect to the heat baths (copper blocks). (b) A flow chart showing a measurement algorithm used for on-chip PIM with micro-ring resonators.

Some instruments (e.g. Thorlabs powermeters) required VISA protocol using standard command sets called SCPI. These instruments have to be communicated using their unique identification numbers. In contrast, the PicoQuant time-tagger HydraHarp (or PicoHarp) has its own communication protocol defined in a C-code library. To use this library in MatLab, a standard MatLab toolbox called *MEX setup* has to be setup.

There are a few advantages of connecting all these instrument to a high level language such as MatLab:

① Any arbitrary automated algorithms can be executed. Such an algorithm will not only collect the quantum data but will also collect the meta data (such as dark counts, coupling of the chips etc) to reflect on the status of the experiment. For example, using MatLab we have followed a procedure to set the correct bias points of the single-photon detectors and measure their overall efficiencies as shown in Fig. B.4 and Fig. B.5. This experiment has been performed together with Dr. Gary Sinclair and Dr. Döndu Sahin.

② Changing the computer or the experimental setup or swapping one instrument with another will not affect the execution of the algorithm. This is because the installed MatLab in all computers are of the same standard.

③ MarLab algorithms written for one setup are readily usable in another setup. This facilitates portability unlike C, which may not follow the same standard from computer to computer (or one operating system to another).

A complex measurement algorithm that conditionally measures an attribute based on the measurement outcome of other instruments or the reconfigurable circuit can be implemented with relative ease with MatLab. One such algorithm is shown by the flow chart in Fig. B.3 (b). Therefore, although writing MatLab communication protocol from scratch for all these instruments was relatively time consuming, later it proved to be very resourceful.

B.6 Heaterboards

As the precision of a few millivolts in setting up the voltage matters in aligning spectra of high Q micro-ring resonators, a study of the two available heaterboards (Qontrol & UEI) precision was performed together with Callum Wilkes. Figure B.6 shows the schematic

of the measurements where a known resistance of $400\ \Omega$ has been connected to two 6 digit precision multi-meters as 4-point measurements and repeat the measurements many times to build a data set for statistical reliability measurements. This way the repeatability of the heater driver board can be monitored as well as the electrical power dissipation in the heater with high accuracy. As the phase $\propto V^2$, an inaccuracy in the second significant digit in the voltage results in the inaccuracy of the phase estimation. Each heaterboard, separately, has been used to change the current or voltage through the resistance. The nominal applied voltage and currents, the readouts from the heaterboards and the recordings of the multi-meters have been plotted together. We have observed that both of the heaterboards successfully changed the voltage across the resistance with 12 digit resolution ($0.0003\ V$), but the readout from the Qontrol heaterboards were very noisy and sometimes inconsistent.

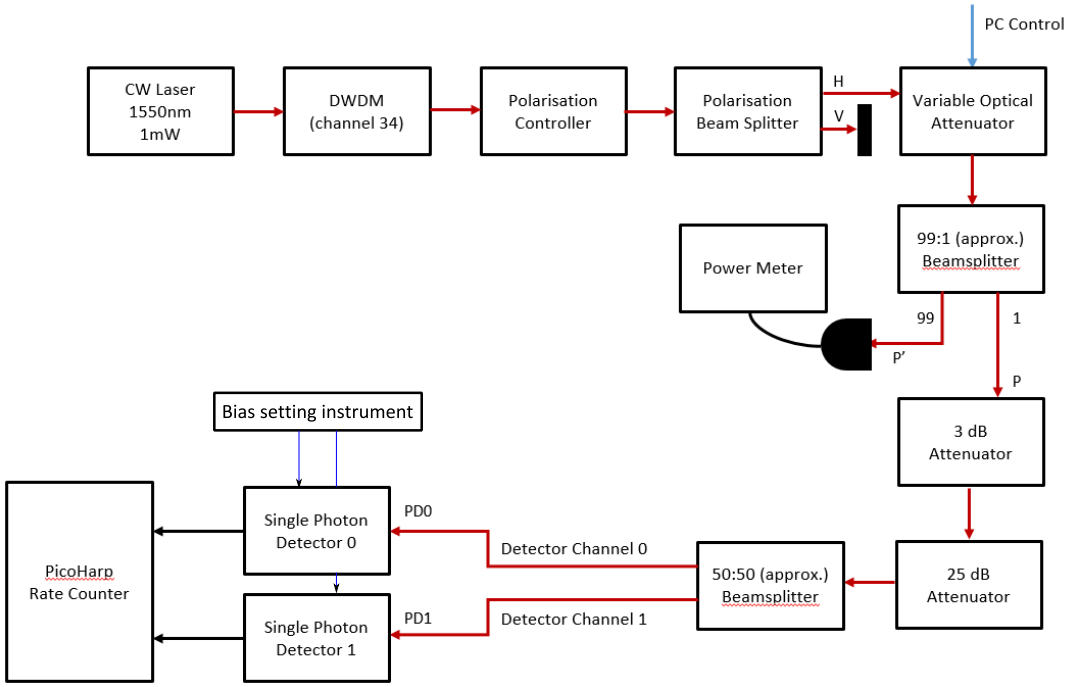

Figure B.4: The diagram shows the method used to measure the detection efficiency and set up the correct bias points of the single-photon detectors, along with measuring the channel efficiency. This diagram has been adapted from a report written by Dr. Gary Sinclair.

B.7 Stimulated four wave mixing and JSI

An automated script written by Luca Milic in python and C preexisted in the lab to measure joint spectral intensity (JSI) using stimulated four wave mixing. Figure B.7 shows the experimental setup used to measure the JSI of our micro-ring resonator HSPSs. The OSA used in our experiment has $30\ pm$ absolute wavelength accuracy while the FWHMs of our resonators are also $\sim 30\ pm$. Therefore the absolute resolution of the JSI were not very high. In one of the mode, OSA reconstructed the intermediate wavelength and have relative wavelength resolution higher than $30\ pm$. We have also recorded the JSI 16 times and averaged it. This helped estimating the statistical error associated with our measurements but averaged our finer details.

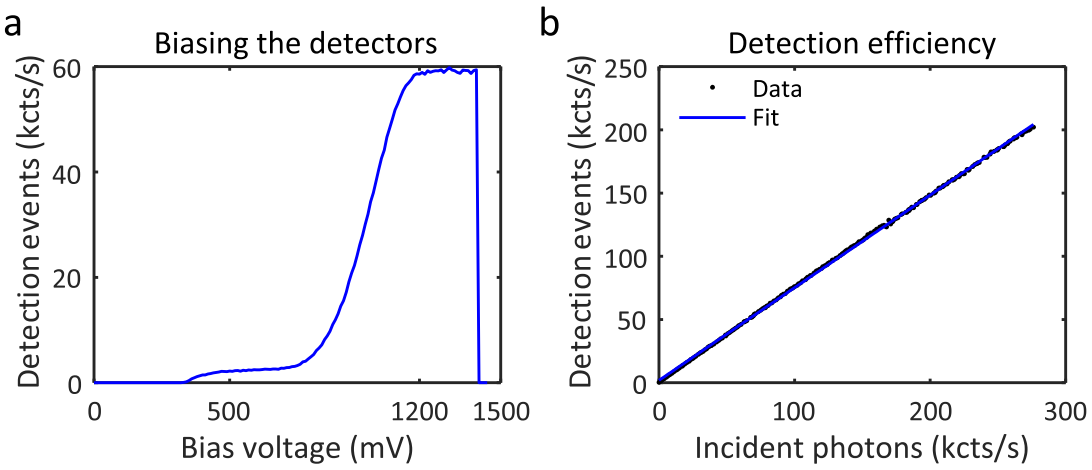

Figure B.5: Setting detector bias and efficiency. (a) The correct bias point is about $1200\ mV$ where it reaches a plateau. About $1400\ mV$ the detector latches. (b) The efficiency of this detector was found to be $\sim 73\%$.

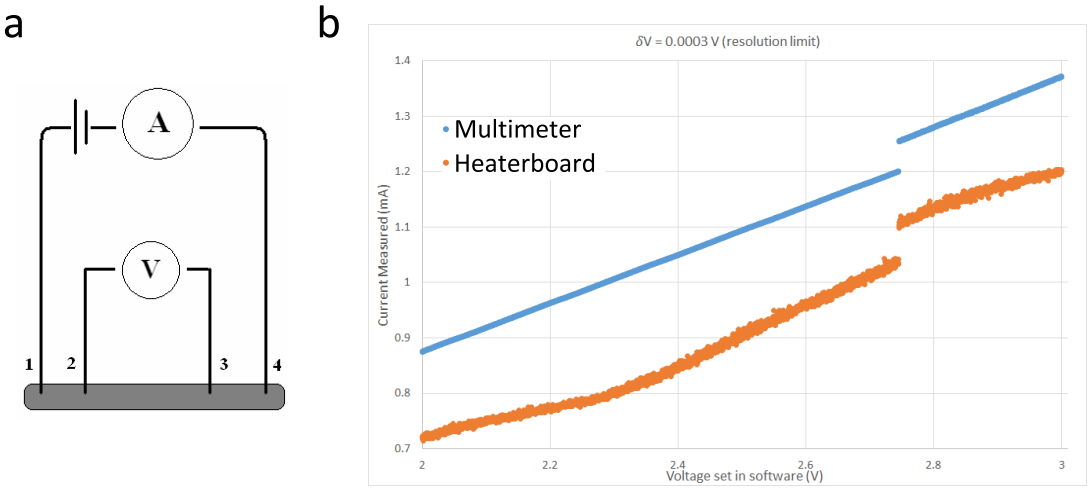

Figure B.6: Heaterboard noise estimation. (a) Shows the four-point measurement method with a known resistance ($400\ \Omega$) and two 6 digit precision multimeter (*Agilent*). This image is adapted from Wikipedia. (b) The difference in the readout voltage of Qontrol PLC and the UEI heaterboard shows that the Qontrol PLC is more noisy. The precision multimeter readings reveal that both of the heaterboards successfully set the voltages with 12 digit resolution. This measurement was performed together with Callum Wilkes.

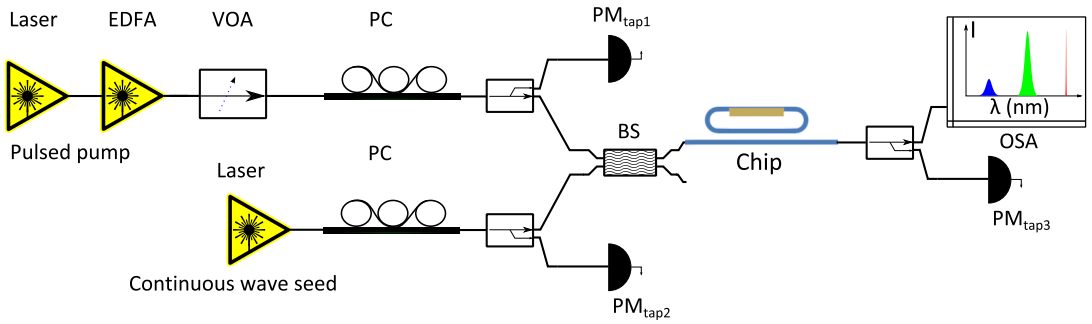

Figure B.7: Stimulated four wave mixing with pulsed pump laser (green) and continuous wave seed laser (red) generate idler (blue). The relative amplitudes of the seed, pump and the idler are measured with an optical spectrum analyser.

Appendix C

Setting-up off-chip Hong-Ou-Mandel interference experiment

Contents

The first free space setup of HOM interference mentioned in Sec. C.3.1 was assembled together with Dr Takafumi Ono.

C.1 Determination of η_{DC}

Using the setup shown in Fig. C.1 and the following equations the splitting ratio of the directional coupler was calculated [32]:

$$P_{o11} = \eta_1\eta_2\eta_{DC}P_{i1} \tag{C.1}$$

$$P_{o12} = \eta_3\eta_2(1-\eta_{DC})P_{i2} \tag{C.2}$$

$$P_{o21} = \eta_1\eta_4(1-\eta_{DC})P_{i1} \tag{C.3}$$

$$P_{o22} = \eta_3\eta_4\eta_{DC}P_{i2} \tag{C.4}$$

$$\frac{\eta_{DC}^2}{(1-\eta_{DC})^2} = \frac{P_{011}P_{o22}}{P_{021}P_{o12}} \tag{C.5}$$

From the measurements, we have found $\eta_{DC} = 0.5861$. With similar measurements, the

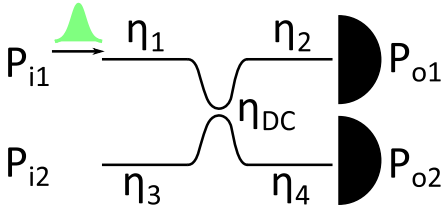

Figure C.1: Estimating η_{DC}.

BS used for HOM interference was found to be $\eta_{BS} = 0.501$.

C.2 Raw $g^{(2)}(0)$ data

Based on the definitions introduced in Chap. 2, the purity from the raw $g^{(2)}(0)$ data is extracted using,

$$g^{(2)}(0) = \frac{CC(\delta\tau \to 0)}{CC(\delta\tau \to \infty)} \tag{C.6}$$

$$P = g^{(2)}(0) - 1 \tag{C.7}$$

As shown in Fig. C.2, the numerator and the denominator are defined by,

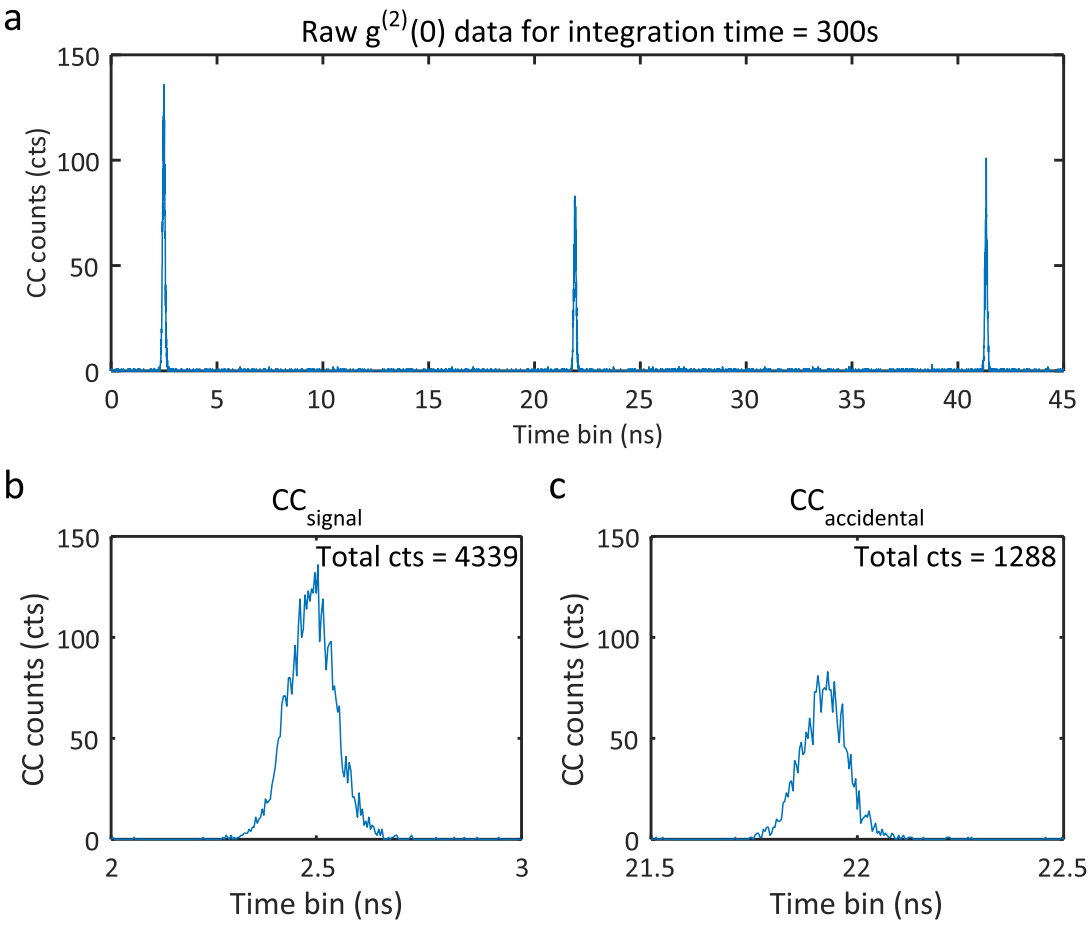

Figure C.2: Raw $g^{(2)}(0)$ data.

$$cc = \sum CC(\delta\tau \to 0) \tag{C.8}$$

$$acc = \sum CC(\delta\tau \to \infty) \tag{C.9}$$

From the figure, $cc = 4339$, $acc1 = 2536$, $acc2 = 2568$ are counted. Considering the Poisson distribution, the error in the measurement is calculated as,

$$e_{g2} = \sqrt{\frac{e_{cc}^2}{e_{acc}^2} + \frac{e_{acc}^2 e_{cc}^2}{e_{acc}^4}} \tag{C.10}$$

$$e_{cc} = \sqrt{cc} \tag{C.11}$$

$$e_{acc} = \sqrt{acc} \tag{C.12}$$

Averaging $ac1$ and $ac2$, we find the measurement as $g2 = 1.7000 \pm 0.0424$.

C.3 Experimental setup of off-chip HOM experiment

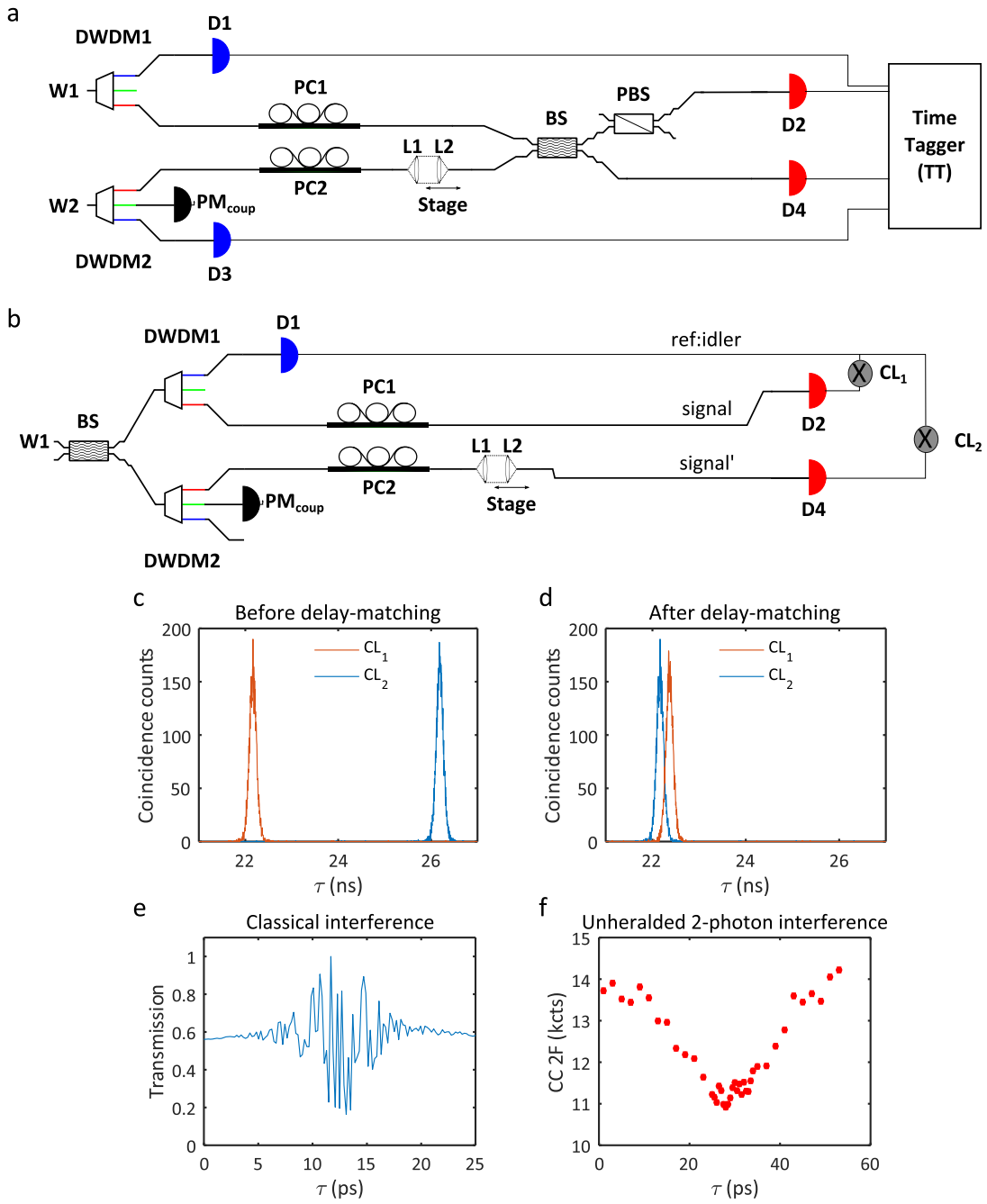

Figure C.3: Free space HOM interference setup. (a) Experimental diagram of free-space setup showing lenses L1 and L2 with the delay stage. (b) Experimental setup of delay-matching. (c,d) Use of coincidence logic unit to calculate the delay. (e) Classical interference and (f) two-fold coincidence measurements to verify the estimated value of the delay.

C.3.1 First free-space setup

In the first free space experimental setup, the delay line was built by free space optics. The light coupled out of the fibre was collimated using a lens and propagated certain distance (delay). Then it is coupled in by another lens on a motorised stage. The insertion loss of this delay line was more than $\sim 2\ dB$ at its best.

The experimental setup to measure the HOM dip has to very precise as we would overlap photons spectra which are about 50 ps wide depending on the filtering employed. As the speed of light is about 30 cm per nanosecond, it means that to have a picosecond resolution, we have to calculate the path lengths of the input arms of the beam splitter in millimetre scale resolution. The reason we need to adjust the path length is mainly because the DWDMs that we use to filter and clean out the pump spectra at signal and idler wavelengths have large dispersions contributing 30 ns or more between channels. None of the DWDMs have similar dispersion with respect to each other. Therefore, if the path lengths are not matched the signal 1 from DWDM 1 will be few nanoseconds apart from signal 2 filtered by DWDM 2. To quantify and balance this time delay between two signal photons, and in order to achieve such millimetre scale resolution we have used the experimental setup used in Fig. C.3. At the output of the chip, we choose only one waveguide, and split the photon pairs equally using a beam splitter. The two output arms of the splitter are then fed through two DWDMs we intend to use for the HOM experiment. These two DWDMs will then separate the signal and idler photons in each of the arms of the beam splitter. For example, the DWDM 1 and DWDM 2 will split the signal and idler in channel 3 and channel 11 respectively for each of the arms. The channel 11 of the DWDM 1 can be taken as a reference. Now channel 3 of DWDM 1 and DWDM 2 have polarisation controllers 1 and 2 respectively before going to the detectors. Also channel 3 of DWDM 2 has a delay line which can be varied from overlapping the photon wavepackets to not overlapping them. At this configuration if we record the two fold coincidence histogram in from ch3 an ch11 of DWDM 1, we will see the coincidence peak at histogram $\tau_1 \sim 22_n s$. The coincidence histogram records the coincidence counts between the two channels in a start stop manner. This means, that if ch11 is the start of the timer, then ch3 is stop of the timer and the time delay between these two events are plotted as the histogram binning parameter. Therefore the coincidence peak of the histogram represents the actual generation event of the signal idler pairs but through the different channels have delayed that τ_1 amount.

Now if we measure the coincidence peak between ch11 of DWDM 1 and ch3 of DWDM 2, and find it to be $\tau_2 \sim 26\ ns$, then the difference between τ_1 and τ_2 will give us the difference between ch3 of each of these DWDM channels. Therefore to overlap the two signal photons coming through these two waveguides we have to match the path lengths of these two channels. For the free-space delay line version, we moved the lens to a different position until $\tau_1 = \tau_2$.

We have calculated the path length mismatch from these two DWDMs to be $25 \pm 5\ cm$ for the fibre pigtailed delay line from OZ optics and made a fiber patch cord of that length. And according to our result we added it to the path of ch3 of DWDM 1.

C.3.2 Classical interference

A classical way of testing this above setup is to use a classical interference as shown in Fig. C.3 (e) for the free-space version. If the classical pulsed spectra that correspond to the photon wavepackets interfere in the beam splitter then the wavepackets of the photons will also overlap. Another quick way to check this setup is to use unheralded two-fold

coincidences (Fig. C.3 (f)) as often used in the literature.

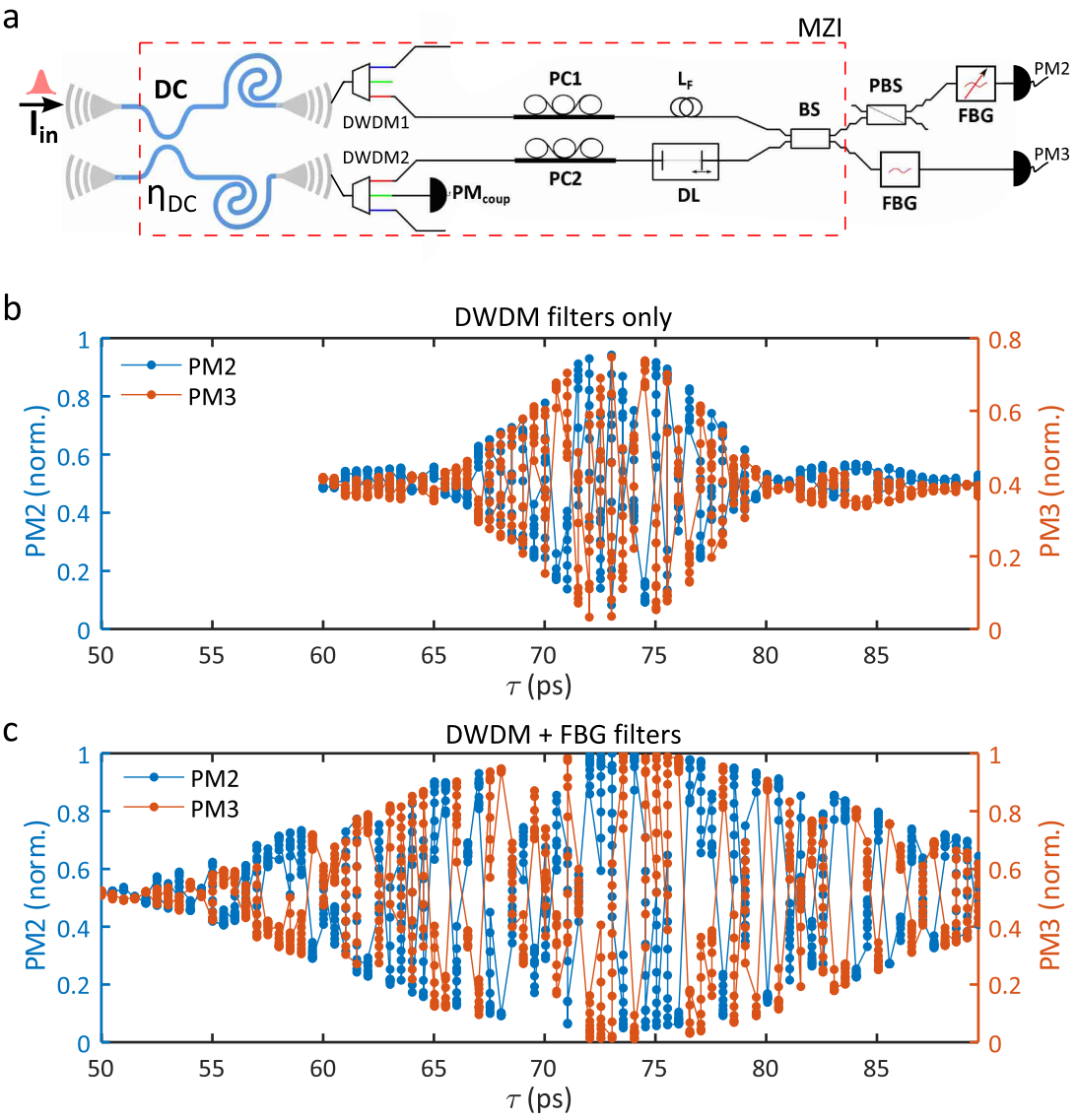

Figure C.4: Classical interference showing the dip of the HOM interference for FBG and DWDM filter settings.

In retrospect we did not need to perform the aforementioned delay matching measurements. If we observe closely, Fig. C.4 (a) shows that the HOM interference setup with our waveguide chip acts as a MZI for the classical light: the beam splitter (DC) inside the chip is the first beam splitter of the MZI, the delay line (DL) is the MZI phase and the output beam splitter (BS) is the second beam splitter of the MZI. The output of this MZI is then monitored as we vary the delay line of about 100 ps. The result is plotted in Fig. C.4 (b) and (c) for two different filter (FBG & DWDM) configurations. As we can see we get an almost perfect interference with a width that corresponds to the pump and filter width. And if we fit the envelope of that interference, we get the maxima/minima at $71\ ps$, referring to the perfect point of overlap of the wavepackets. The reason the classical interference does not go complete zero is because there is about $1\ dB$ loss in the delay line which then cannot completely balance the interference constructively or destructively. The visibility of the classical interference with OZ optics delay line (Fig. C.4 (b)) were higher than the free-space version (Fig. C.3 (e)).

C.3.3 Free space vs all-fibre setup

In a free space arrangements, regular alignments (at least every week and before recording a data set) are necessary due to all the large mechanical parts (lens holders, microscope objectives etc.). In contrast, preparing fibres for precise length requirement through continuous cleaving is a relatively tedious and meticulous process but gains it merits in stability. With the all-fibre pigtailed components, the alignment becomes stable that experiments can be performed for few weeks without alignments.

C.3.4 Monitoring the experimental stability

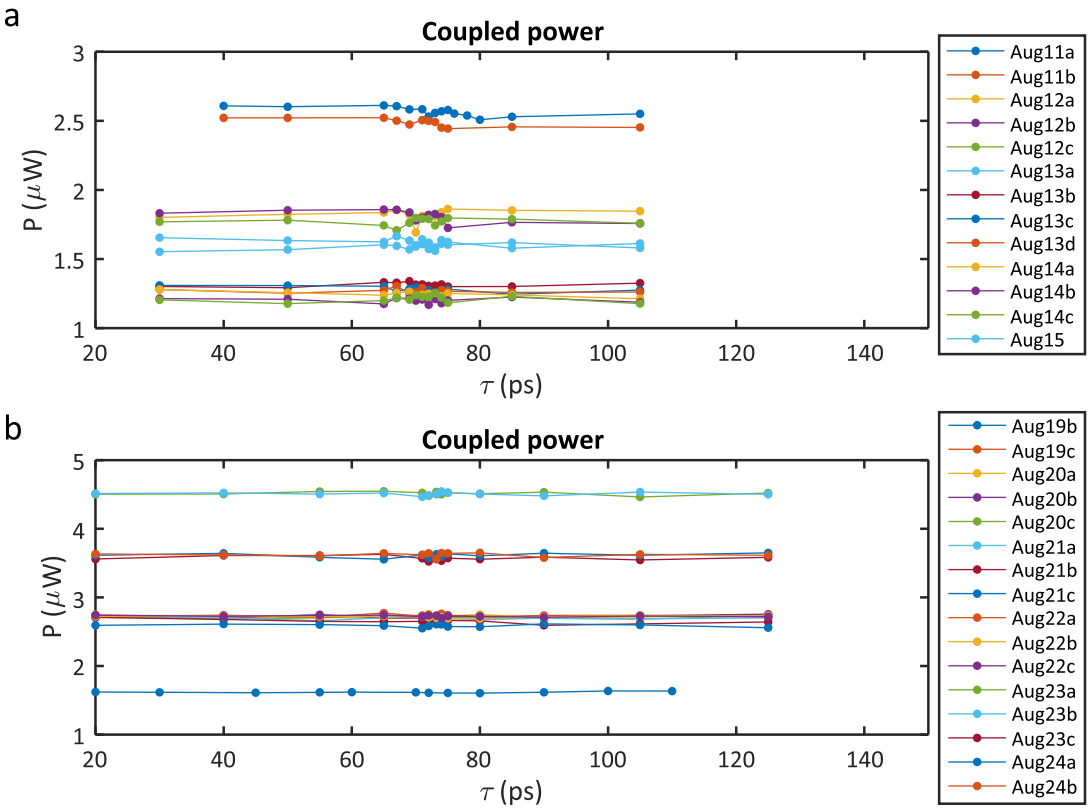

Figure C.5: The monitored output power for each scan are all plotted together to check the stability and group together the similar data set corresponding to the same power in the waveguide.

We have recorded the input tap power and output coupling power for each of the scans and plotted them altogether as can be seen in figure C.5. This gave us an indication of the input power of the waveguide during each of the HOM dip experiment. This is useful as the coupling of the chip can dwindle during each scan and this will not only help us group together the input power in each scan but will also able to tell us what should be the average stability during such scans. It is noticeable that the power drops slightly from the beginning to the end of each scan, indicating the coupling drops slightly from the beginning till the end of the scans. If the coupling power drops less than $0.25dB$ then this will correspond to an average drop of $0.25 \times 4 = 1dB$ in the four-fold coincidences, which is acceptable for the validity of that data set.

Appendix D

Silicon nitride micro-ring resonator and electron beam lithography

Contents

The silicon nitride micro-ring resonator presented in Sec. D.1 was provided by Dr Alberto Politi from University of Southampton. The electron beam lithography (EBL) mentioned in Sec. D.2 to fabricate heaters were performed Sandia National Laboratory, Albuquerque, USA. The EBL procedure was performed together with Mack Johnson.

D.1 Brightness of a silicon nitride micro-ring resonator HSPS

From our preliminary measurement as shown in Fig. D.1, we have found that the group index of the silicon nitride resonators is about $n_g = 2.88$ which is almost $2/3^{rd}$ of the group index of the silicon ($n_g = 4.16$). The FSR of the resonators ($2.3\ pm \leftrightarrow 287\ GHz$) did not match well the DWDM channel spacings ($200\ GHz$). Therefore, we lost most of the coincidence counts. From the noisy data presented in Fig. D.2, we also suspect that the low non-linearity in silicon nitride produced lower coincidence counts compared to silicon.

D.2 Electron beam lithography

At the CINT facility of the Sandia National Laboratory, USA our goal was to fabricate low insertion loss silicon nitride photonic circuits. Specifically, Mack Johnson was investigating etching and sidewall roughness of the waveguides, while I was investigating fabricating thermal phase shifters. Fig. D.3 (a) shows our preliminary simulations on the minimum bend radius for silicon nitride waveguides.

D.2.1 Fabrication facility

The fabrication process was carried on silicon nitride wafers supplied by Sandia facility. The wafers consisted of $250\ nm$ to $275\ nm$ silicon nitride layer on top of a $2\ \mu m$ to $4\ \mu m$ silicon

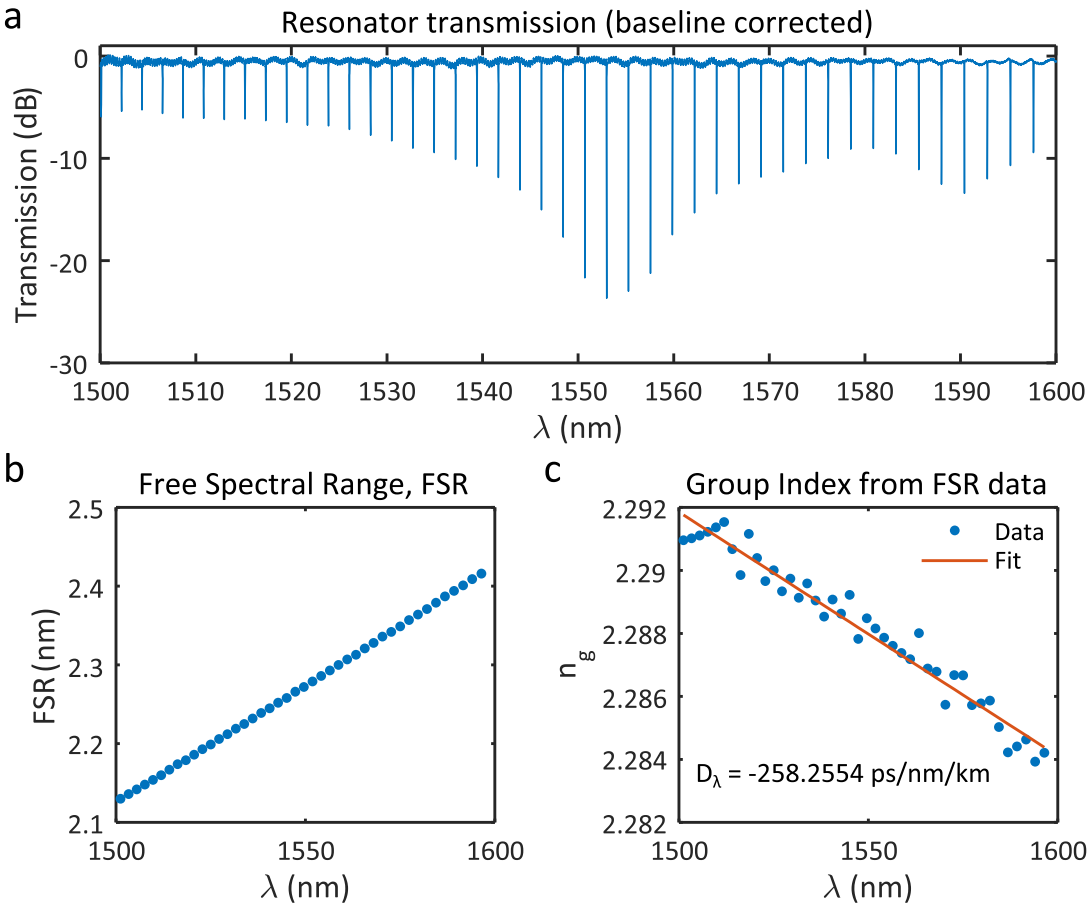

Figure D.1: Group index of a silicon nitride micro-ring resonator. (Resonances of the SiN micro-resonators). (b) The FSR between consecutive resonances as a function of wavelength. (c) Group index estimated from the FSR using Eq. 3.15.

di-oxide (SiO_2) layer that resides on a silicon substrate as shown in Fig. D.3 (b). We have used a few different wafers with different layer thicknesses measured with ellipsometry.

We had the following instruments at our disposal.

- EBL - JEOL,
- SEM: Nova Nano SEM 450, FEI,
- Asher: PDS/PDE-301,
- e-beam evaporation: Temescal FC-2000,
- Annealer: Jipelec, Jetfirst,
- Profilometer: Alpha-Step 500,
- Ellipsometry: V-VASE, J. A. Woollam Co.

All the instruments required training by the facility staff. The electron beam lithography (EBL) system required extensive training due to its complicated and user-unfriendly operating instructions.

D.2.2 Heaters

We have used the heater specifications from IME [166]. The resistive material for the heater was titanium nitride (TiN) material and the contact material was highly conductive

metals such as gold (Au). This correspond to at least two steps of lithography, excluding alignment marks and cladding layer lithography.

Figure D.3 (b) shows the structure of the heater that will be compatible with the waveguides. As only the values of the resistances were important at this point in fabrication, we did not put any SiO_2 claddings in between the heater layer and the waveguide. Nevertheless, this resulted in three lithography steps and two lift-off steps.

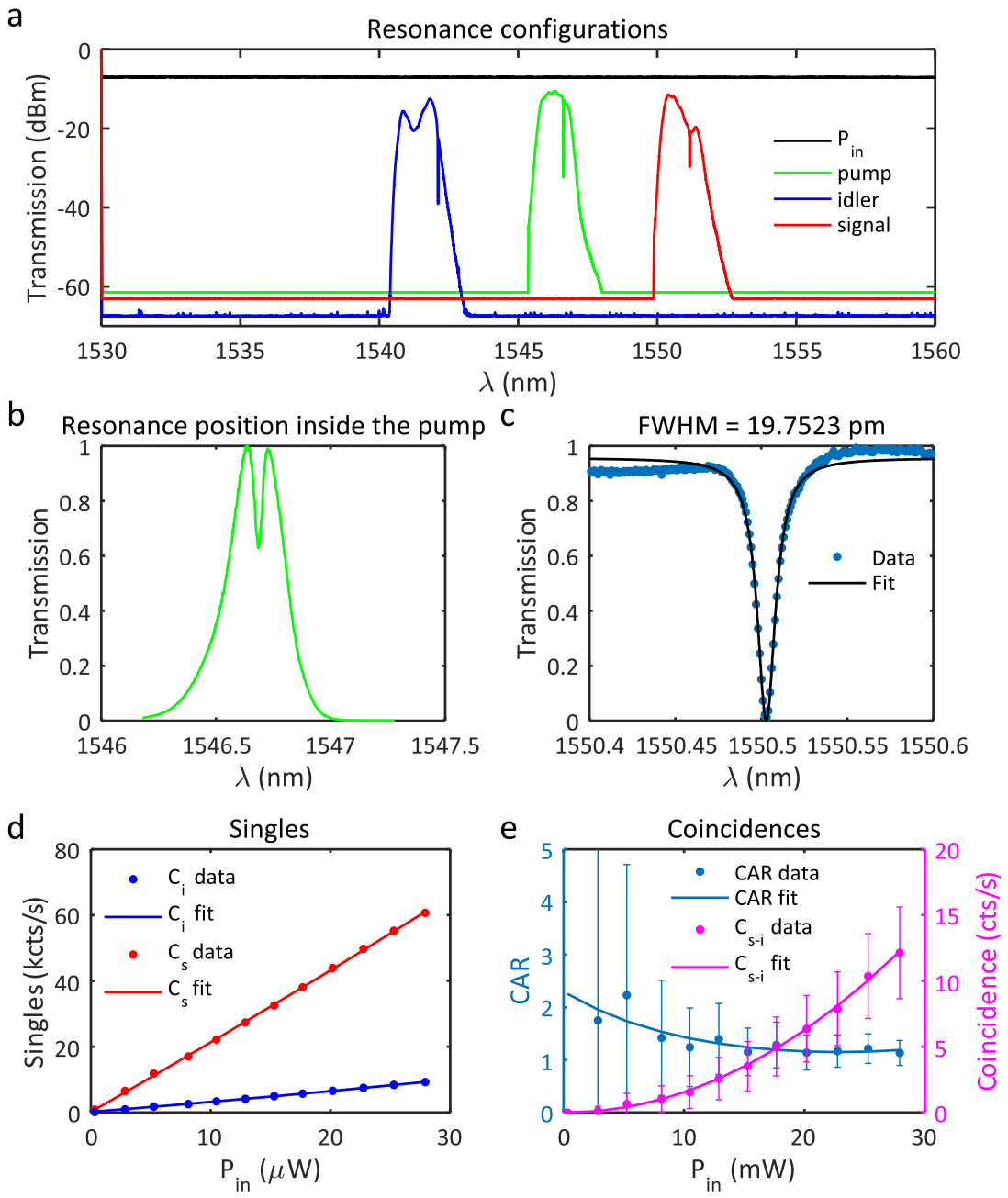

Figure D.2: Brightness of a silicon nitride micro-ring resonator. (a) Resonance configuration. (b) Resonance position inside the pump pulse. (c) Lorentzian fitting shows the FWHM $= 19.75\ pm$, Q = $\sim 8 \times 10^4$. (d) Singles counts. (e) Coincidence counts and the CAR.

The first step was to make alignment marks for successive lithography steps. JEOL EBL system requires global marks and chip marks. Our design has four global marks of Au as a form of cross with $4\ \mu m$ width and $250\ \mu m$ length. The following procedure was used to make the alignment marks:

- Sample preparation: at first, the protective layer of resist is removed by soaking 5 min each in Acetone and IPA. Then the surface is cleaned in Barrel Asher at 100 W for 5 min.
- Resist coating: positive resist PMMA 495 at 3000 rpm for about 400 nm of thickness. Prebake at 170 C for 2 min.
- Patterning: EBL was used to pattern the resist.
- Developing: develop with MIBK:IPA = 1:3 for 1 min. Rinse with IPA, blow dry with N_2 without letting IPA evaporate.
- Cleaning: descum at 10 W for 2 min.
- Gold deposition: deposit Ti:Au = 100:750 Å using EG3. Titanium was used here for adhesion.
- Lift-off: Soak in acetone over 15 min to 1 hour till some reactivity is seen on 90% of the surface. Then use acetone brush to remove all of it and rinse with IPA and blow dry with N_2.

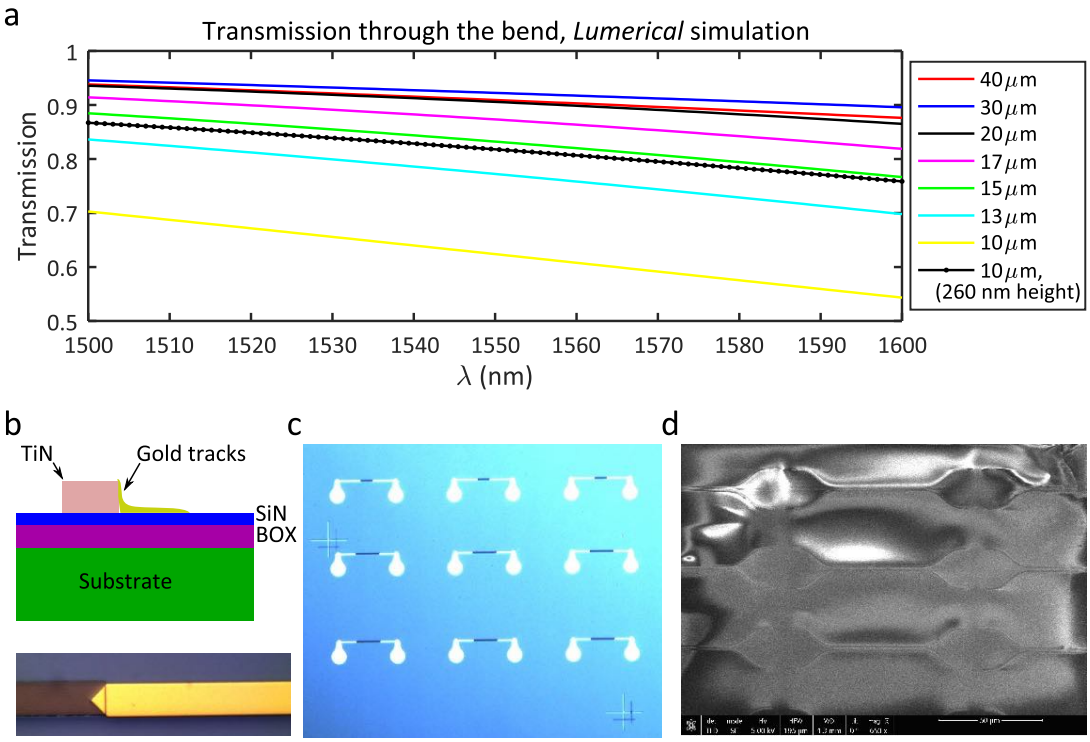

Figure D.3: Silicon nitride EBL. (a). Simulation of minimum bend radius for silicon nitride waveguide using *Lumerical Mode Solver*. (b) Different layers of the heaters and the optical microscope image of the fabricated heaters. (c) Variation of heater lengths. The + signs are the alignments marks. (d) A SEM image of the roughness of the coating of the resist.

Figure D.3 (c) shows the alignment marks (+) used for subsequent lithography steps:

- Patterning the heater structure: the first few steps of the alignment marks procedure were used to pattern the resist layer with EBL for the heater structure.
- Depositions: As TiN is not a standard material, a manual control of the Soak power during deposition process is required to keep the deposition rate steady while the material from TiN crystal chunk evaporates. Keeping the power at about 1.9% and

pressure at about 6×10^{-6} torr for a rate of 0.4 Å/second takes about 50 minutes to deposit about 100 nm of TiN film.

- Lift-off technique was used to remove the excess TiN.
- The third lithography step was performed for the contact pads connected to the heaters.

The final heater structure is shown by the optical microscope image shown in Fig. D.3 (c) and (d). The brown material in this figure is TiN and the golden material is the gold contact.

We have also attempted annealing the heaters at various temperature and observed that the resistance changes if the TiN is annealed. Table D.1 shows the heater resistances before and after annealing.

Length (μm)	R (Ω)	R (Ω) (Annealed)
80	0.463	1.818
200	1.010	4.000

Table D.1: Heater resistances

Appendix E

Matlab implementation of imperfect sources and circuits on PIM

Contents

E.1 Implementing imperfect PIM with non-ideal sources in MatLab

Heralded single-photon sources have finite probabilities of emitting multi-pairs. From the point of view of ideal single-photon sources such multi-pair emission is an imperfection. Also, the photon-pairs may not be emitted in a single optical mode but in multiple optical modes. The appropriate metric of these two effects are photon-number purity and spectral purity. Photon-number purity is measured using conditional HBT interferometer which reveals the amount of multi-pair contribution with respect to the total number of photon detection events. For HSPSs, this metric is determined by the squeezing (i.e. the input pump power). In contrast, the spectral purity is measured by unconditional HBT interferometer or reconstructing JSA which reveals the strength of the primary optical modes with respect to the total strength of all the optical modes.

In the following sections we will first discuss the effect of multi-pair emission on the PIM: starting with three-photon pairs and extending it to 10 photon-pairs thus reproducing [56, 114]. Afterwards, we will extend this model by including a second optical mode in our calculations which implies spectral impurity that exist in all the practical single-photon sources. We will also apply this model to PIM with MZI.

E.1.1 Effect of at most three-photon pairs on the PIM

Let's consider our sources emit at most two-photon pairs at any given time. The wave function of the emitted photon-pairs can be written as,

$$|\Psi\rangle \approx \sqrt{1-x}\left(\sqrt{x}|1_s,1_i\rangle + x|2_s,2_i\rangle\right) \tag{E.1}$$

where, x represents squeezing, "s" and "i" represent signal and idler respectively. If all the losses experienced by a photon are lumped with the detector loss and expressed by the symbol η, then the loss experienced by n-photons is [153],

$$P(1) = \eta \tag{E.2}$$

$$P(2) = 1-(1-\eta)^2 \tag{E.3}$$

The idler photons are used to herald the presence of the signal photons, and the reduced density matrix for the heralded signal photons for each source become,

$$\hat{\rho}_s = \mathcal{N}(1-x)\left(xP(1_s)|1\rangle\langle 1|_s + x^2P(2_s)|2\rangle\langle 2|_s\right) \tag{E.4}$$

where $\mathcal{N}$ is a normalisation constant. Therefore, the density matrix of the system with two sources will be,

$$\hat{\rho} = \hat{\rho}_{s1}\otimes\hat{\rho}_{s2} \tag{E.5}$$

$$\begin{aligned}\approx &\mathcal{N}_1\mathcal{N}_2(1-x_1)(1-x_2)\big(x_1x_2P(1_{i1})P(1_{i2})|1\rangle\langle 1|_{s1}\otimes|1\rangle\langle 1|_{s2} + x_1^2x_2P(2_{i1})P(1_{i2})|2\rangle\langle 2|_{s1}\otimes|1\rangle\langle 1|_{s2}\\ &+ x_1x_2^2P(1_{i1})P(2_{i2})|1\rangle\langle 1|_{s1}\otimes|2\rangle\langle 2|_{s2}\big)\end{aligned} \tag{E.6}$$

In the above expression the $|2\rangle\langle 2|_{s1}\otimes|2\rangle\langle 2|_{s2}$ is omitted as it contains only part of the contribution of total four photon-pairs at a time. Now, after the beam-splitter transformation, the first term becomes,

$$\hat{T}_1^D = x_1x_2P(1_{i1})P(1_{i2})|1\rangle\langle 1|_{s1}\otimes|1\rangle\langle 1|_{s2} \tag{E.7}$$

$$= x_1x_2P(1_{i1})P(1_{i2})\hat{a}^\dagger|0\rangle\langle 0|_{s1}\hat{a}\otimes\hat{b}^\dagger|0\rangle\langle 0|_{s2}\hat{b} \tag{E.8}$$

$$= x_1x_2P(1_{i1})P(1_{i2})\frac{1}{\sqrt{2}}(\hat{c}^\dagger+\hat{d}^\dagger)\frac{1}{\sqrt{2}}(\hat{c'}^\dagger-\hat{d'}^\dagger)|0\rangle\langle 0|_s\otimes|0\rangle\langle 0|_{s'}\frac{1}{\sqrt{2}}(\hat{c}-\hat{d})\frac{1}{\sqrt{2}}(\hat{c'}-\hat{d'}) \tag{E.9}$$

$$= x_1x_2P(1_{i1})P(1_{i2})\frac{1}{2}[\hat{c}^\dagger\hat{c'}^\dagger+\hat{d}^\dagger\hat{c'}^\dagger-\hat{c}^\dagger\hat{d'}^\dagger-\hat{d}^\dagger\hat{d'}^\dagger]|0\rangle\langle 0|_s\otimes|0\rangle\langle 0|_{s'}\frac{1}{2}[\hat{c}\hat{c'}+\hat{d}\hat{c'}-\hat{c}\hat{d'}-\hat{d}\hat{d'}] \tag{E.10}$$

$$\begin{aligned}= &x_1x_2P(1_{i1})P(1_{i2})\frac{1}{4}[P(1_s)P(1_s)|1_c\rangle\langle 1_c|_s\otimes|1_{c'}\rangle\langle 1_{c'}|_s\otimes|0\rangle\langle 0|_{s'} + P(1_{s'})P(1_s)|1_d\rangle\langle 1_d|_s\otimes|1_{c'}\rangle\langle 1_{c'}|_{s'}\\ &+P(1_s)P(1_{s'})|1_c\rangle\langle 1_c|_s\otimes|1_{d'}\rangle\langle 1_{d'}|_{s'} + P(1_{s'})P(1_{s'})|0\rangle\langle 0|_s\otimes|1_d\rangle\langle 1_d|_{s'}\otimes|1_{d'}\rangle\langle 1_{d'}|_{s'}]\end{aligned} \tag{E.11}$$

Here, the subscripts s and s' denote the two output ports of the interferometer (BS or MZI). For the above case of completely distinguishable photons, even when both of the photons come out of s port of the interferometer, they actually correspond to different mode c and c'. As our detection mechanism cannot distinguish c and c' modes, the two photons appears as bunched. Also, in all the four outcomes, photon reflection and transmission have equal probabilities. Now, if the photons are completely indistinguishable, then $c\equiv c'$, and the middle two terms which correspond to photons on both of the output ports (s & s') of the interferometer will cancel out: $+\hat{d}^\dagger\hat{c'}^\dagger-\hat{c}^\dagger\hat{d'}^\dagger = +\hat{d}^\dagger\hat{c}^\dagger-\hat{c}^\dagger\hat{d}^\dagger = 0$ and hence, there will be no 4-fold counts. This is because $\hat{c}^\dagger$ and $\hat{d}^\dagger$ commute. Therefore, the first term for indistinguishable photons becomes,

$$\hat{T}_1^I = x_1x_2P(1_{i1})P(1_{i2})|1\rangle\langle 1|_{s1}\otimes|1\rangle\langle 1|_{s2} \tag{E.12}$$

$$= x_1x_2P(1_{i1})P(1_{i2})\frac{1}{2}[(\hat{c}^\dagger)^2-(\hat{d}^\dagger)^2]|0\rangle\langle 0|_s\otimes|0\rangle\langle 0|_{s'}\frac{1}{2}[(\hat{c})^2-(\hat{d})^2] \tag{E.13}$$

$$= x_1x_2P(1_{i1})P(1_{i2})\frac{1}{4}[2P(2_s)|2_c\rangle\langle 2_c|_s\otimes|0\rangle\langle 0|_{s'}+2P(2_{s'})|0_d\rangle\langle 0_d|_s\otimes|2\rangle\langle 2|_{s'}] \tag{E.14}$$

In order to quantify the quantum interference, we calculate the probability of photons exiting s and s' port of the interferometer which together with heralding idler photons constitute four-fold coincidences,

$$P_1^D(s,s') = \mathcal{N}_1\mathcal{N}_2(1-x_1)(1-x_2)x_1x_2P(1_{i1})P(1_{i2})\langle 1|_s\langle 1|_{s'}\hat{T}_1^D|1\rangle_s|1\rangle_{s'} \tag{E.15}$$

$$= \mathcal{N}_1\mathcal{N}_2(1-x_1)(1-x_2)x_1x_2P(1_{i1})P(1_{i2})\frac{1}{4}[(P(1_s)P(1_{s'})+P(1_{s'})P(1_s)] \tag{E.16}$$

$$P_1^I(s,s') = \mathcal{N}_1\mathcal{N}_2(1-x_1)(1-x_2)x_1x_2P(1_{i1})P(1_{i2})\langle 1|_s\langle 1|_{s'}\hat{T}_1^I|1\rangle_s|1\rangle_{s'} \tag{E.17}$$

$$= 0. \tag{E.18}$$

In the last line the value 0 for detecting four-folds for indistinguishable photons is due to the absence of any cross term in both s and s' modes in Eq. E.14 where both of the photons leave from either s or s' mode. It signifies the bunching of single-photons due to quantum interference as first observed by Hong-Ou-Mandel [46]. If the detection efficiencies in s and s' modes are the same, then for distinguishable case, it shows equal probabilities of photons exiting on both s mode, s and s' modes, s' and s modes and both s' modes.

Similarly, the second term in the Eq. E.6 for both distinguishable and indistinguishable photons become,

$$\hat{T}_2^D = x_1^2x_2P(2_{i1})P(1_{i2})\frac{1}{16}((\hat{c}^\dagger)^2\hat{c'}^\dagger + 2\hat{c}^\dagger\hat{d}^\dagger\hat{c'}^\dagger + (\hat{d}^\dagger)^2\hat{c'}^\dagger - (\hat{c}^\dagger)^2\hat{d'}^\dagger - 2\hat{c}^\dagger\hat{d}^\dagger\hat{d'}^\dagger - (\hat{d}^\dagger)^2\hat{d'}^\dagger)|0\rangle\langle 0|_s \otimes |0\rangle\langle 0|_{s'}$$
$$((\hat{c})^2\hat{c'} + 2\hat{c}\hat{d}\hat{c'} + (\hat{d})^2\hat{c'} - (\hat{c})^2\hat{d'} - 2\hat{c}\hat{d}\hat{d'} - (\hat{d})^2\hat{d'}) \tag{E.19}$$

$$= x_1^2x_2P(2_{i1})P(1_{i2})\frac{1}{16}(2P(2_s)P(1_s)|2_c\rangle\langle 2_c|_s \otimes |1_{c'}\rangle\langle 1_{c'}|_s \otimes |0\rangle\langle 0|_{s'} + 4P(2_s)P(1_{s'})|1_c\rangle\langle 1_c|_s$$
$$\otimes |1_{c'}\rangle\langle 1_{c'}|_s \otimes |1_d\rangle\langle 1_d|_{s'} + 2P(2_{s'})P(1_s)|2_d\rangle\langle 2_d|_{s'} \otimes |1_{c'}\rangle\langle 1_{c'}|_s + 2P(2_s)P(1_s)|2_c\rangle\langle 2_c|_s \otimes |1_{d'}\rangle\langle 1_{d'}|_{s'}$$
$$+ 4P(1_s)P(2_{s'})|1_c\rangle\langle 1_c|_s \otimes |1_d\rangle\langle 1_d|_{s'} \otimes |1_{d'}\rangle\langle 1_{d'}|_{s'}$$
$$+ 2P(2_{s'})P(1_{s'})|0\rangle\langle 0|_s \otimes |2_d\rangle\langle 2_d|_{s'} \otimes |1_{d'}\rangle\langle 1_{d'}|_{s'}) \tag{E.20}$$

$$\hat{T}_2^I = x_1^2x_2P(2_{i1})P(1_{i2})\frac{1}{16}((\hat{c}^\dagger)^3 + \hat{d}^\dagger(\hat{c}^\dagger)^2 - \hat{c}^\dagger(\hat{d}^\dagger)^2 - (\hat{d}^\dagger)^3)|0\rangle\langle 0|_s \otimes |0\rangle\langle 0|_{s'}((\hat{c})^3 + \hat{d}(\hat{c})^2 - \hat{c}(\hat{d})^2 - (\hat{d})^3)$$

$$= x_1^2x_2P(2_{i1})P(1_{i2})\frac{1}{16}(3P(3_s)|3_c\rangle\langle 3_c|_s \otimes |0\rangle\langle 0|_{s'} + 2P(2_s)P(1_{s'})|2_c\rangle\langle 2_c|_s \otimes |1_d\rangle\langle 1_d|_{s'}$$
$$+ 2P(1_s)P(2_{s'})|1_c\rangle\langle 1_c|_s \otimes |2_d\rangle\langle 2_d|_{s'} + 3P(3_{s'})|0\rangle\langle 0|_s \otimes |3_d\rangle\langle 3_d|_{s'}) \tag{E.21}$$

The above terms will contribute to four-fold events for both distinguishable and indistinguishable photons due to multi-pair emission and our bucket detector (i.e. non-PNRD),

$$P_2^D(s,s') = \mathcal{N}_1\mathcal{N}_2(1-x_1)(1-x_2)[\langle 1|_s\langle 1|_{s'}\hat{T}_2^D|1\rangle_s|1\rangle_{s'} + \langle 1|_s\langle 2|_{s'}\hat{T}_2^D|1\rangle_s|2\rangle_{s'}$$
$$+ \langle 2|_s\langle 1|_{s'}\hat{T}_2^D|2\rangle_s|1\rangle_{s'}] \tag{E.22}$$

$$= \mathcal{N}_1\mathcal{N}_2(1-x_1)(1-x_2)x_1^2x_2P(2_{i1})P(1_{i2})\frac{1}{16}[4P(2_s)P(1_{s'})$$
$$+ 2P(2_{s'})P(1_s) + 2P(2_s)P(1_s) + 4P(1_s)P(2_{s'})] \tag{E.23}$$

$$P_2^I(s,s') = \mathcal{N}_1\mathcal{N}_2(1-x_1)(1-x_2)[\langle 2|_s\langle 1|_{s'}\hat{T}_2^I|2\rangle_s|1\rangle_{s'} + \langle 1|_s\langle 2|_{s'}\hat{T}_2^I|1\rangle_s|2\rangle_{s'}] \tag{E.24}$$

$$= \mathcal{N}_1\mathcal{N}_2(1-x_1)(1-x_2)x_1^2x_2P(2_{i1})P(1_{i2})\frac{1}{16}[2P(2_s)P(1_{s'}) + 2P(1_s)P(2_{s'})] \tag{E.25}$$

The last term of Eq. E.6 is then,

$$\begin{aligned}
T_3^D =& x_1 x_2^2 P(1_{i1}) P(2_{i2}) \frac{1}{16} (\hat{c}^\dagger (\hat{c'}^\dagger)^2 - 2\hat{c}^\dagger \hat{c'}^\dagger \hat{d}^\dagger + \hat{c}^\dagger (\hat{d'}^\dagger)^2 + \hat{d}^\dagger (\hat{c'}^\dagger)^2 - 2\hat{c'}^\dagger \hat{d}^\dagger \hat{d'}^\dagger + \hat{d}^\dagger (\hat{d'}^\dagger)^2) |0\rangle\langle 0|_s \otimes |0\rangle\langle 0|_{s'} \\
& (\hat{c}(\hat{c'})^2 - 2\hat{c}\hat{c'}\hat{d} + \hat{c}(\hat{d'})^2 + \hat{d}(\hat{c'})^2 - 2\hat{c'}\hat{d}\hat{d'} + \hat{d}(\hat{d'})^2) \qquad \text{(E.26)} \\
=& x_1 x_2^2 P(1_{i1}) P(2_{i2}) \frac{1}{16} (2P(1_s)P(2_s)|1_c\rangle\langle 1_c|_s \otimes |2_{c'}\rangle\langle 2_{c'}|_s \otimes |0\rangle\langle 0|_{s'} + 4P(2_s)P(1_{s'})|1_c\rangle\langle 1_c|_s \\
& \otimes |1_{c'}\rangle\langle 1_{c'}|_s \otimes |1_d\rangle\langle 1_d|_{s'} + 2P(1_s)P(2_{s'})|1_c\rangle\langle 1_c|_s \otimes |2_{d'}\rangle\langle 2_{d'}|_{s'} + 2P(2_s)P(1_{s'})|2_{c'}\rangle\langle 2_{c'}|_s \otimes |1_d\rangle\langle 1_d|_{s'} \\
& + 4P(1_s)P(2_{s'})|1_{c'}\rangle\langle 1_{c'}|_s \otimes |1_d\rangle\langle 1_d|_{s'} \otimes |1_{d'}\rangle\langle 1_{d'}|_{s'} \\
& + 2P(1_{s'})P(2_{s'})|0\rangle\langle 0|_s \otimes |1_d\rangle\langle 1_d|_{s'} \otimes |2_{d'}\rangle\langle 2_{d'}|_{s'}) \qquad \text{(E.27)} \\
T_3^I =& x_1 x_2^2 P(1_{i1}) P(2_{i2}) \frac{1}{16} ((\hat{c}^\dagger)^3 - \hat{c}^\dagger (\hat{d}^\dagger)^2 - \hat{d}^\dagger (\hat{c}^\dagger)^2 + (\hat{d}^\dagger)^3) |0\rangle\langle 0|_s \otimes |0\rangle\langle 0|_{s'} ((\hat{c})^3 - \hat{c}(\hat{d})^2 - \hat{d}(\hat{c})^2 + (\hat{d})^3) \\
& \qquad \text{(E.28)} \\
=& x_1^2 x_2 P(2_{i1}) P(1_{i2}) \frac{1}{16} (3P(3_s)|3_c\rangle\langle 3_c|_s \otimes |0\rangle\langle 0|_{s'} + 2P(1_s)P(2_{s'})|1_c\rangle\langle 1_c|_s \otimes |2_d\rangle\langle 2_d|_{s'} \\
& + 2P(2_s)P(1_{s'})|2_c\rangle\langle 2_c|_s \otimes |1_d\rangle\langle 1_d|_{s'} + 3P(3_{s'})|0\rangle\langle 0|_s \otimes |3_d\rangle\langle 3_d|_{s'}) \qquad \text{(E.29)}
\end{aligned}$$

These terms also contributes to four-folds for both distinguishable and indistinguishable photons,

$$\begin{aligned}
P_3^D(s,s') =& \mathcal{N}_1 \mathcal{N}_2 (1-x_1)(1-x_2)[\langle 1|_s \langle 1|_{s'} \hat{T}_3^D |1\rangle_s |1\rangle_{s'} + \langle 1|_s \langle 2|_{s'} \hat{T}_3^D |1\rangle_s |2\rangle_{s'} \\
& + \langle 2|_s \langle 1|_{s'} \hat{T}_3^D |2\rangle_s |1\rangle_{s'}] \qquad \text{(E.30)} \\
=& \mathcal{N}_1 \mathcal{N}_2 (1-x_1)(1-x_2) x_1 x_2^2 P(1_{i1}) P(2_{i2}) \frac{1}{16} [4P(2_s)P(1_{s'}) \\
& + 2P(2_{s'})P(1_s) + 2P(2_s)P(1_s) + 4P(1_s)P(2_{s'})] \qquad \text{(E.31)} \\
P_3^I(s,s') =& \mathcal{N}_1 \mathcal{N}_2 (1-x_1)(1-x_2)[\langle 2|_s \langle 1|_{s'} \hat{T}_3^I |2\rangle_s |1\rangle_{s'} + \langle 1|_s \langle 2|_{s'} \hat{T}_3^I |1\rangle_s |2\rangle_{s'}] \qquad \text{(E.32)} \\
=& \mathcal{N}_1 \mathcal{N}_2 (1-x_1)(1-x_2) x_1 x_2^2 P(1_{i1}) P(2_{i2}) \frac{1}{16} [2P(2_s)P(1_{s'}) + 2P(1_s)P(2_{s'})] \qquad \text{(E.33)}
\end{aligned}$$

Let's consider for the simplicity that the idler and signal photons experience the same losses,

$$P(1_{i1}) = \eta_i = P(1_{i2}) = P(1_i) \qquad \text{(E.34)}$$

$$P(1_s) = \eta_s = P(1_{s'}) \qquad \text{(E.35)}$$

Therefore, the total probability of detecting four-fold coincidences for distinguishable photons is,

$$\begin{aligned}
P_{4F}^D =& \sum_{i,j=1}^{2} \langle i|_s \langle j|_{s'} \rho |i\rangle_s |j\rangle_{s'} \qquad \text{(E.36)} \\
=& P_1^D(s,s') + P_2^D(s,s') + P_3^D(s,s') \qquad \text{(E.37)} \\
=& \mathcal{N}_1 \mathcal{N}_2 (1-x_1)(1-x_2) x_1 x_2 P(1_i) P(1_s) [\frac{1}{2} P(1_i) P(1_s + \frac{3}{4}(x_1+x_2) P(2_i) P(2_s] \qquad \text{(E.38)}
\end{aligned}$$

Similarly, the total probability of detecting four-fold coincidences for indistinguishable photons is,

$$P_{4F}^I = \mathcal{N}_1 \mathcal{N}_2 (1-x_1)(1-x_2) x_1 x_2 P(1_i) P(1_s) \frac{1}{4} (x_1+x_2) P(2_i) P(2_s \qquad \text{(E.39)}$$

According to the expression of HOM interference, the effect of multi-pair emission on the raw visibility can be written as,

$$\begin{aligned}
V_{HOM} =& 1 - \frac{P_{4F}^I}{P_{4F}^D} \qquad \text{(E.40)} \\
=& \frac{2P(1_i)P(1_s) + 2(x_1+x_2)P(2_i)P(2_s)}{2P(1_i)P(1_s) + 3(x_1+x_2)P(2_i)P(2_s)} \qquad \text{(E.41)}
\end{aligned}$$

Assuming the brightness of both of the sources are the same and redefining losses to follow [114], we get,

$$x_1 = x_2 = x \tag{E.42}$$

$$P(2_i) = 1 - (1 - \eta_i)^2 = 2\eta_i\gamma_i, \text{ where } \gamma_i = 1 - \eta_i/2 \tag{E.43}$$

$$P(2_s) = 1 - (1 - \eta_s)^2 = 2\eta_s\gamma_s, \text{ where } \gamma_s = 1 - \eta_s/2 \tag{E.44}$$

$$V_{HOM} = \frac{1 + 8x\gamma_i\gamma_s}{1 + 12x\gamma_i\gamma_s} \tag{E.45}$$

The last expression matches the expression in [114].

E.1.2 Verifying the effect of at most three photon-pairs using MatLab

The first step of MatLab implementation is to define the transformation of the creation/annihilation operators and the wavefunctions using symbolic variable. The benefit of symbolic variable is that we can substitute the transformation of the symbolic variable as the photons propagates through the circuit. A major disadvantage of symbolic variable is that it consumes more memory (RAM), therefore, the program slows down exponentially for larger photon-states.

```
%% Transformations and state definitions. N = 2 for upto 3 photon-pairs
syms  x1 psi1 x2 psi2 rho k a b c1 c2 d1 d2 sc1
x1 = mu1; x2 = mu2;
n = 1:N;
as1 = (c1 + d1)/sqrt(2);
bs1 = (c1 - d1)/sqrt(2);
bs2 = (c2 - d2)/sqrt(2);
%% Heralding n idler photon with lumped efficiency eta_i, Pn = 1 -  (1-eta_i)^n
psi1 = (sqrt(x1).^n).*(a.^n./sqrt(factorial(n))).*sqrt(1 - (1-eta_i).^n);
psi2 = (sqrt(x2).^n).*(b.^n./sqrt(factorial(n))).*sqrt(1 - (1-eta_).^n);
```

The transformations `as1, bs1` are for indistinguishable photons and `as1, bs2` are for distinguishable photons. Modes `c1, c2` and `d1, d2` correspond to modes $\hat{c}^\dagger$, $\hat{c'}^\dagger$ and $\hat{d}^\dagger$, $\hat{d'}^\dagger$ respectively. The squeezing strengths `mu1` and `mu2` are numeric values input by the user. In the following analysis, these values are not assigned to `x1, x2`, in order to understand the symbolic manipulation and to derive a symbolic expression of visibility.

The expressions `psi1, psi2` contains the coefficients of the creation operator parts of the heralded density matrices from the two sources respectively. The annihilation operator part of the density matrix is omitted as it contains redundant information of the coefficient: multiplying the coefficient of the creation operator with its' complex conjugate gives us the correct coefficient as we are only interested in the diagonal terms. These expressions are also not normalised and the factor $(1 - x_1)(1 - x_2)$ is omitted as we have seen in the last section that the factor $\mathcal{N}_1\mathcal{N}_2(1 - x_1)(1 - x_2)$ is only a multiplication factor and cancels out in the expression of the visibility. Inputting `N = 2, eta_i = eta_s = 1`, we can verify if the program has produced the correct coefficients,

```
psi1 = [ a*x1^(1/2), (2^(1/2)*a^2*x1)/2]
psi2 = [ b*x2^(1/2), (2^(1/2)*b^2*x2)/2]
```

Now taking an outer product, collecting all the elements and removing the 4 photon-pairs term, we get the coefficients (creation operator parts) of the density matrix of the both sources (i.e. $\hat{\rho}$),

```
%% Choosing the correct terms from psi12
psi12_p = transpose(psi1)*psi2;
psi = children(sum(sum(psi_c)));
psi = psi(2:4);
```

resulting in,

```
psi = [ a*b*x1^(1/2)*x2^(1/2), (2^(1/2)*a*b^2*x1^(1/2)*x2)/2, (2^(1/2)*a^2*b*x1*x2^(1/2))/2]
```

```
%% Calculating cross terms for distinguishable case
psid = subs(psi, [a b], [as1 bs2]);
psid2 = collect(expand(psid), [c1 d1 c2 d2]);
Pdist = [];
for k1 = 1:length(psid2)
    Pdist = [Pdist (children(psid2(k1)))];
end
Pterms = simplify(Pdist);
Nterms = length(Pterms);
%
C_inc1 = zeros(1, Nterms);
C_ind1 = zeros(1, Nterms);
C_inc2 = zeros(1, Nterms);
C_ind2 = zeros(1, Nterms);
for k2 = 1:Nterms
    C_inc1(k2) = feval(symengine, 'degree', Pterms(k2), c1);
    C_ind1(k2) = feval(symengine, 'degree', Pterms(k2), d1);
    C_inc2(k2) = feval(symengine, 'degree', Pterms(k2), c2);
    C_ind2(k2) = feval(symengine, 'degree', Pterms(k2), d2);
end
C_inc1d1 = C_inc1.*C_ind1;
C_inc1d2 = C_inc1.*C_ind2;
C_inc2d1 = C_inc2.*C_ind1;
C_inc2d2 = C_inc2.*C_ind2;
Cross_index = C_inc1d1|C_inc1d2|C_inc2d1|C_inc2d2;
% Calculating the loss coefficients for detection
C_inc = C_inc1 + C_inc2;
alpha_c1c2 = sqrt( 1 - (1-eta_s).^C_inc );
alpha_c1c2(alpha_c1c2==0) = 1;
C_ind = C_ind1 + C_ind2;
alpha_d1d2 = sqrt( 1 - (1-eta_s).^C_ind );
alpha_d1d2(alpha_d1d2==0) = 1;
alpha_cd = alpha_c1c2.*alpha_d1d2;
% Calculating factorial coefficient operated on vacuum
F_c1 = sqrt(factorial(C_inc1));
F_d1 = sqrt(factorial(C_ind1));
F_c2 = sqrt(factorial(C_inc2));
F_d2 = sqrt(factorial(C_ind2));
F_cd = F_c1.*F_d1.*F_c2.*F_d2;
% Calculating coincidence counts
Pcc = subs(Pdist, [c1 d1 c2 d2], [1 1 1 1]);
Pcc = Pcc.*alpha_cd.*F_cd;
Pterms = Pterms.*alpha_cd.*F_cd;
Pcross_terms = Pterms(Cross_index ~= 0);
Pcross_terms = subs(Pcross_terms, [c1 d1 c2 d2], [1 1 1 1]);
```

```
Ppure_terms = Pterms(Cross_index == 0);
Ppure_terms = subs(Ppure_terms, [c1 d1 c2 d2], [1 1 1 1]);
Prob_all = sum(abs(Pcc).^2);
Prob_cross_d = sum(abs(Pcross_terms).^2);
Prob_pure = sum(abs(Ppure_terms).^2);
```

The above code first calculates all the 16 possible outcomes (`Nterms`) of the interferometer, `Pterms` which matches with our calculations in the last section.

```
Pterms = [ ((x1^(1/2)*x2^(1/2))/2)*c1*c2, (-(x1^(1/2)*x2^(1/2))/2)*c1*d2, ((x1^(1/2)
*x2^(1/2))/2)*d1*c2, (-(x1^(1/2)*x2^(1/2))/2)*d1*d2, ((x1^(1/2)*x2)/4)*c1*c2^2,
(-(x1^(1/2)*x2)/2)*c1*c2*d2, ((x1^(1/2)*x2)/4)*c1*d2^2, ((x1^(1/2)*x2)/4)*d1*c2^2,
(-(x1^(1/2)*x2)/2)*d1*c2*d2, ((x1^(1/2)*x2)/4)*d1*d2^2, ((x1*x2^(1/2))/4)*c1^2*c2,
(-(x1*x2^(1/2))/4)*c1^2*d2, ((x1*x2^(1/2))/2)*c1*d1*c2, (-(x1*x2^(1/2))/2)*c1*d1*d2,
((x1*x2^(1/2))/4)*d1^2*c2, (-(x1*x2^(1/2))/4)*d1^2*d2]
```

The terms `C_inc1, C_inc2` etc stores the power/degree of each creation operator and `Cross_index` separates the cross terms which contributes to the four-fold coincidences. The terms `alpha_cd` and `F_cd` calculates the loss incurred by each term and the coefficient of each term. The outcomes of the above piece of code are: `Pcross_terms` which contains all the relevant cross terms from the above expression; `Prob_cross_d` which contains the total probability for distinguishable photons,

```
Prob_cross_d = (abs(x1)*abs(x2))/2 + (3*abs(x1)*abs(x2)^2)/4 + (3*abs(x1)^2*abs(x2))/4
```

```
%% Calculating cross terms for indistinguishable case
psii = subs(psi, [a b], [as1 bs1]);
psii2 = collect(expand(psii), [c1 d1]); %3. No sum here due to statistical mixture
Pindist = [];
for k1 = 1:length(psii2)
    Pindist = [Pindist (children(psii2(k1)))];
end
Pterms = simplify(Pindist);
Nterms = length(Pterms);
%
Ci_inc1 = zeros(1, Nterms);
Ci_ind1 = zeros(1, Nterms);
for k2 = 1:Nterms
    Ci_inc1(k2) = feval(symengine, 'degree', Pterms(k2), c1);
    Ci_ind1(k2) = feval(symengine, 'degree', Pterms(k2), d1);
end
Ci_inc1d1 = Ci_inc1.*Ci_ind1;
Cross_index_id = Ci_inc1d1;
% Calculating the loss coefficients for detection
alphai_c1 = sqrt( 1 - (1-eta_s).^Ci_inc1 );
alphai_c1(alphai_c1==0) = 1;
alphai_d1 = sqrt( 1 - (1-eta_s).^Ci_ind1 );
alphai_d1(alphai_d1==0) = 1;
alphai_cd = alphai_c1.*alphai_d1;
% Calculating factorial coefficient operated on vacuum
Fi_c1 = sqrt(factorial(Ci_inc1));
Fi_d1 = sqrt(factorial(Ci_ind1));
Fi_cd = Fi_c1.*Fi_d1;
% Calculating coincidence counting
Pcc = subs(Pindist, [c1 d1], [1 1]);
```

```
Pcc = Pcc.*alphai_cd.*Fi_cd;
Pterms = Pterms.*alphai_cd.*Fi_cd;
Pcross_terms = Pterms(Cross_index_id ~= 0);
Pcross_terms = subs(Pcross_terms, [c1 d1], [1 1]);
Ppure_terms = Pterms(Cross_index_id == 0);
Ppure_terms = subs(Ppure_terms, [c1 d1], [1 1]);
```

Similarly, all 10 possibilities of 4-fold coincidences are expressed by `Pterms` as can be verified by the calculations of the last section,

```
Pterms =[ ((x1^(1/2)*x2^(1/2))/2)*c1^2, (-(x1^(1/2)*x2^(1/2))/2)*d1^2, ((x1^(1/2)*x2)/4)
*c1^3, (-(x1^(1/2)*x2)/4)*c1^2*d1, (-(x1^(1/2)*x2)/4)*c1*d1^2, ((x1^(1/2)*x2)/4)*d1^3,
((x1*x2^(1/2))/4)*c1^3, ((x1*x2^(1/2))/4)*c1^2*d1, (-(x1*x2^(1/2))/4)*c1*d1^2,
(-(x1*x2^(1/2))/4)*d1^3]
```

The final outcomes are `Pcross_terms` and `Prob_cross_id` which contains the total probability of indistinguishable photons,

```
Prob_cross_id = 2*abs(x1)*abs(x2)^2 + 2*abs(x1)^2*abs(x2)
```

```
%% Calculate visibility
P_id = double(Prob_cross_id);
P_d = double(Prob_cross_d);
V = (1 - P_id/P_d);
```

If we substitute `x1, x2` with `x` then we get the following expression of visibility in terms of symbolic variable `x`,

```
Visibility = simplify(subs(1 - Prob_cross_id/Prob_cross_d, [x1 x2], [x x]))
Visibility = (2*abs(x) + 1)/(3*abs(x) + 1)
```

which is the same as Eq. E.45 with the no losses ($\eta_i = \eta_s = 1$).

E.1.3 Extending to at most ten photon-pairs using MatLab

The above code can be extended to investigate the effect of at most ten photon-pairs on the raw visibility as done by [56] by only changing the second part of the code where the relevant terms are retained after the outer product of the heralded density matrices of the two sources,

```
%% Choosing the correct terms from psi12
psi12_p = transpose(psi1)*psi2;
in_ab = ones(N,N);
for|k1 = 2:N
    in_ab(k1,(N-k1+2):N) = 0;
end
psi_c = psi12_p.*in_ab;
psi = children(sum(sum(psi_c)));
```

The above code only keeps the upper triangular matrix of the outer product as can be understood by Fig. E.1. Following the same codes of the last section for the rest of the calculations we can evaluate the value of raw visibility for specific values of squeezing strength and losses.

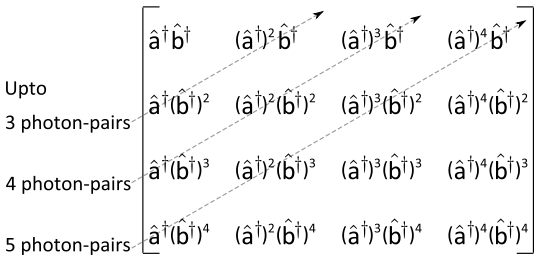

Figure E.1: Choosing the correct terms in reduced density matrix

E.1.4 Extending the multi-pair effect to MZI with imperfect PIM circuit using MatLab

The primary difference between MZI and HOM is the unitary matrix which now constitute of two beam-splitters and a phase shifter in the middle. By varying the phase in this unitary, we get the interference fringe corresponding to interference between two heralded photons. This interference also reveals the quality of the two-photon NOON state and the effect of multi-pair emission.

The imperfection of the PIM circuit is easily implemented in the code by replacing the 50:50 beam-splitter matrix by a beam-splitter with arbitrary splitting ratio η.

```
function [P_id, P_d] = Visisibility_MZI_multi_pair_loss_phi(mu1,mu2,N,alpha,phi,eta)

syms x1 psi1 x2 psi2 rho k a b c1 c2 d1 d2 sc1
x1 = mu1; x2 = mu2;
DC = [sqrt(eta) sqrt(1-eta); -sqrt(1-eta) sqrt(eta)];
M_phi = [1 0; 0 exp(1i*phi)];
U = DC*M_phi*DC;

n = 1:N;
as1 = c1*U(1,1) + d1*U(1,2);
bs1 = c1*U(2,1) + d1*U(2,2);
bs2 = c2*U(2,1) + d2*U(2,2);
% heralding n idler photon with lumped efficiency eta_i, Pn = 1 -% (1-eta_i)^n
psi1 = (sqrt(x1).^n).*(a.^n./sqrt(factorial(n))).*sqrt(1 - (1-alpha).^n);
psi2 = (sqrt(x2).^n).*(b.^n./sqrt(factorial(n))).*sqrt(1 - (1-alpha).^n);
%% Choosing the correct terms from psi12
psi12_p = transpose(psi1)*psi2;
in_ab = ones(N,N);
for k1 = 2:N
    in_ab(k1,(N-k1+2):N) = 0;
end
psi_c = psi12_p.*in_ab;
psi = children(sum(sum(psi_c)));
%% Calculating cross terms for distinguishable case
psid = subs(psi, [a b], [as1 bs2]);
psid2 = collect(expand(psid), [c1 d1 c2 d2]);
Pdist = [];
for k1 = 1:length(psid2)
    Pdist = [Pdist (children(psid2(k1)))];
end
Pterms = simplify(Pdist);
Nterms = length(Pterms);
```

```
% Separating cross terms from pure terms
C_inc1 = zeros(1, Nterms);
C_ind1 = zeros(1, Nterms);
C_inc2 = zeros(1, Nterms);
C_ind2 = zeros(1, Nterms);
for k2 = 1:Nterms
    C_inc1(k2) = feval(symengine, 'degree', Pterms(k2), c1);
    C_ind1(k2) = feval(symengine, 'degree', Pterms(k2), d1);
    C_inc2(k2) = feval(symengine, 'degree', Pterms(k2), c2);
    C_ind2(k2) = feval(symengine, 'degree', Pterms(k2), d2);
end
C_inc1d1 = C_inc1.*C_ind1;
C_inc1d2 = C_inc1.*C_ind2;
C_inc2d1 = C_inc2.*C_ind1;
C_inc2d2 = C_inc2.*C_ind2;
Cross_index = C_inc1d1|C_inc1d2|C_inc2d1|C_inc2d2;
% Calculating the loss coefficients for detection
C_inc = C_inc1 + C_inc2;
alpha_c1c2 = sqrt( 1 - (1-alpha).^C_inc );
alpha_c1c2(alpha_c1c2==0) = 1;
C_ind = C_ind1 + C_ind2;
alpha_d1d2 = sqrt( 1 - (1-alpha).^C_ind );
alpha_d1d2(alpha_d1d2==0) = 1;
alpha_cd = alpha_c1c2.*alpha_d1d2;
% Calculating factorial coefficient operated on vacuum
F_c1 = sqrt(factorial(C_inc1));
F_d1 = sqrt(factorial(C_ind1));
F_c2 = sqrt(factorial(C_inc2));
F_d2 = sqrt(factorial(C_ind2));
F_cd = F_c1.*F_d1.*F_c2.*F_d2;
% Calculating coincidence counts
Pcc = subs(simplify(Pdist), [c1 d1 c2 d2], [1 1 1 1]);
Pcc = Pcc.*alpha_cd.*F_cd;
Pterms = Pterms.*alpha_cd.*F_cd;
Pcross_terms = Pterms(Cross_index ~= 0);
Pcross_terms = subs(Pcross_terms, [c1 d1 c2 d2], [1 1 1 1]);
Ppure_terms = Pterms(Cross_index == 0);
Ppure_terms = subs(Ppure_terms, [c1 d1 c2 d2], [1 1 1 1]);
Prob_all = sum(abs(Pcc).^2);
Prob_cross_d = sum(abs(Pcross_terms).^2);
Prob_pure = sum(abs(Ppure_terms).^2);
if (Prob_all == (Prob_cross_d + Prob_pure))
    display('Probability matched.');
else
    display('Probability for dist. did not match');
end
%% Calculating cross terms for indistinguishable case
psii = subs(psi, [a b], [as1 bs1]);
psii2 = collect(expand(psii), [c1 d1]); %3. No sum due to stat. mix.
Pindist = [];
for k1 = 1:length(psii2)
    Pindist = [Pindist (children(psii2(k1)))];
end
```

```
Pterms = simplify(Pindist);
Nterms = length(Pterms);
% Separating cross terms from pure terms
Ci_inc1 = zeros(1, Nterms);
Ci_ind1 = zeros(1, Nterms);
for k2 = 1:Nterms
    Ci_inc1(k2) = feval(symengine, 'degree', Pterms(k2), c1);
    Ci_ind1(k2) = feval(symengine, 'degree', Pterms(k2), d1);
end
Ci_inc1d1 = Ci_inc1.*Ci_ind1;
Cross_index_id = Ci_inc1d1;
% Calculating the loss coefficients for detection
alphai_c1 = sqrt( 1 - (1-alpha).^Ci_inc1 );
alphai_c1(alphai_c1==0) = 1;
alphai_d1 = sqrt( 1 - (1-alpha).^Ci_ind1 );
alphai_d1(alphai_d1==0) = 1;
alphai_cd = alphai_c1.*alphai_d1;
% Calculating factorial coefficient operated on vacuum
Fi_c1 = sqrt(factorial(Ci_inc1));
Fi_d1 = sqrt(factorial(Ci_ind1));
Fi_cd = Fi_c1.*Fi_d1;
% Calculating coincidence counting
Pcc = subs(Pindist, [c1 d1], [1 1]);
Pcc = Pcc.*alphai_cd.*Fi_cd;
Pterms = Pterms.*alphai_cd.*Fi_cd;
Pcross_terms = Pterms(Cross_index_id ~= 0);
Pcross_terms = subs(Pcross_terms, [c1 d1], [1 1]);
Ppure_terms = Pterms(Cross_index_id == 0);
Ppure_terms = subs(Ppure_terms, [c1 d1], [1 1]);
Prob_all = sum(abs(Pcc).^2);
if isempty(Pcross_terms)
    Prob_cross_id = 0;
else
    Prob_cross_id = sum(abs(Pcross_terms).^2);
end
Prob_pure = sum(abs(Ppure_terms).^2);
if double(Prob_all - (Prob_cross_id + Prob_pure)) < 1e-10
    display('Probability matched.');
else
    fprintf('Probability for indist. did not match, del(P)= %e ',
    double(Prob_all - (Prob_cross_id + Prob_pure)));
    display(Prob_cross_id);
end
%P_id = double(subs(Prob_cross_id, [x1 x2], [mu1 mu2]));
%P_d = double(subs(Prob_cross_d, [x1 x2], [mu1 mu2]));
P_id = double(Prob_cross_id);
P_d = double(Prob_cross_d);
end
```

The above code calculates the 4-fold events for a set phase of the unitary. If we vary the phase and calculate the 4-folds, then we get a fringe, which is then used to estimate the visibility,

```
function [Vi,Vd, Pi, Pd, phi] = Visisibility_MZI_multi_pair_loss(mu1,mu2,N,eta,alpha)
format long g;
display('MZI-loss.');

phi = linspace(0.0001, 2*pi, 100) + pi;
Pi = zeros(1,length(phi));
Pd = Pi;
for k1 = 1:length(phi)
   n_printf = fprintf('phi = %f pi.', phi(k1)/pi);
 [Pi(k1),Pd(k1)]=Visisibility_MZI_multi_pair_loss_phi(mu1,mu2,N,alpha,phi(k1),eta);
end
Pi = Pi/max(Pi);
Pd = Pd/max(Pd);
Vi = (max(Pi)-min(Pi))/(max(Pi)+min(Pi));
Vd = (max(Pd)-min(Pd))/(max(Pd)+min(Pd));
end
```

E.1.5 Implementing the source imperfection

Augmenting a second optical mode to the single-mode twin-beam squeezer, we get a multi-mode twin-beam squeezer. If both of the heralded single-photon sources are multi-mode, then the PIM can be implemented in two possible ways. In the first instant, both of the sources can be thought as identical with identical optical modes. Otherwise, optical modes of one of the sources can be expressed in terms of the other. In that case, the primary optical mode of both of the sources will be the same but the second optical mode will be different from each other.

```
function [Vi,Vd,Pi,Pd,phi_d] ...
= Visisibility_MZI_multi_pair_loss_two_Schmidt_modes_B(mu1,mu2,r1,r2,N,eta_u,alpha)
format long g;
phi_d = linspace(0.0001, 2*pi, 100) + pi;
syms x11 x12 x21 x22 psi1 psi2 phi ...
         a11 a12 b21 b22 c11 c12 c21 c22 d11 d12 d21 d22 eta
eta = eta_u;
DC = [sqrt(eta) sqrt(1-eta); -sqrt(1-eta) sqrt(eta)];
M_phi = [exp(1i*phi/2) 0; 0 exp(-1i*phi/2)];
U = simplify(DC*M_phi*DC);
as11 = c11*U(1,1) + d11*U(1,2);
as12 = c12*U(1,1) + d12*U(1,2);
bs21 = c21*U(2,1) + d21*U(2,2);
bs22 = c22*U(2,1) + d22*U(2,2);
%% Determining the value of squeezing for each Schmidt mode
[mu11, mu12] = find_relative_n(mu1, r1);
x11 = mu11./(1+mu11); x12 = mu12./(1+mu12);
[mu21, mu22] = find_relative_n(mu2, r2);
x21 = mu21./(1+mu21); x22 = mu22./(1+mu22);
%% Truncating the source terms
n = 0:N;
% Determining the truncated terms
Ni = N + 1;
in_s = ones(Ni,Ni);
for k1 = 2:Ni
    in_s(k1,(Ni-k1+2):Ni) = 0;
```

```
end
in_s(1,1) = 0;
% Source 1
psi11 = (sqrt(x11).^n).*(a11.^n./sqrt(factorial(n)));
psi12 = (sqrt(x12).^n).*(a12.^n./sqrt(factorial(n)));
psi1_all = transpose(psi11)*psi12;
psi1 = children(sum(sum(psi1_all.*in_s)));
% heralding at least 1 idler photon with lumped efficiency eta_i, Pn = 1 - (1-eta_i)^n
in_a11 = zeros(1, length(psi1));
in_a12 = zeros(1, length(psi1));
for k1 = 1:length(psi1)
   in_a11(k1) = feval(symengine, 'degree', psi1(k1), a11);
   in_a12(k1) = feval(symengine, 'degree', psi1(k1), a12);
end
in_a = in_a11 + in_a12;
P_heralding1 = 1 - (1-alpha).^in_a;
psi1 = psi1.*sqrt(P_heralding1);
% Source 2
psi21 = (sqrt(x21).^n).*(b21.^n./sqrt(factorial(n)));
psi22 = (sqrt(x22).^n).*(b22.^n./sqrt(factorial(n)));
psi2_all = transpose(psi21)*psi22;
psi2 = children(sum(sum(psi2_all.*in_s)));
% heralding at least 1 idler photon with lumped efficiency eta_i, Pn = 1 - (1-eta_i)^n
in_b21 = zeros(1, length(psi2));
in_b22 = zeros(1, length(psi2));
for k1 = 1:length(psi2)
   in_b21(k1) = feval(symengine, 'degree', psi2(k1), b21);
   in_b22(k1) = feval(symengine, 'degree', psi2(k1), b22);
end
in_b = in_b21 + in_b22;
P_heralding2 = 1 - (1-alpha).^in_b;
psi2 = psi2.*sqrt(P_heralding2);
%% Choosing the correct terms from psi12
psi12_p = transpose(psi1)*psi2;
[in1,in2] = size(psi12_p);
In_a11 = zeros(in1,in2);
In_a12 = In_a11;
In_b21 = In_a11;
In_b22 = In_a11;
for k1 = 1:in1
    for k2 = 1:in2
        In_a11(k1,k2) = feval(symengine, 'degree', psi12_p(k1,k2), a11);
        In_a12(k1,k2) = feval(symengine, 'degree', psi12_p(k1,k2), a12);
        In_b21(k1,k2) = feval(symengine, 'degree', psi12_p(k1,k2), b21);
        In_b22(k1,k2) = feval(symengine, 'degree', psi12_p(k1,k2), b22);
    end
end
in_ab = In_a11 + In_a12 + In_b21 + In_b22;
in_ab(in_ab > (N+1)) = 0;
in_ab(in_ab ~= 0) = 1;
psi_c = psi12_p.*in_ab;
psi = children(sum(sum(psi_c)));
%% Calculating cross terms for distinguishable case
```

```
psid = subs(psi, [a11 a12 b21 b22], [as11 as12 bs21 bs22]);
psid2 = collect(expand(psid), [c11 c12 c21 c22 d11 d12 d21 d22]);
Pdist = [];
for k1 = 1:length(psid2)
    Pdist = [Pdist (children(psid2(k1)))];
end
Pterms = simplify(Pdist);
Nterms = length(Pterms);
% Separating cross terms from pure terms
C_inc11 = zeros(1, Nterms);
C_inc12 = zeros(1, Nterms);
C_ind11 = zeros(1, Nterms);
C_ind12 = zeros(1, Nterms);
C_inc21 = zeros(1, Nterms);
C_inc22 = zeros(1, Nterms);
C_ind21 = zeros(1, Nterms);
C_ind22 = zeros(1, Nterms);
for k2 = 1:Nterms
    C_inc11(k2) = feval(symengine, 'degree', Pterms(k2), c11);
    C_inc12(k2) = feval(symengine, 'degree', Pterms(k2), c12);
    C_ind11(k2) = feval(symengine, 'degree', Pterms(k2), d11);
    C_ind12(k2) = feval(symengine, 'degree', Pterms(k2), d12);
    C_inc21(k2) = feval(symengine, 'degree', Pterms(k2), c21);
    C_inc22(k2) = feval(symengine, 'degree', Pterms(k2), c22);
    C_ind21(k2) = feval(symengine, 'degree', Pterms(k2), d21);
    C_ind22(k2) = feval(symengine, 'degree', Pterms(k2), d22);
end
C_inc = C_inc11 + C_inc12 + C_inc21 + C_inc22;
C_ind = C_ind11 + C_ind12 + C_ind21 + C_ind22;
Cross_index_d = C_inc.*C_ind;
% Calculating the loss coefficients for detection
alpha_c = sqrt( 1 - (1-alpha).^C_inc );
alpha_c(alpha_c==0) = 1;
alpha_d = sqrt( 1 - (1-alpha).^C_ind );
alpha_d(alpha_d==0) = 1;
alpha_cd = alpha_c.*alpha_d;
% Factorial coefficients when operated on vacuum
F_c11 = sqrt(factorial(C_inc11));
F_c12 = sqrt(factorial(C_inc12));
F_c21 = sqrt(factorial(C_inc21));
F_c22 = sqrt(factorial(C_inc22));
F_c = F_c11.*F_c12.*F_c21.*F_c22;
F_d11 = sqrt(factorial(C_ind11));
F_d12 = sqrt(factorial(C_ind12));
F_d21 = sqrt(factorial(C_ind21));
F_d22 = sqrt(factorial(C_ind22));
F_d = F_d11.*F_d12.*F_d21.*F_d22;
F_cd = F_c.*F_d;
% Calculating coincidence counts
Pcc = subs(Pdist, [c11 c12 d11 d12 c21 c22 d21 d22], [1 1 1 1 1 1 1 1]);
Pcc = Pcc.*alpha_cd.*F_cd;
Pterms = Pterms.*alpha_cd.*F_cd;
Pcross_terms = Pterms(Cross_index_d ~= 0);
```

```
Pcross_terms = subs(Pcross_terms, [c11 c12 d11 d12 c21 c22 d21 d22], ...
[1 1 1 1 1 1 1 1]);
Ppure_terms = Pterms(Cross_index_d == 0);
Ppure_terms = subs(Ppure_terms, [c11 c12 d11 d12 c21 c22 d21 d22], ...
 [1 1 1 1 1 1 1 1]);
Pd = zeros(1,length(phi_d));
for k4 = 1:length(phi_d)
    Prob_all = double(sum(abs( subs(Pcc, phi, phi_d(k4)) ).^2));
    Prob_pure = double(sum(abs( subs(Ppure_terms, phi, phi_d(k4)) ).^2));
    Prob_cross_d = double(sum(abs( subs(Pcross_terms, phi, phi_d(k4)) ).^2));
    if (Prob_all - (Prob_cross_d + Prob_pure)) < 1e-10
        display('Probability matched.');
    else
        fprintf('Probability for dist. did not match, del(P)= %e ',...
         double(Prob_all - (Prob_cross_d + Prob_pure)) );
    end
    Pd(k4) = double(Prob_cross_d);
end
%% Calculating cross terms for indistinguishable case
psii = subs(psid, [c21 c22 d21 d22], [c11 c12 d11 d12]);
psii2 = collect(expand(psii), [c11 c12 d11 d12]);
Pindist = [];
for k1 = 1:length(psii2)
    Pindist = [Pindist (children(psii2(k1)))];
end
Pterms = simplify(Pindist);
Nterms = length(Pterms);
% Separating cross terms from pure terms
Ci_inc11 = zeros(1, Nterms);
Ci_inc12 = zeros(1, Nterms);
Ci_ind11 = zeros(1, Nterms);
Ci_ind12 = zeros(1, Nterms);
for k2 = 1:Nterms
    Ci_inc11(k2) = feval(symengine, 'degree', Pterms(k2), c11);
    Ci_inc12(k2) = feval(symengine, 'degree', Pterms(k2), c12);
    Ci_ind11(k2) = feval(symengine, 'degree', Pterms(k2), d11);
    Ci_ind12(k2) = feval(symengine, 'degree', Pterms(k2), d12);
end
Ci_inc11d11 = Ci_inc11.*Ci_ind11;
Ci_inc11d12 = Ci_inc11.*Ci_ind12;
Ci_inc12d11 = Ci_inc12.*Ci_ind11;
Ci_inc12d12 = Ci_inc12.*Ci_ind12;
Cross_index_id = Ci_inc11d11|Ci_inc11d12|Ci_inc12d11|Ci_inc12d12;
% Calculating the loss coefficients for detection
Ci_inc = Ci_inc11 + Ci_inc12;
alphai_c = sqrt( 1 - (1-alpha).^Ci_inc );
alphai_c(alphai_c==0) = 1;
Ci_ind = Ci_ind11 + Ci_ind12;
alphai_d = sqrt( 1 - (1-alpha).^Ci_ind );
alphai_d(alphai_d==0) = 1;
alphai_cd = alphai_c.*alphai_d;
% Factorial coefficients when operated on vacuum
Fi_c11 = sqrt(factorial(Ci_inc11));
```

```
Fi_c12 = sqrt(factorial(Ci_inc12));
Fi_d11 = sqrt(factorial(Ci_ind11));
Fi_d12 = sqrt(factorial(Ci_ind12));
Fi_cd = Fi_c11.*Fi_c12.*Fi_d11.*Fi_d12;
% Calculating coincidence counting
Pcc = subs(Pindist, [c11 c12 d11 d12], [1 1 1 1]);
Pcc = Pcc.*alphai_cd.*Fi_cd;
Pterms = Pterms.*alphai_cd.*Fi_cd;
Pcross_terms = Pterms(Cross_index_id ~= 0);
Pcross_terms = subs(Pcross_terms, [c11 c12 d11 d12], [1 1 1 1]);
Ppure_terms = Pterms(Cross_index_id == 0);
Ppure_terms = subs(Ppure_terms, [c11 c12 d11 d12], [1 1 1 1]);
Pi = zeros(1,length(phi_d));
for k4 = 1:length(phi_d)
    Prob_all = double(sum(abs( subs(Pcc, phi, phi_d(k4)) ).^2));
    Prob_pure = double(sum(abs( subs(Ppure_terms, phi, phi_d(k4)) ).^2));
    Prob_cross_id = double(sum(abs( subs(Pcross_terms, phi, phi_d(k4)) ).^2));

    if (Prob_all - (Prob_cross_id + Prob_pure)) < 1e-10
        display('Probability matched.');
    else
        fprintf('Probability for indist. did not match, del(P)= %e ', ...
        Prob_all - (Prob_cross_id + Prob_pure));
    end
    Pi(k4) = double(Prob_cross_id);
end
Pi = Pi/max(Pi);
Pd = Pd/max(Pd);
Vi = (max(Pi)-min(Pi))/(max(Pi)+min(Pi));
Vd = (max(Pd)-min(Pd))/(max(Pd)+min(Pd));
end

function [mu11, mu12] = find_relative_n(nbar, r)
syms n11 positive;
mu11 = double(solve((1-r)*n11^2 + ( (1+r) - (1-r)*nbar )*n11 - nbar ));
mu12 = double( r*mu11./( 1 + (1-r)*mu11 ) );
end
```

E.2 Fitting the MZI fringe data

There are few ways to fit the PIM data as described below.

E.2.1 Fitting with multi-pair and multi-mode

The above code which implements Eq. 5.35, can be used to fit the raw PIM data obtained in Chap. 6. The fitting parameters will be $\eta_{MZI}, x_1, x_2, r_1, r_2, \eta_i, \eta_s$ and maximum 4-fold counts C_{max}. The above code is resource hungry to fit all of these parameters with the data, especially, when $N > 3$. The resource requirement is reduced by first performing a series of measurements to determine: η_{MZI} by inputting classical light through the MZI and fitting the output intensities and x_1, x_2, eta_i, η_s from brightness measurements. The spectral purity is determined by the ratio of the squeezing strengths of the Schmidt modes, represented by r_1, r_2 which is assumed from the simulation from Chap. 5. Using these values for a range of squeezing strength the maximum 4-fold counts C_{max} is fitted to match the data.

E.2.2 Fitting assuming multi-mode only

Assuming no multi-pair emission, the PIM data can be fitted as a weighted sum of completely indistinguishable photons and completely distinguishable photons,

```
phi_c = @(Y,theta) (Y(1)*(theta + Y(2)));
U11 = @(eta,phi) ( 1 + eta*(exp(1i*phi) - 1) );
U12 = @(eta,phi) ( sqrt(eta*(1-eta))*(exp(1i*phi) - 1) );
U21 = @(eta,phi) ( sqrt(eta*(1-eta))*(exp(1i*phi) - 1) );
U22 = @(eta,phi) ( exp(1i*phi) - eta*(exp(1i*phi) - 1) );
CC4F_fit_function = @(X, theta) ( X(1)*( X(2)*abs(U11(X(3),phi_c([X(4) X(5)],...
theta)).*U22(X(3),phi_c([X(4) X(5)],theta)) + U12(X(3),phi_c([X(4) X(5)],theta))...
.*U21(X(3),phi_c([X(4) X(5)],theta))).^2 + (1-X(2))*(abs(U11(X(3),phi_c([X(4) ...
X(5)],theta)).*U22(X(3),phi_c([X(4) X(5)],theta))).^2 + abs(U12(X(3),phi_c([X(4) ...
X(5)],theta)).*U21(X(3),phi_c([X(4) X(5)],theta))).^2) ) );
Cmax = max(FF_S);
eta_ov = 0.14;
eta = 0.4;
scaling = 1;
theta0 = 0;
X0 = [0.93*Cmax eta_ov eta scaling theta0];
CC4F_test = CC4F_fit_function_2(X0, phase_res*pi);
[xfit,resnorm] = lsqcurvefit(CC4F_fit_function,X0,phase*pi,FF_S);
```

The fitting parameters for IME01 PIM data are,

η_{MZI}	η_{ov}	C_{max}	θ_0	$scaling$
39.191 ± 2.977	67.315 ± 10.988	242.7964 ± 15.044	-0.7468 ± 0.093	1.045 ± 0.026

Table E.1: Fitting parameters of IME01 PIM considering multi-mode only

E.2.3 Fitting assuming multi-pair only

Assuming no multi-mode effect, the PIM data can be fitted as a weighted sum of single-pair interference and multi-pair interference which is exactly out of phase,

```
CC4F_fit_function = @(X, theta) ( X(1)*( abs(U11(X(3),phi_c([X(4) X(5)],theta))...
.*U22(X(3),phi_c([X(4) X(5)],theta)) + U12(X(3),phi_c([X(4) X(5)],theta)).*U21(X(3),...
phi_c([X(4) X(5)],theta))).^2 + X(2)* cos(phi_c([X(4) X(5)+pi/2],theta)).^2) );
```

Dissemination

Scientific audience

① **I. I. Faruque**, G. F. Sinclair, D. Bonneau, J. G. Rarity, M. G. Thompson. "On-chip quantum interference with heralded photons from two independent micro-ring resonator sources in silicon photonics," Optics Express 26(16), pages 20379-20395 (2018).

② **I. I. Faruque**, G. F. Sinclair, D. Bonneau, T. Ono, J. G. Rarity, M. G. Thompson. "Indistinguishability of heralded single-photons from nanowire waveguides in silicon photonics," (In preparation).

③ D. Llewellyn†, Y. Ding†, **I. I. Faruque**†, S. Paesani, D. Bacco, R. Santagati, G. F. Sinclair, Y. Li, M. Huber, M. Malik, K. Rottwitt, J. L. O'Brien, J. G. Rarity, Q. Gong, L. K. Oxenløwe, J. Wang M. G. Thompson. "Multi-photon toolbox for quantum communication," (In preparation).

† equal contribution

④ **I. I. Faruque**, D. Bonneau, G. F. Sinclair, M. G. Thompson. "Heralded quantum interference of on-chip micro-ring resonator sources in silicon photonics," CLEO, 14-19 May 2017, San Jose, CA, USA.

⑤ **I. I. Faruque**, D. Llewellyn, Y. Ding, S. Paesani, R. Santagati, D. Bonneau, G. F. Sinclair, D. Bacco, K. Rottwitt, L. K. Oxenløwe, J. L. O'Brien, J. Wang, J. G. Rarity M. G. Thompson. "Indistinguishable photon-pairs from pure and bright silicon micro-ring resonator sources," CLEO, 13-18 May 2018, San Jose, CA, USA.

⑥ D. Llewellyn, Y. Ding, **I. Faruque**, S. Paesani, R. Santagati, J. Kennard, D. Bacco, K. Rottwitt, L. K. Oxenløwe, J. L. O'Brien, J. Wang M. G. Thompson. "Generation and manipulation of multi-photon entangled states on a silicon photonic device," CLEO, 13-18 May 2018, San Jose, CA, USA.

General audience

① Discussion with the general public during the "European researchers' night," Bristol, 25 September 2015.

② Exhibited the research based on this thesis with a poster and a silicon photonic chip demo in University of Bristol flagship outreach, "Research without Borders," 12 May 2017.

③ Quantum in the conversation: Geometry of the ring-resonator. `https://quantumtalksblog.wordpress.com/2017/04/18/the-geometry-of-ring-resonator-research-stories-with-imad-faruque/`

References

[1] Naomi S. Ginsberg, Sean R. Garner and Lene Vestergaard Hau, “Coherent control of optical information with matter wave dynamics,” Nature 445, pages 623-626 (2007).

[2] Patricio Leboeuf and Simon Moulieras, “Superfluid Motion of Light,” Phys. Rev. Lett. 105, 163904 (2010).

[3] Alberto Amo, Jérôme Lefrère, Simon Pigeon, Claire Adrados, Cristiano Ciuti, Iacopo Carusotto, Romuald Houdré, Elisabeth Giacobino and Alberto Bramati, “Superfluidity of polaritons in semiconductor microcavities,” Nature Physics 5, pages 805-810 (2009).

[4] Yuya Morimoto and Peter Baum, “Diffraction and microscopy with attosecond electron pulse trains,” Nature Physics 14, pages 252-256 (2018).

[5] F. Calegari, D. Ayuso, A. Trabattoni, L. Belshaw, S. De Camillis, S. Anumula, F. Frassetto, L. Poletto, A. Palacios, P. Decleva, J. B. Greenwood, F. Martín and M. Nisoli, “Ultrafast electron dynamics in phenylalanine initiated by attosecond pulses,” Science 346(6207), pages 336-339 (2014).

[6] Gregory S. Engel, Tessa R. Calhoun, Elizabeth L. Read, Tae-Kyu Ahn, Tomáš Mančal, Yuan-Chung Cheng, Robert E. Blankenship and Graham R. Fleming, “Evidence for wavelike energy transfer through quantum coherence in photosynthetic systems,” Nature 446, pages 782-786 (2007).

[7] Seth Lloyd, “Quantum coherence in biological systems,” J. Phys.: Conf. Ser. 302, 012037 (2011).

[8] Philip Ball, “Physics of life: The dawn of quantum biology,” Nature 474, pages 272-274 (2011).

[9] T. J. Kippenberg, R. Holzwarth and S. A. Diddams, “Microresonator-Based Optical Frequency Combs,” Science 332(6029), pages 555-559 (2011).

[10] Jeremy L. O’Brien, “Optical Quantum Computing,” Science 318(5856), pages 1567-1570 (2007).

[11] Peter W. Shor, “Polynomial-Time Algorithms for Prime Factorization and Discrete Logarithms on a Quantum Computer,” SIAM Rev., 41(2), 303-332 (1999).

[12] R. L. Rivest, A. Shamir and L. Adleman, “A Method for Obtaining Digital Signatures and Public-Key Cryptosystems,” Communications of the ACM 21(2), pages 120-126 (1978).

[13] Daniel Gottesman and Isaac L. Chuang, “Demonstrating the viability of universal quantum computation using teleportation and single-qubit operations,” Nature 402, pages 390-393 (1999).

[14] Robert Raussendorf and Hans J. Briegel, “A One-Way Quantum Computer,” Phys. Rev. Lett. 86, 5188 (2001).

[15] Mercedes Gimeno-Segovia, “Towards Practical Linear Optical Quantum Computing,” PhD Thesis, Imperial College London (2015).

[16] E. Knill, R. Laflamme and G. J. Milburn, “A scheme for efficient quantum computation with linear optics,” Nature 409, pages 46-52 (2001).

[17] Chen Sun, Mark T. Wade, Yunsup Lee, Jason S. Orcutt, Luca Alloatti, Michael S. Georgas, Andrew S. Waterman, Jeffrey M. Shainline, Rimas R. Avizienis, Sen Lin, Benjamin R. Moss, Rajesh Kumar, Fabio Pavanello, Amir H. Atabaki, Henry M. Cook, Albert J. Ou, Jonathan C. Leu, Yu-Hsin Chen, Krste Asanović, Rajeev J. Ram, Miloš A. Popović and Vladimir M. Stojanović, “Single-chip microprocessor that communicates directly using light,” Nature 528, pages 534-538 (2015).

[18] Terry Rudolph, “Why I am optimistic about the silicon-photonic route to quantum computing,” APL Photonics 2, 030901 (2017).

[19] John F. Clauser, “Experimental distinction between the quantum and classical field-theoretic predictions for the photoelectric effect,” Phys. Rev. D 9, 853 (1974).

[20] Robert W. Boyd, “Nonlinear Optics,” Elsevier (2008).

[21] E. T. Jaynes and F. W. Cummings, “Comparison of quantum and semiclassical radiation theories with application to the beam maser,” Proceedings of the IEEE 51(1), pages 89-109 (1963).

[22] Jake Iles-Smith, Dara P. S. McCutcheon, Ahsan Nazir and Jesper Mørk, “Phonon scattering inhibits simultaneous near-unity efficiency and indistinguishability in semiconductor single-photon sources,” Nature Photonics 11, pages 521-526 (2017).

[23] Dara P. S. McCutcheon, “Optical signatures of non-Markovian behavior in open quantum systems,” Phys. Rev. A 93, 022119 (2016).

[24] Lingbang Zhu, Xianxin Guo, Chi Shu, Heejeong Jeong and Shengwang Du, “Bright narrowband biphoton generation from a hot rubidium atomic vapor cell,” Appl. Phys. Lett. 110, 161101 (2017).

[25] Xiao-Liu Chu, Stephan Götzinger and Vahid Sandoghdar, “A single molecule as a high-fidelity photon gun for producing intensity-squeezed light,” Nature Photonics 11, pages 58-62 (2017).

[26] Graham D. Marshall, Torsten Gaebel, Jonathan C. F. Matthews, Jörg Enderlein, Jeremy L. O’Brien and James R. Rabeau, “Coherence properties of a single dipole emitter in diamond,” New J. Phys. 13, 055016 (2011).

[27] Gary F. Sinclair and Mark G. Thompson, “Effect of self- and cross-phase modulation on photon pairs generated by spontaneous four-wave mixing in integrated optical waveguides,” Phys. Rev. A 94, 063855 (2016).

[28] Christopher C. Gerry and Peter L. Knight, “Introductory Quantum Optics,” Cambridge University Press (2004).

[29] O. Alibart, J. Fulconis, G. K. L. Wong, S. G. Murdoch, W. J. Wadsworth and J. G. Rarity, “Photon pair generation using four-wave mixing in a microstructured fibre: theory versus experiment,” New J. Phys. 8, 67 (2006).

[30] Andreas Christ, Kaisa Laiho, Andreas Eckstein, Katiúscia N Cassemiro and Christine Silberhorn, “Probing multimode squeezing with correlation functions,” New J. Phys. 13, 033027 (2011).

[31] Zhenshan Yang, Marco Liscidini and John E. Sipe, “Spontaneous parametric down-conversion in waveguides: A backward Heisenberg picture approach,” Phys. Rev. A 77, 033808 (2008).

[32] Damien Bonneau, “Integrated quantum photonics at telecommunication wavelength in silicon-on-insulator and lithium niobate platforms,” PhD thesis, University of Bristol (2013).

[33] Lukas G. Helt, Marco Liscidini and John E. Sipe, “How does it scale? Comparing quantum and classical nonlinear optical processes in integrated devices,” Journal of the Optical Society of America B 29(8), pages 2199-2212 (2012).

[34] Lukas G. Helt, Zhenshan Yang, Marco Liscidini and John E. Sipe, “Spontaneous four-wave mixing in microring resonators,” Optics Letters 35(18), pages 3006-3008 (2010).

[35] Ken-ichi Harada, Hiroki Takesue, Hiroshi Fukuda, Tai Tsuchizawa, Toshifumi Watanabe, Koji Yamada, Yasuhiro Tokura and Sei-ichi Itabashi, “Frequency and Polarization Characteristics of Correlated Photon-Pair Generation Using a Silicon Wire Waveguide,” IEEE Journal of Selected Topics in Quantum Electronics 16(1), pages 325-331 (2010).

[36] Damien Bonneau, Joshua W. Silverstone and Mark G. Thompson, “Silicon Quantum Photonics,” In: Pavesi L., Lockwood D. (eds) Silicon Photonics III. Topics in Applied Physics, vol 122. Springer, Berlin, Heidelberg (2016).

[37] Wolfgang Mauerer, Malte Avenhaus, Wolfram Helwig and Christine Silberhorn, “How colors influence numbers: Photon statistics of parametric down-conversion,” Phys. Rev. A 80, 053815 (2009).

[38] Chaoxuan Ma, Xiaoxi Wang, Vikas Anant, Andrew D. Beyer, Matthew D. Shaw and Shayan Mookherjea, “Silicon photonic entangled photon-pair and heralded single photon generation with CAR > 12,000 and $g^{(2)}(0) < 0.006$,” Optics Express 25(26), pages 32995-33006 (2017).

[39] Riccardo Marchetti, Cosimo Lacava, Ali Khokhar, Xia Chen, Ilaria Cristiani, David J. Richardson, Graham T. Reed, Periklis Petropoulos and Paolo Minzioni, “High-efficiency grating-couplers: demonstration of a new design strategy,” Scientific Reports 7, 16670 (2017).

[40] Angelo Bozzola, Lee Carroll, Dario Gerace, Ilaria Cristiani and Lucio Claudio Andreani, “Optimising apodized grating couplers in a pure SOI platform to -0.5 dB coupling efficiency,” Optics Express 23(12), pages 16289-16304 (2015).

[41] Zachary Vernon, Marco Liscidini and John E. Sipe, “No free lunch: the trade-off between heralding rate and efficiency in microresonator-based heralded single photon sources,” Optics Letters 41(4), pages 788-791 (2016).

[42] Yoon-Ho Kim and Warren P. Grice, “Measurement of the spectral properties of the two-photon state generated via type II spontaneous parametric downconversion,” Optics Letters 30(8), pages 908-910 (2005).

[43] Andreas Eckstein, Guillaume Boucher, Aristide Lemaître, Pascal Filloux, Ivan Favero, Giuseppe Leo, John E. Sipe, Marco Liscidini and Sara Ducci, “High resolution spectral characterization of two photon states via classical measurements,” Laser and Photonics Reviews 8(5), pages L76-L80 (2014).

[44] Iman Jizan, Bryn Bell, Lukas G. Helt, Alvaro Casas Bedoya, Chunle Xiong and Benjamin J. Eggleton, “Phase-sensitive tomography of the joint spectral amplitude of photon pair sources,” Optics Letters 41(20), pages 4803-4806 (2016).

[45] Sunil Mittal, Venkata Vikram Orre, Alessandro Restelli, Reza Salem, Elizabeth A. Goldschmidt and Mohammad Hafezi, “Temporal and spectral manipulations of correlated photons using a time lens,” Phys. Rev. A 96, 043807 (2017).

[46] C. K. Hong, Z. Y. Ou and L. Mandel, “Measurement of subpicosecond time intervals between two photons by interference,” Phys. Rev. Lett. 59, 2044 (1987).

[47] J. G. Rarity, P. R. Tapster, E. Jakeman, T. Larchuk, R. A. Campos, M. C. Teich and B. E. A. Saleh, “Two-photon interference in a Mach-Zehnder interferometer,” Phys. Rev. Lett. 65, 1348 (1990).

[48] Z. Y. Ou, X. Y. Zou, L. J. Wang and L. Mandel, “Experiment on nonclassical fourth-order interference,” Phys. Rev. A 42, 2957 (1990).

[49] Fumihiro Kaneda and Paul G. Kwiat, “High-efficiency single-photon generation via large-scale active time multiplexing,” ArXiv ID: 1803.04803 (2018).

[50] Hui Wang, Yu He, Yu-Huai Li, Zu-En Su, Bo Li, He-Liang Huang, Xing Ding, Ming-Cheng Chen, Chang Liu, Jian Qin, Jin-Peng Li, Yu-Ming He, Christian Schneider, Martin Kamp, Cheng-Zhi Peng, Sven Höfling, Chao-Yang Lu and Jian-Wei Pan, “High-efficiency multiphoton boson sampling,” Nature Photonics 11, pages 361-365 (2017).

[51] Ranjeet Kumar, Jun Rong Ong, Marc Savanier and Shayan Mookherjea, “Controlling the spectrum of photons generated on a silicon nanophotonic chip,” Nature Communications 5, 5489 (2014).

[52] L. G. Helt, Agata M. Brańczyk, Marco Liscidini and M. J. Steel, “Parasitic Photon-Pair Suppression via Photonic Stop-Band Engineering,” Phys. Rev. Lett. 118, 073603 (2017).

[53] Iman Jizan, L. G. Helt, Chunle Xiong, Matthew J. Collins, Duk-Yong Choi, Chang Joon Chae, Marco Liscidini, M. J. Steel, Benjamin J. Eggleton and Alex S. Clark, “Bi-photon spectral correlation measurements from a silicon nanowire in the quantum and classical regimes,” Scientific Reports 5, 12557 (2015).

[54] Piotr Roztocki, Michael Kues, Christian Reimer, Benjamin Wetzel, Stefania Sciara, Yanbing Zhang, Alfonso Cino, Brent E. Little, Sai T. Chu, David J. Moss and Roberto Morandotti, “Practical system for the generation of pulsed quantum frequency combs,” Optics Express 25(16), pages 18940-18949 (2017).

[55] Davide Grassani, Angelica Simbula, Stefano Pirotta, Matteo Galli, Matteo Menotti, Nicholas C. Harris, Tom Baehr-Jones, Michael Hochberg, Christophe Galland, Marco Liscidini and Daniele Bajoni, “Energy correlations of photon pairs generated by a silicon microring resonator probed by Stimulated Four Wave Mixing,” Scientific Reports 6, 23564 (2016).

[56] Ken-ichi Harada, Hiroki Takesue, Hiroshi Fukuda, Tai Tsuchizawa, Toshifumi Watanabe, Koji Yamada, Yasuhiro Tokura and Sei-ichi Itabashi, “Indistinguishable photon pair generation using two independent silicon wire waveguides,” New J. Phys. 13, 065005 (2011).

[57] C. Xiong, X. Zhang, Z. Liu, M. J. Collins, A. Mahendra, L. G. Helt, M. J. Steel, D. -Y. Choi, C. J. Chae, P. H. W. Leong and B. J. Eggleton, “Active temporal multiplexing of indistinguishable heralded single photons,” Nature Communications 7, 10853 (2016).

[58] Xiang Zhang, Runyu Jiang, Bryn A. Bell, Duk-Yong Choi, Change Joon Chae and Chunle Xiong, “Interfering Heralded Single Photons from Two Separate Silicon Nanowires Pumped at Different Wavelengths,” Technologies 4(3), 25 (2016).

[59] Stefan F. Preble, Michael L. Fanto, Jeffrey A. Steidle, Christopher C. Tison, Gregory A. Howland, Zihao Wang and Paul M. Alsing, “On-Chip Quantum Interference from a Single Silicon Ring-Resonator Source,” Phys. Rev. Applied 4, 021001 (2015).

[60] S. Clemmen, K. Phan Huy, W. Bogaerts, R. G. Baets, Ph. Emplit and S. Massar, “Continuous wave photon pair generation in silicon-on-insulator waveguides and ring resonators,” Optics Express 17(19), pages 16558-16570 (2009).

[61] Wen-Tan Fang, Yin-Hai Li, Zhi-Yuan Zhou, Li-Xin Xu, Guang-Can Guo and Bao-Sen Shi, “On-chip generation of time-and wavelength-division multiplexed multiple time-bin entanglement,” Optics Express 26(10), pages 12912-12921 (2018).

[62] Ming Zhang, Lan-Tian Feng, Zhi-Yuan Zhou, Yang Chen, Hao Wu, Ming Li, Guo-Ping Guo, Guang-Can Guo, Dao-Xin Dai and Xi-Feng Ren, “Generation of multiphoton entangled quantum states with a single silicon nanowire,” ArXiv ID: 1803.01641 (2018).

[63] Lan-Tian Feng, Ming Zhang, Yang Chen, Guo-Ping Guo, Guang-Can Guo, Dao-Xin Dai and Xi-Feng Ren, “On-chip transverse-mode entangled photon source,” ArXiv ID: 1802.09847 (2018).

[64] Cale M. Gentry, Gil Triginer Garćes, Xiaoge Zeng, and Miloš A. Popović, “Tailoring of Individual Photon Lifetimes as a Degree of Freedom in Resonant Quantum Photonic Sources,” Conference on Lasers and Electro-Optics, California United States, JTu5A.17 (2016).

[65] Z. Vernon, M. Menotti, C. C. Tison, J. A. Steidle, M. L. Fanto, P. M. Thomas, S. F. Preble, A. M. Smith, P. M. Alsing, M. Liscidini and J. E. Sipe, “Truly unentangled photon pairs without spectral filtering,” Optics Letters 42(18), pages 3638-3641 (2017).

[66] J. B. Christensen, J. G. Koefoed, K. Rottwitt and C. J. McKinstrie, “Engineering spectrally unentangled photon pairs from nonlinear microring resonators by pump manipulation,” Optics Letters 43(4), pages 859-862 (2018).

[67] Jelena Notaros, Fabio Pavanello, Mark T. Wade, Cale M. Gentry, Amir Atabaki, Luca Alloatti, Rajeev J. Ram and Miloš A. Popović, “Ultra-Efficient CMOS Fiber-to-Chip Grating Couplers,” Optical Fiber Communication Conference, Washington, D.C. United States, M2I.5 (2016).

[68] P. Del’Haye, O. Arcizet, A. Schliesser, R. Holzwarth and T. J. Kippenberg, “Full Stabilization of a Microresonator-Based Optical Frequency Comb,” Phys. Rev. Lett. 101, 053903 (2008).

[69] Christian Reimer, Lucia Caspani, Matteo Clerici, Marcello Ferrera, Michael Kues, Marco Peccianti, Alessia Pasquazi, Luca Razzari, Brent E. Little, Sai T. Chu, David J. Moss and Roberto Morandotti, “Integrated frequency comb source of heralded single photons,” Optics Express 22(6), pages 6535-6546 (2014).

[70] Alessia Pasquazi, Lucia Caspani, Marco Peccianti, Matteo Clerici, Marcello Ferrera, Luca Razzari, David Duchesne, Brent E. Little, Sai T. Chu, David J. Moss and Roberto Morandotti, “Self-locked optical parametric oscillation in a CMOS compatible microring resonator: a route to robust optical frequency comb generation on a chip,” Optics Express 21(11), pages 13333-13341 (2013).

[71] Steven Rogers, Daniel Mulkey, Xiyuan Lu, Wei C. Jiang and Qiang Lin, “High Visibility Time-Energy Entangled Photons from a Silicon Nanophotonic Chip,” ACS Photonics 3 (10), pages 1754-1761 (2016).

[72] Nobuyuki Matsuda and Hiroki Takesue, “Generation and manipulation of entangled photons on silicon chips,” Nanophotonics 5(3), pages 440-455 (2016).

[73] C. M. Wilkes, X. Qiang, J. Wang, R. Santagati, S. Paesani, X. Zhou, D. A. B. Miller, G. D. Marshall, M. G. Thompson and J. L. O’Brien, “60 dB high-extinction auto-configured Mach-Zehnder interferometer,” Optics Letters 41(22), pages 5318-5321 (2016).

[74] Hansuek Lee, Tong Chen, Jiang Li, Oskar Painter and Kerry J. Vahala, “Ultra-low-loss optical delay line on a silicon chip,” Nature Communications 3, 867 (2012).

[75] Guoliang Li, Jin Yao, Hiren Thacker, Attila Mekis, Xuezhe Zheng, Ivan Shubin, Ying Luo, Jin-hyoung Lee, Kannan Raj, John E. Cunningham and Ashok V. Krishnamoorthy, “Ultralow-loss, high-density SOI optical waveguide routing for macrochip interconnects,” Optics Express 20(11), pages 12035-12039 (2012).

[76] Stefan Abel, Felix Eltes, J. Elliott Ortmann, Andreas Messner, Pau Castera, Tino Wagner, Darius Urbonas, Alvaro Rosa, Ana M. Gutierrez, Domenico Tulli, Ping Ma, Benedikt Baeuerle, Arne Josten, Wolfgang Heni, Daniele Caimi, Lukas Czornomaz, Alexander A. Demkov, Juerg Leuthold, Pablo Sanchis and Jean Fompeyrine, “Large Pockels effect in micro- and nanostructured barium titanate integrated on silicon,” Nature Materials 18, 42-47 (2019).

[77] Shiyang Zhu and Guo-Qiang Lo, “Vertically Stacked Multilayer Photonics on Bulk Silicon Toward Three-Dimensional Integration,” Journal of Lightwave Technology 34(2), pages 386-392 (2016).

[78] Diego Pérez-Galacho, Carlos Alonso-Ramos, Florent Mazeas, Xavier Le Roux, Dorian Oser, Weiwei Zhang, Delphine Marris-Morini, Laurent Labonté, Sébastien Tanzilli, Éric Cassan and Laurent Vivien, “Optical pump-rejection filter based on silicon subwavelength engineered photonic structures,” Optics Letters 42(8), pages 1468-1471 (2017).

[79] Micol Previde Massara, Matteo Menotti, Nicola Bergamasco, Nicholas C. Harris, Tom Baehr-Jones, Michael Hochberg, Christophe Galland, Marco Liscidini, Matteo Galli and Daniele Bajoni, “Nonlinear characterization of a silicon integrated Bragg waveguide filter,” Optics Letters 43(5), pages 1171-1174 (2018).

[80] T. Heindel, C. Schneider, M. Lermer, S. H. Kwon, T. Braun, S. Reitzenstein, S. Höfling, M. Kamp and A. Forchel, “Electrically driven quantum dot-micropillar single photon source with 34% overall efficiency,” Appl. Phys. Lett. 96, 011107 (2010).

[81] F. Hargart, C. A. Kessler, T. Schwarzbäck, E. Koroknay, S. Weidenfeld, M. Jetter and P. Michler, “Electrically driven quantum dot single-photon source at 2 GHz excitation repetition rate with ultra-low emission time jitter,” Appl. Phys. Lett. 102, 011126 (2013).

[82] Igor Aharonovich, Dirk Englund and Milos Toth, “Solid-state single-photon emitters,” Nature Photonics 10, pages 631-641 (2016).

[83] Juan C. Loredo, Nor A. Zakaria, Niccolo Somaschi, Carlos Anton, Lorenzo de Santis, Valerian Giesz, Thomas Grange, Matthew A. Broome, Olivier Gazzano, Guillaume Coppola, Isabelle Sagnes, Aristide Lemaitre, Alexia Auffeves, Pascale Senellart, Marcelo P. Almeida and Andrew G. White, “Scalable performance in solid-state single-photon sources,” Optica 3(4), pages 433-440 (2016).

[84] N. Somaschi, V. Giesz, L. De Santis, J. C. Loredo, M. P. Almeida, G. Hornecker, S. L. Portalupi, T. Grange, C. Antón, J. Demory, C. Gómez, I. Sagnes, N. D. Lanzillotti-Kimura, A. Lemaítre, A. Auffeves, A. G. White, L. Lanco and P. Senellart, “Near-optimal single-photon sources in the solid state,” Nature Photonics 10, pages 340-345 (2016).

[85] Hui Wang, Z.-C. Duan, Y.-H. Li, Si Chen, J.-P. Li, Y.-M. He, M.-C. Chen, Yu He, X. Ding, Cheng-Zhi Peng, Christian Schneider, Martin Kamp, Sven Höfling, Chao-Yang Lu and Jian-Wei Pan, “Near-Transform-Limited Single Photons from an Efficient Solid-State Quantum Emitter,” Phys. Rev. Lett. 116, 213601 (2016).

[86] Je-Hyung Kim, Shahriar Aghaeimeibodi, Christopher J. K. Richardson, Richard P. Leavitt and Edo Waks, “Super-Radiant Emission from Quantum Dots in a Nanophotonic Waveguide,” Nano Lett. 18(8), pages 4734-4740 (2018).

[87] Ross C. Schofield, Kyle D. Major, Samuele Grandi, Sebastien Boissier, E. A. Hinds and Alex S. Clark, “Efficient excitation of dye molecules for single photon generation,” ArXiv ID: 1803.10115 (2018).

[88] D. J. P. Ellis, A. J. Bennett, C. Dangel, J. P. Lee, J. P. Griffiths, T. A. Mitchell, T. -K. Paraiso, P. Spencer, D. A. Ritchie and A. J. Shields, “Independent indistinguishable quantum light sources on a reconfigurable photonic integrated circuit,” ArXiv ID: 1803.04468 (2018).

[89] Feng Liu, Alistair J. Brash, John O’Hara, Luis M. P. P. Martins, Catherine L. Phillips, Rikki J. Coles, Benjamin Royall, Edmund Clarke, Christopher Bentham, Nikola Prtljaga, Igor E. Itskevich, Luke R. Wilson, Maurice S. Skolnick and A. Mark Fox, “High Purcell factor generation of indistinguishable on-chip single photons,” Nature Nanotechnology 13, pages 835-840 (2018).

[90] Milad Khoshnegar, Tobias Huber, Ana Predojević, Dan Dalacu, Maximilian Prilmüller, Jean Lapointe, Xiaohua Wu, Philippe Tamarat, Brahim Lounis, Philip Poole, Gregor Weihs and Hamed Majedi, “A solid state source of photon triplets based on quantum dot molecules,” Nature Communications 8, 15716 (2017).

[91] Alexander Schlehahn, Sarah Fischbach, Ronny Schmidt, Arsenty Kaganskiy, André Strittmatter, Sven Rodt, Tobias Heindel and Stephan Reitzenstein, “A stand-alone fiber-coupled single-photon source,” Scientific Reports 8, 1340 (2018).

[92] Toan Trong Tran, Christopher Elbadawi, Daniel Totonjian, Charlene J. Lobo, Gabriele Grosso, Hyowon Moon, Dirk R. Englund, Michael J. Ford, Igor Aharonovich and Milos

Toth, “Robust Multicolor Single Photon Emission from Point Defects in Hexagonal Boron Nitride,” ACS Nano 10(8), pages 7331-7338 (2016).

[93] Emma R. Schmidgall, Srivatsa Chakravarthi, Michael Gould, Ian R. Christen, Karine Hestroffer, Fariba Hatami and Kai-Mei C. Fu, “Frequency Control of Single Quantum Emitters in Integrated Photonic Circuits,” Nano Lett. 18(2), pages 1175-1179 (2018).

[94] Morgan M. Weston, Helen M. Chrzanowski, Sabine Wollmann, Allen Boston, Joseph Ho, Lynden K. Shalm, Varun B. Verma, Michael S. Allman, Sae Woo Nam, Raj B. Patel, Sergei Slussarenko and Geoff J. Pryde, “Efficient and pure femtosecond-pulse-length source of polarization-entangled photons,” Optics Express 24(10), pages 10869-10879 (2016).

[95] Fumihiro Kaneda, Karina Garay-Palmett, Alfred B. U’Ren and Paul G. Kwiat, “Heralded single-photon source utilizing highly nondegenerate, spectrally factorable spontaneous parametric downconversion,” Optics Express 24(10), pages 10733-10747 (2016).

[96] Feiyan Hou, Xiao Xiang, Runai Quan, Mengmeng Wang, Yiwei Zhai, Shaofeng Wang, Tao Liu, Shougang Zhang and Ruifang Dong, “An efficient source of frequency anti-correlated entanglement at telecom wavelength,” Appl. Phys. B 122:128, pages 122-128 (2016).

[97] Francesco Graffitti, Peter Barrow, Massimiliano Proietti, Dmytro Kundys and Alessandro Fedrizzi, “Independent high-purity photons created in domain-engineered crystals,” Optica 5(5), pages 514-517 (2018).

[98] Linda Sansoni, Kai Hong Luo, Christof Eigner, Raimund Ricken, Viktor Quiring, Harald Herrmann and Christine Silberhorn, “A two-channel, spectrally degenerate polarization entangled source on chip,” npj Quantum Information 3(5) (2017).

[99] Nicola Montaut, Linda Sansoni, Evan Meyer-Scott, Raimund Ricken, Viktor Quiring, Harald Herrmann and Christine Silberhorn, “High-Efficiency Plug-and-Play Source of Heralded Single Photons,” Phys. Rev. Applied 8, 024021 (2017).

[100] Peter J. Mosley, Jeff S. Lundeen, Brian J. Smith, Piotr Wasylczyk, Alfred B. U’Ren, Christine Silberhorn and Ian A. Walmsley, “Heralded Generation of Ultrafast Single Photons in Pure Quantum States,” Phys. Rev. Lett. 100, 133601 (2008).

[101] Ryan S. Bennink, “Optimal collinear Gaussian beams for spontaneous parametric down-conversion,” Phys. Rev. A 81, 053805 (2010).

[102] P. Ben Dixon, Danna Rosenberg, Veronika Stelmakh, Matthew E. Grein, Ryan S. Bennink, Eric A. Dauler, Andrew J. Kerman, Richard J. Molnar and Franco N. C. Wong, “Heralding efficiency and correlated-mode coupling of near-IR fiber-coupled photon pairs,” Phys. Rev. A 90, 043804 (2014).

[103] Olivier Alibart, Virginia D’Auria, Marc De Micheli, Florent Doutre, Florian Kaiser, Laurent Labonté, Tommaso Lunghi, Éric Picholle and Sébastien Tanzilli, “Quantum photonics at telecom wavelengths based on lithium niobate waveguides,” J. Opt. 18, 104001 (2016).

[104] Mian Zhang, Cheng Wang, Rebecca Cheng, Amirhassan Shams-Ansari and Marko Lončar, “Monolithic ultra-high-Q lithium niobate microring resonator,” Optica 4(12), pages 1536-1537 (2017).

[105] Cheng Wang, Mian Zhang, Brian Stern, Michal Lipson and Marko Lončar, "Nanophotonic lithium niobate electro-optic modulators," Optics Express 26(2), pages 1547-1555 (2018).

[106] Panagiotis Vergyris, Thomas Meany, Tommaso Lunghi, Gregory Sauder, James Downes, M. J. Steel, Michael J. Withford, Olivier Alibart and Sébastien Tanzilli, "On-chip generation of heralded photon-number states," Scientific Reports 6, 35975 (2016).

[107] Simone Atzeni, Adil S. Rab, Giacomo Corrielli, Emanuele Polino, Mauro Valeri, Paolo Mataloni, Nicolò Spagnolo, Andrea Crespi, Fabio Sciarrino and Roberto Osellame, "Integrated sources of entangled photons at the telecom wavelength in femtosecond-laser-written circuits," Optica 5(3), pages 311-314 (2018).

[108] Xiang Guo, Chang-ling Zou, Carsten Schuck, Hojoong Jung, Risheng Cheng and Hong X Tang, "Parametric down-conversion photon-pair source on a nanophotonic chip," Light: Science & Applications 6, page e16249 (2017).

[109] Rolf Horn, Payam Abolghasem, Bhavin J. Bijlani, Dongpeng Kang, A. S. Helmy and Gregor Weihs, "Monolithic Source of Photon Pairs," Phys. Rev. Lett. 108, 153605 (2012).

[110] Justin B. Spring, Patrick S. Salter, Benjamin J. Metcalf, Peter C. Humphreys, Merritt Moore, Nicholas Thomas-Peter, Marco Barbieri, Xian-Min Jin, Nathan K. Langford, W. Steven Kolthammer, Martin J. Booth and Ian A. Walmsley, "On-chip low loss heralded source of pure single photons," Optics Express 21(11), pages 13522-13532 (2013).

[111] Justin B. Spring, Paolo L. Mennea, Benjamin J. Metcalf, Peter C. Humphreys, James C. Gates, Helen L. Rogers, Christoph Söller, Brian J. Smith, W. Steven Kolthammer, Peter G. R. Smith and Ian A. Walmsley, "Chip-based array of near-identical, pure, heralded single-photon sources," Optica 4(1), pages 90-96 (2017).

[112] Matthew T. Posner, T. Hiemstra, Paolo L. Mennea, Rex H. S. Bannerman, Ulrich B. Hoff, Andreas Eckstein, W. Steven Kolthammer, Ian A. Walmsley, Devin H. Smith, James C. Gates and Peter G. R. Smith, "High-birefringence direct UV-written waveguides for use as heralded single-photon sources at telecommunication wavelengths," Optics Express 26(19), pages 24678-24686 (2018).

[113] Bin Fang, Offir Cohen, Jamy B. Moreno and Virginia O. Lorenz, "State engineering of photon pairs produced through dual-pump spontaneous four-wave mixing," Optics Express 21(3), pages 2707-2717 (2013).

[114] J Fulconis, O Alibart, W J Wadsworth and J G Rarity, "Quantum interference with photon pairs using two micro-structured fibres," New J. Phys. 9, 276 (2007).

[115] Bin Fang, Offir Cohen, Marco Liscidini, John E. Sipe and Virginia O. Lorenz, "Fast and highly resolved capture of the joint spectral density of photon pairs," Optica 1(5), pages 281-284 (2014).

[116] D. Cruz-Delgado, R. Ramirez-Alarcon, E. Ortiz-Ricardo, J. Monroy-Ruz, F. Dominguez-Serna, H. Cruz-Ramirez, K. Garay-Palmett and A. B. U'Ren, "Fiber-based photon-pair source capable of hybrid entanglement in frequency and transverse mode, controllably scalable to higher dimensions," Scientific Reports 6, 27377 (2016).

[117] Gabriel J. Mendoza, Raffaele Santagati, Jack Munns, Elizabeth Hemsley, Mateusz Piekarek, Enrique Martín-López, Graham D. Marshall, Damien Bonneau, Mark G. Thompson and Jeremy L. O'Brien, "Active temporal and spatial multiplexing of photons," Optica 3(2), pages 127-132 (2016).

[118] A. L. Migdall, D. Branning and S. Castelletto, "Tailoring single-photon and multi-photon probabilities of a single-photon on-demand source," Phys. Rev. A 66, 053805 (2002).

[119] Evan Jeffrey, Nicholas A Peters and Paul G Kwiat, "Towards a periodic deterministic source of arbitrary single-photon states," New J. Phys. 6, 100 (2004).

[120] Chaitali Joshi, Alessandro Farsi, Stéphane Clemmen, Sven Ramelow and Alexander L. Gaeta, "Frequency multiplexing for quasi-deterministic heralded single-photon sources," Nature Communications 9, 847 (2018).

[121] Robert J. A. Francis-Jones, Rowan A. Hoggarth and Peter J. Mosley, "All-fiber multiplexed source of high-purity single photons," Optica 3(11), pages 1270-1273 (2016).

[122] Xi-Lin Wang, Luo-Kan Chen, W. Li, H.-L. Huang, C. Liu, C. Chen, Y.-H. Luo, Z.-E. Su, D. Wu, Z.-D. Li, H. Lu, Y. Hu, X. Jiang, C.-Z. Peng, L. Li, N.-L. Liu, Yu-Ao Chen, Chao-Yang Lu and Jian-Wei Pan, "Experimental Ten-Photon Entanglement," Phys. Rev. Lett. 117, 210502 (2016).

[123] T. Gerrits, F. Marsili, V. B. Verma, L. K. Shalm, M. Shaw, R. P. Mirin and S. W. Nam, "Spectral correlation measurements at the Hong-Ou-Mandel interference dip," Phys. Rev. A 91, 013830 (2015).

[124] Vahid Ansari, Markus Allgaier, Linda Sansoni, Benjamin Brecht, Jonathan Roslund, Nicolas Treps, Georg Harder and Christine Silberhorn, "Temporal-mode tomography of single photons," Conference on Lasers and Electro-Optics, California United States, FTh4E.4 (2016).

[125] Kevin Zielnicki, Karina Garay-Palmett, Daniel Cruz-Delgado, Hector Cruz-Ramirez, Michael F. O'Boyle, Bin Fang, Virginia O. Lorenz, Alfred B. U'Ren and Paul G. Kwiat, "Joint spectral characterization of photon-pair sources," Journal of Modern Optics 65(10), pages 1141-1160 (2018).

[126] M. Beck, "Comparing measurements of $g^{(2)}(0)$ performed with different coincidence detection techniques," Journal of the Optical Society of America B 24(12), pages 2972-2978 (2007).

[127] Roger A. Smith, Dileep V. Reddy, Dashiell L.P. Vitullo and M. G. Raymer, "Double-heralded generation of two-photon-states by spontaneous four-wave-mixing in the presence of noise," Optics Express 24(6), pages 5809-5821 (2016).

[128] Xi-Lin Wang, Yi-Han Luo, He-Liang Huang, Ming-Cheng Chen, Zu-En Su, Chang Liu, Chao Chen, Wei Li, Yu-Qiang Fang, Xiao Jiang, Jun Zhang, Li Li, Nai-Le Liu, Chao-Yang Lu and Jian-Wei Pan, "18-Qubit Entanglement with Six Photons' Three Degrees of Freedom," Phys. Rev. Lett. 120, 260502 (2018).

[129] J. M. Donohue, M. Mastrovich and K. J. Resch, "Spectrally Engineering Photonic Entanglement with a Time Lens," Phys. Rev. Lett. 117, 243602 (2016).

[130] Simon Laibacher and Vincenzo Tamma, "Symmetries and entanglement features of inner-mode resolved correlations of interfering nonidentical photons," ArXiv ID: 1706.05578 (2017).

[131] Ao Shen, Bo Du, Ze-Hao Wang, Yang Dong, Xiang-Dong Chen, Guang-Can Guo and Fang-Wen Sun, “Indistinguishability-induced classical-to-nonclassical transition of photon statistics,” Phys. Rev. A 95, 053851 (2017).

[132] Hatim Salih, “Counterfactual quantum erasure: spooky action without entanglement,” R. Soc. open sci. (2018).

[133] Luca S. Costanzo, Antonio S. Coelho, Nicola Biagi, Jaromír Fiurášek, Marco Bellini and Alessandro Zavatta, “Measurement-Induced Strong Kerr Nonlinearity for Weak Quantum States of Light,” Phys. Rev. Lett. 119, 013601 (2017).

[134] Yong Sup Ihn, Yosep Kim, Vincenzo Tamma and Yoon-Ho Kim, “Second-Order Temporal Interference with Thermal Light: Interference beyond the Coherence Time,” Phys. Rev. Lett. 119, 263603 (2017).

[135] Qing Li, Marcelo Davanço and Kartik Srinivasan, “Efficient and low-noise single-photon-level frequency conversion interfaces using silicon nanophotonics,” Nature Photonics 10, pages 406-414 (2016).

[136] Z. Vernon, M. Liscidini and J. E. Sipe, “Quantum frequency conversion and strong coupling of photonic modes using four-wave mixing in integrated microresonators,” Phys. Rev. A 94, 023810 (2016).

[137] Lucia Caspani, Christian Reimer, Michael Kues, Piotr Roztocki, Matteo Clerici, Benjamin Wetzel, Yoann Jestin, Marcello Ferrera, Marco Peccianti, Alessia Pasquazi, Luca Razzari, Brent E. Little, Sai T. Chu, David J. Moss and Roberto Morandotti, “Multifrequency sources of quantum correlated photon pairs on-chip: a path toward integrated Quantum Frequency Combs,” Nanophotonics 5(2), pages 351-362 (2017).

[138] Daniel Tiarks, Steffen Schmidt, Gerhard Rempe and Stephan Dürr, “Optical π phase shift created with a single-photon pulse,” Science Advances 2(4), e1600036 (2016).

[139] Kutlu Kutluer, María Florencia Pascual-Winter, Julian Dajczgewand, Patrick M. Ledingham, Margherita Mazzera, Thierry Chanelière and Hugues de Riedmatten, “Spectral-hole memory for light at the single-photon level,” Phys. Rev. A 93, 040302(R) (2016).

[140] Smart cut SOI wafer, https://www.soitec.com/en/products/smart-cut.

[141] Rezwanul Haque Khandokar, Masuduzzaman Bakaul, Stan Skafidas, Thas Nirmalathas and Md Asaduzzaman, “Performance of Planar, Rib, and Photonic Crystal Silicon Waveguides in Tailoring Group-Velocity Dispersion and Mode Loss,” IEEE Journal of Selected Topics in Quantum Electronics 22(2), pages 73-80 (2016).

[142] Rong Sun, Po Dong, Ning-ning Feng, Ching-yin Hong, Jurgen Michel, Michal Lipson and Lionel Kimerling, “Horizontal single and multiple slot waveguides: optical transmission at λ=1550 nm,” Optics Express 15(26), pages 17967-17972 (2007).

[143] Bahaa E. A. Saleh and Malvin Carl Teich, “Fundamentals of Photonics,” John Wiley & Sons, Inc (2001).

[144] P. Kaspar, R. Kappeler, D. Erni and H. Jäckel, “Relevance of the light line in planar photonic crystal waveguides with weak vertical confinement,” Optics Express 19(24), pages 24344-24353 (2011).

[145] Lukas Chrostowski, UBCx: Phot1x Silicon Photonics Design, Fabrication and Data Analysis.

[146] Chao Li, Huijuan Zhang, Mingbin Yu and G. Q. Lo, “CMOS-compatible high efficiency double-etched apodized waveguide grating coupler,” Optics Express 21(7), pages 7868-7874 (2013).

[147] Jaime Cardenas, Carl B. Poitras, Kevin Luke, Lian-Wee Luo, Paul Adrian Morton and Michal Lipson, “High Coupling Efficiency Etched Facet Tapers in Silicon Waveguides,” IEEE Photonics Technology Letters 26(23), pages 2380-2382 (2014).

[148] Yunhong Ding, Christophe Peucheret, Haiyan Ou and Kresten Yvind, “Fully etched apodized grating coupler on the SOI platform with -0.58 dB coupling efficiency,” Optics Letters 39(18), pages 5348-5350 (2014).

[149] Andy Eu-Jin Lim, Junfeng Song, Qing Fang, Chao Li, Xiaoguang Tu, Ning Duan, Kok Kiong Chen, Roger Poh-Cher Tern and Tsung-Yang Liow, “Review of Silicon Photonics Foundry Efforts,” IEEE Journal of Selected Topics in Quantum Electronics 20(4), 8300112 (2014).

[150] Erman Engin, Damien Bonneau, Chandra M. Natarajan, Alex S. Clark, M. G. Tanner, R. H. Hadfield, Sanders N. Dorenbos, Val Zwiller, Kazuya Ohira, Nobuo Suzuki, Haruhiko Yoshida, Norio Iizuka, Mizunori Ezaki, Jeremy L. O’Brien and Mark G. Thompson, “Photon pair generation in a silicon micro-ring resonator with reverse bias enhancement,” Optics Express 21(23), pages 27826-27834 (2013).

[151] Evan Meyer-Scott, Nicola Montaut, Johannes Tiedau, Linda Sansoni, Harald Herrmann, Tim J. Bartley and Christine Silberhorn, “Limits on the heralding efficiencies and spectral purities of spectrally filtered single photons from photon-pair sources,” Phys. Rev. A 95, 061803(R) (2017).

[152] P. A. Temple and C. E. Hathaway, “Multiphonon Raman Spectrum of Silicon,” Phys. Rev. B 7, pages 3685-3697 (1973).

[153] Pieter Kok and Samuel L. Braunstein, “Postselected versus nonpostselected quantum teleportation using parametric down-conversion,” Phys. Rev. A 61, 042304 (2000).

[154] J. W. Silverstone, D. Bonneau, K. Ohira, N. Suzuki, H. Yoshida, N. Iizuka, M. Ezaki, C. M. Natarajan, M. G. Tanner, R. H. Hadfield, V. Zwiller, G. D. Marshall, J. G. Rarity, J. L. O’Brien and M. G. Thompson, “On-chip quantum interference between silicon photon-pair sources,” Nature Photonics 8, pages 104-108 (2014).

[155] J. G. Rarity, “Interference of Single Photons from Separate Sourcesa,” Annals of the New York Academy of Sciences 755(1), pages 624-631 (1995).

[156] Charles H. Bennett, Gilles Brassard, Claude Crépeau, Richard Jozsa, Asher Peres and William K. Wootters, “Teleporting an unknown quantum state via dual classical and Einstein-Podolsky-Rosen channels,” Phys. Rev. Lett. 70, 1895 (1993).

[157] James L. Park, “The concept of transition in quantum mechanics,” Foundations of Physics 1(1), pages 23-33 (1970).

[158] D. Dieks, “Communication by EPR devices,” Physics Letters A 92(6), pages 271-272 (1982).

[159] W. K. Wootters and W. H. Zurek, “A single quantum cannot be cloned,” Nature 299, pages 802-803 (1982).

[160] Giacomo Mauro D'Ariano, Chiara Macchiavello and Paolo Perinotti, "Superbroadcasting of Mixed States," Phys. Rev. Lett. 95, 060503 (2005).

[161] V. Bužek and M. Hillery, "Quantum copying: Beyond the no-cloning theorem," Phys. Rev. A 54, 1844 (1996).

[162] Dik Bouwmeester, Jian-Wei Pan, Klaus Mattle, Manfred Eibl, Harald Weinfurter and Anton Zeilinger, "Experimental quantum teleportation," Nature 390, pages 575-579 (1997).

[163] A. Furusawa, J. L. Sørensen, S. L. Braunstein, C. A. Fuchs, H. J. Kimble and E. S. Polzik, "Unconditional Quantum Teleportation," Science 282(5389), pages 706-709 (1998).

[164] Mark Fox, "Quantum Optics: An Introduction," Oxford University Press Oxford (2006).

[165] Lukas Chrostowski and Michael Hochberg, "Silicon Photonics Design From Devices to Systems," Cambridge University Press (2015).

[166] Wesley D. Sacher, Ying Huang, Guo-Qiang Lo and Joyce K. S. Poon, "Multilayer Silicon Nitride-on-Silicon Integrated Photonic Platforms and Devices," Journal of Lightwave Technology 33(4) (2015).